

# Sheffield Hallam University

*Research and development in optical biosensors for determination of toxic environmental pollutants.*

TSARGORODSKA, Anna.

Available from the Sheffield Hallam University Research Archive (SHURA) at:

<http://shura.shu.ac.uk/20458/>

## A Sheffield Hallam University thesis

This thesis is protected by copyright which belongs to the author.

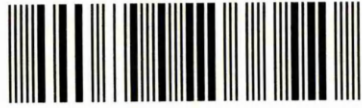
The content must not be changed in any way or sold commercially in any format or medium without the formal permission of the author.

When referring to this work, full bibliographic details including the author, title, awarding institution and date of the thesis must be given.

Please visit <http://shura.shu.ac.uk/20458/> and <http://shura.shu.ac.uk/information.html> for further details about copyright and re-use permissions.

Adsetts Centre City Campus  
Sheffield S1 1WB

101 876 059 8



Sheffield Hallam University  
Learning and IT Services  
Adsetts Centre City Campus  
Sheffield S1 1WB

# REFERENCE

**Return to Learning Centre of issue**  
**Fines are charged at 50p per hour**



ProQuest Number: 10701104

All rights reserved

INFORMATION TO ALL USERS

The quality of this reproduction is dependent upon the quality of the copy submitted.

In the unlikely event that the author did not send a complete manuscript and there are missing pages, these will be noted. Also, if material had to be removed, a note will indicate the deletion.



ProQuest 10701104

Published by ProQuest LLC (2017). Copyright of the Dissertation is held by the Author.

All rights reserved.

This work is protected against unauthorized copying under Title 17, United States Code  
Microform Edition © ProQuest LLC.

ProQuest LLC.  
789 East Eisenhower Parkway  
P.O. Box 1346  
Ann Arbor, MI 48106 – 1346

**RESEARCH and DEVELOPMENT in  
OPTICAL BIOSENSORS for  
DETERMINATION of TOXIC  
ENVIRONMENTAL POLLUTANTS**

**Anna Tsargorodska**

A thesis submitted in partial fulfilment of the requirements of  
Sheffield Hallam University for the degree of Doctor of Philosophy



June 2007

# Declarations

I hereby declare that this thesis submitted for the degree of PhD is the result of my own research and that this thesis has not been submitted for a higher degree to any other University or Institution.

A handwritten signature in black ink, appearing to be 'A. Tsargorodska', with a long horizontal stroke extending to the right.

Signed

/Anna Tsargorodska/

# Abstract

The detection of pollutants (such as toxins, heavy metal ions, and pesticides) in water and food plays an important role in human health and safety regulations. Different optical biosensing techniques enabling the monitoring of these compounds were chosen for this study.

Low molecular weight (LMW) environmental toxins, such as simazine, atrazine, nonylphenol and T-2 mycotoxin were registered with the methods of surface plasmon resonance (SPR) and the recently developed total internal reflection ellipsometry (TIRE). The immune assay approach was exploited for *in situ* registration of the above toxins with specific antibodies immobilized onto a gold surface via a polyelectrolyte layer using electrostatic self-assembly (ESA) technique. TIRE showed a higher sensitivity than the SPR technique. The obtained responses of the TIRE method were higher than estimated for the immune binding of single molecules of nonylphenol or T-2 mycotoxin. The mechanism of the binding of large aggregates of these toxins to respective antibodies was suggested as a possible reason for this. The formation of large molecular aggregates of toxin molecules on the surface was later proven by the AFM study.

The prototype of the portable sensor array device for water pollution monitoring was based on a  $\text{SiO}_2/\text{Si}_3\text{N}_4$  planar waveguide with a sensing window coated with ESA film containing pH sensitive organic chromophore molecules and different enzymes (namely, urease, acetyl- and butyryl- cholinesterase) adsorbed on a disposable nylon membrane. The sensor was capable of registration of enzyme reactions as well as their inhibition by traces of some typical water pollutants, such as heavy metal ions  $\text{Cd}^{2+}$ ,  $\text{Pb}^{2+}$ , and  $\text{Ni}^{2+}$ , and pesticides imidacloprid and DVDP over a wide range of concentrations (from 1000 ppb down to 0.1 ppb). A portable prototype sensor array device comprises a fan-beam laser diode, a semi-cylindrical lens, a planar waveguide with a three-channel cell attached, and a CCD array photodetector. Dedicated software was developed for CCD image processing and further data analysis with an artificial neural network.

The large internal surface area within a small volume, efficient room-temperature visible photoluminescence and biocompatibility of porous silicon (PS) has stimulated recent interest in its applications for sensor development. The method of spectroscopic ellipsometry was applied to study *in situ* the adsorption of bovine serum albumin (BSA) into PS. The porosity and amount of adsorbed BSA were determined by fitting the ellipsometric data to the Bruggeman effective medium approximation model. The presence of intermediate adsorbed layers of polyelectrolytes was found to increase protein adsorption.

# Acknowledgements

I would like to thank all the people who assisted me in this research.

Special appreciations and cordial thanks to my director of studies, Dr. Alexei Nabok for being really patient and truly solid support throughout these years, for his wise guidance and useful advices. I thank him for his excellent supervision and discussion of various aspects of science and life. His wide knowledge has been of great value for me.

I would like to express my deep and sincere gratitude to my first supervisor, Dr. Aseel Hassan for his help, support, interest, and valuable hints.

It is difficult to overstate my gratitude to my fellow PhD colleague, Suryajaya whom I truly indebted for his help and support all these years.

My special thanks to Prof. Nikolay F. Starodub (Institute of Biochemistry, National Academy of Sciences of Ukraine) for fruitful discussion during his visits to Sheffield Hallam University.

I would also like to thank Dr. Alan Holloway and Dr. Saharudin Haron for valuable information, discussion, and suggestions.

Finally, I have to say “thank-you” to all my friends and family, wherever they are... and I cannot leave out my little fellow, Prof. Myaus (проф. Мяус) for his wisdom and persistence.

---

# Contents

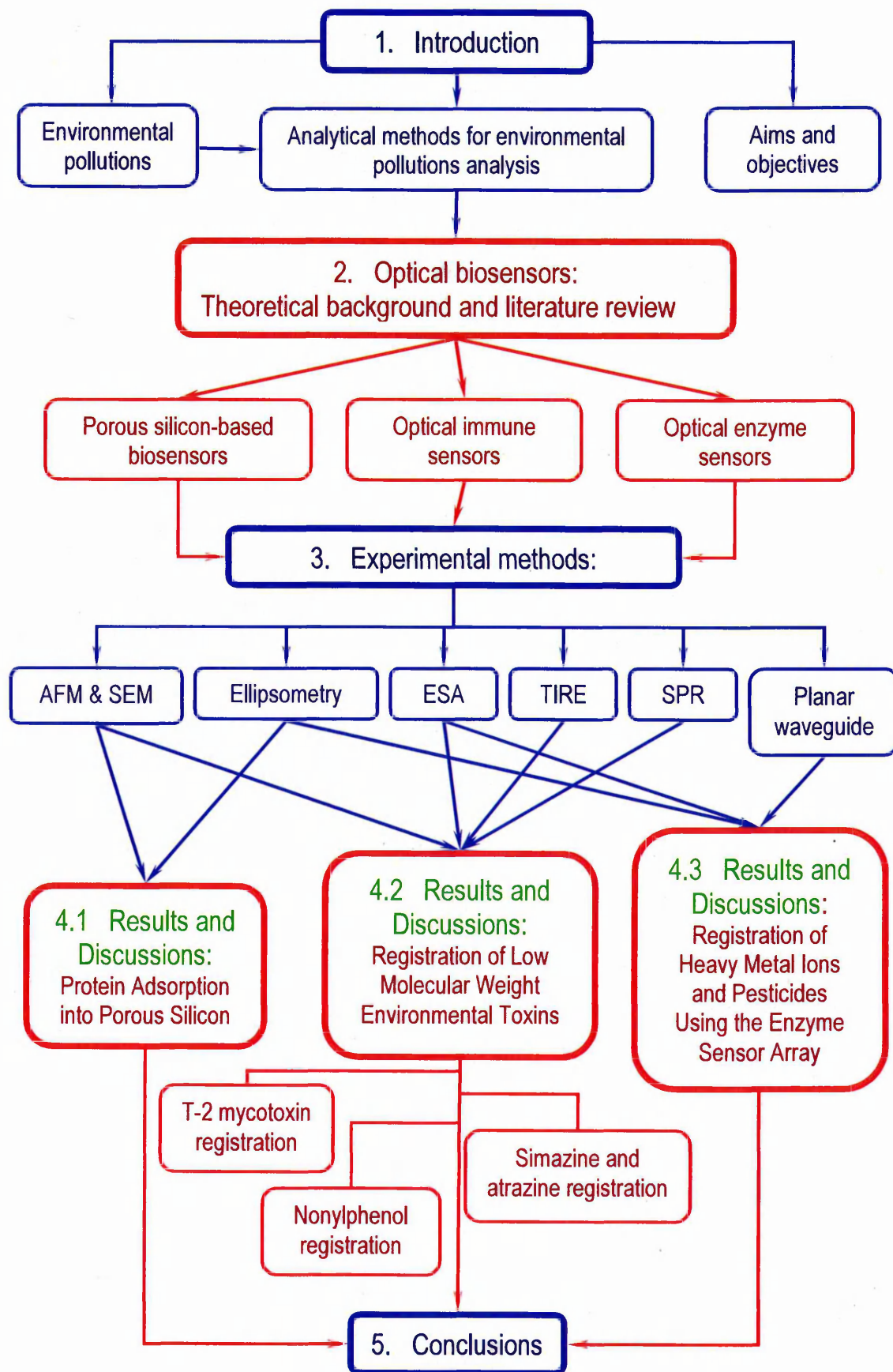
<b>Declarations</b>	<b>ii</b>
<b>Abstract</b>	<b>iii</b>
<b>Acknowledgements</b>	<b>iv</b>
<b>Contents</b>	<b>v</b>
<b>List of Publications</b>	<b>ix</b>
<b>List of Abbreviations</b>	<b>x</b>
<b>1 INTRODUCTION</b>	<b>1</b>
1.1 Environmental Pollutions	2
1.2 Analytical Methods for Environmental Pollutions Analysis	6
1.3 Biosensors for Analytical Measurements	8
1.3.1 Biosensors concept	8
1.3.2 Recognition elements	9
1.3.3 Transducers	12
1.4 Aims and Objectives of this Thesis	15
References	17
<b>2 OPTICAL BIOSENSORS:</b>	
<b>THEORETICAL BACKGROUND and LITERATURE REVIEW</b>	<b>22</b>
2.1 Adsorption of Biomolecules into Porous Silicon	23
2.1.1 Porous silicon basics	23
2.1.2 Porous silicon for biosensing applications	31
2.2 Optical Immune Sensors	37
2.2.1 Surface plasmon resonance	37
2.2.2 Spectroscopic ellipsometry	46
2.2.3 Total internal reflection ellipsometry	53
2.2.4 Planar optical waveguide	58
2.3 Optical Enzyme Sensors	65
2.4 Low Molecular Weight Analytes in Optical Immune Sensors	77
2.5 Summary	83
References	84

<b>3</b>	<b>EXPERIMENTAL METHODS</b>	<b>96</b>
3.1	Methods of Morphology Study	97
3.1.1	Introduction to scanning probe microscopy technique	97
3.1.2	Introduction to scanning electron microscopy technique	105
3.2	Ellipsometric Data Analysis Routine	109
3.3	Ellipsometric Study of Adsorption of BSA into Porous Silicon	115
3.3.1	Experimental set-up for porous silicon formation	115
3.3.2	Cell design for ellipsometric measurements	117
3.3.3	Chemicals	118
3.3.4	Experimental procedure	119
3.3.5	Influence of polyelectrolytes on BSA adsorption	120
3.3.6	Modelling and fitting routine	121
3.4	Total Internal Reflection Ellipsometry Detection of Low Molecular Weight Environmental Toxins	122
3.4.1	Surface plasmon resonance: experimental set-up	123
3.4.2	Total internal reflection ellipsometry: experimental set-up	124
3.4.3	Sample preparation	125
3.4.4	Measurements routine	126
3.4.5	Kinetics measurements	128
3.4.6	Samples for AFM	128
3.4.7	Real samples	129
3.5	Electrostatic Self-Assembly Technique for Protein Immobilization	131
3.6	Portable Planar Waveguide Enzyme Sensor Array	136
3.6.1	Planar waveguide transducer	136
3.6.2	Formation of the sensing windows	137
3.6.3	Formation of the sensing layer using ESA technique	138
3.6.4	ESA deposition process	144
3.6.5	Experimental set-up for a multi-channel enzyme sensor array	145
3.6.6	Measurements procedure for pollutants registration	148
3.6.7	Software description	149
3.6.8	Analysis of pollutants using an artificial neural network algorithm	150
3.7	Kinetics of Bio-reactions	153
3.8	Summary	158
	References	160

---

<b>4</b>	<b>RESULTS and DISCUSSIONS</b>	<b>164</b>
4.1	Protein Adsorption into Porous Silicon: Ellipsometric Study	165
4.2	Registration of Low Molecular Weight Environmental Toxins with Method of Total Internal Reflection Ellipsometry	177
4.2.1	Simazine and atrazine registration	177
4.2.2	T-2 mycotoxin registration	183
4.2.3	Nonylphenol registration	199
4.3	Registration of Heavy Metal Ions and Pesticides Using the Enzyme Sensor Array	213
4.4	Summary	230
	References	231
<b>5</b>	<b>CONCLUSIONS and RECOMMENDATIONS</b>	<b>232</b>
5.1	Thesis Conclusions	233
5.2	Recommendations for Future Work	236
	<b>APPENDICES</b>	<b>238</b>
A	Software Description for Portable Planar Waveguide Enzyme Sensor Array Device	A1
B	TIRE Modelling	A13
C	ANN Basics	A22
D	AFM Data Definition	A25
E	Abstracts	A28

# The links between the chapters



# List of Publications

## Journal publications related to this study

1. Nabok A., Tsargorodskaya A., Holloway A., Starodub N. F., Demchenko A. *Specific binding of large aggregates of amphiphilic molecules to respective antibodies*, *Langmuir* **23** (2007) 8485-8490.
2. Nabok A. V., Tsargorodskaya A. *The method of total internal reflection ellipsometry for thin films' characterisation and sensing*, *Thin Solid Films* (2007) accepted.
3. Nabok A. V., Tsargorodskaya A., Holloway A., Starodub N. F., Gojster O. *Registration of T-2 mycotoxin with total internal reflection ellipsometry and QCM impedance methods*, *Biosensors and Bioelectronics* **22** (2007) 885-890.
4. Nabok A. V., Tsargorodskaya A., Hassan A. K., Starodub N. F. *Total internal reflection ellipsometry and SPR detection of low molecular weight environmental toxins*, *Applied Surface Science* **246** (2005) 381-386.
5. Tsargorodskaya A., Nabok A. V., Ray A. K. *Ellipsometric study of adsorption of BSA into porous silicon*, *Nanotechnology* **15** (2004) 703-709.

## Conference proceedings related to this study

- Nabok A., Tsargorodskaya A., Lishchuk S. V. *Investigation into specific binding of alkylphenol micelles to respective antibodies*, 12<sup>th</sup> International Conference on Organized Molecular Films – LB-12, Kraków (Poland), 1-5 July 2007.
- Nabok A., Tsargorodskaya A., Suryajaya *Application of total internal reflection ellipsometry for thin film characterisation and sensing*, 4<sup>th</sup> International Conference on Spectroscopic Ellipsometry, Stockholm (Sweden), 11-15 June 2007, p.348.
- Nabok A., Tsargorodskaya A. *The method of TIRE for thin films characterisation and sensing*, Nano-Molecular Analysis for Emerging Technologies II, NPL, Teddington (UK), 17-18 Oct 2006, p.61.
- Nabok A., Tsargorodskaya A. *The method of total internal reflection ellipsometry for thin films' characterisation and sensing*, The European Conference on Organised Films – ECOF-10, Riga (Latvia) 21-24 Aug 2006, p.76-77.
- Nabok A., Tsargorodskaya A. *Planar waveguide enzyme sensors arrays based on composite electrostatically self-assembled films*, The European Conference on Organised Films – ECOF-10, Riga (Latvia) 21-24 Aug 2006, p.125-126.
- Nabok A., Tsargorodskaya A., Holloway A., Starodub N. F., Davis. F. *The method of total internal reflection ellipsometry for bio-sensing*, The 9<sup>th</sup> World Congress on Biosensors, Toronto (Canada), 10-12 May 2006, p.O19.
- Nabok A., Tsargorodskaya A., Haron S., Travis J. *Planar waveguide enzyme sensor array for water pollution monitoring*, the Institution of Engineering and Technology Seminar on MEMS Sensors & Actuators, London (UK), 27-28 Apr 2006, pp.121-126.
- Nabok A. V., Tsargorodskaya A., Holloway A., Starodub N. F., Demchenko A., Gojster O. *Registration of low molecular weight environmental toxins with total internal reflection ellipsometry*, *IEEE Proceedings – Sensors* **3** (2004) 1195-1198.

# List of Abbreviations

AB	antibody
AFM	atomic force microscopy
AChE	acetylcholine esterase
ANN	artificial neuron network
ATR	attenuated total reflection
BChE	butyrylcholine esterase
BSA	bovine serum albumin
CCD	charge-coupled device
CTCT	cyclo-tetra-chromotroprylene tetra-sulfonic sodium salt
ChE	cholinesterase
DNA	deoxyribonucleic acid,
EL	electroluminescence
EMA	effective medium approximation
ESA	electrostatic self-assembly
LMW	low molecular weight (analyte)
MSE	mean squared error
MW	molecular weight
PAH	poly(allylamine hydrochloride)
PL	photoluminescence
PS	porous silicon
PSS	poly(styrenesulfonate) sodium salt
ppb	Parts per billion
ppm	Parts per million
PTFE	poly-tetra-fluoroethylene or Teflon
QCM	quartz crystal microbalance
SEM	scanning electron microscopy
SPR	surface plasmon resonance
TIRE	total internal reflection ellipsometry
TIRF	total internal reflection fluorescence

# *CHAPTER 1.*

## **INTRODUCTION**

This chapter presents a brief review of the problem of environmental pollution, analytical methods for their monitoring, and gives a short description of the biosensors concept.

## 1.1 Environmental Pollutions

A major current ecological problem is the contamination of the environment with by-products of industrial and agricultural activities, such as heavy metal ions, pesticides, herbicides and toxins – because of toxicity leading to health problems.

The use of some pesticides and herbicides, such as *atrazine* and *simazine*, is subject to control due to their high level of toxicity to humans and organisms in the ecosystem and their low degradability in the environment. However, in 1995 approximately  $149 - 160 \cdot 10^6$  kg of atrazine were used across the world<sup>[1]</sup>. Due to extensive use, persistence, water solubility, and relatively weak adsorption in the soil, atrazine is present in the aquatic environment via agricultural run-off, leaching and atmospheric input and is therefore regularly and most frequently detected in surface water<sup>[2]</sup>.

More chemicals were developed and used to increase agricultural productivity; among them were insecticides, pesticides, and herbicides. The release of pesticides (even those having relatively low human toxicity, such as an *imidacloprid*) into the environment has led to both surface and ground water pollution, and the risk to human health is increased because they enter into drinking water<sup>[3]</sup>. In other instances, organophosphates, such as *dichlorvos*, have been designed for use as insecticides but can also be used as agents of warfare<sup>[4]</sup>. Dichlorvos has a high acute toxicity and has been classified by the World Health Organization as “highly hazardous”. Like many organophosphate insecticides, it inhibits cholinesterase levels in humans, which may result in disruption to the nervous and muscular systems. The compound can leach into groundwater due to its high solubility<sup>[5]</sup>. Despite the fact that dichlorvos is a mutagen and a suspected carcinogen, it is still in use in many countries across the world as an insecticide.

Many chemicals are released into the environment irrespectively of their toxicological risks. Many of them have the capacity to disrupt the functioning of the endocrine system<sup>[6]</sup>. *Nonylphenol* has attracted attention as an estrogenic environmental contaminant and has been implicated in the disruption of endocrine function in wildlife<sup>[7]</sup>. Nonylphenol is widely used as an antioxidant and polymer stabilizer, and is

also utilized in the synthesis of non-ionic surfactants. It has been identified in sewage and river water. A survey of 190 food samples purchased in Japanese markets revealed that some fish, meat and vegetables are contaminated with nonylphenol at the levels of 10 – 723, 9 – 180 and 7 – 131 ng/g, respectively<sup>[8]</sup>. In other surveys, the plastics used in food processing and packaging often contained a high level of nonylphenol, and it was suggested that nonylphenol in these plastics can migrate into the fatty foods upon contact<sup>[9, 10, 11]</sup>.

*T-2* (also known as “Yellow Rain”), a trichothecene *mycotoxin*, is a naturally-occurring mould, a by-product of *fusarium* fungus which is toxic to humans and animals. It is the only mycotoxin known to have been used as a biological weapon. It can be produced from mouldy whole grains such as wheat, oats, barley, maize. It has even been encountered at very high concentrations in feed mixtures for poultry breeding<sup>[12]</sup>. Toxic residues in contaminated poultry products, such as meat, liver or eggs as well as those delivered via the food chain have been proved harmful to humans<sup>[13]</sup>. The world-wide problem of mycotoxicosis is reflected by the fact that the legislation controlling mycotoxins in both animal feed and human food exists in over 60 countries<sup>[14]</sup>.

Despite the introduction of water quality targets in the European Union (EU) (*i.e.* EU Drinking Water Directive (98/83/EC), EU Dangerous Substances Directive (76/464/EC), and EU Groundwater Directive (80/68/EC)), there has been no overall improvement of water quality since the beginning of the 1990s. An estimated 20% of all surface water in the EU is seriously contaminated<sup>[15]</sup>.

There are many sources of water pollution which can be split in two categories: point contamination sources and diffuse contamination sources. Point sources include effluent outlets from factories and waste treatment plants, that emit fluid of varying quality directly into urban water supplies<sup>[16]</sup>. Although the industrial and agricultural contamination of water resources is controlled by EU legislation, these pollutants can still be found in water. Diffuse sources include contaminants that enter into the water supply from soil or ground waters and from the atmosphere via rain water. Diffuse-originated pollutants are determined by the sort of activity taking place in the area: in urban and industrial areas, the pollution is mostly caused by heavy metal ions, aromatic and aliphatic hydrocarbons, while in agricultural areas, it is mainly due to nutrients, herbicides and insecticides<sup>[17]</sup>.

According to Pearce and Mackenzie<sup>[18]</sup> the level of contaminants in rain water regularly exceed the legislation limit for drinking water. It was reported<sup>[19]</sup> that in rain and roof runoff, the maximal pesticide concentration, originating primarily from agricultural use, occurs during and immediately after the application of pesticides. According to this research, the maximum average concentrations of *atrazine* (903 ng/l), *alachor* (191 ng/l), and *R-dichlorprop* (106 ng/l) were registered after a rainfall in Switzerland. These chemicals appeared to have evaporated from the fields and were present in the clouds. For obvious reasons diffuse sources are much more difficult to control.

The quality of drinking water in Britain is controlled by standards set by the EU and Water Quality Regulations<sup>[20]</sup>. 99.93% of all tests carried out on drinking water supplies in Sheffield, UK, complied with the Water Quality Regulations<sup>[21]</sup> (see Table 1.1-1).

**Table 1.1-1** Guidelines for some chemical parameters in the Water Quality Regulation and results of water analysis in Sheffield (UK) and Kiev (Ukraine).

<i>Pollutant</i>	<i>EU legislation, µg/l</i>	<i>Sheffield (UK) Real value, min – max<sup>a</sup>, µg/l</i>	<i>Kiev (Ukraine) Excess of limit in comparison with EU legislation<sup>[22]</sup>, %</i>
<i>Aluminium</i>	200	8 – 55	13 – 510
<i>Cadmium</i>	5	0.03 – 0.07	0
<i>Iron</i>	200	11 – 112	5 – 100
<i>Lead</i>	25	0.14 – 5.68	0
<i>Mercury</i>	1	0.04 – 0.046	0
<i>Nickel</i>	20	0.5 – 1.12	No information
<i>Pesticides – Total Substances</i>	0.5	0.05	No information
<i>Atrazine</i>	0.1	0.0008	55 – 255 (total content of organic substances)
<i>Dichlorvos</i>	0.1	0.0017	
<i>Simazine</i>	0.1	0.001 – 0.0017	

<sup>a</sup> Reporting period: 1<sup>st</sup> January 2005 – 31<sup>st</sup> December 2005

In spite of the number of regulations in the Ukraine (*i.e.* Water Code of Ukraine (1995), Ukrainian Law on Environmental Protection (1991) etc.) the quality of water is unsatisfactory<sup>[23]</sup>. In 1998, the content of iron, aluminium, and organic substances in the water supply in Kiev was in excess of the EU limits (see Table 1.1-1). Almost all river basins in the Ukraine are classified as “polluted” or “very polluted”<sup>a</sup>. The large rivers (Dnepr, Dnestr, Southern Bug) are all polluted with oxygen-consuming substances, heavy metal ions, oils, and phenols<sup>[24]</sup>. Since water resources are interconnected, pollution in one region can spread widely and uncontrollably to another.

The EU environmental legislation is based on human health criteria, and also challenges the technical limits of current state-of-the-art analytical instrumentation as it is determined by the current ability to detect pollutants. For instance, the maximum permitted concentration for any individual pesticide given in the EU Drinking Water Directive is 0.1 µg/l<sup>[25]</sup> which corresponds to one-tenth of a parts per billion (ppb). Therefore, detection of heavy metal ions, environmental toxins, and biological warfare agents especially in drinking water in the range below 0.1 µg/l is playing an increasingly important role in human health and safety regulations<sup>[26]</sup>.

---

<sup>a</sup> Nevertheless, there are plenty of fish in these rivers.

## 1.2 Analytical Methods for Environmental Pollutions Analysis

In areas such as environmental control, food quality control, medical diagnostics, industrial process control, and monitoring of biological warfare agents, information about the presence or absence of additives, contaminants, and natural compounds is required. Nowadays, the quantitative analysis of different environmental pollutants in water and food is carried out using standard analytical methods, such as high-performance liquid chromatography, gas chromatography, mass spectroscopy, and microbial inhibition tests<sup>[27]</sup>. These methods have been proven to be both highly sensitive and reliable. However, they are mostly laboratory based and not suitable for on-site express analysis. They are both time consuming and need highly trained technicians; the sample preparation procedure is complicated. As a result, the above methods are generally too expensive<sup>[28-33]</sup>.

Alternative environmental analysis techniques based on different principles are therefore required for environmental pollutant monitoring. Many methods for the detection and analysis of inorganic and organic compounds in water, food and other environments are already available and a comprehensive review of the devices currently employable has recently been published<sup>[34]</sup>. Among the most widely used tools are sensors. These devices are usually low cost and can be used either *in situ* or on-line for the rapid assessment of contamination<sup>[35]</sup>.

Sensors can be systematized by the type of chemical reaction registered, or by the type of transducer, or by the signal processing principle, etc. For instance, depending on the environment, sensors can be divided into two categories: gas sensors, and sensors working in a liquid environment. Based on the nature of chemical processes in the sensitive membrane, two types of sensors can be defined: sensors of multiple use, and single shot (or disposable) sensors. A device that uses a biological element, such as an immobilized enzyme, cell, immunosystems, tissues etc. to detect (bio-) chemical compounds, as a sensor is called *biosensors*<sup>[36]</sup>.

Biosensors can also be divided into two large classes:

1. Affinity sensors based upon highly specific binding of biomolecules, such as reactions between antibodies and antigens in immune sensors;

2. Catalytic sensors, which, in addition to specific binding of analyte molecules from the environment, decompose them into smaller products.

There are many advantages associated with the use of biosensor technology as a sensitive detection method. The most important of these include specificity as a result of using biological sensing elements, which can distinguish between the analyte of interest and other molecules and relatively rapid response time<sup>[37]</sup>.

## 1.3 Biosensors for Analytical Measurements

### 1.3.1 The concept of biosensors

A *biosensor* is an analytical device which converts a biological/biochemical reaction into any measurable physical parameter (current, potential, optical constants, mass etc.)<sup>[38]</sup>. Generally, biosensors use two types of biological molecules as a sensing element: (i) *enzymes*, which specifically catalyse the reaction of decomposition of substratum and (ii) *antibodies*, which bind specifically target molecules.

Monitoring those molecular interactions and the use of those molecules as recognition elements (bioreceptors) will give information on the presence of the target analyte and its concentration. As shown in Figure 1.3-1, a biosensor comprises of three major elements:

1. Bioreceptor, where molecular recognition, or biochemical reactions occur;
2. Transducer which transforms the reactions into some physical parameters;
3. Signal processing system to quantify this physical parameter and to deliver information in a suitable form to the external receiver<sup>[39]</sup>.

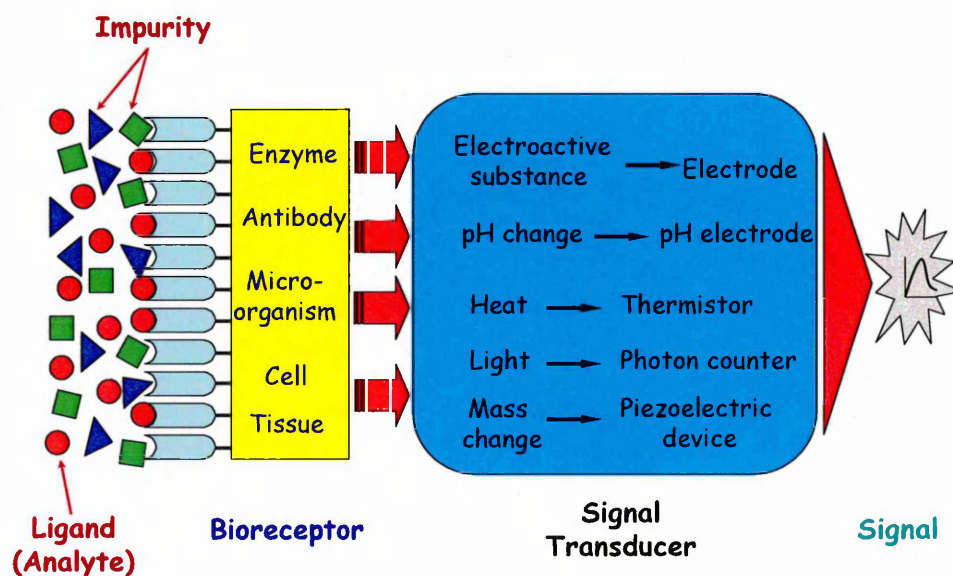


Figure 1.3-1 Schematic of a biosensor (adapted from Ref.<sup>[40]</sup>).

The most important characteristics of biosensors are sensitivity or resolution, selectivity to the target analyte (i.e. the ability to discriminate between different analytes), response time, recovery time (i.e. the time before the biosensor is ready to analyse the next sample), and working lifetime (usually determined by the instability of the biological material)<sup>[41]</sup>.

### 1.3.2 Recognition elements

Various types of biosensors have been developed in the field of environmental monitoring. Depending on the nature of the biological sensing element, they can be divided into *microbial* sensors, *affinity* sensors, and *enzyme* sensors.

#### *a. The concept of microbial sensors*

The microbial sensors principle is based on the fact that microorganisms consume oxygen during their metabolism. Microorganisms can assimilate organic compounds, resulting in a change in respiration activity, and can produce electroactive metabolites<sup>[41]</sup>.

The oxygen concentration or electrode-active compounds, such as ammonium ions, hydrogen sulphide, or carbon dioxide can be measured by monitoring pH. The measurement of the index of organic pollution in water (biological oxygen demand)<sup>[42]</sup>, the detection of the presence of toxic compounds for the food industry<sup>[43]</sup>, and environmental monitoring<sup>[44]</sup> are the major application fields for microbial biosensors. The response time of microbial sensors varies from 0.1 to 360 minutes; and the detection limit is 0.04 – 125 mg/l<sup>[41, 45]</sup>.

The main advantages of microbial sensors are the following: they are cheap because an active enzyme does not have to be isolated, and they are tolerant of suboptimal pH and temperature. However, they have a long recovery time, often contain many enzymes and therefore, may have low selectivity<sup>[41, 46]</sup>.

*b. Affinity sensors concept*

Affinity biosensors depend on the use of antibodies, proteins or DNA to recognise and bind a particular target analyte<sup>[47]</sup>. The most common affinity biosensors are antibody-based biosensors and are known as immunosensors<sup>[48]</sup>.

It is well established<sup>[46]</sup> that *antibodies* are synthesised by animals as a part of the response to the presence of foreign substances. Macromolecules capable of eliciting such a response are known as *antigens* or immunogens. In order to elicit the antibody formation the *hapten* (low molecular weight substance) must be bound to a macromolecule. The specificity of an antibody is associated with a particular site on an antigen, which is known as the antigenic determinant or *epitope*. An antibody will combine specifically with the corresponding antigen or hapten.

When this occurs an antibody-antigen complex, which has different physical-chemical properties such as mass, volume, current etc., is formed (for electrochemical detection of an immunoreaction is necessary to use enzymes that will generate electrochemically-active products<sup>[49]</sup>). Transducers that enable the detection of changes in the physical properties of the system (electrochemical, optical or acoustical) can be used in such measurements<sup>[49, 50]</sup>. Due to their high specificity, immunosensors satisfy the requirements of the EU legislation for detecting pesticide residues in drinking water<sup>[51]</sup>.

As has been mentioned above, antibodies are not the only receptor that can be used as the recognition element, but also DNA, cells, and tissues. The main advantages of these types of biosensors are the wide range of affinities available, thus expanding the number of analytes that can be selectively detected<sup>[52]</sup>.

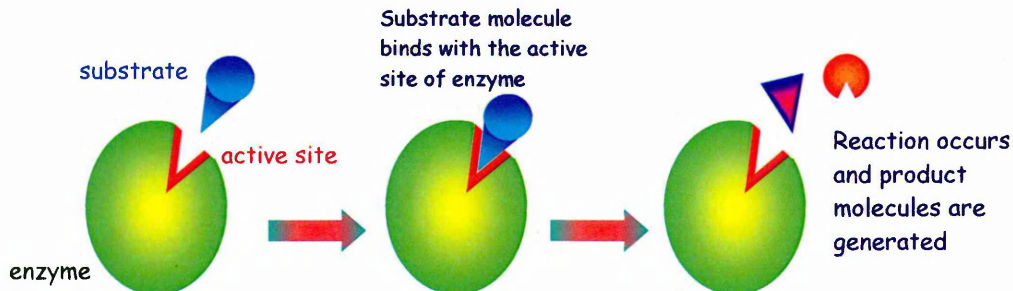
*c. Enzyme sensors concept*

In enzyme (or catalytic) biosensors the bio-recognition element is an *enzyme*, which reacts selectively with its *substratum* (i.e. a molecule upon which the enzyme acts). The effect of inhibition of enzymes by pollutants is used for their detection<sup>[53]</sup>. The substrate binds with the enzyme's active site (i.e. the region where binding of the substrate and the reaction occurs). An enzyme combines with its substratum to form an

enzyme-substrate complex, the substratum is then decomposed into several reaction products and released from the active site (Figure 1.3-2)<sup>[54]</sup>.

Two simultaneous processes control the reaction: the enzymatic alteration of the substrate to the product and the diffusion of the product from the enzyme layer. The enzyme reaction is usually accompanied by a change in pH, heat emission, and the expenditure or production of compounds (such as, oxygen or ammonia), which can be detected by the transducer<sup>[55]</sup>. It is possible to use enzyme reactions to monitor environmental pollutants, such as heavy metal ions, pesticides, and herbicides, which act as inhibitors of enzyme activity. The majority of enzyme biosensors are based on either electrochemical transducers or ion-selective field-effect transistors (ISFET)<sup>[56]</sup>.

### (a) Reaction



### (b) Inhibition

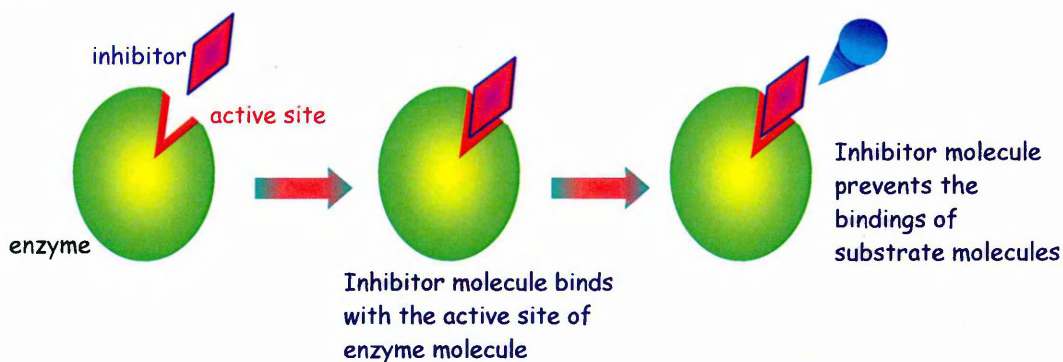


**Figure 1.3-2** Enzyme reaction (a) and inhibition (b) (adapted from Ref.<sup>[57]</sup>).

The sensitivity of such sensors is in the ppm (parts per million) range, which is at the limit of electrochemical and ISFET sensors, which does not match the EU legislation levels for environmental control<sup>[51]</sup>. However, the response time for

electrochemical sensors varies from 0.1 to 30 minutes, and for ISFET is of the order of milliseconds<sup>[38, 56]</sup>.

Among the advantages of enzyme biosensors are their high selectivity and fast response time. However, enzymes are expensive and they often lose their activity when immobilized on transducers<sup>[41]</sup>.

### 1.3.3 Transducers

Depending on the analyte, the transducer, which is linked to the bioreceptor, could utilise one of the following sensing principles described below.

#### *a. Thermal transducers*

Thermometric (or calorimetric) biosensors exploit the adsorption or emission of heat, which is proportional to the molar enthalpy and to the total number of product molecules created in the biochemical reaction<sup>[58, 59]</sup>. This is reflected as a change in the temperature within the reaction medium. The majority of thermal transducers use enzymes as biological recognition elements, so-called enzyme thermistors<sup>[60]</sup>.

According to Ramanathan et al.<sup>[61]</sup>, enzymatic reactions generally have a heat emission of 28 –100 kJ/mol, which makes them suitable for versatile applications. For affinity reactions, such as antibody-antigen, the thermal changes are not substantial<sup>[62]</sup>.

#### *b. Electrochemical transducers*

There are two main principles used in biosensors based on electrochemical transducers<sup>[63]</sup>:

(a) The *potentiometric*: Approaches depend on changes in the electric potential at a constant current.

(b) The *amperometric*: Approaches detect changes in the current as a function of the concentration of electroactive species.

Potentiometric biosensors are usually based on ion-selective electrodes. These devices measure the changes in ion concentration during the reaction. A simple sensor consists of an immobilized enzyme membrane surrounding the probe of a pH meter where the catalysed reaction takes place. For example, the change in pH, which can be easily read, is induced by the formation of an organic acid during the hydrolysis of the *choline ester* by an appropriate esterase. Using this principle, Tran-Minh et al.<sup>[64]</sup>, achieved the detection of 0.3 ppb (parts per billion) *paraoxon*, *acetylcholinesterase* (AChE) being immobilized on a glass pH electrode by cross-linking with polyacrylamide. With the exception of this work, the detection limits reported are generally close to 3 ppb<sup>[51]</sup>.

Amperometric detection is based on measurements at the fixed potential of the current generated when electroactive species are either oxidized or reduced at the electrode. The current produced is directly related to the concentration of the electroactive species<sup>[65]</sup>.

### c. *Gravimetric transducers*

The physical phenomenon behind acoustic (also called “gravimetric”<sup>[39]</sup>) transducers is based on interaction of the acoustic waves with the material, and the changes in either the added mass or acoustic wave velocity due to molecular adsorption or biochemical reactions on the surface of the piezoelectric material (for instance, quartz crystal). The crystals are placed in an oscillating electric field and the resonant frequency of the crystal is measured. This resonant frequency depends on the crystal’s chemical nature, its size, shape, and mass<sup>[39, 66]</sup>.

Two different types of acoustic biosensors are known: bulk acoustic waves (BAW) also known as quartz crystal microbalance (QCM) and surface acoustic waves (SAW).

The principle of QCM transducers is based on measurement of a resonance frequency of quartz crystal, which is affected by the added mass of adsorbed molecules. The method of SAW transducers is based on the registration of changes in the velocity of surface acoustic waves due to molecular adsorption<sup>[39]</sup>.

*d. Optical transducers*

Optical transducers, based on fundamental optical principles such as reflectance, fluorescence, interference, and polarization, allow the quantitative characterisation of optical radiation such as amplitude, phase, frequency, and polarization<sup>[67, 68]</sup>. Optical biosensors often employ different techniques such as ellipsometry, surface plasmon resonance, total internal reflection fluorescence, or planar waveguides to measure changes in the refractive index, thickness or light intensity of the bio-layer caused by different biochemical reactions.

*e. Porous silicon transducers*

Porous silicon (PS) based biosensors are another special type of biosensors to be mentioned. Due to the extremely large surface area ( $200 - 500 \text{ m}^2 \text{ cm}^{-3}$ )<sup>[69]</sup> of PS and thus the great adsorption properties, and low cost, PS has been employed as a matrix for immobilisation for a variety of bio-molecules, such as enzymes<sup>[70]</sup>, DNA<sup>[71; 72]</sup>, and antibodies<sup>[73, 74]</sup>. Electronic or optical properties of porous silicon could be utilized to transduce biomolecular interactions in biosensor applications<sup>[75]</sup>. Several physical principles were exploited in PS transducers, namely, optical Fabry-Perot interferometry<sup>[76]</sup>, ellipsometry<sup>[73]</sup>, photoluminescence<sup>[77]</sup>, and electroluminescence<sup>[78]</sup>.

Current work has focused on the use of optical transducers for immune and enzyme sensors. A detailed description of their working principles and applications is given in chapter 2.

## 1.4 Aims and Objectives of this Thesis

The main goal of this thesis is to develop optical transducers (sensors) for the detection of environmental pollutants. To achieve this aim the research has been divided into three parts.

The aim of the *first* part is:

To investigate and quantify the adsorption of proteins into porous silicon (PS) using the methods of spectroscopic ellipsometry.

In order to achieve this goal the following objectives are listed below:

- The development of the experimental set-up and technological protocol for the preparation of PS with required pore size.
- To design an experimental set-up and reaction cells for ellipsometric measurements.
- To immobilize proteins in the PS matrix and to study protein adsorption in PS with the ellipsometry method.
- To determine the thickness of the adsorbed layers by modelling and fitting the ellipsometric spectra.
- To study PS morphology using AFM and SEM techniques.

The aim of the *second* part is:

To employ the method of total internal reflection ellipsometry (TIRE) for the registration of low molecular weight environmental toxins, such as *atrazine*, *simazine*, *T-2 mycotoxin*, and *nonylphenol* in low concentrations down to ng/ml range.

For this task, the following objectives were specified:

- To develop the TIRE experimental set-up on the bases of an M-2000V J. A. Woollam spectroscopic ellipsometer using the Kretschmann's surface plasmon resonance geometry and a flow reaction cell.

- To immobilize antibodies on a solid surface using the method of ESA.
- To register low molecular weight (LMW) environmental toxins using a cost effective direct immune assay approach, when molecules of toxins are binding to immobilized specific antibodies.
- To perform fitting of the TIRE spectra in order to establish a model of specific binding of LMW toxins.

The aim of the *third* part is:

To develop a portable prototype sensor array device intended to detect *in situ* heavy metal ions and pesticides in water and to evaluate their concentration. The system is based on the Si/SiO<sub>2</sub>/Si<sub>3</sub>N<sub>4</sub>/SiO<sub>2</sub><sup>a</sup> planar waveguide transducer operating in the regime of attenuated total reflection (ATR), with a sensing window, coated with an electrostatically self-assembled sensing membrane. This membrane contains pH sensitive organic chromophore molecules; enzymes were immobilized on nylon membranes and placed on the top of the coating. The measurements of both the enzyme reactions and their inhibition by traces of some water pollutants are used.

The following objectives are specified for this part of the research work:

- To design a portable CCD-based sensor array device and a multi-channel reaction cell and to develop the software for CCD image processing.
- To produce composite sensitive membranes comprising of disposable nylon sheets with immobilized enzymes and pH sensitive electrostatically self-assembled (ESA) films containing chromophore molecules of *cyclo-tetra-chromotrolyene tetra-sulfonic sodium salt* (CTCT).
- To investigate the response of the produced composite membranes to different pollutants using the effect of attenuation of light intensity propagated through the planar waveguide.
- To build a database of sensor array responses to different pollutants; then to identify and quantify the pollutants using a standard MATLAB pattern recognition algorithm.

---

<sup>a</sup> Si/SiO<sub>2</sub>/Si<sub>3</sub>N<sub>4</sub>/SiO<sub>2</sub> = Silicon/Silicon dioxide/Silicon nitride/Silicon dioxide

## References

## § 1.1

- [1] Short P. and Colborn T. *Pesticide use in the U.S. and policy implications: focus on herbicides*, *Toxicology and Industrial Health* **15** (1999) 240-275.
- [2] Gfrerer M., Wenzl T., Quan X., Platzer B. and Lankmayr E. *Occurrence of triazines in surface and drinking water of Liaoning province in eastern China*, *Journal of Biochemical and Biophysical Methods* **53** (2002) 217-228.
- [3] Kiso Y., Nishimura Y., Kitao T. and Nishimura K. *Rejection properties of non-phenolic pesticides with nanofiltration membranes*, *Journal of Membrane Science* **171** (2000) 229-237.
- [4] Fukuto T. R. *Organophosphorus and carbamate esters: the anticholinesterase insecticides*. In J. W. Biggar & J. N. Seiber (Eds.), *Fate of pesticides in the environment*. Proceedings of a Technical Seminar (1987) 5-18.
- [5] Schramm J. D. and Hua I. *Ultrasonic irradiation of dichlorvos: decomposition mechanism*, *Water Research* **35** (2001) 665-674.
- [6] Lutz I. and Kloas W. *Amphibians as a model to study endocrine disruptors: 1. Environmental pollution and estrogen receptor binding*, *Science of the Total Environment* **225** (1999) 49-57.
- [7] Sakai A. *p-Nonylphenol acts as a promoter in the BALB/3T3 cell transformation*, *Genetic Toxicology and Environmental Mutagenesis* **493** (2001) 161-166.
- [8] Sasaki Kumiko, Takatsuki Satoshi, Nemoto Satoru, Imanaka Masaaki, Eto Shoichi, Murakami Emiko and Toyoda Masatake *Determination of alkylphenols and 2,4-dichlorophenol in foods*, *Journal of Food Hygienic Society of Japan* **40** (1999) 460-472.
- [9] Junk G. A., Svec H. J., Vick R. D. and Avery M. J. *Contamination of water by synthetic polymer tubes*, *Environmental Science and Technology* **8** (1974) 1100-1106.
- [10] Kawamura Yoko, Maehara Tamae, Iijima Hiroyo and Yamada Takashi *Nonylphenol in food contact plastics and toys*, *Journal of Food Hygienic Society of Japan* **41** (2000) 212-218.
- [11] Nemoto Satoru, Takatsuki Satoshi, Sasaki Kumiko and Toyoda Masatake *Determination of nonylphenol in fish on the market*, *Journal of Food Hygienic Society of Japan* **41** (2000) 377-380.
- [12] Labuda R., Parich A., Berthiller F. and Tančinová D. *Incidence of trichothecenes and zearalenone in poultry feed mixtures from Slovakia*, *International Journal of Food Microbiology* **105** (2005) 19-25.
- [13] D'Mello J. P. F., Placinta C. M. and Macdonald A. M. C. *Fusarium mycotoxins: a review of global implications for animal health, welfare and productivity*, *Animal Feed Science and Technology* **80** (1999) 183-205.
- [14] Vanegmond H. P. *Mycotoxins – regulations, quality assurance and reference materials*, *Food Additives and Contaminants* **12** (1995) 321-30.
- [15] <http://europa.eu.int/scadplus/leg/en/s15005.htm> (accessed 15 January 2007).
- [16] Sabir S. M., Khan S. W. and Gardezi S. S. *Effect of environmental pollution on quality of water in district Bagh, Azad Kashmir, Pakistan*, *Journal of Biological Science* **6/9** (2003) 831-835.

- [17] López-Flores R., Quintana X. D., Salvadó V., Hidalgo M., Sala L. and Moreno-Amich R. *Comparison of nutrient and contaminant fluxes in two areas with different hydrological regimes*, Water Research **37** (2003) 3034-3046.
- [18] Pearce F. and Mackenzie D. *It's raining pesticides*, New Scientist **2180** (1999) 23.
- [19] Bucheli T. D., Müller S. R., Heberle S. and Schwarzenbach R. P. *Occurrence and behavior of pesticides in rainwater, roof runoff, and artificial stormwater infiltration*, Environmental Science and Technology **32** (1998) 3457-3464.
- [20] The Water Supply (Water Quality) Regulation, 2000. <http://www.opsi.gov.uk> (accessed 15 January 2007).
- [21] Drinking Water Quality Report, Yorkshire Water Services, 2004.
- [22] [http://www.mama-86.org.ua/files/drwater2\\_eng.pdf](http://www.mama-86.org.ua/files/drwater2_eng.pdf) (accessed 24 May 2006).
- [23] European Environmental Agency Report, 2003. [http://reports.eea.europa.eu/environmental\\_assessment\\_report\\_2003\\_10/en/kyiv\\_chapt\\_08.pdf](http://reports.eea.europa.eu/environmental_assessment_report_2003_10/en/kyiv_chapt_08.pdf) (accessed 4 June 2006).
- [24] Drinking Water in Ukraine. [http://www.mama-86.org.ua/files/drwater2\\_eng.pdf](http://www.mama-86.org.ua/files/drwater2_eng.pdf) (accessed 15 January 2007).
- [25] Council Directive 98/83/EC. *On the quality of water intended for human consumption*, Official Journal of the European Communities **L330** (1998) 32-54.
- [26] Tschmelaka J., Prolla G., Riedta J., Kaiserb J., Kraemmerb P., Bárzagac L., Wilkinsond J. S., Huad P., Holed P. J., Nudde R., Jacksone M., Abukneshaf R., Barcelóg D., Rodriguez-Mozazg S., López de Aldag M. J., Sacherh F., Stienh J., Slobodníki J., Oswaldi P., Kozmenkoi H., Korenková E., Tóthováj L., Krascsenitsj Z. and Gauglitz G. *Automated Water Analyser Computer Supported System (AWACSS). Part I: Project objectives, basic technology, immunoassay development, software design and networking*, Biosensors and Bioelectronics **20** (2005) 1499-1508.
- § 1.2
- [27] Sherma J. *Planar Chromatography*, Analytical Chemistry **70** (1998) 7R-26R.
- [28] Clement R. E., Yang P. W. and Koester C. J. *Environnemental analysis*, Analytical Chemistry **69** (1997) 251R-287R.
- [29] Steen R. J. C. A., Freriks I. L., Cofino W. P. and Brinkman U. A. Th. *Large-volume injection in gas chromatography-ion trap tandem mass spectrometry for determination of pesticides in the marine environment at the low ng/l level*, Analytica Chimica Acta **353** (1997) 153-163.
- [30] Angelino S. and Gennaro M. C. *An ion-interaction RP-HPLC method for the determination of the eleven EPA priority pollutant phenols*, Analytica Chimica Acta **346** (1997) 61-71.
- [31] Rodriguez-Mozaz S., Reder S., Lopez de Alda M., Gauglitz G. and Barceló D. *Simultaneous multi-analyte determination of estrone, isoproturon and atrazine in natural waters by the RIver ANALyser (RIANA), an optical immunosensor*, Biosensors and Bioelectronics **19** (2004) 633-640.
- [32] Andreescu S., Barthelmebs L. and Marty J.-L. *Immobilization of acetylcholinesterase on screen-printed electrodes: comparative study between three immobilization methods and applications to the detection of organophosphorus insecticides*, Analytica Chimica Acta **464** (2002) 171-180.
- [33] Bovanová L. and Brandšteterová E. *Direct analysis of food samples by high-performance liquid chromatography*, Journal of Chromatography A **880** (2000) 149-168.

- [34] Namiesnik J., Wasik A., Zabiegala B., Partyka M. and Kot-Wasik A. *Passive sampling and/or extraction techniques in environmental analysis: a review*, Analytical and Bioanalytical Chemistry **381** (2005) 279-301.
- [35] Allan I. J., Vrana B., Greenwood R., Mills G. A., Roig B. and Gonzalez C. A "toolbox" for biological and chemical monitoring requirements for the European Union's Water Framework Directive, Talanta **69** (2005) 302-322.
- [36] Nabok A. *Organic and inorganic nanostructures*, Artech House, Boston – London, 2005.
- [37] Wilson G. S. and Gifford R. *Biosensors for real-time in vivo measurements*, Biosensors and Bioelectronics **20** (2005) 2388-2403.
- § 1.3
- [38] Tran-Minh C. *Biosensors*, Chapman&Hall, 1993
- [39] Nabok A. *Organic and inorganic nanostructures*, Artech House, Boston–London, 2005.
- [40] Terry L. A., White S. F. and Tigwell L. J. *The application of biosensors to fresh produce and the wider food industry*, Journal of Agricultural and Food Chemistry **53** (2005) 1309-1316.
- [41] Eggins B. *Biosensors: an introduction*, John Wiley&Sons. Inc., 1999.
- [42] Yang Z., Suzuki H., Sasaki S. and Karube I. *Disposable sensor for biochemical oxygen demand*, Applied Microbiology and Biotechnology **46** (1996) 10-14.
- [43] D'Souza S. F. *Microbial biosensors*, Biosensors and Bioelectronics **16** (2001) 337-353.
- [44] Karube I., Nomura Y. and Arikawa Y. *Biosensors for environmental control*, Trends in Analytical Chemistry **14** (1995) 295-299.
- [45] Ramsay G. *Commercial biosensors: applications to clinical, bioprocess, and environmental samples*, John Wiley&Sons. Inc., 1998.
- [46] Cass A. E. G. *Biosensors: a practical approach*, Oxford University Press, 1990.
- [47] Sharpe M. *It's a bug's life: biosensors for environmental monitoring*, Journal of Environmental Monitoring **5** (2003) 109-113.
- [48] Hock B. *Antibodies for immunosensors: a review*, Analytica Chimica Acta **347** (1997) 177-186.
- [49] Mallat E., Barceló D., Barzen C., Gauglitz G. and Abuknesha R. *Immunosensors for pesticide determination in natural waters*, Trends in Analytical Chemistry **20** (2001) 124-132.
- [50] Brecht A. and Gauglitz G. *Label free optical immunoprobes for pesticide detection*, Analytica Chimica Acta **347** (1997) 219-233.
- [51] Marty J.-L., Leca B. and Noguer T. *Biosensors for the detection of pesticides*, Analysis Magazine, **26** (1998) 144-149.
- [52] Marco M.-P. and Barceló D. *Environmental applications of analytical biosensors*, Measurement Science and Technology **7** (1996) 1547-1562.
- [53] Hall E. *Biosensors*, Open University Press, Milton Keynes, 1990.
- [54] Enzyme. <http://en.wikipedia.org/wiki/Enzyme> (accessed 18 August 2006).

- [55] Amine A., Mohammadi H., Bourais I. and Palleschi G. *Enzyme inhibition-based biosensors for food safety and environmental monitoring*, *Biosensors and Bioelectronics* **21** (2006) 1405-1423; Liu G. and Lin Y. *Biosensors based on self-assembling acetylcholinesterase on carbon nanotubes for flow injection/amperometric detection of organophosphate pesticides and nerve agents*, *Analytical Chemistry* **78** (2006) 835-843.
- [56] Dzyadevych S., Soldatkin A., El'skaya A., Martelet C. and Jaffrezic-Renault N. *Enzyme biosensors based on ion-selective field-effect transistors*, *Analytica Chimica Acta* **568** (2006) 248-258.
- [57] Enzyme. <http://en.wikipedia.org/wiki/Enzyme> (accessed 18 August 2006).
- [58] Spink C. and Wadsö I. *Calorimetry as an analytical tool in biochemistry and biology*, *Methods of Biochemical Analysis* **23** (1976) 1-159.
- [59] Ramanathan K. and Danielsson B. *Principles and applications of thermal biosensors*, *Biosensors and Bioelectronics* **16** (2001) 417-423.
- [60] Danielsson B. and Mosbach K. *Enzyme thermistors*, *Methods in Enzymology: Immobilized Enzymes and Cells* **137** (1988) 181-197.
- [61] Ramanathan K., Rank M., Svitel J., Dzgoev A. and Danielsson B. *The development and applications of thermal biosensors for bioprocess monitoring*, *Tibtech* **17** (1999) 499-505.
- [62] Xie B., Ramanathan K. and Danielsson B. *Mini/micro thermal biosensors and other related devices for biochemical/clinical analysis and monitoring*, *Trends in Analytical Chemistry* **19** (2000) 340-349.
- [63] Deisingh A. *Biosensors for microbial detection*, *Microbiologist* **6** (2003) 30-33.
- [64] Tran-Minh C., Pandey P. C. and Kumaran S. *Studies on acetylcholine sensor and its analytical application based on the inhibition of cholinesterase*, *Biosensors and Bioelectronics* **5** (1990) 461-471.
- [65] Thévenot D. R., Toth K., Durst R. A. and Wilson G. S. *Electrochemical biosensors: recommended definitions and classification*, *Pure and Applied Chemistry* **71** (1999) 2333-2348.
- [66] Luong J. H. and Guilbault G. G. *Analytical applications of piezoelectric crystal biosensors*, *Bioprocess Technology* **15** (1991) 107-138.
- [67] Brecht A. and Gauglitz G. *Optical probe and transducers*, *Biosensors and Bioelectronics* **10** (1995) 923-936.
- [68] Brecht A. and Gauglitz G. *Recent developments in optical transducers for chemical or biochemical applications*, *Sensors and Actuators B* **38-39** (1997) 1-7.
- [69] De Stefano L., Rossi M., Staiano M. et al. *Glutamine-binding protein from Escherichia coli specifically binds a wheat gliadin peptide allowing the design of a new porous silicon-based optical biosensor*, *Journal of Proteome Research* **5** (2006) 1241-1245.
- [70] Thust M., Schöning M. J., Schroth P., Malkoc Ü., Dicker C. I., Steffen A., Kordos P. and Lüth H. *Enzyme immobilisation on planar and porous silicon substrates for biosensor applications*, *Journal of Molecular Catalysis B* **7** (1999) 77-83.
- [71] Steinem C., Janshoff A., Lin V. S.-Y., Völcker N. H. and Ghadiri R. M. *DNA hybridization-enhanced porous silicon corrosion: mechanistic investigation and prospect for optical interferometric biosensing*, *Tetrahedron* **60** (2004) 11259-11267.

- [72] Chan S., Yi Li, Rothberg L. J., Miller B. L. and Fauchet P. M. *Nanoscale silicon microcavities for biosensing*, *Materials Science and Engineering C* **15** (2001) 277-282.
- [73] Arwin H. *Ellipsometry on thin organic layers of biological interest: characterization and applications*, *Thin Solid Films* **377-378** (2000) 48-56.
- [74] Luca De Stefano, Lucia Rotiroti, Ivo Rendina, Luigi Moretti, Viviana Scognamiglio, Mosè Rossi and Sabato D'Auria *Porous silicon-based optical microsensor for the detection of L-glutamine*, *Biosensors and Bioelectronics* **21** (2006) 1664-1667.
- [75] Min H.-K., Yang H.-S. and Cho S. M. *Extremely sensitive optical sensing of ethanol using porous silicon*, *Sensors and Actuators B* **67** (2000) 199-202.
- [76] Victor S.-Y. Lin, Kianoush Motesharei, Keiki-Pua S. Dancil, Michael J. Sailor and M. Reza Ghadiri *A porous silicon-based optical interferometric biosensor*, *Science* **278** (1997) 840-843.
- [77] Starodub N. F., Fedorenko L. L., Starodub V. M., Dikij S. P. and Svechnikov S. V. *Use of the silicon crystals photoluminescence to control immunocomplex formation*, *Sensors and Actuators B* **35-36** (1996) 44-47.
- [78] Osaka T. *Electrochemical formation and microstructure in thin films for high functional device*, *Electrochimica Acta* **42** (1997) 3015-3022.

## *CHAPTER 2.*

# **OPTICAL BIOSENSORS: THEORETICAL BACKGROUND and LITERATURE REVIEW**

This chapter comprises four sections and provides the literature review and theoretical background related to this study. It begins (section 2.1) with a brief theory of porous silicon formation and optical properties of porous silicon from the bio-sensing point of view.

The next section 2.2 is devoted to the theory, principles of work and applications of optical immune sensors; principles of immune reactions and optical methods of their registrations, such as ellipsometry, surface plasmon resonance, total internal reflection ellipsometry, and planar waveguide are taken into consideration.

Section 2.3 reviews a background of the concept of optical enzyme sensors for organophosphates and heavy metal ions detection.

Finally, section 2.4 introduces and gives a brief description of analytes of interest.

## 2.1 Porous Silicon Based Optical Biosensors

### 2.1.1 Porous silicon basics

#### a. Pore formation

Porous silicon (PS) is fabricated by an *electrochemical etching* of silicon (Si) in a hydrofluoric (HF) acid solution. Pore initiation occurs at surface defects or irregularities<sup>[1]</sup>. Because of the electrochemical reaction occurring on the surface of the silicon, a partial dissolution of Si occurs. The exact chemistry of silicon dissolution is still uncertain, and several models have been proposed<sup>[2, 3]</sup>. Excellent reviews of PS technology are available (see Ref. <sup>[4]</sup>, for instance).

Lehmann and Gösele<sup>[5]</sup> have proposed a surface bound oxidation scheme of the formation of the divalent silicon oxidation state by capturing a hole and subsequent emission of the electron, as shown in Fig. 2.1-1.

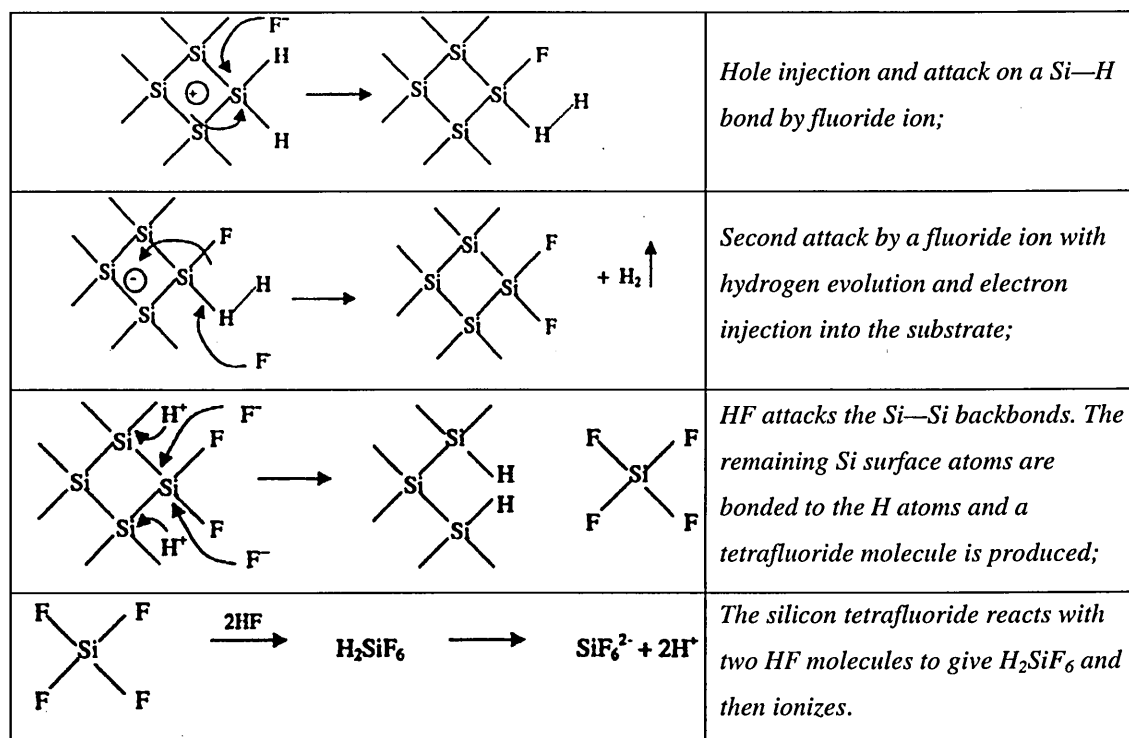


**Figure 2.1-1** Silicon dissolution scheme proposed by Lehmann and Gösele (after Ref. <sup>[6]</sup>).

This model has become the most popular. According to this model, the silicon dissolution process requires the presence of fluorine ions ( $F^-$ ) and holes  $h^+$ . The fluorine ions supplied by the HF solution and the holes on the silicon surface must be supplied from the bulk. In order to achieve a significant hole current in  $n$ -type  $Si^a$ , external illumination of the sample is required, depending on the doping level<sup>[7]</sup>.

### *b. PS fabrication*

A principal sketch of the cell for PS fabrication is given in Fig. 2.1-2. A silicon wafer (2) with the contact on the back is fixed on a holder (1) and brought into contact with the Teflon (PTFE) cup (4) filled with electrolyte (5) through the rubber O-ring (3). After applying a voltage (positive anode on Si and negative cathode on platinum (Pt) electrode (6)) between the back side contact of the wafer and an electrode in the HF solution, a pore growth by silicon dissolution eventually starts<sup>[8]</sup>.

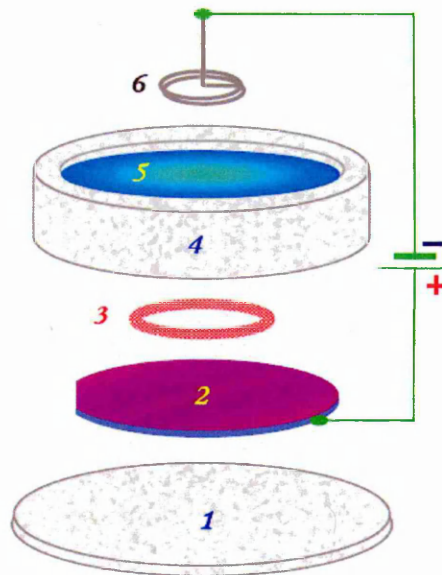


**Figure 2.1-2** Scheme of a cell for porous silicon fabrication; 1 – Teflon base; 2 – Si wafer with back side contact; 3 – rubber O-ring; 4 – Teflon cup; 5 – electrolyte; 6 – Pt electrode.

<sup>a</sup> Si has four electrons in its valence band. An  $n$ -type Si is obtained by doping, i.e. adding a valence-five element (for instance, arsenic (As)) in order to increase the number of free charge carriers. When a Si crystal is doped with As, some Si atoms are replaced by As atoms, which have five valence electrons. The “extra” electron moves into the conduction band and can carry current. If a Si crystal is doped with an element that has three valence electrons (such as boron (B)), holes are introduced into the crystals. Holes can “jump” from atom to atom, carrying current. These are called  $p$ -type  $Si^{[1]}$ .

Due to the hydrophobic character of the clean Si surface, ethanol ( $C_2H_6O$ ) is usually added to the HF solution in order to increase the wettability of the Si surface (water is part of the electrolyte merely because the hydrofluoric acid was supplied in a ~49% aqueous form). Moreover, during the reaction there is hydrogen evolution. Bubbles form and stick on the Si surface in pure HF aqueous solution, whereas they are promptly removed if ethanol or other surfactant is present<sup>[9]</sup>.

### *c. PS morphology*

SEM images of PS reveal that PS consists of isolated crystallites and/or chains of crystallites linked by narrow silicon walls<sup>[10]</sup>. The properties of PS, such as porosity, thickness, and pore diameter depend on<sup>[11]</sup>:

- (i) Doping type;
- (ii) Doping level;
- (iii) Anodization current density;
- (iv) Electrolyte composition;
- (v) HF concentration;
- (vi) Anodization time.

For instance, porosity increases with increases of the current density and anodization time. Increases of the HF concentration lead to porosity decreases. For *p*-type doped substrates (at given HF concentration) the porosity increases with increasing current density. In *n*-type doped Si, the porous layers obtained at low current density have a finer structure.

A *p*-type silicon substrate forms a uniform and highly interconnected network of random pores, resulting in a spongy structure (Fig. 2.1-3a). In *n*-type samples, the pores are formed only under illumination and are relatively linear (Fig. 2.1-3b).

At higher current densities, the pores widen further; in *n*-type, the linear pores tend to become pipe-like. At very high currents, silicon is uniformly etched away, leading to electropolishing<sup>[12, 13]</sup>.

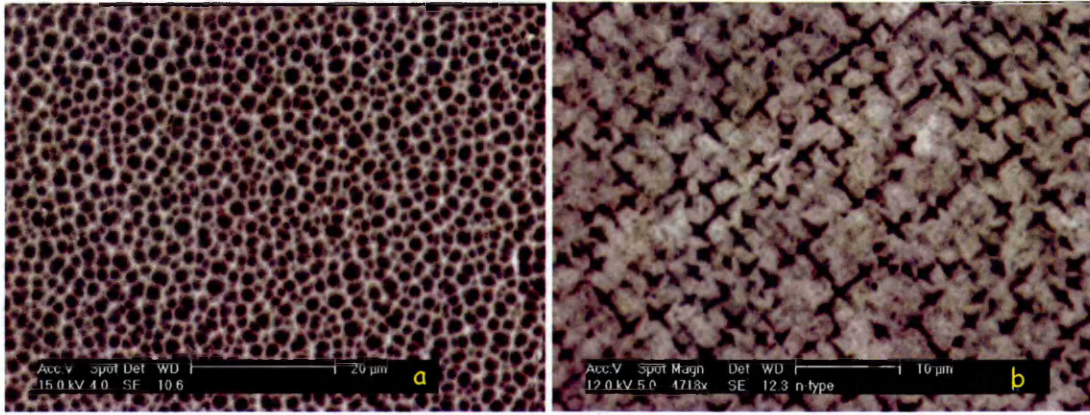


**Figure 2.1-3** Scanning electron micrographs of PS samples made from *p*-silicon (a) and *n*-type silicon (b).

*d. Current-Voltage characteristics*

The current-voltage (*I-V*) curves show two distinct current peaks<sup>[14]</sup> (see Fig. 2.1-4a,b). PS formation occurs in zone A, when the current *I* is less than the value at the first peak  $I_{PS}$  (Fig. 2.1-4c). Zone B is a transition region to the electropolishing regime depicted as zone C.

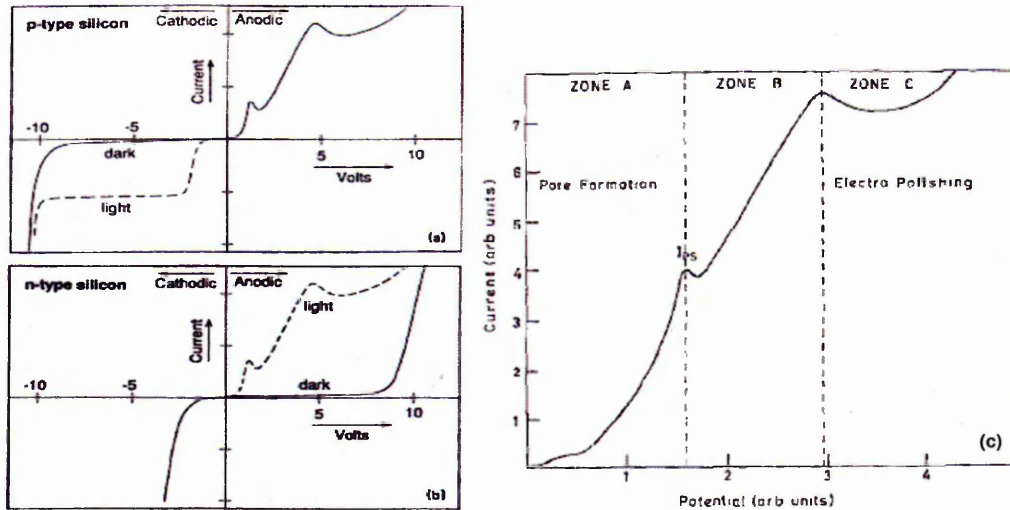


**Figure 2.1-4** a, b – Current-voltage (*I-V*) curves for *p*- and *n*-type silicon, respectively (after Refs.<sup>[15, 16]</sup>). The solid line indicates the dark response and the dashed line shows a response under illumination; c – typical anodic *I-V* characteristic for silicon in HF. The three zones represent the pore formation regime, a transition region and the electropolishing regime (taken from Ref.<sup>[17]</sup>).

When Si is the anode, the system is forward biased for *p*-type silicon, whereas for *n*-type silicon it is reversely biased. Under illumination, *n*-type and *p*-type Si exhibit similar *I-V* characteristics.

*e. Porosity*

The sample porosity is the most exploited macroscopic parameter used to describe the PS morphologies. Porosity is defined as a fraction of voids within the PS layer and can be determined by weight measurements. The silicon wafer is weighted before anodization ( $m_1$ ), after anodization ( $m_2$ ), and after removal of the whole PS layer from the substrate ( $m_3$ ) by dissolution in a 3% potassium hydroxide (KOH) solution. The porosity  $p$  can be calculated as<sup>[6]</sup>:

$$p = \frac{m_1 - m_2}{m_1 - m_3} \cdot 100\% .$$

Porosity can be controlled by the etching current density. As it has been mentioned before, the Si dissolution process requires the presence of fluorine ions ( $F^-$ ) and holes ( $h^+$ ). At the low current density (pore formation regime), when the fluorine ions are delivered faster than the holes, the outer-pore regions of PS are depleted of holes, and further etching occurs only at the pore tips, where the holes are focused by the electric field (see Fig. 2.1-5). Decreasing the current density leads to a drop in the number of holes at the pore tips, and this leads to a smaller pore size<sup>[18]</sup>.

The International Union of Pure and Applied Chemistry (IUPAC) has proposed the classification of pores according to their sizes<sup>[19]</sup> as follows:

1. Pores with diameter exceeding 50 nm are called *macropores*;
2. Pores of diameters between 2 nm and 50 nm are called *mesopores*;
3. Pores with diameters less than 2 nm are called *micropores*.

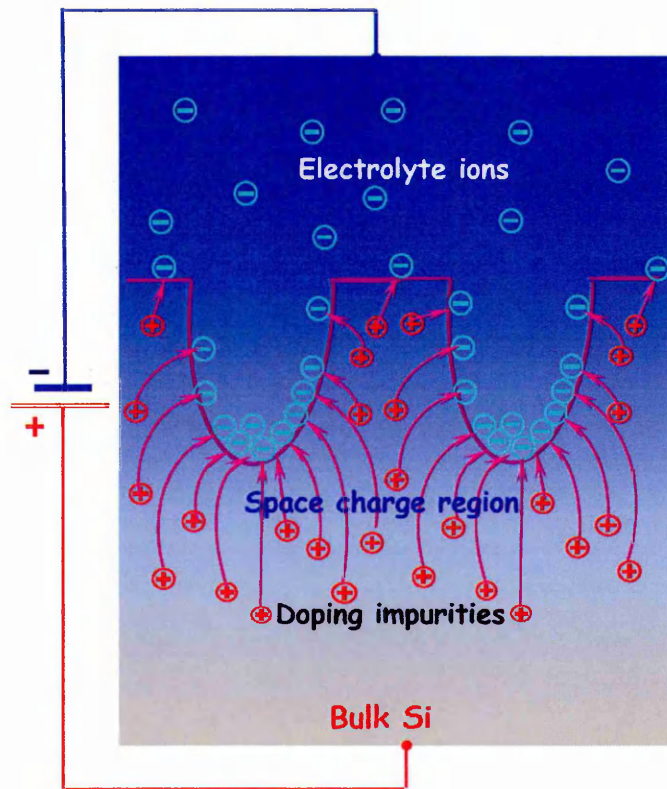


**Figure 2.1-5** Schematic distribution of the electric field lines in the space charge region during anodization in the electrolyte (adapted from Ref.<sup>[20]</sup>).

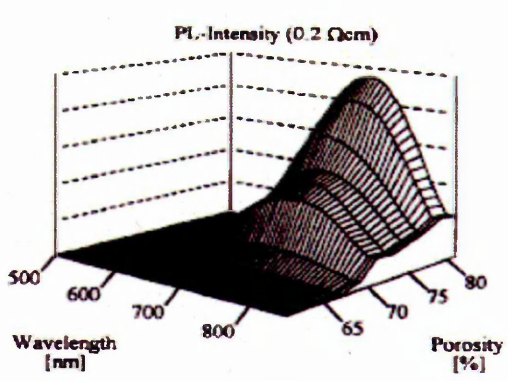
*f. Optical properties of PS: photoluminescence*

Normally crystalline silicon does not emit light due to its *indirect* band gap structure (i.e. the minimum energy in the conduction band is shifted by a  $k$ -vector relative to the valence band). However, PS samples having a porosity of more than 60% and a pore size of less than 2 nm are found to luminesce in the visible region<sup>[21]</sup> (see Table 2.1-1).

PS can (under different circumstances) produce photoluminescence in the near infrared, visible, and near UV ranges. The properties and origins of photoluminescence bands of PS are reviewed and discussed by Fauchet<sup>[22]</sup>.

**Table 2.1-1** PS luminescence bands (based on Ref.<sup>[6]</sup>) and PL spectra of low p-doped PS layers of various porosities (taken from the Ref.<sup>[8]</sup>).

<i>Spectral range</i>	<i>Peak wavelength</i>
UV	~350 nm
Blue-green	~470 nm
Blue-red	400 – 800 nm
Near IR	1100 – 1500 nm



*g. Optical properties of PS: electroluminescence*

Halimaoui and colleagues<sup>[23]</sup> first observed visible electroluminescence (EL) from PS in 1991. PS exhibits EL during anodization in aqueous solution (wet EL) and also in solid state structures. Wet EL is not permanent and is quenched rapidly because of the oxide formation at the Si surface<sup>[12]</sup>. The peak position of EL depends on applied voltage; therefore, the colour of emission can be varied from dark red to bright green. Savir et al.<sup>[24]</sup> investigated wet EL intensity of PS upon applying an electrical current (Fig. 2.1-6).

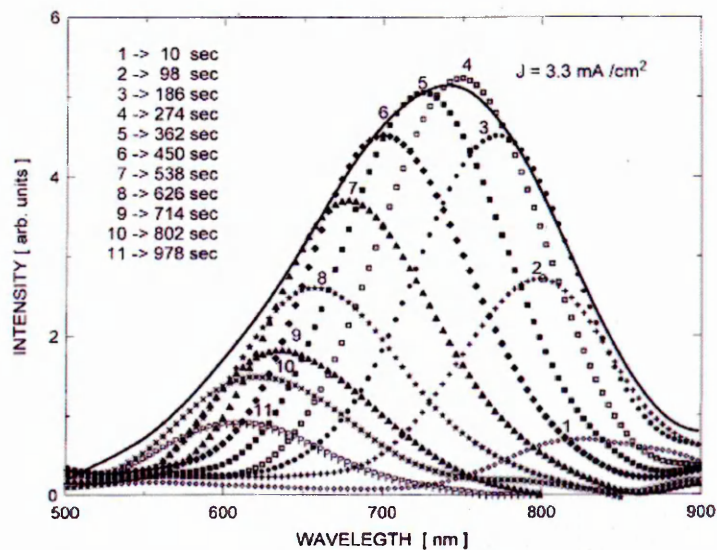


**Figure 2.1-6** Several EL spectra (assorted symbols) obtained at different times of the EL current flow. The solid curve represents the PL spectra (after Ref.<sup>[24]</sup>).

EL intensity first rises with time, reaches a maximum, and then decays to zero. At the same time, the peak of the EL spectrum shifts from  $\lambda = 850$  nm in the beginning to  $\lambda = 600$  nm at the end of the process. An envelope of all emitted EL spectra during the anodic oxidation of a sample (i.e. time integrated spectra) is similar to the PL spectrum of that sample<sup>[24]</sup>.

John and Singh in their review<sup>[12]</sup>, suggested that the similarity between the time integrated EL and the PL spectrum is the result of a similar nature of radiative recombination in both processes. However, the mechanisms of the carriers involvement in radiative recombination are different. Carriers for PL are generated optically.

In the case of electroluminescence, the contribution to the EL, at the beginning, is mainly from the larger nanocrystallites. This is because such particles are associated with smaller energy gaps, so that electron injection from the electrolyte requires less energy (lower voltage). With time, these nanocrystallites become covered with oxide due to the EL current flow. At this point, the current is diverted to smaller nanocrystallites and electron injection into such crystallites requires a higher voltage.

## 2.1.2 Porous silicon for biosensing applications

The large internal surface area within a small volume, efficient room-temperature visible photoluminescence and biocompatibility of PS has stimulated recent interest in its applications for sensor development. The main advantages of sensors based on PS technology are<sup>[25]</sup>:

(i) The pore size can be easily adjusted from nanometers to micrometers by choosing appropriate etching conditions<sup>[26]</sup>;

(ii) Sensing components (e.g. biomolecules like enzymes and other proteins) are protected against fast leaching out due to the sponge/maze morphology of PS;

(iii) A large surface area of PS promotes the miniaturization of sensors since the measuring signal (for instance, capacitance) raises with the increase of the effective sensor area<sup>[27]</sup>;

(iv) Due to a high concentration of adsorption sites on the PS surface, the sensitivity of PS transducers to molecular adsorption can be increased. The amplification of sensitivity via increasing the surface area can be achieved, for example, using antibody-coated nanoparticles<sup>[28]</sup> or surface-enlarging layers of polymers<sup>[29, 30]</sup>. However, these methods are expensive, time consuming, and sample preparation procedure is complicated, also porosity is much smaller.

The immobilization of proteins<sup>[31]</sup> on solid surface has an important function in the technologies employing bio-recognition events. Understanding of the protein (enzyme)–solid substrate interaction and diffusion of biomolecules inside the PS matrix has a great impact on PS-based biosensor techniques<sup>[32]</sup>. Several experimental attempts have been made to study molecular adsorption and to perform different chemical and bio-chemical reactions in a PS matrix. The most popular optical principles exploited in PS transducers include ellipsometry, Fabry-Perot interferometry, and photoluminescence.

#### *a. Ellipsometry*

The use of the powerful analytical tool of ellipsometry<sup>a</sup> to monitor changes in optical parameters of PS in the course of bio-reaction was demonstrated by Arwin<sup>[33]</sup>. The advantages of this transducing technique lie in a combination of the high sensibility of ellipsometry with the large adsorption area of PS and allow the registration of small molecules bonded to receptor proteins. Moreover, variable angle spectroscopic ellipsometry can be used for characterization of PS layer thickness, porosity and microstructure<sup>[34, 35, 36]</sup> and to monitor and quantify protein uptake by a PS matrix<sup>[37, 38]</sup>.

Detection of the specific binding of small molecules to receptor molecules requires high sensitivity. Another spongy medium of porous silicon dioxide surfaces has been used by van Noort et al.<sup>[39]</sup> for monitoring the specific binding of low molecular weight molecules (biotin and oligopeptide) to streptavidin with the ellipsometry technique.

---

<sup>a</sup> A detailed overview of ellipsometry working principles is given in chapter 2.2.2.

The performance of porous silicon dioxide (SiO<sub>2</sub>) as a potential surface in biosensor applications was compared with a planar silicon dioxide surface. Porous silicon dioxide showed a 10-fold amplification of the response as compared to the planar silicon dioxide. It was possible to monitor the binding of biotin and oligopeptide in the concentration range of 2 – 40 μM and this proved the effectiveness of using ellipsometry for the detection of small molecules in the range 0.2 – 2 kDa.

*b. Fabry-Perot interferometry*

The sensors described in Refs.<sup>[40, 41, 42]</sup> operate by measuring the interference pattern (Fabry-Perot fringes) created by multiple reflections of the incident white light at the top and the bottom of the porous silicon layer as shown in Fig. 2.1-7.

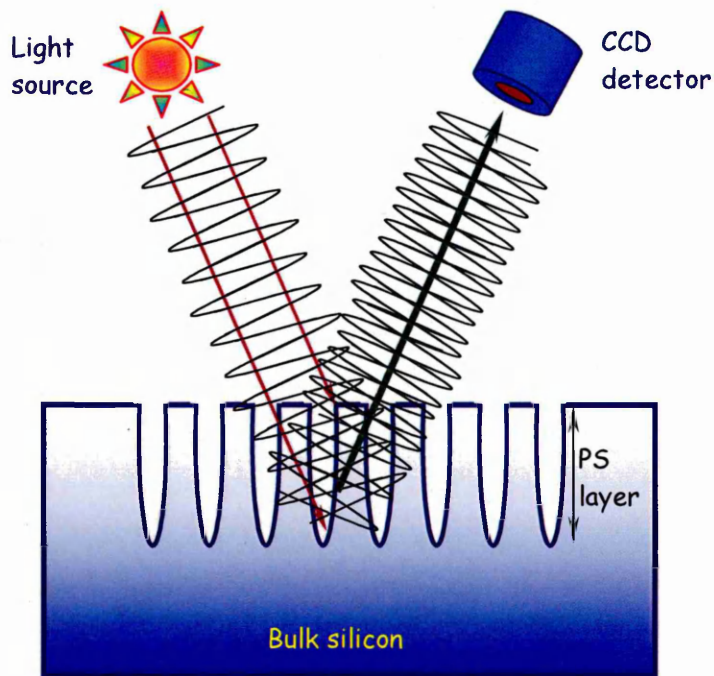


**Figure 2.1-7** The scheme of the PS based optical interferometer (adapted from Ref.<sup>[40]</sup>).

Since the reflectometric interference spectrum is sensitive to both the refractive index  $n$  and effective optical thickness  $L$  of the PS layer, the wavelength shift in the fringe pattern can be induced when new molecules bind to the PS surface<sup>[43]</sup>:

$$m\lambda = 2nL,$$

where  $m$  is the diffraction order and  $\lambda$  is the wavelength of light. Binding of analytes to its bio-receptors, immobilized on the PS surface, induces changes in the refractive index of the PS layer and results in a wavelength shift of diffraction fringes.

Lin et al.<sup>[44]</sup> and Steinem et al.<sup>[45]</sup> used the hybridization of DNA oligonucleotide in neutral aqueous solutions with the complementary sequences immobilized into a PS matrix to test the selectivity and limits of detection of a Fabry-Perot interferometric sensor. In the presence of complementary DNA sequences (DNA concentration ranging from  $2 \cdot 10^{-15}$  to  $2 \cdot 10^{-6} M$ ), an unexpectedly large shift in the Fabry-Perot interference pattern to lower wavelengths was observed implying a decrease in the effective optical thickness of the PS matrix (Fig. 2.1-8a). In the presence of non-complimentary DNA sequences no significant shift in the wavelength of the interference fringe pattern was detected (Fig. 2.1-8b) under similar conditions.

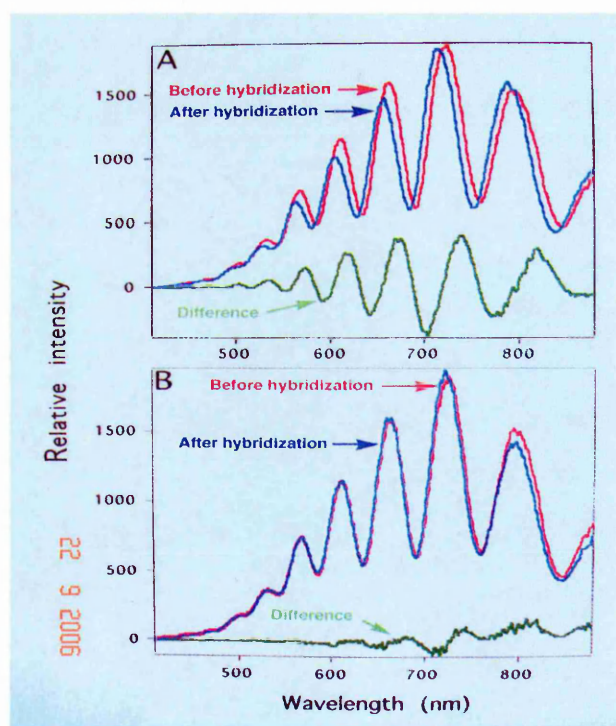


**Figure 2.1-8** Interferometric reflectance spectra of DNA-modified PS layers (taken from Ref.<sup>[44]</sup>).

Steinem et al.<sup>[45]</sup> suggested that the observed optical effect is due to the enhanced corrosion (oxidation–hydrolysis) of the PS layer triggered by the formation of complementary DNA duplexes. Authors postulated that the slow background corrosion process initiated at the exposed Si–H<sub>x</sub> groups is dramatically enhanced as a result of

changes in the carrier charge density of the porous silicon layer in response to the local increase in the electric field generated by hybridization of the nucleic acids.

The observed phenomenon is thus an example of an active sensor matrix, in which the molecular recognition signal is transduced and amplified by profound changes in the chemical reactivity and physical properties of the solid support itself. The lowest DNA concentration measured with the PS interferometric sensor is  $9 \text{ fg/mm}^2$ . For comparison, the detection limit of the surface plasmon resonance technique is  $0.3 \text{ pg/mm}^2$  [46].

Biological interactions take place in an aqueous environment, usually at pH~7, and the PS surface has to be stable under these conditions. However, PS manifests various degrees of stability in aqueous media depending on the surface preparation. Stability of PS layers in aqueous solution has been investigated by Janshoff et al [47]. In their study the stabilities of freshly etched, oxidised, and linker-modified surfaces were investigated. PS stability towards corrosion in aqueous media varies substantially in the following decreasing order: linker modified > thermally oxidised > ozone oxidised > Si-H terminated. The observed decrease in the effective optical thickness with time appears to be caused by the oxidation or dissolution of porous silicon. Furthermore, dissolution of the porous layer can lead to a decrease in the layer thickness or an increase in the porosity.

Dancil et al. [40] investigated the use of PS as an immobilisation and transducing matrix for monitoring protein-protein binding, namely *protein A* with IgG. The Fabry-Perot transduction was achieved by monitoring the change in the effective optical thickness of a PS film upon analyte binding. The stability of PS surface towards oxidation in an aqueous buffer solution, reversibility, insensitivity to nonspecific interactions, and the correlation of signal response with analyte mass were observed in this work.

### c. *Photoluminescence*

PS has received getting increasing attention in the biosensor field due to its luminescence being strongly reactive with the environment [8]. The intensity and the

spectral shape of PS luminescence are strongly dependent on the chemistry of its surface; moreover, adsorbed molecules can quench the photoluminescence (PL)<sup>[48]</sup>. Light emitting properties of PS were used by Starodub et al.<sup>[49]</sup> to create an immunosensor capable of detecting *myoglobin*<sup>a</sup> in a buffer solution and human serum. The effect of the extinguishing of PS photoluminescence, due to the molecular adsorption and immunocomplex formation on the PS surface, was exploited by Starodub and colleagues<sup>[50]</sup>. It was shown that the absorption of immune components in PS and the following immune reactions affect the intensity of PL; the sensitivity of the above sensor was 10 ng/ml.

Di Francia and co-workers<sup>[51]</sup> have reported on the fabrication of an optical label-free DNA sensor using luminescent PS as an active transducer. The specific single strand DNA (ss-DNA)–complementary strand DNA (c-DNA) interaction has been directly “sensed” as a variation in the PS photoluminescence. The authors functionalised the PS surface by a linker and then exposed it to ss-DNA. The PL showed a 12% variation when the derivatised samples were exposed to 10 µM aqueous solution of c-DNA, while no effect was recorded with the non-complimentary (nc-DNA) at the same concentrations. The effect of the length and composition of DNA oligonucleotides on the PL intensity and peak position were also reported.

Bindings of short oligonucleotides of DNA to probe molecules immobilised on the PS chip were observed by Chan et al.<sup>[52]</sup> through the wavelength shifts in the photoluminescence peaks. Full-length viral DNA molecules were also detected in this work; a larger shift in the photoluminescence peaks was observed, due to the larger refractive index change of the binding molecules.

#### *d. Electroluminescence*

As a technique, electroluminescence (EL) seems to be more attractive because it combines the high sensitivity of luminescence measurements with the much easier and cost-effective method of its excitation as compared to PL. Moreover, EL can be performed by simple measurements of emitted light intensity at a fixed wavelength. In

---

<sup>a</sup> *Myoglobin* serves as marker of the development of the heart disease

addition, the use of an electrolyte contact in EL measurements allows easy operation with chemical and bio-reactions in the aqueous phase<sup>[53]</sup>. However, much less work has been done so far on the application of EL for chemical and bio-sensing. The influence of polyelectrolytes on reproducibility and stability of EL in PS and effect of adsorption of bovine serum albumin (BSA) (as an example of common proteins) on EL quenching have been studied by Nabok et al.<sup>[54]</sup>.

*e. Non-optical principles*

A novel enzymatic PS-based potentiometric method for detection of triglycerides<sup>a</sup> has been reported by Reddy et al.<sup>[55]</sup>. PS was thermally oxidized and used to immobilise *lipase*, an enzyme which hydrolyses triglycerides resulting in the formation of fatty acids. This caused a change in the pH of the solution. The structure enzyme solution–oxidized porous silicon–crystalline silicon was used to detect changes in pH during the hydrolysis of triglyceride as a shift in the capacitance–voltage characteristics.

Biochemical sensors with a PS capacitor have been also developed by Lüth et al.<sup>[56]</sup>, and according to their research, the measured capacitance value increased up to a factor of 30 due to the enlargement of the active sensor area.

---

<sup>a</sup> The amount of *triglycerides* is a clinical parameter that is correlated to heart disease.

## 2.2 Optical Immune Sensors

Adsorption of quite bulky antibodies on the surface is usually accompanied by a substantial increase in the mass and thickness of the sensitive layer and can be easily detected with optical biosensors, based on evanescent wave technology, such as surface plasmon resonance, ellipsometry, and planar waveguides as described below.

### 2.2.1 Surface plasmon resonance

#### *a. Surface plasmon waves*

The principles of surface plasmon resonance (SPR) are explained in detail elsewhere<sup>[57, 58, 59]</sup>. In brief, the SPR is the result of a resonant coupling between a light wave and a surface plasma (plasmon) wave (SPW) along the interface between a metal and a dielectric.

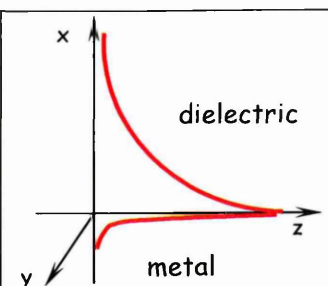
SPW is a TM-polarized electromagnetic wave (magnetic vector is perpendicular to the direction of propagation of the SPW and parallel to the plane of the interface) connected with a charge-density oscillation that may exist on the interface between a dielectric and a metal. The most suitable metals for the excitation of the SPR are those with a high negative value of the real part of the dielectric constant, like silver, gold and aluminium<sup>[60, 61]</sup>.

The SPW propagates along the metal/dielectric interface, and the associated electric field decays exponentially away from the surface<sup>[62]</sup> as an evanescent wave (“evanescent” from the Latin for *vanishing*). This decay is characterized by a *penetration depth* which is the distance from the interface (coordinate  $x$ ), at which the amplitude of the electric field falls by a factor  $1/e$ , and a *propagation length*, which is the distance along the interface (coordinate  $z$ ), at which the power decays by the factor  $1/e$ . The field profile with a characteristic decay in the direction normal to the interface is depicted in the inset of Table 2.2-1.

Typical values of the propagation lengths and penetration depths on the interface water/gold and water/silver for two different wavelengths are shown in Table 2.2-1.

**Table 2.2-1** Characteristics of the SPW on the interfaces water/gold and water/silver (adapted from the Ref.<sup>[63]</sup>)

Metal	Gold		Silver	
	650	800	650	800
Wavelength, nm	650	800	650	800
Propagation length, $\mu\text{m}$	4.1	16	20	44
Penetration depth into metal, nm	28	26	23	23
Penetration depth into dielectric, nm	180	320	230	380



*b. Kretschmann's configuration for the excitation of SPR*

Two different experimental systems for excitation of the SPW were developed by Otto<sup>[64]</sup> and Kretschmann<sup>[65]</sup>. The only significant difference between these configurations is the location of the metal film. In the Kretschmann arrangement, the film is deposited directly on the coupling prism, whereas in the Otto-type device the film is separated from the prism by air (or an other dielectric material) at a distance of approximately one wavelength of excitation light<sup>[66]</sup>. Kretschmann's configuration, which is more convenient and widely used, is described below.

Kretschmann's configuration exploits the phenomenon of the total internal reflection (TIR). As illustrated in Figure 2.2-1, when a beam of light strikes the interface between two transparent media directed from the medium of higher refractive index ( $n_1 > n_2$ ), the total internal reflection occurs when the angle of reflection  $\Theta$  is larger than the critical angle  $\Theta_c$ ,  $\Theta_c = \sin^{-1}\left(\frac{n_2}{n_1}\right)$ <sup>[67]</sup>. Although the incident light is totally reflected, a component of this light, the evanescent wave, propagates along the surface but decays exponentially perpendicularly to it<sup>[68]</sup>.

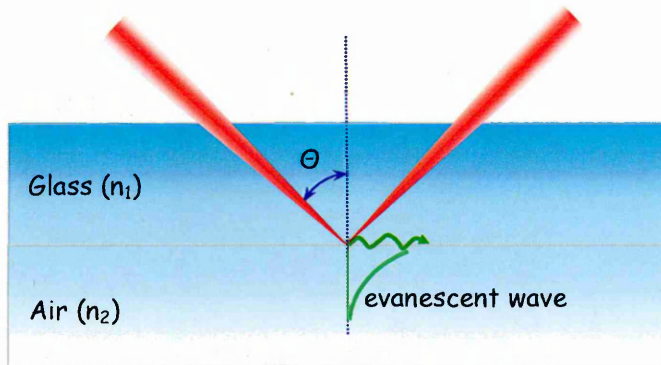


Figure 2.2-1 Total internal reflection.

SPR occurs when a thin conducting film is placed at the interface between the two optical media (see Fig. 2.2-2). At the specific incident angle  $\Theta_{SPR}$ , greater than the TIR angle, a light beam penetrates through the metal and excites a SPW on the interface between the metal and the sample. In the conducting film, the SPW resonantly couples to the light (monochromatic,  $p$ -polarized) due to the matching frequencies. Since the propagation length of the SPW is very limited (see Table 2.2-1), coupling of SPW is only possible for thin metal films. In most cases, the required metal film thickness for optimal coupling is about 40 nm for silver and 48 nm for gold<sup>[69]</sup>.

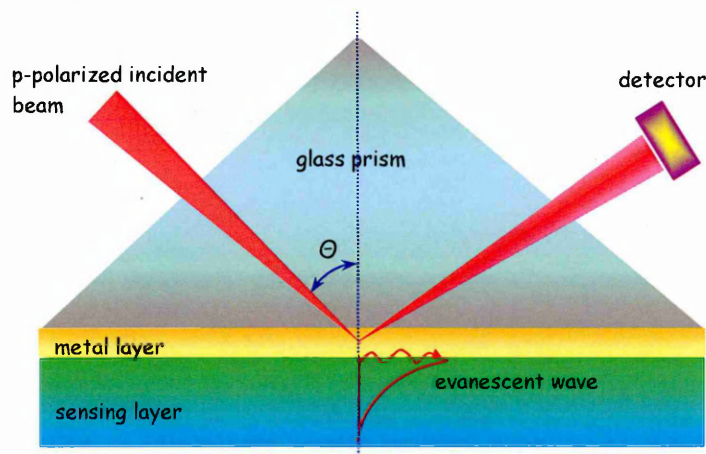


Figure 2.2-2 A Kretschmann's configuration for excitation of SPW.

The wave vector of the evanescent field  $k_{ev}$  is given by equation:

$$k_{ev} = k_0 n_{glass} \sin \Theta, \quad (2.1)$$

where  $k_0 = \frac{2\pi}{\lambda}$  is the wave vector in vacuum,  $n_{glass}$  is the refractive index of the dense medium (glass prism), and  $\Theta$  is the angle of incidence of the light. The wave vector of SPW  $k_{SPW}$  can be written as

$$k_{SPW} = k_0 \sqrt{\frac{\epsilon_m n_d^2}{\epsilon_m + n_d^2}}, \quad (2.2)$$

where  $\epsilon_m = \text{Re} \epsilon_m + \text{Im} \epsilon_m$  is a dielectric function of the metal, and  $n_d$  is the refractive index of the dielectric<sup>[70]</sup>. The evanescent wave of the incoming light is able to couple with the SPW at a specific angle of incidence corresponding to the condition:

$$k_{SPW} = k_{ev}, \quad (2.3)$$

and thus the surface plasmon is resonantly excited. This causes the energy of the incident light to be transferred to the SPW and to be adsorbed in the metal film due to the energy dissipation, resulting in a reduction in the intensity of reflected light, which can be detected.

The reflectance of the incident light at a given angle  $\Theta$  can be calculated using the three-layer Fresnel equations relating  $p$ -polarization for the sensing system consisting of three media: glass prism/metallic film/sensing layer (which are abbreviated  $p$ ,  $m$ , and  $s$ , respectively) as follows<sup>[71]</sup>:

$$R = \left| \frac{r_{pm} + r_{ms} \exp(2ik_{mz}d)}{1 + r_{rm} r_{ms} \exp(2ik_{mz}d)} \right|^2. \quad (2.4)$$

with the amplitude reflectance  $r_{pm}$  for “glass prism–metal film” and  $r_{ms}$  for “metal film–sensing layer” interfaces, which are given by the following equations:

$$r_{pm} = \frac{k_{pz} \epsilon_m - k_{mz} \epsilon_p}{k_{pz} \epsilon_m + k_{mz} \epsilon_p}, \quad (2.5)$$

$$r_{ms} = \frac{k_{mz} \epsilon_s - k_{sz} \epsilon_m}{k_{mz} \epsilon_s + k_{sz} \epsilon_m}, \quad (2.6)$$

$$k_{jz} = \left( \epsilon_j \frac{\omega^2}{c^2} - k_x^2 \right)^{\frac{1}{2}} \quad \text{for } j = p, m, s \quad (2.7)$$

$$k_x = \sqrt{\epsilon_p} \frac{\omega}{c} \sin \Theta, \quad (2.8)$$

where  $\epsilon_j$  and  $k_{jz}$  are the dielectric constant and the wave-vector component perpendicular to the interface in the medium  $j$ ;  $k_x$  is the component of the incident wave vector parallel to the interface;  $d$  is the thickness of the metallic film;  $\omega = \frac{2\pi c}{\lambda}$  is the frequency of the incident light;  $c$  is the velocity of the light<sup>[72, 73]</sup>.

In practice, one of the two detection schemes of SPR can be employed<sup>[74]</sup>:

*The angular SPR:* the wavelength is fixed and the reflected light intensity is recorded during the scanning of the angle of incidence;

*The spectral SPR:* the incident angle is fixed near the angle of total internal reflection and the spectrum of the reflected light intensity is measured by scanning over the wavelength range.

The SPR manifests as a characteristic dip in an angular or wavelength spectrum as shown in Fig. 2.2-3.

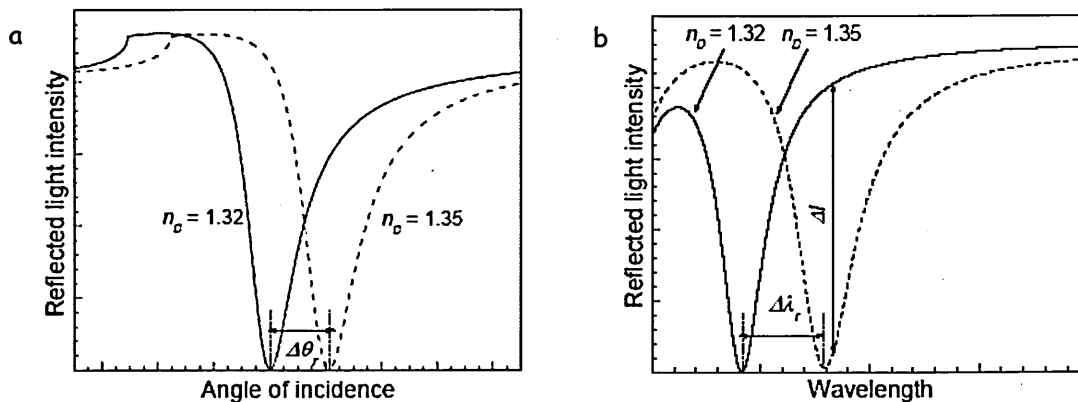


**Figure 2.2-3** a – a typical angular spectrum of SPR; b – spectral SPR (angle of incidence 54°) (taken from the Ref.<sup>[75]</sup>).

The angular (or spectral) position and the shape of the SPR spectrum depend on the optical parameters (refractive index  $n$  and extinction coefficient  $k$ ) and the thickness of the metal film. If these parameters are changed due to adsorption of molecules (see

Fig. 2.2-4), a change in the angle of incidence is required to excite the SPW. Moreover, by monitoring the angle (or wavelength) at which resonance occurs (the SPR angle) during the adsorption process with time, the kinetics of molecular adsorption can be studied<sup>[76, 77]</sup>.

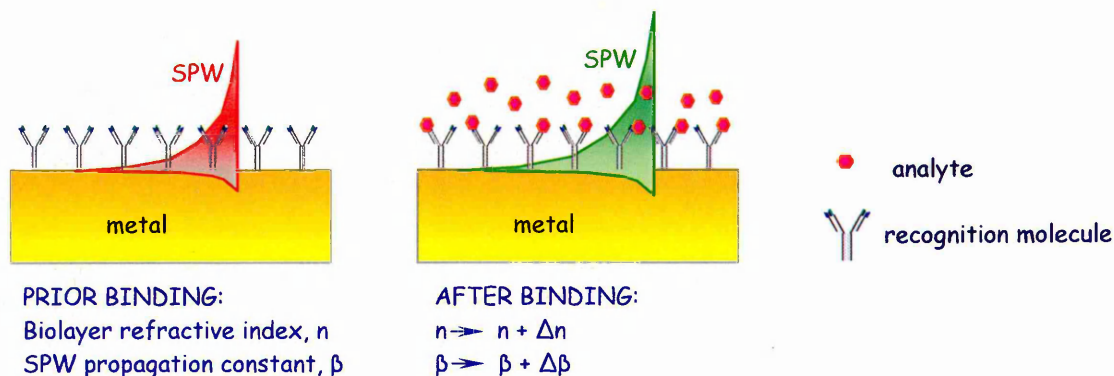


**Figure 2.2-4** Principle of SPR biosensing (adapted from the Ref.<sup>[70]</sup>).

### c. Surface plasmon resonance-based biosensors

The use of SPR for sensing biomolecular interactions was first proposed by Liedberg and colleagues in 1983<sup>[78]</sup>. Nowadays, rapid and label-free commercially available SPR apparatus (for example, Biacore<sup>®</sup> (Uppsala, Sweden), Integrated SPR Sensors (Texas Instruments, USA), IBIS System (Windsor Scientific, UK), SPR-4 and SPR-5 (Ukraine) etc.) are designed to monitor different bio-reactions both qualitatively and quantitatively in real time.

The SPR technique has been widely used for the analysis of kinetics of the binding and desorption of the interacting molecules, concentration measurements of biomolecules and molecule recognition involving protein–protein, DNA–DNA, receptor–ligand interactions<sup>[79]</sup>. An excellent review paper of fundamentals and recent advances in the development and applications of SPR biosensors has been written by Homola<sup>[70]</sup>.

There are three most widely used configurations of SPR sensors, namely the prisms coupler-, which is described above, the grating coupler-, and the optical waveguide- based SPR systems (see Fig. 2.2-5).

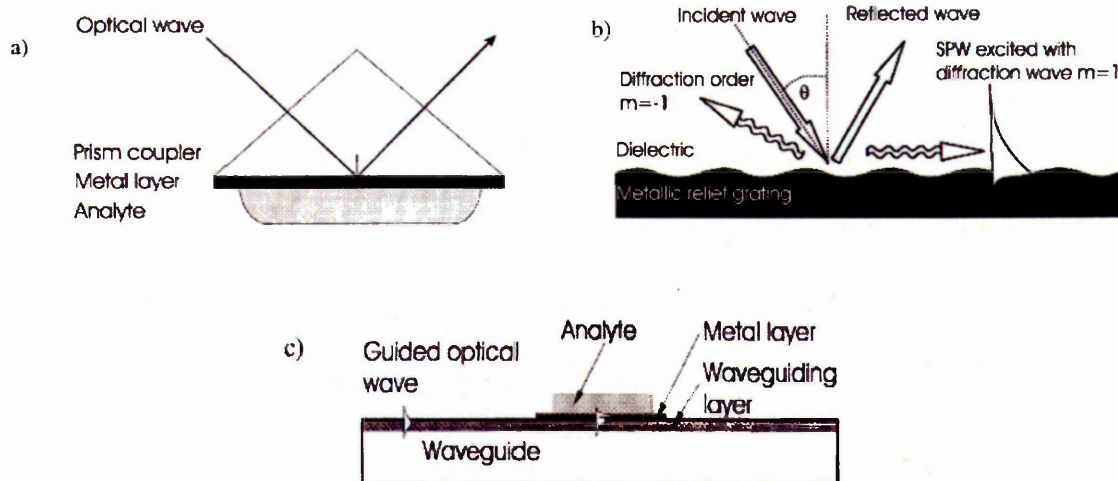


**Figure 2.2-5** Most widely used configurations of SPR sensors: a – prism coupler-based SPR system; b – grating coupler-based SPR system; c – optical waveguide-based SPR system (taken from the Ref.<sup>[57]</sup>).

In the diffraction grating SPR coupler, an optical wave strikes at a periodically modulated surface of a metallic grating with grooves perpendicular to the plane of incidence. Upon incidence on the grating, the light wave splits into reflected and diffracted waves (see Fig. 2.2-5b)<sup>[80]</sup>. When the propagation constants of the optical wave and the SPW are equal, the coupling between the two waves can occur<sup>[81]</sup>. The excitation of the SPW leads to an energy transfer between the optical wave and SPW and hence it is accompanied with a decrease in the reflected light intensity. This drop in reflectivity produces a narrow absorption dip in the angular or wavelength reflectivity spectrum<sup>[80]</sup>. Gold-based SPR grating sensors have been used for monitoring biomolecular interactions in aqueous environments<sup>[82, 83]</sup>. A more detailed description of the grating couples-based SPR sensors and their practical applications can be found in Refs.<sup>[84, 85]</sup>.

In the optical waveguide-based SPR-sensing structures, a light wave is guided by the waveguide, enters the region with a thin metal overlayer, and evanescently penetrates through the metal layer. If the SPW and the guided mode are phase-matched, the light wave excites an SPW at the outer interface of the metal. The sensitivity of waveguide-based SPR devices is approximately the same as that of the corresponding TIR configurations<sup>[86]</sup>.

A variation of the SPR biosensor in an integrated optical format (IOSPR) has been reported by Harris et al.<sup>[87]</sup>. A schematic representation of a practical IOSPR

biosensor is shown in Fig. 2.2-6. The IOSPR device based on a channel single-mode integrated optical waveguide working with a reference arm, has been tested for *simazine* detection. The lower limit of the detection has been determined to be  $0.16 \mu\text{g/l}$  using anti-simazine IgG antibodies.

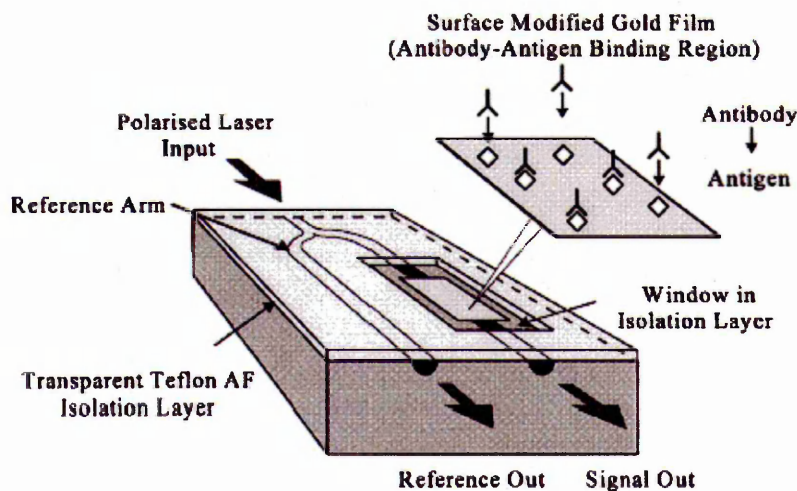


**Figure 2.2-6** A schematic diagram of the integrated optical SPR immunoprobe showing the binding of antibodies to the surface modified gold film (taken from Ref.<sup>[88]</sup>).

SPR sensors based on optical fibers offer a possibility of remote sensing. A sensor element can be placed on the tip of an optical fiber and inserted into a hazardous area<sup>[89]</sup>. Homola et al.<sup>[90]</sup> excited a SPW on a thin metal film on a side-polished single-mode optical fiber as shown in Fig. 2.2-7. Variations in the refractive index of analyte were detected by measuring changes in the intensity of the light back-reflected from a mirrored end face of the fiber. It has been demonstrated that the sensor is capable of detecting changes in the refractive index below  $4 \cdot 10^{-5}$ .

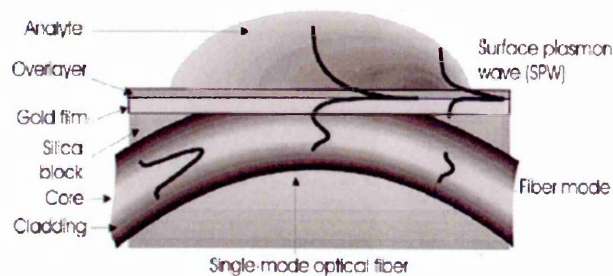


**Figure 2.2-7** Optical fiber SPR sensing structure (taken from Ref.<sup>[90]</sup>).

A multichannel SPR biosensor has been developed by Taylor et al.<sup>[91]</sup>. The sensor is based on the excitation of SPW in different sensing channels at different wavelengths and encoding information from different sensing channels into different regions of the light spectrum (Fig. 2.2-8A). The quantitative and simultaneous detection of four species of food-born bacterial pathogens has been done using an eight-channel SPR sensor based on wavelength separation multiplexing.

Another multichannel SPR biosensor described by Homola et al.<sup>[92]</sup> employs a thin dielectric over-layer, which shifts the resonant wavelength for a part of the sensing surface to longer wavelengths (Fig. 2.2-8B).

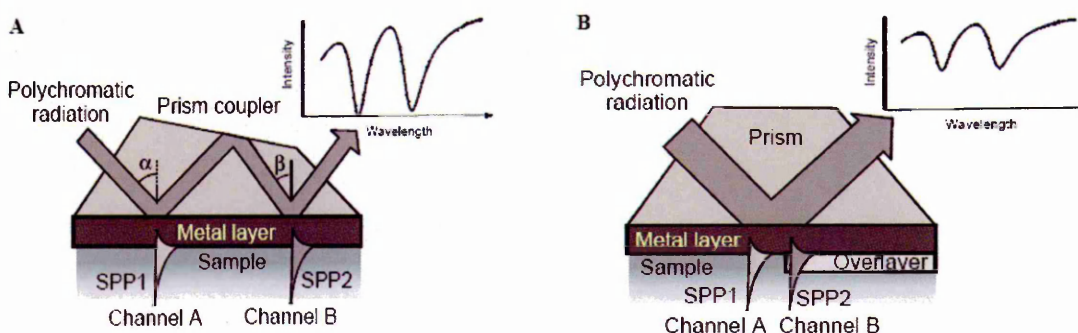


**Figure 2.2-8** Dual-surface-plasmon spectroscopy: **A** – geometry with two different angle of incidence; **B** – geometry with a high refractive index over-layer (taken from Ref.<sup>[93]</sup>).

SPR biosensors are the main optical immunosensors developed for environmental monitoring and food safety analysis<sup>[94]</sup>. Minunni and Mascini<sup>[95]</sup> used the commercial SPR apparatus BIAcore™ to detect the herbicide *atrazine*. They achieved a detection limit of 0.05 ppb, which is surprisingly small. SPR has been successfully applied to the detection of pathogens bacteria by Taylor et al.<sup>[96]</sup> and Oh et al.<sup>[97]</sup>.

The development of SPR as a biosensor for investigation of specific biological interactions including adsorption and desorption kinetics, and antigen–antibody binding, has become the fastest growing application for SPR<sup>[98]</sup>. A general method for the immobilization of proteins for applications of SPR as a biosensor uses a carboxymethyl-dextran matrix bound to the gold substrate, to which antibodies can be attached enabling specific antibody–antigen interactions to be investigated. This hydrophilic layer increases the SPR sensitivity, and protects the gold substrate from

non-specific protein adsorption. In addition, the reversible binding chemistry of the antibody to this matrix allows the surface to be regenerated and reused<sup>[99]</sup>.

Small molecule SPR-based immunoassays have suffered from poor limits of detection (LOD) due to high concentrations of primary antibody being needed to generate an adequate signal. Mitchell and co-workers<sup>[100]</sup> have developed techniques for gold nanoparticle enhancement of sensitivity in small molecule immunoassays, demonstrating a 13-fold signal enhancement and an improvement in LOD of more than two orders of magnitude. These methods offer a promising new means of assaying important small biomolecules at low concentrations previously inaccessible with SPR technology.

SPR has an advantage over other types of biosensors in its versatility and capability of monitoring binding interactions without the need for fluorescence or radioisotope labelling of the biomolecules as well as the ability to assay crude samples without purification. However, the main drawbacks of this technique lie in its complexity (specialised staff are required) and the high cost of equipment.

## 2.2.2 Spectroscopic ellipsometry

### *a. Ellipsometry basic*

The mathematical theory for ellipsometric analysis based on the Fresnel reflection and transmission equations for polarized light encountering boundaries in planar multi-layers materials<sup>[101]</sup> have been described elsewhere<sup>[102, 103]</sup>. A brief description of ellipsometry will be presented here.

A description of ellipsometry as an optical technique is based on the Maxwell's theory. According to this theory, light is a wave represented by two orthogonal vectors of electric field ( $E$ ) and magnetic field ( $B$ ). Both  $E$  and  $B$  are perpendicular to the direction of propagation  $z$ . The electromagnetic wave is described by its amplitude and frequency<sup>[104]</sup>:

$$E = E_0 \exp(i(kz - \omega t)), \quad (2.9)$$

where  $E_0$  represents the maximum amplitude of  $E$  that propagates in the  $+z$  direction,  $\omega$  is the angular frequency ( $\omega = \frac{2\pi c}{\lambda}$ );  $t$  is time;  $k$  is the wave number ( $k = \frac{2\pi}{\lambda}$ ) and the magnitude of the propagation vector  $k$  ( $k = (2\pi/\lambda)z$ ). After introducing the phase term  $\delta$ , the equation (2.9) becomes:

$$E = E_0 \cos(kz - \omega t + \delta). \quad (2.10)$$

The vector  $E$  is represented by a superposition of the two components:  $E_x$  and  $E_y$  that are orthogonal to the direction of propagation  $+z$  ( $E_z = 0$ )<sup>[103]</sup>:

$$\begin{aligned} E_x &= E_{01} \cos(kz - \omega t + \delta_x) \\ E_y &= E_{02} \cos(kz - \omega t + \delta_y) \end{aligned} \quad (2.11)$$

where  $\delta_x$  and  $\delta_y$  are the phase constants, and  $E_{01}$  and  $E_{02}$ , amplitudes of the components (x,y) of  $E$ .

Preferential orientation of  $E$  (or  $B$ ) vector is called *polarization*. Any ordinary source of light is known as *unpolarized* because  $E$  oscillates randomly in the plane perpendicular to the propagation direction (the polarization state of light is represented only by  $E$  because it is a larger effect as compared with  $B$ )<sup>[104]</sup>.

There are several ways to produce polarized light, for example, by reflection from a surface. One of the most common ways of producing linearly polarized light from unpolarized light is by using a *polarizer*. To verify the state of polarization of light after passing the polarizer, a second polarizer is necessary (*analyzer*) and no light is transmitted through the two crossed polarizers<sup>[104]</sup> as shown in Figure 2.2-9a.

Regard, as in Figure 2.2-9b, light with two arbitrary azimuths propagating in the  $+z$  direction. If  $\delta$  ( $\delta = \delta_y - \delta_x$ ) is a multiple of  $\pm\pi$  ( $\delta = m \cdot \pi$ ,  $m = 0, \pm 1, \pm 2, \dots$ ), the propagating wave is linearly polarized. If the amplitudes of the  $E_x$  and  $E_y$  components are equal ( $E_{01} = E_{02} = E_0$ ), and  $\delta$  is a multiple of  $\pm\pi/2$ , the wave is called right-circularly polarized or left-circularly polarized when  $E$  rotates clockwise or counter clockwise, respectively. In the case of elliptically polarized light, the resultant  $E$  rotates and

changes in magnitude in such a way that the locus of ends of the vectors traces an ellipse<sup>[104]</sup>.

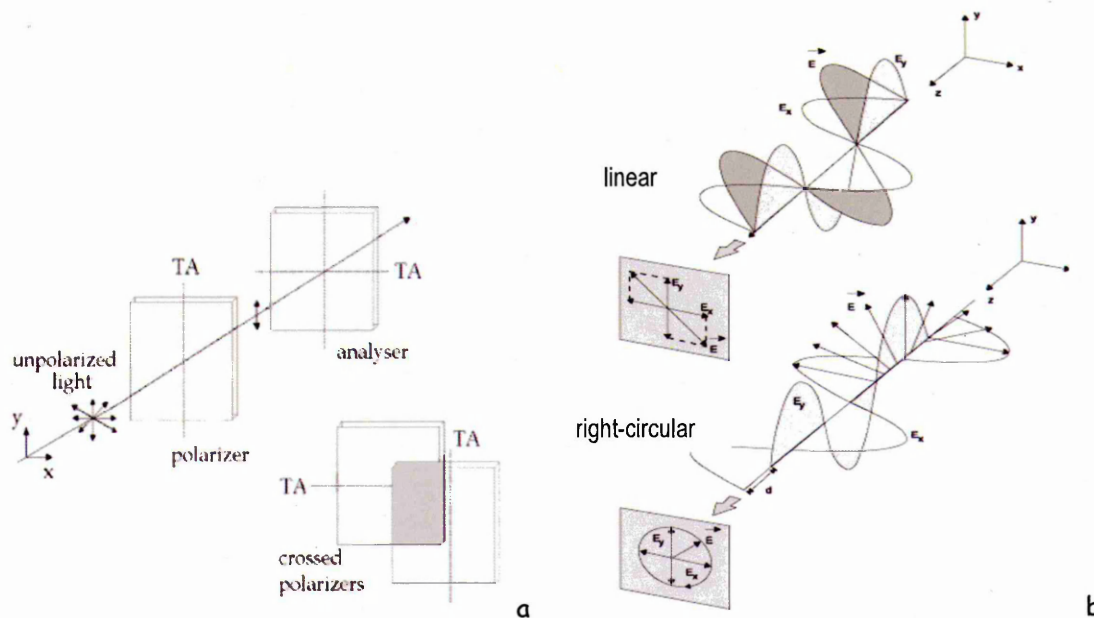


**Figure 2.2-9** a – A linear polarizer, an analyser, and two crossed polarizers with no light transmitted through the analyser; b – linear and right-circularly polarized light (taken from Ref.<sup>[104]</sup>).

The elliptically polarized light can be produced by reflection from a flat surface. *Ellipsometry* is an optical method based upon the registration of changes in the polarization of light after its reflection from the investigated sample (see Fig. 2.2-10).

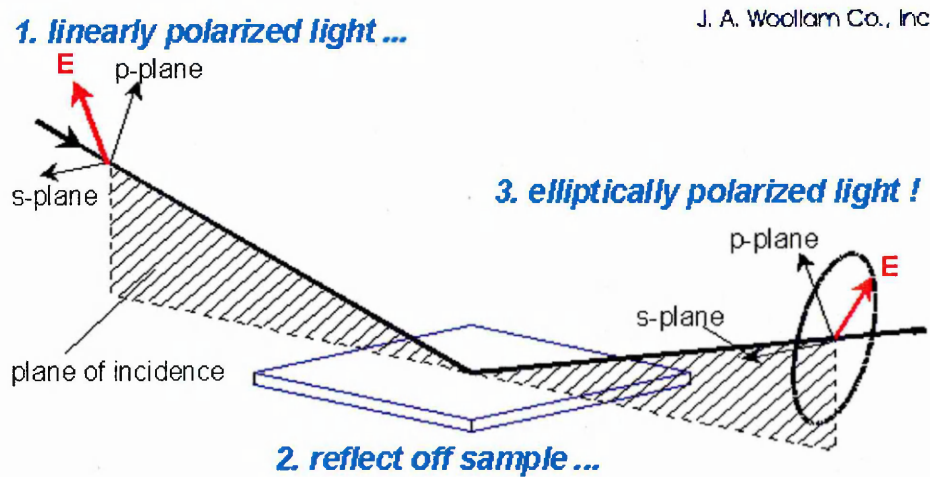


**Figure 2.2-10** Geometry of an ellipsometric measurement (taken from Ref.<sup>[105]</sup>).

Figure 2.2-11 illustrates the reflection of linearly polarized light from the surface. The plane of incidence (POI) includes the incident beam and the sample surface normal  $N$ , which is in the plane of the paper. The phase and amplitude between two components  $E_p$  (parallel) and  $E_s$  (perpendicular) change upon reflection in a distinct way depending on the optical properties of the surface<sup>[104]</sup>.

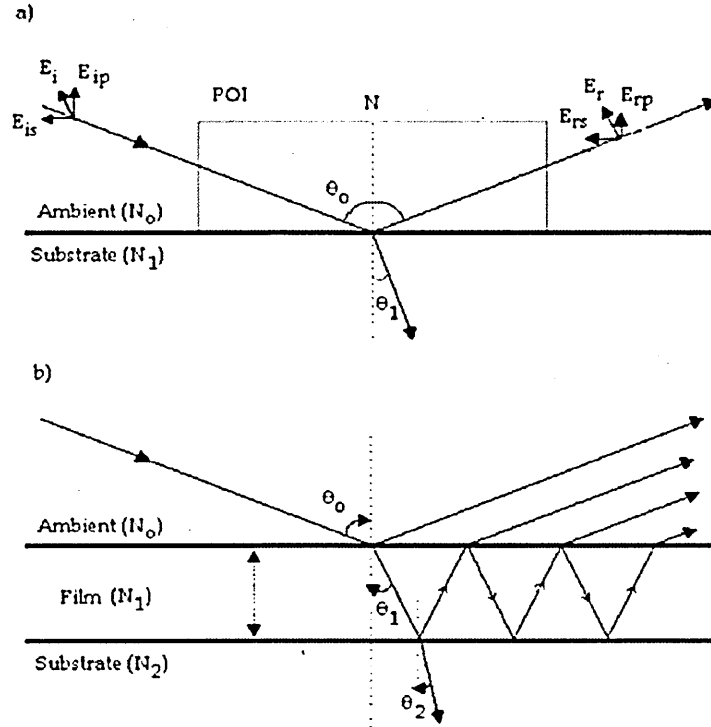


**Figure 2.2-11** Reflection of polarized light: a – bare surface; b – film-covered surface (taken from Ref.<sup>[105]</sup>).

The state of polarization of the reflected electromagnetic wave can be described in terms of a ratio of complex Fresnel reflection coefficients for  $s$ - and  $p$ - components of polarized light<sup>[102]</sup>, and the ellipsometric measurement is normally expressed in terms of the ellipsometric angles  $\Psi$  and  $\Delta$ :

$$\rho = \frac{r_p}{r_s} = \tan \Psi \exp(i\Delta), \quad (2.12)$$

where  $i = \sqrt{-1}$ ;  $\Psi$  is a ratio of Fresnel amplitudes of  $s$ - and  $p$ - components of polarized light ( $r_p$  and  $r_s$ ), and  $\Delta$  is a difference in their phases ( $\delta_s$  and  $\delta_p$ ):

$$\tan \Psi = \frac{|r_p|}{|r_s|}, \quad \Delta = \delta_p - \delta_s. \quad (2.13)$$

where  $\delta_p$  and  $\delta_s$  are the phase changes for the  $p$ - and  $s$ - components.

The expressions for  $r_p$  and  $r_s$  consider a single interface between medium  $0$  (ambient), having a complex refractive index  $N_0$ , and medium  $1$  (substrate) having a complex refractive index  $N_1$  as follows:

$$r_p \equiv \frac{E_{rp}}{E_{ip}} = |r_p| \exp(i\delta_p) = \frac{N_1 \cos \Theta_0 - N_0 \cos \Theta_1}{N_1 \cos \Theta_0 + N_0 \cos \Theta_1}, \quad (2.14)$$

$$r_s \equiv \frac{E_{rs}}{E_{is}} = \frac{N_0 \cos \Theta_0 - N_1 \cos \Theta_1}{N_0 \cos \Theta_0 + N_1 \cos \Theta_1}.$$

The reflection coefficients for a surface covered with a thin film are:

$$R_p = |r_p|^2 \quad R_s = |r_s|^2. \quad (2.15)$$

In the case of three layers (*ambient/film/substrate*) systems  $R_p$  and  $R_s$  are given as:

$$R_p = \frac{r_{01_p} + r_{12_p} \exp(-i2\beta)}{1 + r_{01_p} r_{12_p} \exp(-i2\beta)} \quad \text{and} \quad R_s = \frac{r_{01_s} + r_{12_s} \exp(-i2\beta)}{1 + r_{01_s} r_{12_s} \exp(-i2\beta)}, \quad (2.16)$$

where  $\beta$  expresses the film thickness ( $L$ ) (here medium  $1$ ) and the complex refractive index at the wavelength of incident light  $\lambda$  at the angle of incidence  $\Theta_0$ :

$$\beta = 2\pi \left( \frac{L_1}{\lambda} \right) N_1 \cos \Theta_0. \quad (2.17)$$

The resulting change in polarization after reflection from a surface can be expressed by Eq. (2.12), that for a model *substrate/film/ambient* can be written as:

$$\rho = f(N_0, N_1, N_2, \lambda, L_1, \Theta_0), \quad (2.18)$$

where  $N_0$ ,  $N_1$  and  $N_2$  are the indices of refraction for the ambient, film and substrate, respectively. Usually,  $N_0$ ,  $\lambda$  and  $\Theta_0$  are known and  $N_2$ ,  $N_1$  and  $L_1$  can be measured. The method of ellipsometry is extremely sensitive to changes in optical parameters of the reflecting substrate, i.e. the complex refractive index  $N$  which represents the real and imaginary parts of the refractive index:

$$N = n + ik, \quad (2.19)$$

where  $n$  is the refractive index and  $k$  is the extinction coefficient, which describe a change in the phase velocity and amplitude, respectively, of the electromagnetic wave propagating through a medium. For transparent materials, due to the high penetration

depths of light, the  $k$  values are very close to zero and  $N = n$ . However, for many other materials,  $n$  and  $k$  are not constant parameters, but dependent on  $\lambda$ , an effect known as *dispersion*.

Introduction of another layer(s) makes the procedure of adding the reflected and transmitted waves impractical. In the case of multilayered system the method of a scattering matrix ( $\mathbf{S}$ ) should be used instead.  $\mathbf{S}$  can be expressed as a product of the interface matrices ( $\mathbf{I}$ ) and layer matrices ( $\mathbf{L}$ )<sup>[102]</sup>:

$$S = I_{01} \times L_1 \times I_{12} \times L_2 \times \dots \times I_{j-1,j} \times L_j \times I_{j,j+1}. \quad (2.20)$$

For instance, in the case of a four layers system containing two more layers ( $1$  and  $2$ ) deposited on the substrate:

$$S = I_{01} \times L_1 \times I_{12} \times L_2 \times I_{23} = \begin{pmatrix} 1 \\ t_{01} t_{12} t_{23} \end{pmatrix} \begin{bmatrix} 1 & r_{01} \\ r_{01} & 1 \end{bmatrix} \begin{bmatrix} e^{i\beta_1} & 0 \\ 0 & e^{-i\beta_1} \end{bmatrix} \begin{bmatrix} 1 & r_{12} \\ r_{12} & 1 \end{bmatrix} \begin{bmatrix} e^{i\beta_2} & 0 \\ 0 & e^{-i\beta_2} \end{bmatrix} \begin{bmatrix} 1 & r_{23} \\ r_{23} & 1 \end{bmatrix}, \quad (2.21)$$

where  $t$  and  $r$  are Fresnel transmission and reflection coefficients at all interfaces and  $\beta_1$  and  $\beta_2$  are phase thickness of layers  $1$  and  $2$ , respectively.

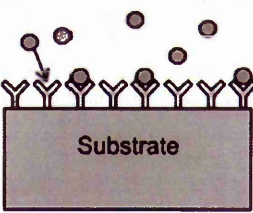
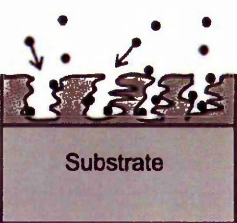
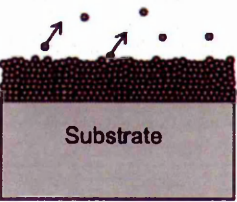
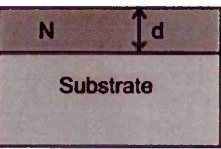
### b. *Spectroscopic ellipsometry: Biosensor applications*

Optical methods, such as SPR and ellipsometry, are well established analytical tools for thin film characterisation and the evaluation of optical parameters, such as thickness and refractive index. Because of a high sensitivity to small changes in the above parameters, these methods have become suitable for the study of molecular adsorption and different chemical reactions on solid surfaces and have thus found a wide range of applications in chemical and bio-sensing.

Very attractive features of spectroscopic ellipsometry for sensor applications are the possibility to work with non-labelled molecules and the high resolution of the thickness and refractive index. For instance, sub-nanometre resolution can be achieved in bioaffinity-based sensing<sup>[106]</sup> and parts per million sensitivity in gas sensing<sup>[107]</sup>. Ellipsometric sensor systems are based on monitoring changes in the thickness, the refractive index or the microstructure of a sensing layer. These changes are induced by the substance or process measured.

A discussion of the possibilities for sensor applications based on ellipsometric read-out and a classification of sensing layers has been done by Arwin<sup>[108]</sup> and summarised in Table 2.2-2.

**Table 2.2-2** Classification of sensing layers (based on data from Ref.<sup>[108]</sup>).

<i>Sensing layer</i>	<i>Mechanism</i>	<i>Physical parameter measured</i>	<i>Examples and References</i>
 <p>AL: Affinity layer</p>	<p>A sensing layer is deposited on a substrate and ideally only specific interactions with the molecules to be detected should take place.</p>	<p>Change in the effective layer thickness</p>	<p>Determination of antigen–antibody binding in immunoassays<sup>[109]</sup>, monitoring DNA-hybridization<sup>[110]</sup>.</p>
 <p>ML: Matrix layer</p>	<p>The sensing takes place inside a thin (10 – 1000 nm) surface layer – the matrix. This matrix may be a porous layer into which molecules can diffuse and interact with its internal surfaces.</p>	<p>Both thickness and refractive index changes</p>	<p>Gas sensors<sup>[107]</sup>.</p>
 <p>IL: Integrating layer</p>	<p>The basic idea is to monitor the change (desorption or film growth) in layer thickness <i>in situ</i>.</p>	<p>Change in the effective layer thickness</p>	<p><i>In situ</i> monitoring of film growth<sup>[111]</sup>, (can be used for sensing as well).</p>
 <p>HL: Homogeneous layer</p>	<p>Physical/chemical influences on the homogeneous layers' thicknesses and refractive indices are monitored due to temperature or pressure variations in the ambient.</p>	<p>Both thickness and refractive index changes</p>	<p>Sensor systems with polymer layers that can dissolve gases and thereby swell and change properties<sup>[112, 113]</sup>.</p>

There are two main sensing principles used in ellipsometric biosensors:

- The affinity reaction of specific binding to receptors immobilised on the surface where the increase in the surface mass or thickness of the layer on a surface is measured.

- The use of a polymer (or porous) soft sensing layer, which can absorb the substance to be detected. Absorption can lead to swelling of the layer and thereby to changes in its optical properties and thickness<sup>[114]</sup>.

Various aspects of protein adsorption, mainly on reflecting metal surfaces and ceramic surfaces have been reviewed by Elwing<sup>[115]</sup>. Special consideration has been given to biologically related surface phenomena, such as protein conformation changes and protein displacement effects. Ellipsometry gives the possibility of detailed and accurate determination of real-time adsorption kinetics of proteins without labelling the protein. It is also possible to detect protein adsorption with the use of antibodies that adsorb onto the antigen-coated surfaces.

### 2.2.3 Total internal reflection ellipsometry

#### *a. Total internal reflection ellipsometry: Basics*

A relatively novel method of total internal reflection ellipsometry (TIRE) is a combination of internal reflection and ellipsometry. As a result, the method of TIRE combines the advantages of the accuracy of the spectroscopic ellipsometry instrumentation with the conveniences of Kretschmann SPR geometry<sup>[116]</sup>.

Although theoretically the TIRE method was known a long time ago<sup>[102]</sup>, its experimental realisation has been achieved relatively recently<sup>[117, 118]</sup>. In spite of ellipsometry and SPR being usually considered as separate detection methods, both effects, and hence the TIRE, can be described theoretically by Fresnel's equations. The first simulations of the ellipsometric response under internal and external reflection and for different sample configurations has been done by H. Arwin and co-workers<sup>[116]</sup>.

The difference between TIRE and conventional external reflection ellipsometry is, first of all, in the way of the light incidence and thus in the order of layers. In TIRE, the light enters the system from the glass side; so, the layers are placed as follows:

- (0) substrate (air or water);
- (1) dielectric film (i.e. transparent ( $k = 0$ ) organic layer with the refractive index described by the Cauchy dispersion formula<sup>[119]</sup>:

$$n = A + \frac{B}{\lambda^2} + \frac{C}{\lambda^4}. \quad (2.22)$$

- (2) thin gold film;
- (3) ambient (glass prism), as shown in Fig. 2.2-12.

Secondly, the angle of incidence should be close to the angle of total internal reflection, which dictates the choice of the prism<sup>[116]</sup> and approximately can be given by the following equation<sup>[117]</sup>:

$$\Theta = \arcsin \left[ \frac{1}{N_1} \sqrt{\frac{\epsilon_m N_2^2}{\epsilon_m + N_2^2}} \right], \quad (2.23)$$

where  $N_1$  and  $N_2$  are the refractive indices of the glass prism and of the dielectric film, respectively;  $\epsilon_m$  is the real part of the dielectric constant of the metal film.

Finally, the presence of a thin metal film is vital for TIRE because of the phenomenon of plasmon resonance in the interaction of the evanescent field with the surface plasmons in the metal film.

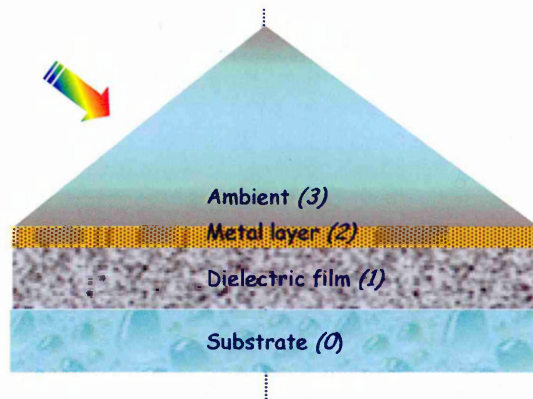


Figure 2.2-12 The four layer system in TIRE.

*b. External and internal reflection ellipsometry: Comparison*

The calculations of  $\Psi$  and  $\Delta$  spectra have been performed by A. Nabok<sup>[120]</sup> for both external reflection ellipsometry and TIRE in two media (air and water) by solving

the main ellipsometry equation (Eq. 2.12) for different thicknesses (varied from 0 to 30 nm with the step of 5 nm) and fixed refractive index of the dielectric layer or vice-versa for the fixed thickness ( $d = 10 \text{ nm}$ ) and varied refractive indices. The results of such cumbersome calculations can be summarised as follows:

- TIRE is about 10 times more sensitive towards the changes in both the thickness and refractive index of thin films as compared to conventional external reflection ellipsometry;
- Within TIRE, the parameter  $\Psi$  represents the amplitude ratio of  $p$ - and  $s$ -components of polarised light, and thus  $\Psi(\lambda)$  spectra are equivalent to SPR curves, while  $\Delta(\lambda)$  spectra give new information on the phase shift between  $p$ - and  $s$ -components of polarised light.  $\Delta$  is about 10 times more sensitive than  $\Psi$  to changes in both the thickness and refractive index of thin films. It can be therefore concluded that the  $\Delta(\lambda)$  spectrum in TIRE is about 10 times more sensitive than conventional SPR. This makes such phase SPR measurements highly desirable for film characterisation and sensing;
- The spectral shift of  $\Delta$  is of the same order as that of  $\Psi$  but slightly larger. This enables another possibility for the kinetics study by monitoring the spectral shift of either  $\Psi$  or  $\Delta$  during molecular adsorption as well as any chemical and bio- reactions on the surface.

### c. *Total internal reflection ellipsometry: Applications*

The method of TIRE is a new field in the sensor area, even though the approaches to detect the phase information under SPR conditions<sup>a</sup> have been discussed previously<sup>[121]</sup>, it still seems to be a *terra nova* among the measurement techniques. Before the pioneer work by Westphal and Bornmann<sup>[117]</sup> there was no demonstration of full ellipsometric measurements combined with SPR that showed the immobilization of antibodies or DNA in a spectral or time dependent manner.

---

<sup>a</sup> The system utilized a frequency-stabilised laser as a detection light source and was suitable for real-time phase measurement in SPR-sensing applications. The phase shift in an angular dispersion SPR excitation setup was measured around the SPR excitation region.

In 2002 Westphal and Bornmann first used a method of TIRE (they called it a “surface plasmon enhanced ellipsometry” (SPEE)) to detect changes in the effective thickness of biomolecular layers. They demonstrated that SPEE/TIRE is actually able to detect the immobilization of small molecules. The experiments of immobilization of biotinylated DNA oligonucleotides and afterwards the hybridization of the complementary DNA oligonucleotides were performed and the hybridization process was clearly detected (see Fig. 2.2-13).

The method yields the sensitivity sufficient to detect changes in the effective thickness of biomolecular layers of less than 0.01 nm. In addition, the authors noticed that the method of SPEE/TIRE is less sensitive than traditional SPR to external stray light and to the intensity fluctuations of the incident light.

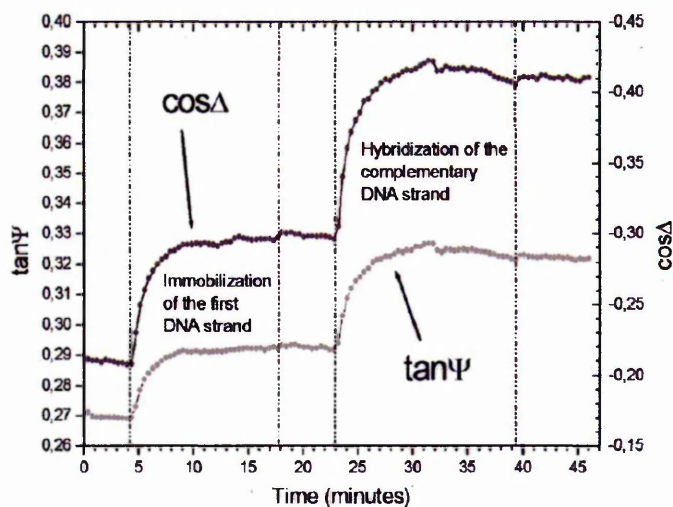


**Figure 2.2-13** Kinetic measurements of the immobilization of biotinylated DNA oligonucleotides and the subsequent hybridization of the complementary DNA oligonucleotides (taken from Ref.<sup>[117]</sup>).

The method of TIRE was employed for *in situ* reaction monitoring at a solid-liquid interface for the investigation of protein adsorption on thin semitransparent gold films by Poksinski and Arwin<sup>[118]</sup>. Adsorption of a monolayer of the protein ferritin (1 mg/ml) was monitored *in situ*. The ferritin layer optical properties were modelled with a Cauchy dispersion model resulting in a layer thickness of 9.2 nm in good agreement with the dimension of the ferritin molecules. Figure 2.2-14 shows the spectral variation of the parameter  $\Delta$  measured before and after adsorption (angle of incidence  $\phi = 65.5^\circ$ ).

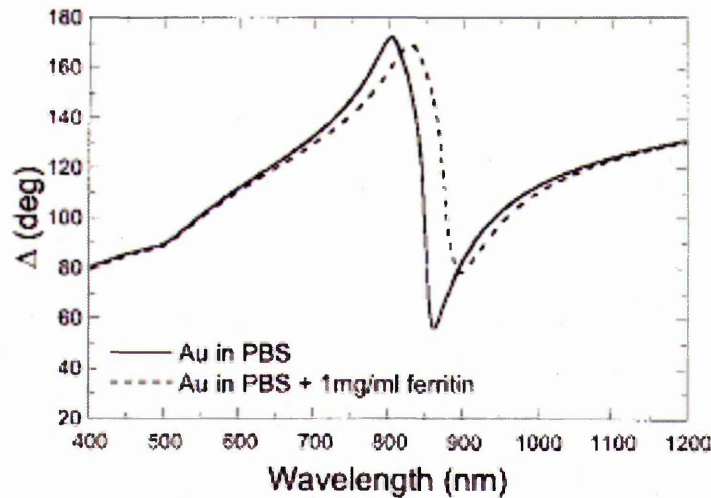


**Figure 2.2-14** Spectral variation in  $\Delta$  in phosphate-buffered saline (PBS) before and after adsorption of ferritin at a protein concentration of 1 mg/ml at an angle of incidence of 65.6 deg. (taken from Ref.<sup>[118]</sup>).

Near the resonance ( $\lambda \approx 850 \text{ nm}$ ), a change of more than  $90^\circ$  in the ellipsometric parameter  $\Delta$  was observed in contrast to a  $3^\circ$  response of conventional ellipsometric measurements on gold<sup>[122]</sup>.

The two other applications studied at the same research group, are more technical, with possible industrial relevance: adsorption and subsequent cleaning of substances from milk<sup>[123]</sup> (useful for pipeline monitoring in the dairy industry) and copper corrosion monitoring<sup>[124]</sup> (with potential application in the microelectronics industry for circuit board control).

The last two examples are not connected with the optical biosensors but included here to give the full range of TIRE method applications. The TIRE method has been successfully exploited by Suryajaya et al.<sup>[125]</sup> for monitoring the process of alternative deposition of poly-allylamine hydrochloride and semiconducting colloid nanoparticles (CdS or ZnS). Nanoparticles were deposited as thin films using the technique of electrostatic self-assembly. The fitting of TIRE spectra allowed the evaluation of the parameters (thickness, refractive index, and extinction coefficients) of all consecutively deposited layers.

The application and some advantages of the TIRE method over the conventional Kretschmann SPR technique for determination of organic vapours are demonstrated by Basova<sup>[126]</sup>. In this work, the sensor response of thin films of octasubstituted copper phthalocyanine derivative ( $\text{CuPcR}_8$ ) with bulky substituents to the vapour of benzene,

chloroform, ethanol and butanol were investigated. The ability to conduct spectroscopic measurements of two ellipsometric parameters ( $\Psi$  and  $\Delta$ ) in the TIRE method constitutes its main advantage over the SPR technique, where only one parameter was measured at a certain wavelength of incident light. During exposure to organic vapour, an appreciable shift of  $\Delta$  was observed to give a better view of the effect of vapour exposure.

## 2.2.4 Planar optical waveguide

### a. *Multiple internal reflections principle*

Planar optical waveguide is another technique that exploits the evanescent wave principle. As has been mentioned in paragraph 2.2.1, under condition of total internal reflection the evanescent wave is established by the dissipation of the incident intensity at the interface at each reflection. The evanescent wave intensity at the interface ( $I_e$ ) per unit incident intensity ( $I_i$ ) is given by<sup>[127]</sup>:

$$\frac{I_e}{I_i} = \frac{n_2 \cdot 4 \cos \Theta_i}{n_1 \left( 1 - \left( \frac{n_2}{n_1} \right)^2 \right)}, \quad (2.24)$$

where  $n_1$  and  $n_2$  are refractive indices of the more and less dense medium, respectively;  $\Theta$  is the angle of incidence. The depth of penetration  $d_p$  of the evanescent wave is given by the equation:

$$d_p = \frac{\lambda / n_1}{2\pi \sqrt{\sin^2 \Theta_i - \left( \frac{n_2}{n_1} \right)^2}}. \quad (2.25)$$

As can be seen from Eq.(2.25), when  $\Theta_i$  is close to the critical angle, the evanescent field will penetrate more deeply into the medium with lesser density, and hence more light energy becomes available for interaction with the external medium. The depth of penetration is also proportional to the wavelength ( $\lambda$ ) of the light and it is greater at longer wavelengths. However, a larger penetration depth will cause a larger

lateral shift of the reflected beam at the interface. The lateral shift,  $\Delta z$  (see Fig. 2.2-15), known as the Goos-Hänchen shift, depends on the angle of incidence and the penetration depth. It is:

$$\Delta z \approx 2 \cdot d_p \tan \Theta_i, \quad (2.26)$$

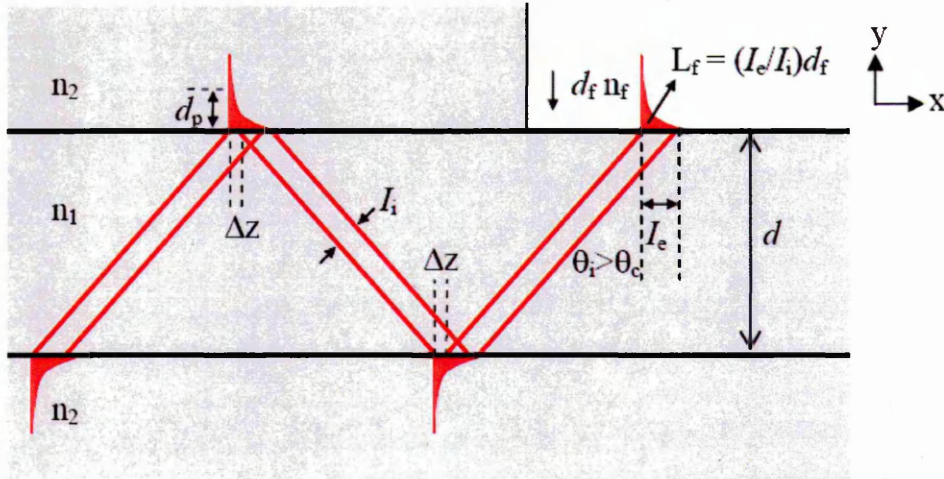


**Figure 2.2-15** Multiple internal reflections in a planar optical waveguide with a part of the dense medium surface covered with a thin absorbing material (Figure was modified from Ref.<sup>[128]</sup>).

A large lateral shift may cause considerable impact on the distance between each neighbouring reflection. In this case the number of reflections  $N$  at the interface of the waveguide is described as follows:

$$N = \frac{L}{2(d \tan \Theta_i + \Delta z)}, \quad (2.27)$$

where  $L$  and  $d$  are the length and the thickness of the waveguide, respectively. As can be seen from Eq.(2.27), a decrease in the thickness of the waveguide will reduce the distance between reflections and hence increase the number of reflections. A close gap between the reflection points may produce a continuous evanescent energy distribution along the path of propagation.

However, not all light waves that have an angle of incidence greater than the critical angle will be propagated in the dense medium. This is because the light wave will interfere with itself as it travels through the waveguide. In order to propagate successfully, the light wave must not interfere destructively, and only certain reflection

angles give rise to the constructive interference, which means only certain waves can exist in the waveguide. These constructive interference waves are called *guided modes* and are designated by an integer  $m = 0, 1, 2, \dots$ . The number of guided modes is dependent upon the light wavelength, waveguide thickness and refractive index, and can be estimated according to the equation below<sup>[129]</sup>:

$$M = \text{Int}\left(\frac{2d(n_1^2 - n_2^2)^{1/2}}{\lambda}\right) + 1, \quad (2.28)$$

where  $\text{Int}(x)$  is the integer function which drops the decimal fraction of  $x$ . A general waveguide condition for guided waves is given in the form:

$$\frac{2\pi \cdot n_1 d}{\lambda} \cos \Theta_m - \phi_m = \pi n, \quad (2.29)$$

where  $\Theta_m$  is the incident angle at the interface for the specific guided mode; and  $\phi_m$  is the phase change  $\phi_m$  of the transverse electric field wave<sup>[129]</sup>:

$$\phi_m = 2 \tan^{-1} \left( \frac{\sqrt{\sin^2 \Theta_m - \left(\frac{n_2}{n_1}\right)^2}}{\cos \Theta_m} \right). \quad (2.30)$$

Thus, if the waveguide thickness, refractive index ratio and the light wavelength are known, the values of  $\phi_m$  and  $\Theta_m$  can be calculated<sup>[130]</sup>.

Light propagates through the waveguide without significant attenuation, since both mediums are transparent in the visible range. However, if a sensitive thin film has a non-zero absorption coefficient deposited on the dense medium, optical loss will occur each time reflection takes place at the interface between the medium and the sensing film. In this case, the attenuation of the transmitted intensity,  $I_{out}$  (output light intensity) will normally occur according to the Beer-Lambert law:

$$I_{out} = I_{in} \exp(-A \cdot N), \quad (2.31)$$

where  $I_{in}$  is the input light intensity, and  $A$  is the fractional absorption from each encounter with the sensing film, given by:

$$A = 1 - \exp(-\alpha \cdot \delta), \quad (2.32)$$

where  $\alpha$  and  $\delta$  are the absorption coefficient of the film and the interaction length per reflection, respectively. For a very thin film, the product ( $\alpha \cdot \delta$ ) is very small and Beer-Lambert approximation of  $\exp(-\alpha \cdot \delta) \approx 1 - \alpha \cdot \delta$  can be applied to Eqs.(2.31) and (2.32):

$$I_{out} = I_{in} \exp(-\alpha \cdot \delta \cdot N). \quad (2.33)$$

The interaction length,  $\delta$  is calculated from the expression<sup>[128]</sup>:

$$\delta \approx L_f = \frac{I_e}{I_i} d_f, \quad (2.34)$$

where  $L_f$  is the evanescent path length related to the thickness of the thin film,  $d_f$ . By substituting  $I_e/I_i$  from Eq.(2.24) into Eq.(2.34), the interaction length can be expressed as follows:

$$\delta = \frac{4 \cdot n_f d_f \cos \Theta_m}{n_1 \left[ 1 - \left( \frac{n_f}{n_1} \right)^2 \right]}, \quad (2.35)$$

where  $n_f$  is the refractive index of the thin film and  $\Theta_m$  is the incidence angle at the guided mode  $m$ .

Multiple internal reflections in a planar waveguide can provide an extremely sensitive tool for registration of small changes in optical absorption in the thin film. The optical techniques that most frequently use the multiple internal reflections principle are attenuated total reflection (ATR), total internal reflection fluorescence (TIRF) and planar interferometry.

## *b. Modifications of the planar optical waveguide*

### *1. Planar waveguide as an attenuated total reflection (ATR) transducer*

The presence of optically absorbing material on the waveguide interface is monitored as light energy absorbed from the evanescent wave of the internally reflected light beam. The sensitivity of the measurement increases linearly with the number of

total internal reflections at the sample containing surface<sup>[129]</sup>. The optical losses at each reflection are proportional to the absorption coefficient and thickness of the deposited sensing film. ATR technique provides a direct measurement of the analyte with a simple preparation of the waveguide and experimental setup. Some examples of application of the biosensors based on ATR transducers have been described elsewhere<sup>[131, 132, 133, 134]</sup>. Basic principles of ATR transducers will be described in chapter 3, section 3.6.

## 2. *Planar waveguide as a total internal reflection fluorescence transducer*

A TIRF transducer is constructed by placing a fluorescent material (labelled molecules) in contact with the reflecting surface of a planar waveguide. The evanescent energy generated from the propagating light may not only be absorbed as in the case of the ATR technique, but could also be used for excitation of fluorescence. The intensity of the emitted fluorescence is measured for quantification of the studied analytes. The TIRF technique provides high sensitivity and selectivity for detection of various analyte. However, it involves complex preparation prior to the experiment such as the target analyte or the sensing element needing to be labelled with fluorescent material. The sensitivity of an ATR transducer is lower than other optical techniques; examples of applications (as a proof of this statement) are given in Refs.<sup>[135, 136, 137, 138]</sup>.

## 3. *Planar waveguide as a planar interferometer transducer*

Planar interferometry is based on the change in the propagation velocity of the light passing through a planar waveguide. Two variations of the planar interferometer used are the Mach-Zehnder interferometer and the planar polarization interferometer.

### a. *Mach-Zehnder interferometer*

The Mach-Zehnder interferometer (MZI) consists of a planar waveguide, having a core layer with a slightly larger refractive index than that of the cladding. The waveguide splits into two arms, as shown in Figure 2.2-16. One of the arms has a sensing window etched in to the top of the cladding layer. This arm, with the window coated with a chemically sensitive layer (membrane), forms a sensing channel, while the other arm serves as a reference.

The output signal of the MZI forms by the interference of two waves from two arms at the point at which they meet, and thus depends on the phase difference between the main and reference channels. Adsorption of (bio-) molecules accompanied by changes in the refractive index and a phase shift between two branches, will develop, and result in periodic changes in the output signal, as shown in Figure 2.2-16 inset<sup>[139]</sup>.

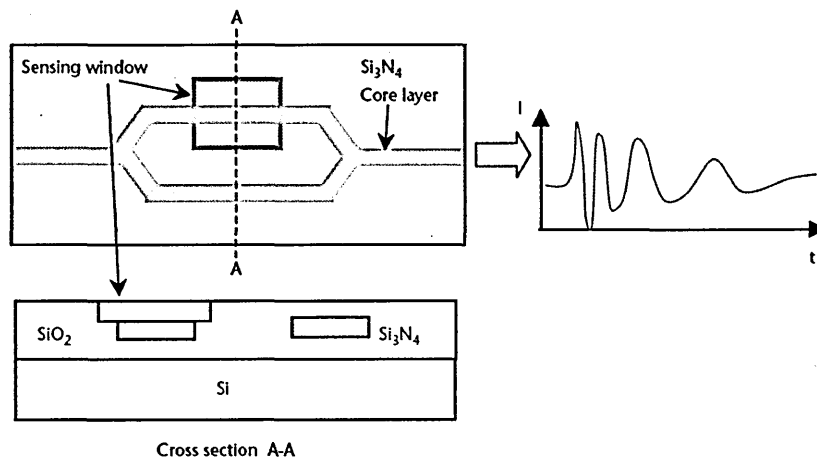


**Figure 2.2-16** Mach-Zehnder interferometer: the top view and cross-section along the A-A line. The inset shows periodic changes in the output signal (taken from Ref. <sup>[139]</sup>).

*b. Planar polarization interferometer (PPI)*

The same idea of an interferential transducer is realised in a simple planar wave-guiding structure, but with no grooving and splitting of the core. The wave-guiding structure SiO<sub>2</sub>/Si<sub>3</sub>N<sub>4</sub>/SiO<sub>2</sub> with thicknesses of 1.2 μm, 0.18 μm, and 1.2 μm, respectively, as shown in Fig. 2.2-17, accommodates a single mode of HeNe laser beam ( $\lambda = 633$  nm). A sensing window is etched in the top SiO<sub>2</sub> layer.

When a polarized laser beam propagates through the waveguide, the *p*-component of electromagnetic wave is affected by molecular adsorption or chemical and biochemical reactions, while the *s*-component is almost intact, and serves as a reference. The phase difference between *p*- and *s*-components, developed in the course of reaction, causes the rotation of the polarization, which can be registered by placing the analyzer in the output. The resulting periodic change in the output light intensity is very similar to that in the MZI.

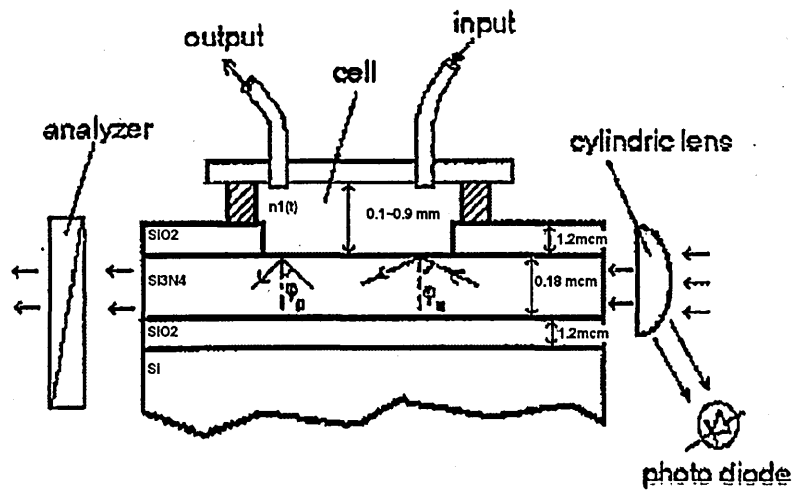


**Figure 2.2-17** Optical diagram of a sensor based on the planar-polarization interferometer (after Ref.<sup>[140]</sup>).

The PPI and MZI described above are used for the registration of adsorption of proteins and immune reactions (see, for instance Refs.<sup>[141, 142, 143, 144, 145]</sup>). However, the disadvantage of both MZI and PPI transducers are a very slow rate of adsorption.

## 2.3 Optical Enzyme Sensors

Chronologically, the first biosensor was an enzyme sensor developed by Clark and Lyons in 1962<sup>[146]</sup>. Since then, numerous enzyme sensors in different configurations have been developed. The motivation for designing enzyme biosensors for toxicity monitoring is to provide a reliable alternative to expensive and time-consuming classical chromatographic methods currently used. The majority of enzyme sensors on the market are electrochemical.

The main advantages of electrochemical methods are simplicity and low cost. The sensitivity of electrochemical methods is not high, but it is sufficient for the majority of biomedical applications. Optical enzyme sensors have proven to be both fast and highly selective<sup>[147]</sup>. Therefore, they have become the target of intense research and development. Recent developments in the field of enzyme sensors and relevant technologies as applied to environmental monitoring were reviewed by Karube and Nomura<sup>[147]</sup>.

A successful enzyme biosensor should offer analytical performance comparable to, or even better than, the traditional chromatographic systems. Ideally, such sensors should be small, cheap, simple to handle and able to provide reliable information in real-time with, or without, minimal sample preparation. The use of the enzyme should also provide increased sensitivity and selectivity for the analyte of interest<sup>[148]</sup>.

The capability of enzyme sensors to operate in various media (i.e. aqueous solutions, organic solvents, and air) has been shown by different research groups (see, for instance, Refs.<sup>[149, 150, 151]</sup>). Another advantage of enzyme sensors is the wide selection of enzymes commercially available.

In enzyme-based biosensors, the biological element is the enzyme which catalyses the reaction selectively with its substrate<sup>[152]</sup>. In general, the detection of environmental pollutants is not based on their enzymatic transformation but on their capability to act as inhibitors of an enzyme reaction. The inhibiting effect of the chemicals on the response of the biosensor can be expressed as a relative decay of the response value after the contact of the biosensor with the sample tested. The determination of the inhibiting effect involves at least three stages<sup>[153]</sup>:

1. Determination of the initial response value ( $I_0$ );

2. The contact of a biosensor with an inhibitor;
3. Determination of the reduced response value ( $I_i$ ).

a. *Parameters affecting the performance of enzymatic biosensors*

1. *Effect of pH:*

Enzymes are generally only active in limited pH ranges and each enzyme has his own optimal pH value<sup>[154]</sup>. For instance, the activity of the immobilized *acetylcholine esterase (AChE)* as a function of pH has been studied between pH 2 and 9 by Stoytcheva<sup>[155]</sup>. Author reported a decrease in the activity of approximately 70% at pH 2 compared to that at pH 7. The presence of an inhibitor changes different ionisation states of the system governing the enzymatic activity<sup>[156]</sup>. Enzyme sensors utilising various *esterases* are most sensitive to organophosphates at pH 8 – 9; *urease* is proposed for the determination of heavy metal ions at pH 8 – 10.

2. *Effect of substrate concentration:*

The substrate concentration can affect the degree of inhibition<sup>[154]</sup>. According to Kok et al.<sup>[157]</sup>, the inhibition level (%) increases with increasing the substrate concentration. Dzyadevych et al.<sup>[158]</sup> however, showed that the sensitivity of a *butyryl cholinesterase (BChE)* biosensor to *tomatine* decreases with an increase in the substrate concentration.

3. *Effect of enzyme concentration:*

The enzyme loading on the sensor element drastically influences the upper and lower limits of detection. The highest sensitivity to inhibitors was found for a membrane containing low enzyme loading<sup>[159]</sup>. This statement has been confirmed by Ciucu et al.<sup>[160]</sup> research: they studied a set of five membranes with different amounts of *AChE* and found that the response of the biosensors decreased with a decrease of the enzyme concentration.

### b. Cholinesterase-based optical biosensors for pesticide detection

*Cholinesterases* (*ChE*) are important enzymes which hydrolyze the neurotransmitter *acetylcholine* in the nervous system<sup>[161]</sup>. In the human body, *ChE* is responsible for the transmission of nerve impulses to the cholinergic synapses and is connected with human memory and Alzheimer's disease. *ChE* is commonly employed for toxicity monitoring for environmental, agricultural, food or military applications. Cholinesterases are commercially available and have a good stability and sensitivity.

The activity of *ChE* is inhibited by a variety of organophosphorus and carbamate pesticides<sup>[162]</sup>. Thus, biosensors based on the inhibition of enzyme cholinesterase such as *acetylcholine esterase* (*AChE*) or *butyrylcholine esterase* (*BChE*) are most frequently proposed for use in pesticide detection (see Fig. 2.3-1). When *AChE* is used alone, the detection can be based on pH changes because *AChE* hydrolyzes *acetylcholine* to *acetic acid* and *choline* (*choline* is a substratum for *choline oxidase*)<sup>[163]</sup>:

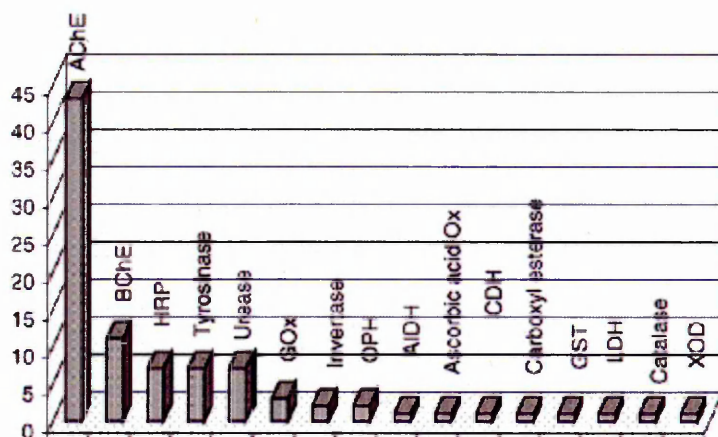
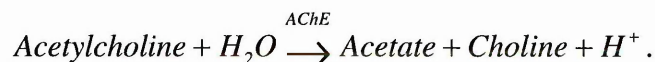


**Figure 2.3-1** Distribution of enzymes used for the design of biosensors used for detection of inhibitors (taken from Ref.<sup>[164]</sup>).

A number of biosensors that function on the principle of *AChE* inhibition have been proposed, including commercial *AChE*-based sensors (Charm Sciences, Malden, USA<sup>[165]</sup>). Numerous prototypes based on potentiometric<sup>[166]</sup>, amperometric<sup>[167]</sup>, piezoelectric<sup>[168]</sup> and optical<sup>[169]</sup> transducers have been developed.

Most *cholinesterase* biosensors using optical transducers have utilised the fibre-optic device as the light waveguide and used either pH-sensitive fluorescence or organic dye as the light indicator. For instance, Andres and Narayanaswamy<sup>[170]</sup> described a fibre-optic pesticide biosensor based on covalently immobilized *AChE* on pre-activated isothiocyanate glass mixed with the *thymol blue* indicator bound on the aminopropyl glass. The liberated *acetic acid* during the hydrolysis of *acetylcholine chloride* caused a local decrease in pH, and the resulting colour change of *thymol blue* indicator was detected, thereby leading to the increase in the reflected light intensity at  $\lambda = 600$  nm. The introduction of pesticides in the flow cell reduced the sensor response linearly in the concentration range from  $5 \cdot 10^{-8}$  to  $5 \cdot 10^{-7}$  M for *carbofuron* and  $5 \cdot 10^{-7}$  to  $5 \cdot 10^{-6}$  M for *paraoxon*. The detection limits, calculated at 10% inhibition, were 3.1 ppb and 24.7 ppb for *carbofuron* and *paraoxon*, respectively.

An *AChE* fibre-optic biosensor using litmus dye indicator was reported by Choi et al.<sup>[171]</sup>. Instead of being immobilised in the sensor reaction cell, the litmus dye was dissolved in the potassium phosphate buffer and mixed with the enzyme substratum, *acetylthiocholine iodide* before it flowed to the reaction cell. The *AChE* was immobilised by the electrostatic adsorption on a support polymer *viologen*, which was transferred on a glass slide by the Langmuir-Blodgett technique.

Decreases in pH value, due to the formation of *acetic acid* from hydrolysis of *acetylthiocholine iodide* by *AChE*, caused the original blue colour of the litmus dye to change to red, which caused an increase in the absorption at 633 nm. When the pesticide was introduced a difference in the decrease of absorbance occurred due to the inhibition of *AChE*, which was proportional to pesticide concentration. The sensor showed a narrow detection range for *paraoxon* that was of 0.2 to 2.0 ppm.

A few years later Choi and colleagues<sup>[172]</sup> developed a new type of sensing scheme of fibre-optic biosensors for direct detection of organophosphorus pesticide (such as *paraoxon* as a model pesticide). This fibre-optic biosensor employed the colourless substratum, *o-nitrophenyl acetate*, which was converted into a yellow product *o-nitrophenol* in the presence of *AChE*. The *AChE* was immobilised using a similar method as that described before<sup>[171]</sup>. In the absence of the pesticide, *o-nitrophenyl acetate* was completely hydrolysed, while in the presence of the pesticide the amount of yellow product was reduced. This change of absorbance at 400 nm by *o-*

*nitrophenol* production was related to the amount of phosphorus pesticide, and thus the enzyme reaction was not affected by the pH. This type of sensor deviated from the indirect detection method (from measuring the absorbance change of a pH-sensitive dye due to the formation of an acidic product), which was widely used by other optical *AChE*-biosensors. However, the detection range of the sensor was about 0.2 to 2 ppm, which was similar to the range obtained from the optical enzyme sensor described by Choi et al.<sup>[171]</sup> before.

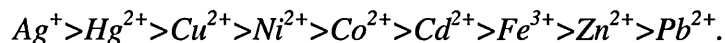
Doong and Tsai<sup>[173]</sup> proposed an *AChE* fibre-optic biosensor with a better sensitivity to *paraoxon*. This sensor consisted of pH-sensitive fluorescent indicator encapsulated together with the enzyme *AChE* in a sol-gel network on a glass cap, which could be fixed on an optical fibre, and then integrated with a flow reaction to the cell for continuous monitoring. Nine fluorescent indicators were tested and *FITC-dextran* was found to be the most suitable indicator due to the advantages of high sensitivity, low leaching rate, and low toxicity to *AChE*. The fluorescence colour of *FITC-dextran* was blue in alkaline solutions and became colourless as pH decreased to 2. Therefore, the enzymatic activity of *AChE*, resulting in pH change, was given in terms of the decrease of fluorescence light intensity. The ability of the sensor to detect the organophosphorus pesticides was investigated with 152 ppb of *paraoxon*. A 30% inhibition of the sensor response was obtained after the *paraoxon* was introduced into the system.

Certainly *ChE* biosensors have limitations, which could be directly related to their selectivity in multi-composite mixtures and complex matrices and their inability to identify a specific toxic analyte. However, their sensitivity is enough to detect the minimum level of pesticides and heavy metals imposed by regulatory agencies<sup>[174]</sup>.

### c. Enzyme sensors for heavy metal ions detection

In the case of heavy metal ions determination, the enzyme *urease* is commonly used as the bioreceptor. Preininger and Wolfbeis<sup>[175]</sup> have reported a quick and simple test for detection of heavy metals based on the inhibition of free *urease* contained in a disposable polystyrene cuvette. The wall of the cuvette was covered with membrane sensitive to either *ammonia* or *ammonium* ion. The sensing scheme of this biosensor was based on the change of light absorption by the *ammonium* sensitive membrane due

to the *urease* enzymatic reaction in the cuvette. Heavy metals were detected by their inhibitory effect. Heavy metal ions were found to inhibit *urease* in the following decreasing order:



The lowest limits of detection were found for  $Ag^+$  (20 ppb),  $Hg^{2+}$  (70 ppb) and  $Cu^{2+}$  (250 ppb) (see Table 2.3-1). The authors also discussed the inhibitory effect of metal combinations on the activity of the enzyme and the effects of an incubation time.

**Table 2.3-1** Limits of detection (LOD) and metal concentration giving 50% inhibition ( $I_{50}$ ) of selected heavy metal ions (after Ref.<sup>[175]</sup>).

<i>Heavy metal</i>	<i>LOD (ppm)</i>	<i>I<sub>50</sub> (ppm)</i>
$Ag^+$	0.02	0.13
$Hg^{2+}$	0.07	0.65
$Cu^{2+}$	0.25	0.55
$Ni^{2+}$	3	7
$Co^{2+}$	10	30
$Cd^{2+}$	20	95
$Fe^{3+}$	30	50
$Zn^{2+}$	50	85
$Pb^{2+}$	100	210

Registration of heavy metal ions based on the absorbance changes of a light was also described by Nabok et al.<sup>[176]</sup>. Here, a pH-sensitive dye *cyclotetrachromotropylen* (CTCT) was used. A composite film consisting of enzyme *urease* and CTCT was deposited on a glass slide using electrostatic self-assembly (ESA) to form a sensitive element of the sensor. The films obtained were characterised with UV-visible absorption spectroscopy. The lowest concentration of detected metal ions was 100 ppm. The spectral changes were not very significant for low concentrations of metal ions but the principle of optical registration of enzyme reaction by combining the enzyme *urease* and CTCT in the same membrane using ESA method was demonstrated.

Much higher sensitivity of registration of heavy metal ions was achieved by Nabok and co-workers<sup>[169]</sup> with a novel type of enzyme optical sensor based on a

combination of  $\text{SiO}_2/\text{Si}_3\text{N}_4/\text{SiO}_2$  planar waveguide as an attenuated total reflection transducer with the composite electrostatic self-assembly coating containing both organic chromophore and enzyme *urease* molecules. The sensitivity of registration of  $\text{Cd}^{2+}$  and  $\text{Pb}^{2+}$  in the range of 1 ppb was reported.

Optical fibre chemical sensors (optrodes) are other systems that have been employed for quantitative determination of heavy metal ions. These systems are based on the use of immobilised indicators and are attached to the optical fibre tip, changing their colour or optical properties in the presence of metal ions (see for instance, Refs.<sup>[177, 178]</sup>).

#### d. *Multi-enzyme sensor array*

In the field of biosensors, multi-analyte detection has been an emerging area of interest in the last decade. The specificity of analyte detection can be increased by the use of an array of several enzymatic sensors acting concurrently. As a result, multi-enzyme sensor arrays have been proposed to monitor various environmental pollutants simultaneously. Some of these sensor arrays are combined with an automated data analysis system (i.e. artificial neural networks (ANN)) to identify the analytes. The use of multi-enzyme sensor array sensors coupled with an ANN for data analysis could significantly improve biosensor selectivity and allow exact identification of the analyte present in a sample.

This approach has been used by Bachmann and Schmid<sup>[179]</sup>. They described a sensitive screen-printed amperometric multienzyme biosensor for the determination of the pesticides *paraoxon* and *carbofuran* and their mixtures. The multi-enzyme sensor used different types of native, recombinant and mutant *AChE* as the bioreceptors, which were immobilized on a four-electrode thick film transducer. The immobilized *AChE* hydrolyzed *acetylthiocholine chloride* to produce *thiocholine*, and this reaction was determined by *thiocholine* oxidation. The change of output current measured by a four-channel potentiostat was correlated to the *AChE* activity<sup>[179]</sup>.

The sensitivity of the multi-enzyme sensor towards pesticide was analysed using individual and binary mixtures of *paraoxon* and *carbofuran* in a concentration range of 0 to 20  $\mu\text{g/l}$ . These authors reported that the biosensor was able to detect both pesticides

in very low concentration down to 0.2  $\mu\text{g/l}$ . However, the relationship between concentration and inhibition observed for binary mixtures was not linear where each enzyme electrode displayed individual inhibition patterns, depending on the type and concentration of the pesticide analysed. ANN data processing was used to discriminate between the two tested pesticides<sup>[179]</sup>.

Most of the sensor arrays are based on integrated ion-selective field effect transistors (ISFETs). For instance, Arkhyova et al.<sup>[180]</sup> proposed an enzyme sensor array based on the combination of a potentiometric ISFET transducer with three types of biologically active membranes consisting enzyme *urease*, *AChE* and *BChE*. It was found that the inhibition of *cholinesterase* enzyme by pesticides (*trichlorfon* and *carbofuran*) and toxic ions ( $\text{Ag}^+$  and  $\text{Hg}^{2+}$ ) depended on pollutants' concentration in different ways, while *urease* is not inhibited by tested pesticides but shows considerable inhibition by mercury ions (see Table 2.3-2).

**Table 2.3-2** Level of inhibition (%) of enzymes by different toxic substances<sup>[180]</sup>.

<i>Analyte</i>	<i>Urease</i>	<i>BChE</i>	<i>AChE</i>
10 $\mu\text{M}$ trichlorfon	0	50	5
50 $\mu\text{M}$ trichlorfon	0	70	25
1 mM trichlorfon	0	100	85
100 $\mu\text{M}$ carbofuran	0	100	50
10 $\mu\text{M}$ $\text{Ag}^+$	0	3	25
50 $\mu\text{M}$ $\text{Ag}^+$	10	7	70
10 $\mu\text{M}$ $\text{Hg}^{2+}$	15	3	10
50 $\mu\text{M}$ $\text{Hg}^{2+}$	40	7	70
10 $\mu\text{M}$ $\text{Ag}^+$ +10 $\mu\text{M}$ $\text{Hg}^{2+}$ +10 $\mu\text{M}$ trichlorfon+10 $\mu\text{M}$ carbofuran	20	100	30
50 $\mu\text{M}$ $\text{Ag}^+$ +20 $\mu\text{M}$ $\text{Hg}^{2+}$ +50 $\mu\text{M}$ trichlorfon+20 $\mu\text{M}$ carbofuran	95	100	90
50 $\mu\text{M}$ $\text{Ag}^+$ +50 $\mu\text{M}$ $\text{Hg}^{2+}$ +50 $\mu\text{M}$ trichlorfon+50 $\mu\text{M}$ carbofuran	100	100	100

With this sensor array, authors used a multi-enzyme analysis to recognize the heavy metal ions in solutions containing a mixture of different metal ions, as well as for determination of their content in the analysed samples. These authors demonstrated that multi-enzyme analysis followed by mathematical processing is an efficient approach to develop sensor arrays for the detection of toxic substrates.

Starodub and Kukla<sup>[181, 182]</sup> introduced a multi-enzyme electrochemical sensors array based on electrolyte-insulator-semiconductor (EIS) structures consisting of five sensors with an integrated flow-injection system (Figure 2.3-2).

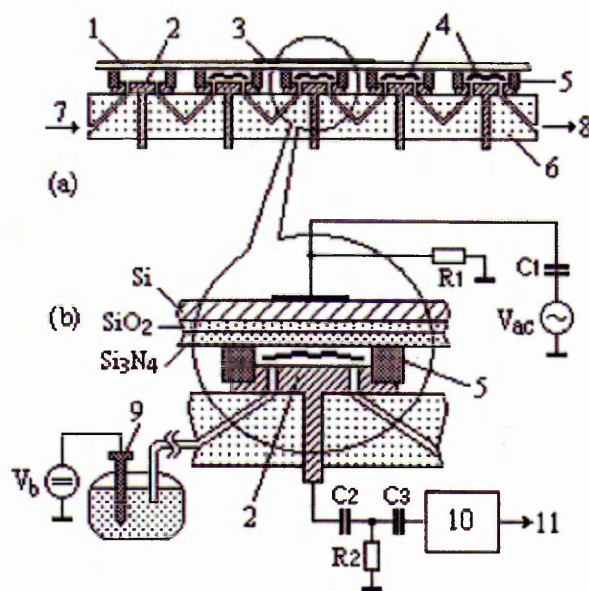


**Figure 2.3-2** Schematic view of the 5-channel EIS enzyme sensor: *1* – sensitive Si-SiO<sub>2</sub>-Si<sub>3</sub>N<sub>4</sub> structure, *2* – steel contrary electrode, *3* – Al contact to Si, *4* – enzymatic membranes, *5* – rubber sealing, *6* – organic glass support, *7* – flow input, *8* – flow output; *9* – reference electrode, *10* – C/V converter, *11* – connection to PC (taken from Ref.<sup>[182]</sup>).

All sensors were placed on the silicon nitride surface of the same silicon plate. The flow system consists of five separate parallel channels, each with its own input and output. Four channels contained enzymatic membranes and one channel served as a reference. Each channel consisted of a pH-sensitive multilayer Si-SiO<sub>2</sub>-Si<sub>3</sub>N<sub>4</sub> structure, an electrolyte and a metallic electrode. The acid produced during the enzyme reaction releases H<sup>+</sup> ions that are detected by the pH-sensitive Si<sub>3</sub>N<sub>4</sub> layer. The operating principle of each sensor channel is based on the measurement of high-frequency C-V curves for the aforesaid multilayer structure. The changes of this parameter with time served as a response of the sensor channel during enzyme reactions.

The enzyme membranes were prepared by deposition of 10% enzyme solutions on the nitrocellulose sheets. Enzymes *urease*, *AChE*, *BChE* and *glucose oxidase* were used for heavy metal ions detection. The registration procedure was as follows. At first, the responses of enzymatic reactions for pure substrata or their mixtures of known

concentrations were measured. Then metal salt solution without substratum was added into the system and held there for approximately 15 minutes. After this, the responses of the sensor channels under similar conditions were recorded again. The residual enzyme activity  $\Delta R$  was estimated from the response drop compared with its initial value. The concentrations of pesticides and heavy metal ions, which were detected by this sensor, were within the range of  $10^{-4}$  to  $10^{-7}$  M. The residual activity of *BChE* and urease<sup>a</sup> (as an example) inhibited by the heavy metal ions is shown in Fig. 2.3-3.

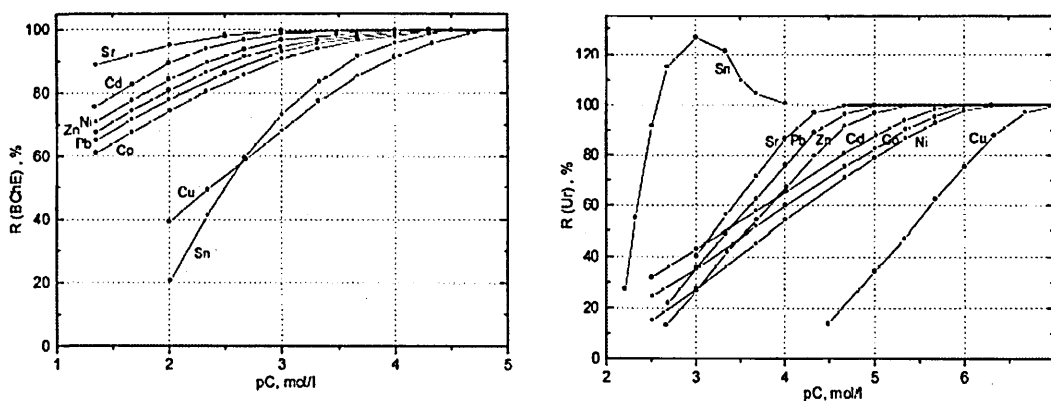


**Figure 2.3-3** Residual activity  $R$  of *BChE* (a) and urease (b) as a function of the concentrations of the following heavy metal ions:  $\text{Sn}^{2+}$ ,  $\text{Cu}^{2+}$ ,  $\text{Co}^{2+}$ ,  $\text{Pb}^{2+}$ ,  $\text{Zn}^{2+}$ ,  $\text{Ni}^{2+}$ ,  $\text{Cd}^{2+}$ ,  $\text{Sr}^{2+}$  (after Ref.<sup>[182]</sup>).

The sensitivity of *BChE* and *AChE* to the heavy metal ions was substantially lower than that of urease. Moreover, the inhibition of these enzymes by metal ions is reversible. Their activity can be restored by washing the enzymatic membranes with the buffer solution.

The sensitivity of the sensor array described above is in the parts-per-million range, which is at the limit of electrochemical sensors, but not high enough for environmental control tasks. Further increases in the sensitivity can be achieved with optical methods.

A highly sensitive optical enzyme sensors array for monitoring typically agricultural and industrial water pollutants has been proposed by Nabok and Haron<sup>[183]</sup>. The sensor is based on  $\text{SiO}_2/\text{Si}_3\text{N}_4$  planar waveguide (as an ATR transducer) and has a sensing window coated with electrostatically self-assembled film containing pH

<sup>a</sup> *AChE* enzyme behaves like *BChE*, the only difference being a higher inhibition effect of metal ions on it.

sensitive organic chromophore molecules (namely, CTCT) and different enzymes i.e. *urease*, *acetyl- and butyryl- cholinesterase*.

The sensor was capable of registration of enzyme reactions as well as their inhibition by traces of some typical water pollutants, such as heavy metal ions ( $\text{Cd}^{2+}$ ,  $\text{Pb}^{2+}$ , and  $\text{Ni}^{2+}$ ), and pesticides (*imidacloprid*, *dichlorvos* and *paraoxon*).

For this purpose the authors designed a multi-channel reaction cell and light guiding system (see Fig.2.3-4). A mechanical chopper rotated by a stepper-motor and having four asymmetrical slits allowed a part of a laser beam to enter the section of the waveguide. By rotating the chopper, this light spot could be moved along the edge of the waveguide (see the inset in Fig. 2.3-4). The light coming out of the waveguide was collected by the power-meter.

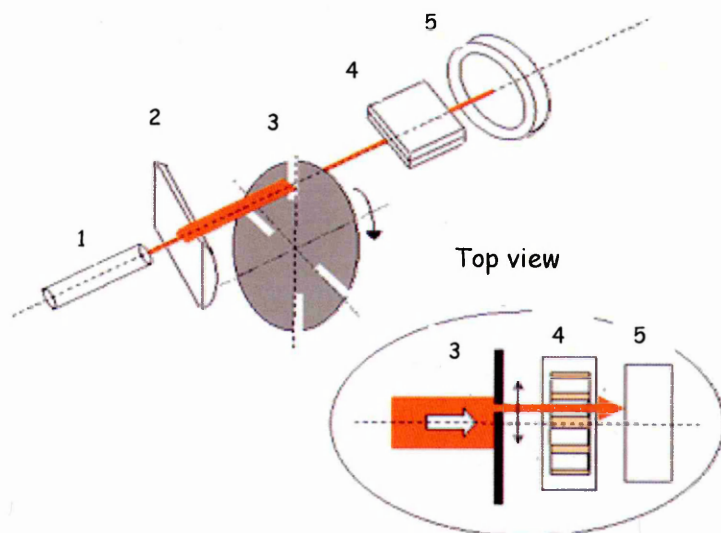


**Figure 2.3-4** The experimental set-up for planar waveguide sensor array: *1* – laser diode; *2* – semi-cylindrical lens; *3* – beam chopper; *4* – planar waveguide; *5* – optical power-meter (after Ref.<sup>[183]</sup>).

Residual activity of the enzyme ( $\Delta R$ , %) was calculated as a ratio of relative responses of fresh enzymes  $\Delta I_0$  and those after inhibition by pollutants  $\Delta I_r$ , as shown in Fig. 2.3-5:

$$\Delta R (\%) = \frac{\Delta I_r}{\Delta I_0} \cdot 100\% .$$

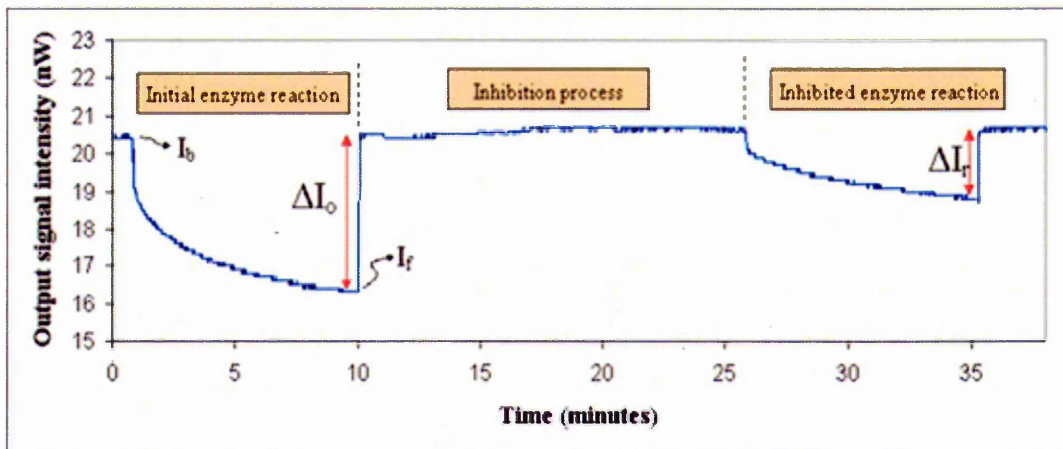


**Figure 2.3-5** Typical response of CTCT/urease film to urea substratum: initial enzyme reaction (first 10 min); inhibition process (next 15 min) and finally, inhibited enzyme reaction (last 10 min) (after Ref.<sup>[183]</sup>).

The analysis of the experimental results demonstrated that the multi-channel enzyme sensor was able to produce adequate responses to the presence of different pollutants of industrial and agricultural origin, in the concentration range from 1 ppb to 1000 ppb. The distinct pattern of sensor responses was analyzed by the implementation of an artificial neural network algorithm. Despite a rather small amount of experimental data, the trained neural networks were able to classify and quantify the pollutants.

## 2.4 Low Molecular Weight Analytes in Optical Immune Sensors

Pollutants, such as pesticides, herbicides, mycotoxins and alkyphenols (such as *nonylphenol*) found in water, food or environmental samples are frequently small molecules with low molecular weight (LMW) ( $MW < 1000 \text{ g/mol}$ ).

Generally, optical transducers (which are the point of interest in this thesis) respond to the change in refractive index or light intensity on the sensor surface. The extent of the change is proportional to the mass of the molecules bound to the sensor surface. Therefore, a signal that is due to the binding of molecules with LMW is much smaller than one that is due to binding of high molecular weight compounds (if equal numbers are assumed). Moreover, the sensor surface area where the receptors can be immobilised is limited; and this also negatively affects the number of analyte molecules that can be bound<sup>[184]<sup>a</sup></sup>. That is why LMW compounds are usually measured in indirect assays, such as competition or inhibition assays, where molecules with high molecular weight are introduced into the assay and their binding behaviour is monitored. In the following section these assay formats are described in detail.

### *a. Competition assay*

The recognition molecule (e.g. antibody) is immobilised on the sensor surface. The sample is mixed with molecules, which in addition to the analyte also bind to the recognition molecule. These are called the *tracers*. The tracer is usually a large molecular weight compound (such as a globular protein); therefore, it can be easily detected by optical direct biosensors. The analyte and tracer now compete with each other for the available binding sites of the recognition molecule (Fig. 2.4-1a). The number of these binding sites on the sensor surface is limited. Only the bound tracer will give a signal, but the amount of analyte present will reduce the tracer signal. As a result, the obtained signal depends on the sample concentration<sup>[185]</sup>.

---

<sup>a</sup> The idea of increasing sensor surface area has been realised in porous silicon-based biosensors.

*b. Inhibition assay*

The inhibition assay is often used for the detection of small analytes like herbicides or drugs<sup>[186]</sup>. In the first step, the tracer molecules are immobilised on the sensor surface and the recognition molecules are mixed with the sample. Analyte molecules in the sample bind to antibodies and block their binding sites. After an incubation period, the sample with antibodies is brought to the surface with immobilised analyte molecules. According to the concentration of target molecules, a certain quantity of antibodies are prevented from binding to the sensor surface. The response is proportional to the analyte concentration (Fig. 2.4-1b).

*c. Direct assay*

In a direct detection assay, the analyte in a sample interacts with a biomolecular recognition element (antibody) which is immobilised on the sensor surface. The resulting signal change is directly proportional to the concentration of the analyte (Fig. 2.4-1c).

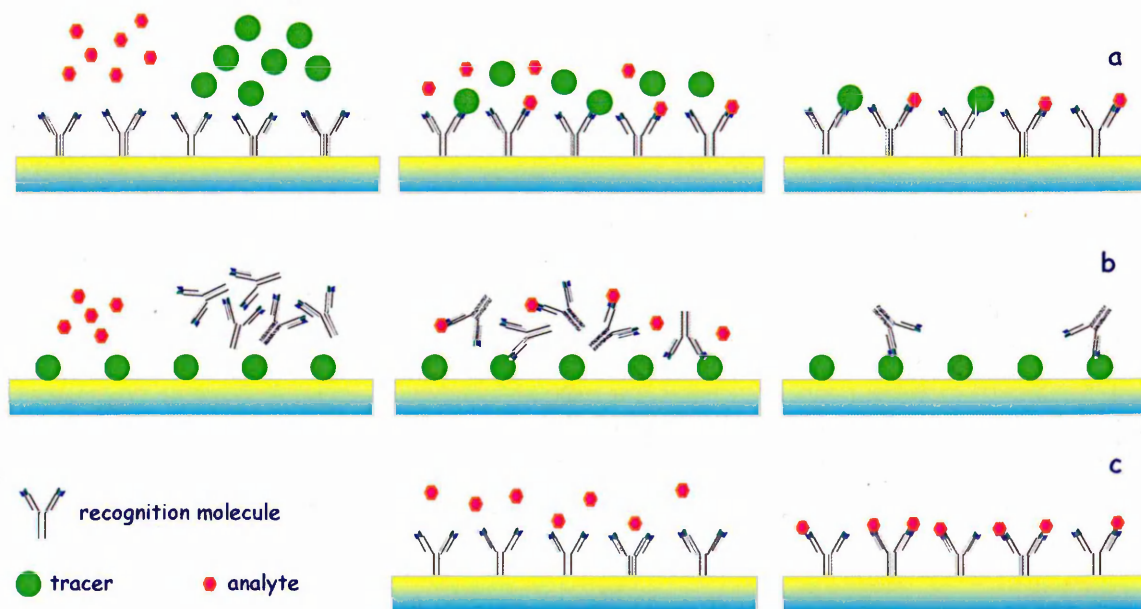


**Figure 2.4-1** Competition (a), inhibition (b) and direct (c) assays for the detection of low molecular weight analyte.

Experimentally determined detection limits of optical techniques for the detection of LMW environmental pollutants are summarised in (Table 2.4-1).

**Table 2.4-1** Experimentally determined detection limits of optical biosensors for the detection of LMW pollutants.

<i>Principle</i>	<i>Analyte</i>	<i>Detection limit</i>	<i>Refs.</i>
Surface Plasmon Resonance (SPR)	<i>Simazine</i>	0.2 µg/l	[187]
	<i>Atrazine</i>	0.05 µg/l	[188]
	<i>Estradiol and Estrone</i>	0.1 µg/l	[189]
	<i>Aflatoxin B1</i>	0.2 ng/ml	[190]
	<i>Ochratoxin A</i>	0.1 ng/ml	[190]
	<i>Fumonisin B1</i> (direct assay)	50 ng/ml	[190]
Integrated optical SPR	<i>Simazine</i> (competition assay)	0.22 µg/l	[191]
	<i>Simazine</i> (inhibition assay)	0.11 – 0.16 µg/l	[192]
Grating-Coupler	<i>Simazine</i>	0.25 µg/l	[193]
Ellipsometry	<i>Biotin</i> (direct assay)	2 µg/l	[194]
Resonant Mirror	<i>Atrazine</i>	1 µg/l	[195]
Mach-Zender Interferometry	<i>Atrazine</i>	0.1 µg/l	[196]
	<i>Simazine</i>	0.1 µg/l	[197]
TIRF	<i>Simazine</i>	26 ng/l	[198]

#### *d. Target analytes*

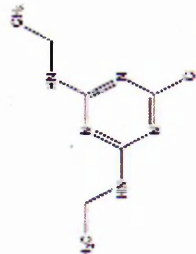
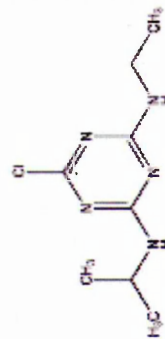
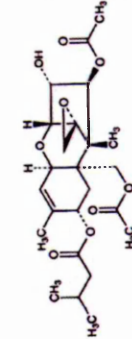
SPR combined with the direct immune assay approach does not provide sufficient sensitivity. That is why, generally, the SPR technique exploits other assays, such as competition and inhibition. More sensitive techniques are needed and the method of TIRE could be one of them.

In this study, the method of TIRE was adopted for the registration of low molecular weight toxins, such as common herbicides *simazine* and *atrazine*, *T-2 mycotoxin* (from the dioxins family) and oestrogen mimicking *nonylphenol*.

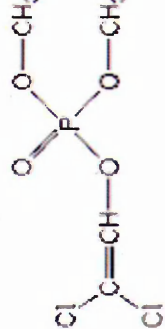
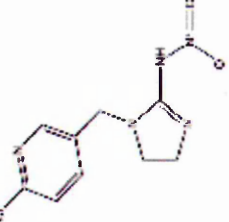
Registration of toxins was achieved using a direct immune assay approach, when molecules of toxins were specifically bound to respective antibodies. Antibodies were immobilised on solid surfaces (i.e. gold or silicon) using a method of electrostatic self-assembly. These low molecular weight toxins were registered in very low concentrations down to single ng/ml.

Analytes tested in this thesis are listed in Table 2.4-2.

Table 2.4-2 Target analytes tested in this thesis.

Analyte / Use type	Chemical formula	Molecular weight	Toxicity information and Maximum Contaminant Level (MCL) or Lethal Dose <sub>50</sub> (LD <sub>50</sub> )
<i>Simazine</i> <sup>a[199]</sup> / Herbicide	<chem>C7H12ClN5</chem> 	201.66 g/mol	Acutely toxic, groundwater pollutant, reproductive and developmental toxicant, suspected endocrine disruptor and probable carcinogen. MCL = 4 µg / l
<i>Atrazine</i> <sup>[200]</sup> / Herbicide	<chem>C8H14ClN5</chem> 	215.69 g/mol	Highly acutely toxic, carcinogen, groundwater pollutant, suspected endocrine disruptor. MCL = 3 µg / l
<i>T-2 mycotoxin</i> <sup>[201]</sup> / Biological warfare agent	<chem>C24H34O9</chem> 	466.57 g/mol	Highly toxic, DNA inhibitor, highly irritating to skin and mucous membranes. Direct contact may cause extensive inflammation and tissue necrosis. LD <sub>50</sub> = 1.0 mg / kg (oral) <sup>[202]</sup>

<sup>a</sup> Pesticides *atrazine* and *simazine* have been withdrawn from the market in the UK. Last date for use or storage of *atrazine* and *simazine* is 10/09/05 [<http://www.pesticides.gov.uk>].

Analyte / Use type	Chemical formula	Molecular weight	Toxicity information and Maximum Contaminant Level (MCL) or Lethal Dose50 (LD <sub>50</sub> )
<p><i>Nonylphenol</i><sup>[203]</sup>/ Chemical intermediate for antioxidants for rubber and plastics, surfactants, and polyvinyl chloride plasticizers. Antioxidant in the manufacture of polystyrene</p>	<p>C<sub>15</sub>H<sub>24</sub>O</p> 	<p>220.39 g/mol</p>	<p>Strong endocrine disrupting effects, suspected carcinogen. LD<sub>50</sub> = 1.3 g/kg<sup>[204]</sup></p>
<p><i>Dichlorvos (DVDP)</i><sup>a[205]</sup>/ Organophosphate insecticide</p>	<p>C<sub>4</sub>H<sub>7</sub>Cl<sub>2</sub>O<sub>4</sub>P</p> 	<p>220.98 g/mol</p>	<p>Highly acutely toxic, cholinesterase inhibitor, carcinogen, contaminate groundwater. MCL = 0.3 µg/l<sup>[206]</sup></p>
<p><i>Imidacloprid</i><sup>[207]</sup>/ Insecticide</p>	<p>C<sub>9</sub>H<sub>10</sub>ClN<sub>5</sub>O<sub>2</sub></p> 	<p>255.7 g/mol</p>	<p>Groundwater pollutant, reproductive and developmental toxicant, suspected endocrine disruptor; MCL = 399 µg/l<sup>[208]</sup></p>

<sup>a</sup> Banned in the UK and Denmark, registered for use in Finland and Sweden [<http://www.pesticides.gov.uk>]

## 2.5 Summary

This chapter provided the literature review and theoretical background related to this study. A brief theory of porous silicon formation and optical properties of porous silicon from the bio-sensing point of view were given. Porous silicon has received a great deal of attention due to its large surface area and easy fabrication procedure based on well-established silicon technology. It has been proven as a promising material for development of novel immunosensors.

This chapter also contained a review of optical immune and enzyme sensors developed for environmental analysis. Optical biosensors, based on evanescent wave technology, such as surface plasmon resonance, ellipsometry, total internal reflection ellipsometry, and planar waveguide were described.

In addition, the principles of detection of pesticides and heavy metal ions using the inhibition of cholinesterase enzyme and urease, respectively, were explained in detail. The theory of multiple internal reflections was revised and several types of waveguide structures such as ATR, TIRF and interferometer were reviewed.

The number of publications in the area of optical immune and enzyme biosensors is vast and, certainly, all of these cannot be reviewed in this thesis; only a few of the most interesting and successful works were described here.

Finally, the analytes of interest were introduced.

---

## References

### § 2.1

- [i] Yu P. Y. and Cardona M. *Fundamentals of semiconductors: physics and materials properties*, Springer, 2004.
- [1] Lehmann V. *The physics of macropore formation in low doped n-type silicon*, Journal of Electrochemical Society **140** (1993) 2836-2843.
- [2] Smith R. L. and Collins S. D. *Porous silicon formation mechanisms*, Journal of Applied Physics **71** (1992) R1-R22.
- [3] Carstensen J., Christophersen M. and Föll H. *Pore formation mechanisms for the Si-HF system*, Material Science and Engineering B **69-70** (2000) 23-28.
- [4] Föll H., Christophersen M., Carstensen J. and Hasse G. *Formation and application of porous silicon*, Materials Science and Engineering R **39** (2002) 93-141.
- [5] Lehmann V. and Gösele U. *Porous silicon formation: a quantum wire effect*, Applied Physics Letters **58** (1991) 856-858.
- [6] Bisi O., Ossicini S. and Pavesi L. *Porous silicon: a quantum sponge structure for silicon based optoelectronics*, Surface Science Reports **38** (2000) 1-126.
- [7] Gaburro Z., Daldosso N. and Pavesi L. *Porous silicon*, 2006.
- [8] Theiß W. *Optical properties of porous silicon*, Surface Science Reports **29** (1997) 91-192.
- [9] Kordás K., Remes J., Beke S., Hu T. and Leppävuori S. *Manufacturing of porous silicon; porosity and thickness dependence on electrolyte composition*, Applied Surface Science **178** (2001) 190-193.
- [10] Searson P. C., Macaulay J. M. and Ross F. M. *Pore morphology and the mechanism of pore formation in n-type silicon*, Journal of Applied Physics **72** (1992) 253-258.
- [11] Beale M. I. J., Chew N. G., Uren M. J., Cullis A. G. and Benjamin J. D. *Microstructure and formation mechanism of porous silicon*, Applied Physics Letters **46** (1985) 86-88.
- [12] John G. C. and Singh V. A. *Porous silicon: theoretical studies*, Physics Reports **263** (1995) 93-151.
- [13] Searson P. C. and Macaulay J. M. *The fabrication of porous silicon structures*, Nanotechnology **3** (1992) 188-191.
- [14] Lehmann V. *Porous silicon formation and other photoelectrochemical effect at silicon electrodes anodized in hydrofluoric acid*, Applied Surface Science **106** (1996) 402-495.
- [15] Zhang X. G., Collins S. D. and Smith R. L. *Porous silicon formation and electropolishing of silicon by anodic polarization in HF solution*, Journal of Electrochemical Society **136** (1989) 1561-1565.
- [16] Föll H. *Properties of silicon-electrolyte junctions and their application to silicon characterization*, Applied Physics A **53** (1991) 8-19.
- [17] Parkhutik V. *Porous silicon – mechanisms of growth and applications*, Solid-State Electronics **43** (1999) 1121-1141.

- [18] Ouyang H. and Fauchet F. M. *Biosensing using porous silicon photonic bandgap structures*, SPIE Optics East (2005) 1-15.
- [19] Lehmann V. and Föll H. *Formation mechanism and properties of electrochemically etched trenches in n-type silicon*, Journal of Electrochemical Society **137** (1990) 653-659.
- [20] Sing K. S. W., Everett D. H., Haul R. A. W., Moscou L., Pierotti R. A., Rouquerol J. and Siemieniewska T. *Reporting physisorption data for gas/solid systems with special reference to the determination of surface area and porosity*, Pure and Applied Chemistry **57** (1985) 603-619.
- [21] Canham L.T. *Silicon quantum wire array fabrication by electrochemical and chemical dissolution of wafers*, Applied Physics Letters **57** (1990) 1046-1048.
- [22] Fauchet P. M. *Photoluminescence and electroluminescence from porous silicon*, Journal of Luminescence **70** (1996) 294-309.
- [23] Halimaoui A., Oules C., Bomchil G., Bsiesy A., Gaspard F., Herino R., Ligeon M. and Muller F. *Electroluminescence in the visible range during anodic-oxidation of porous silicon films*, Applied Physics Letters **59** (1991) 304-306.
- [24] Savir E., Jedrzejewski J., Many A., Goldstein Y., Weisz S. Z., Gomez M., Fonseca L. F. and Resto O. *Relation between electroluminescence and photoluminescence in porous silicon*, Materials Science and Engineering B **72** (2000) 138-141.
- [25] Zhu Z., Zhang J. and Zhu J. *An overview of Si-based biosensors*, Sensors Letters **3** (2005) 71-88.
- [26] Tinsley-Bown A. M., Canham L. T., Hollings M., Anderson M. H., Reeves C. L., Cox T. I., Nicklin S., Squirrel D. J., Perkins E., Hutchinson A., Sailor M. J. and Wun A. *Tuning the pore size and surface chemistry of porous silicon for immunoassays*, Physica Status Solidi A **182** (2000) 547-553.
- [27] Schöning M. J., Ronkel F., Crott M., Thust M., Schultze J. W., Kordos P. and Luth H. *Miniaturization of potentiometric sensors using porous silicon microtechnology*, Electrochimica Acta **42** (1997) 3185-3193.
- [28] Mandenius C. F. and Mosbach K. *Detection of biospecific interactions using amplified ellipsometry*, Analytical Biochemistry **170** (1988) 68-72.
- [29] Mandenius C. F., Mosbach K., Welin S. and Lundström I. *Reversible and specific interaction of dehydrogenases with a coenzyme coated surface continuously monitored with a reflectometer*, Analytical Biochemistry **157** (1986) 283-288.
- [30] Löfås S. and Johnsson B. *A novel hydrogel matrix on gold surface plasmon resonance sensors for fast and efficient covalent immobilization of ligands*, Journal of the Chemical Society – Chemical Communications **21** (1990) 1526-1528.
- [31] DeLouise L. A. and Miller B. L. *Enzyme immobilization in porous silicon: quantitative analysis of the kinetics parameters for glutathione-S-transferases*, Analytical Chemistry **77** (2005) 1950-1956.
- [32] Tay L., Rowell N. L., Poitras D., Fraser J. W., Lockwood D. J. and Boukherroub R. *Bovine serum albumin adsorption on passivated porous silicon layers*, Canadian Journal of Chemistry **82** (2004) 1545-1553.
- [33] Arwin H. *Ellipsometry on thin organic layers of biological interest: characterization and applications*, Thin Solid Films **377-378** (2000) 48-56.

- [34] Gaillet M., Guendouz M., Ben Salah M., Le Jeune B. and Le Brunc G. *Characterization of porous silicon composite material by spectroscopic ellipsometry*, Thin Solid Films **455-456** (2004) 410-416.
- [35] Wongmanerod C., Zangoie S. and Arwin H. *Determination of pore size distribution and surface area of thin porous silicon layers by spectroscopic ellipsometry*, Applied Surface Science **172** (2001) 117-125.
- [36] Lohner T., Fried M., Petrik P., Polgár O., Gyulai J. and Lehnert W. *Ellipsometric characterization of oxidized porous silicon layer structures*, Materials Science and Engineering B **69-70** (2000) 182-193.
- [37] Karlsson L. M., Tengvall P., Lundström I. and Arwin H. *Penetration and loading of human serum albumin in porous silicon layers with different pore size and thicknesses*, Journal of Colloid and Interface Science **266** (2003) 40-47.
- [38] Zangoie S., Bjorklund R. and Arwin H. *Protein adsorption in thermally oxidized porous silicon layers*, Thin Solid Films **313-314** (1998) 825-830.
- [39] Danny van Noort, Stefan Welin-Klintström, Hans Arwin, Shahin Zangoie, Ingemar Lundström and Carl-Fredrik Mandenius *Monitoring specific interaction of low molecular weight biomolecules on oxidized porous silicon using ellipsometry*, Biosensors and Bioelectronics **13** (1998) 439-449.
- [40] Dancil K-P. S., Greiner D. P. and Sailor M. J. *A porous silicon optical biosensor: detection of reversible binding of IgG to protein A – modified surface*, Journal of American Chemical Society **121** (1999) 7925-7930.
- [41] De Stefano L., Rotiroti L., Rendina I., Moretti L., Scognamiglio V., Rossi M. and D’Auria S. *Porous silicon-based optical microsensors for the detection of L-glutamine*, Biosensors and Bioelectronics **21** (2006) 1664-1667.
- [42] Min H.-K., Yang H.-S. and Cho M. S. *Extremely sensitive optical sensing of ethanol using porous silicon*, Sensors and Actuators B **67** (2000) 199-202.
- [43] Сивухин Д. В. *Общий курс физики. Том IV: Оптика*, ФИЗМАТЛИТ МФТИ, 2002.
- [44] Victor S.-Y. Lin, Kianoush Moteshareei, Keiki-Pua S. Dancil, Michael J. Sailor, M. Reza Ghadiri *A porous silicon-based optical interferometric biosensor*, Science **278** (1997) 840-843.
- [45] Claudia Steinem, Andreas Janshoff, Victor S.-Y. Lin, Nicolas H. Völcker and M. Reza Ghadiri *DNA hybridization-enhanced porous silicon corrosion: mechanistic investigations and prospect for optical interferometric biosensing*, Tetrahedron **60** (2004) 11259-11267.
- [46] Brecht A. and Gauglitz G. in *Frontiers in biosensorics II: Practical applications*, eds. Scheller F.W. et al. Birkhäuser, Basel, Switzerland (1997) 1-16.
- [47] Janshoff A., Dancil K.-P., Steinem C. and Greiner D. P. *Macroporous p-type silicon Fabry-Perot layers. Fabrication, characterization, and applications in biosensing*, Journal of American Chemical Society **120** (1998) 12108-12116.
- [48] Starodub V. M., Fedorenko L. L. and Starodub N. F. *Optical immune sensors for the monitoring protein substances in the air*, Sensors and Actuators B **68** (2000) 40-47.
- [49] Starodub V. M., Fedorenko L. L., Sisetskiy A. P. and Starodub N. F. *Control of myoglobin level in a solution by an immune sensor based on the photoluminescence of porous silicon*, Sensors and Actuators B **58** (1999) 409-414.
- [50] Starodub N. F., Fedorenko L. L., Starodub V. M., Dikij S. P. and Svechnikov S. V. *Use of the*

- silicon crystals photoluminescence to control immunocomplex formation*, Sensors and Actuators B **35-36** (1996) 44-47.
- [51] Girolamo Di Francia, Vera La Ferrara, Sonia Manzo and Salvatore Chiavarini *Towards a label-free optical porous silicon DNA sensor*, Biosensors and Bioelectronics **21** (2005) 661-665.
- [52] Chan S., Li Y., Rothberg L. J., Miller B. L. and Fauchet P. M. *Nanoscale silicon microcavities for biosensing*, Material Science and Engineering C **15** (2001) 277-282.
- [53] Osaka T. *Electrochemical formation and microstructure in thin films for high functional device*, Electrochimica Acta **42** (1997) 3015-3022.
- [54] Tsargorodskaya A., Nabok A. V. and Ray A. K. *Study of electroluminescence in porous silicon for sensing applications*, IEE Proceedings – Circuits Devices Systems **150** (2003) 355-360.
- [55] Reddy R., Chadha A. and Bhattacharya E. *Porous silicon based potentiometric triglyceride biosensor*, Biosensors and Bioelectronics **16** (2001) 313-317.
- [56] Lüth H., Thust M., Steffen A., Kordos P. and Schöning M. J. *Biochemical sensors with structured and porous silicon capacitors*, Materials Science and Engineering B **69-70** (2000) 104-108.
- § 2.2
- [57] Homola J., Yee S. S. and Gauglitz G. *Surface plasmon resonance sensors: review*, Sensors and Actuators B **54** (1999) 3-15.
- [58] Nelson S. G., Johnston K. S. and Yee S. S. *High sensitivity surface plasmon resonance sensor based on phase detection*, Sensors and Actuators B **35-36** (1996) 187-191.
- [59] Sambles J. R., Bradbery G. W. and Fuzi Y. *Optical excitation of surface plasmons: an introduction*, Contemporary Physics **32** (1991) 173-183.
- [60] Ordal M. A., Long L. L., Bell R. J., Bell S. E., Bell R. R., Alexander R. W., Jr. and Ward C. A. *Optical properties of the metals Al, Co, Cu, Au, Fe, Pb, Ni, Pd, Pt, Ag, Ti, and W in the infrared and far infrared*, Applied Optics **22** (1983) 1099-1119.
- [61] Liedberg B., Nylander C. and Lundström I. *Biosensing with surface plasmon resonance – how it all started*, Biosensors & Bioelectronics **10** (1995) i-ix.
- [62] Englebienne P., van Hoonacker A. and Verhas M. *Surface plasmon resonance: principles, methods and applications in biomedical sciences*, Spectroscopy **17** (2003) 255-273.
- [63] Tobiška P. *Advanced data processing for SPR biosensors*, Doctoral Thesis, Institute of Radio Engineering and Electronics Academy of Science of the Czech Republic, Prague, 2005.
- [64] Otto A. *Excitation of nonradiative surface plasma waves in silver by the method of frustrated total reflection*, Zeitschrift für Physik **216** (1968) 398-410.
- [65] Kretschmann E. and Raether H. *Radiative decay of non-radiative surface plasmons excited by light*, Zeitschrift für Naturforschung **23A** (1968) 2135-2136.
- [66] Salamon Z., Macleod H. A. and Tollin G. *Surface plasmon resonance spectroscopy as a tool for investigating the biochemical and biophysical properties of membrane protein systems. II: Applications to biological systems*, Biochimica et Biophysica Acta **1331** (1997) 131-152.
- [67] *Commercial Biosensors. Applications to clinical, bioprocess, and environmental samples*, Ed. by Ramsay G. John Wiley & Sons, New York, 1998.

- [68] Green R. J., Frazier R. A., Shakesheff K. M., Davies M. C., Roberts C. J. and Tendler S. J. B. *Surface plasmon resonance analysis of dynamic biological interactions with biomaterials*, *Biomaterials* **21** (2000) 1823-1835.
- [69] Wilkop T. *Thin film calixresorcinarene membranes for chemical sensing*, Thesis for the degree of Doctor of Philosophy, Sheffield Hallam University, 2001.
- [70] Homola J. *Present and future of surface plasmon resonance biosensors*, *Analytical and Bioanalytical Chemistry* **377** (2003) 528-539.
- [71] Kurihara K., Nakamura K. and Suzuki K. *Asymmetric SPR sensor response curve-fitting equation for the accurate determination of SPR resonance angle*, *Sensors and Actuators B* **86** (2002) 49-57.
- [72] Englebienne P., van Hoonacker A. and Verhas M. *Surface plasmon resonance: principles, methods and applications in medical sciences*, *Spectroscopy* **17** (2003) 255-273.
- [73] Kurihara K. and Suzuki K. *Theoretical understanding of an absorption-based surface plasmon resonance sensor based on Kretschmann's theory*, *Analytical Chemistry* **74** (2002) 696-701.
- [74] Ince R. and Narayanaswamy R. *Analysis of the performance of interferometry, surface plasmon resonance and luminescence as biosensors and chemosensors*, *Analytica Chimica Acta* **569** (2006) 1-20.
- [75] Homola J., Vaisocherová H., Dostálek J. and Piliarik M. *Multi-analyte surface plasmon resonance biosensing*, *Methods* **37** (2005) 26-36.
- [76] Mullett W. M., Lai E. P. C. and Yeung J. M. *Surface plasmon resonance-based immunoassays*, *Methods* **22** (2000) 77-91.
- [77]
- [78] Liedberg B., Nylander C. and Lundström I. *Surface plasmon resonance for gas detection and biosensing*, *Sensors and Actuators* **4** (1983) 299-304.
- [79] <http://www.biacore.com> (accessed 9 November 2006).
- [80] Dostálek J., Homola J. and Miler M. *Rich information format surface plasmon resonance biosensor based on array of diffraction gratings*, *Sensors and Actuators B* **107** (2005) 154-161.
- [81] H. Raether, *Surface plasmons on smooth and rough surfaces and on gratings*, Springer-Verlag, Berlin, 1988.
- [82] Cullen D. C. and Lowe C. R. *A direct surface plasmon-polariton immunosensor: preliminary investigation of the non-specific adsorption of serum components to the sensor interface*, *Sensors and Actuators B* **1** (1990) 576-579.
- [83] Cullen D. C., Brown R. G. and Lowe C. R. *Detection of immunocomplex formation via surface plasmon resonance on goldcoated diffraction gratings*, *Biosensors* **3** (1987) 211-225.
- [84] Homola J., Koudela I. and Yee S. S. *Surface plasmon resonance sensors based on diffraction gratings and prism couplers: sensitivity comparison*, *Sensors and Actuators B* **54** (1999) 16-24.
- [85] Adam P., Dostálek J. and Homola J. *Multiple surface plasmon spectroscopy for study of biomolecular systems*, *Sensors and Actuators B* **113** (2006) 774-781.
- [86] Homola J., Yee S. S. and Gauglitz G. *Surface plasmon resonance sensors: review*, *Sensors and Actuators B* **54** (1999) 3-15.
- [87] Harris R. D. and Wilkinson J. S. *Waveguide surface plasmon resonance sensors*, *Sensors and Actuators B* **29** (1995) 261-267.

- [88] Harris R. D., Luff B. J., Wilkinson J. S., Piehler J., Brecht A., Gauglitz G. and Abuknesha R. A. *Integrated optical surface plasmon resonance immunoprobe for simazine detection*, *Biosensors & Bioelectronics* **14** (1999) 377-386.
- [89] Abdelghani A., Chovelon J. M., Jaffrezic-Renault N., Ronot-Trioli C., Veillas C. and Gagnaire H. *Surface plasmon resonance fibre-optic sensor for gas detection*, *Sensors and Actuators B* **38-39** (1997) 407-410.
- [90] Slavík R., Homola J. and Čtyrský J. *Single-mode optical fiber surface plasmon resonance sensor*, *Sensors and Actuators B* **54** (1999) 74-79.
- [91] Taylor A. D., Ladda J., Yu Q., Chen S., Homola J. and Jiang S. *Quantitative and simultaneous detection of four foodborne bacterial pathogens with a multi-channel SPR sensor*, *Biosensors and Bioelectronics* **22** (2006) 752-758.
- [92] Homola J., Lu H. B., Nenninger G. G., Dostálek J. and Yee S. S. *A novel multichannel surface plasmon resonance biosensor*, *Sensors and Actuators B* **76** (2001) 403-410.
- [93] Homola J., Vaisocherová H., Dostálek J. and Piliarik M. *Multi-analyte surface plasmon resonance biosensing*, *Methods* **37** (2005) 26-36.
- [94] Mello I. D. and Kubota L. T. *Review of the use of biosensors as analytical tools in the food and drink industries*, *Food Chemistry* **77** (2002) 237-256.
- [95] Minunni M. and Mascini M. *Detection of pesticides in drinking water using real-time biospecific interaction analysis*, *Analytical Letters* **26** (1993) 1441-1460.
- [96] Taylor A.D., Yu Q., Chen S., Homola J. and Jiang S. *Comparison of E. coli O157:H7 preparation methods used for detection with surface plasmon resonance sensor*, *Sensors and Actuators B* **107** (2005) 202-208.
- [97] Byung-Keun Oh, Woochang Lee, Bum Suk Chun, Young Min Bae, Won Hong Lee and Jeong-Woo Choi *The fabrication of protein chip based on surface plasmon resonance for detection of pathogens*, *Biosensors and Bioelectronics* **20** (2005) 1847-1850.
- [98] Green R. J., Frazier R. A., Shakesheff K. M., Davies M. C., Roberts C. J. and Tendler S. J. B. *Surface plasmon resonance analysis of dynamic biological interactions with biomaterials*, *Biomaterials* **21** (2000) 1823-1835.
- [99] Liedberg B., Lundstrom I. and Stenberg E. *Principles of biosensing with extended coupling matrix and surface plasmon resonance*, *Sensors Actuators B* **11** (1993) 63-72.
- [100] Mitchell J. S., Wu Yinqiu, Cook C. J. and Main L. *Sensitivity enhancement of surface plasmon resonance biosensing of small molecules*, *Analytical Biochemistry* **343** (2005) 125-135.
- [101] Woollam J. A., Johs B., Herzinger C. M. et al. *Overview of variable angle spectroscopic ellipsometry (VASE), Part I: Basic theory and typical applications*, *Critical Reviews of Optical Science and Technology* **CR 72** (1999) 3-28.
- [102] Azzam R. M. A. and Bashara N. M. *Ellipsometry and polarized light*, North-Holland, Amsterdam, 1992.
- [103] *Handbook of ellipsometry*, Eds. Tompkins H. G. and Irene E. A., William Andrew, 2005.
- [104] Gonçalves D. and Irene E. A. *Fundamentals and applications of spectroscopic ellipsometry*, *Química Nova* **25** (2002) 794-800.

- [105] [http://www.jawoollam.com/tutorial\\_1.html](http://www.jawoollam.com/tutorial_1.html) (accessed 28 December 2006).
- [106] Ostroff R. M., Hopkins D., Haeberli A. B. et al. *Thin-film biosensor for rapid visual detection of nucleic acid targets*, *Clinical Chemistry* **45** (1999) 1659-1664.
- [107] Zangoie S., Bjorklund R. and Arwin H. *Vapor sensitivity of thin porous silicon layers*, *Sensors Actuators B* **43** (1997) 168-174.
- [108] Arwin H. *Is ellipsometry suitable for sensor applications?* *Sensors and Actuators A* **92** (2001) 43-51.
- [109] Ostroff R. M., Maul D., Bogart G. R. et al. *Fixed polarizer ellipsometry for simple and sensitive detection of thin-films generated by specific molecular interactions: applications in immunoassays and DNA sequence detection*, *Clinical Chemistry* **44** (1998) 2031-2035.
- [110] Ostroff R. M., Hopkins D., Haeberli A. B. et al. *Thin-film biosensor for rapid visual detection of nucleic acid targets*, *Clinical Chemistry* **45** (1999) 1659-1664.
- [111] Malmsten M. and Lidman B. *Ellipsometry studies of cleaning of hard surfaces. Relation to the spontaneous curvature of the surfactant monolayer*, *Langmuir* **5** (1989) 1105-1111.
- [112] Guo S., Rochotzki R., Lundström I. and Arwin H. *Ellipsometric sensitivity to halothane vapors of hexamethyldisiloxane plasma polymer films*, *Sensors and Actuators B* **44** (1997) 243-247.
- [113] Mårtensson J., Arwin H. and Lundström I. *Thin-films of phthalocyanines studied with spectroscopic ellipsometry: an optical gas sensor?* *Sensors and Actuators B* **1** (1990) 134-137.
- [114] Arwin H. *Spectroscopic ellipsometry and biology: recent developments and challenges*, *Thin Solid Films* **313-314** (1998) 764-774.
- [115] Elwing H. *Protein absorption and ellipsometry in biomaterial research*, *Biomaterials* **19** (1998) 397-406.
- [116] Arwin H., Poksinski M. and Johansen K. *Total internal reflection ellipsometry: principles and applications*, *Applied Optics* **43** (2004) 3028-3036.
- [117] Westphal P. and Bornmann A. *Biomolecular detection by surface plasmon enhanced ellipsometry*, *Sensors and Actuators B* **84** (2002) 278-282.
- [118] Poksinski M. and Arwin H. *Protein monolayers monitored by internal reflection ellipsometry*, *Thin Solid Films* **455-456** (2004) 716-721.
- [119] *Guide to Using WVASE<sup>®</sup>*, J. A. Woollam Co. Inc., 2003.
- [120] Nabok A. *The method of total internal reflection ellipsometry for thin film characterization and sensing*, Oral presentation, ECOF-10, Riga, Latvia, 2005.
- [121] Shen S., Liu T. and Guo J. *Optical phase-shift detection of surface plasmon resonance*, *Applied Optics* **37** (1998) 1747-1751.
- [122] Mårtensson J., Arwin H., Nygren H. and Lundström I. *Adsorption and optical properties of ferritin layers on gold studied with spectroscopic ellipsometry*, *Journal of Colloid Interface Science* **174** (1995) 79-85.
- [123] Poksinski M. and Arwin H. *In situ monitoring of adsorption from milk on metal surfaces using total internal reflection ellipsometry*, *Sensors and Actuators B* **94** (2003) 247-252.

- [124] Poksinski M., Dzuho H. and Arwin H. *Copper corrosion monitoring with total internal reflection ellipsometry*, Journal of Electrochemical Society **150** (2003) B536-B539.
- [125] Suryajaya, Nabok A. and Hassan A. *Electrostatically self-assembled films containing II-VI semiconductor: optical and electrical properties*, Oral presentation, ECOF-10, Riga, Latvia, 2005.
- [126] Basova T. Private communications.
- [127] Saavedra S. S. and Reichert W. M. *Integrated optical attenuated total reflection spectrometry of aqueous superstrates using prism-coupled polymer waveguides*, Analytical Chemistry **62** (1990) 2251-2256.
- [128] Plowman T. E., Saavedra S. S. and Reichert W. M. *Planar integrated optical methods for examining thin films and their surface adlayers*, Biomaterials **19** (1998) 341-355.
- [129] Kasap S. O. *Optoelectronic and photonics: principles and practices*, Prentice Hall, Upper Saddle River, NJ, 2001.
- [130] Walker D. S., Hellinga H. W., Saavedra S. S. et al. *Integrated optical waveguide attenuated total reflection spectrometry and resonance Raman spectroscopy of adsorbed cytochrome c*, Journal of Physical Chemistry **97** (1993) 10217- 10222.
- [131] Cropek D. M. and Bohn P. W. *Surface molecular orientations determined by electronic linear dichroism in optical waveguide structures*, Journal of Physical Chemistry **94** (1990) 6452-6457.
- [132] Sutherland R. M. and Dahne C. *IRS devices for optical immunoassays in Biosensors: fundamentals and applications*, Eds. Turner A. P. F., Karube I. and Wilson G. S., Oxford University Press, pp.655-679, 1987.
- [133] Saavedra S. S. and Reichert W. M. *In situ quantitation of protein adsorption density by integrated optical waveguide attenuated total reflection spectrometry*, Langmuir **7** (1991) 995-999.
- [134] Nabok A., Haron S. and Ray A. *Registration of heavy metal ions and pesticides with ATR planar waveguide enzyme sensors*, Applied Surface Science **238** (2004) 423-428.
- [135] Zhou Y., Laybourn P. J. R., Magill J. V. and De La Rue R. M. *An evanescent fluorescence biosensor using ion-exchanged buried waveguides and the enhancement of peak fluorescence*, Biosensors and Bioelectronics **6** (1991) 595-607.
- [136] Tschmelak J., Kumpf M., Käppel N. et al. *Total internal reflectance fluorescence (TIRF) biosensor for environmental monitoring of testosterone with commercially available immunochemistry: Antibody characterization, assay development and real sample measurements*, Talanta **69** (2006) 343-350.
- [137] Qian F., Asanov A. N. and Oldham P. B. *A total internal reflection fluorescence biosensor for aluminum (III)*, Microchemical Journal **70** (2001) 63-68.
- [138] Attridge J. W., Daniels P. B., Deacon J. K., Robinson G. A. and Davidson G. P. *Sensitivity enhancement of optical immunosensors by the use of a surface plasmon resonance fluoroimmunoassay*, Biosensors and Bioelectronics **6** (1991) 201-214.
- [139] Nabok A. *Organic and inorganic nanostructures*, Artech House, Boston-London, 2005.
- [140] Shirshov Y. M., Svechnikov S. V., Kiyanovskii A. P., Ushenin Yu. V., Venger E. F., Samoylov A. V. and Merker R. *A sensor based on the planar-polarization interferometer*, Sensors and Actuators A **68** (1998) 384-387.

- [141] Heideman R. G., Kooyman R. P. H. and Greve J. *Development of an optical waveguide interferometric immunosensor*, Sensors and Actuators B **4** (1991) 297-299.
- [142] Lechuga L. M., Lenferink A. T. M., Kooyman R. P. H. and Greve J. *Feasibility of evanescent wave interferometer immunosensors for pesticide detection: chemical aspects*, Sensors and Actuators B **25** (1995) 762-765.
- [143] Brosinger F., Freimuth H., Lacher M., Ehrfeld W., Gedig E., Katerkamp A., Spener F. and Cammann K. *A label-free affinity sensor with compensation of unspecific protein interaction by a highly sensitive integrated optical Mach-Zehnder interferometer on silicon*, Sensors and Actuators B **44** (1997) 350-355.
- [144] Shirshov Y. M., Svechnikov S. V., Kiyanovskii A. P., Ushenin Yu. V., Venger E. F., Samoylov A. V. and Merker R. *A sensor based on the planar-polarization interferometer*, Sensors and Actuators A **68** (1998) 384-387.
- [145] Shirshov Y. M., Snopok B. A., Samoylov A. V., Kiyanovskij A. P., Venger E. F., Nabok A. V. and Ray A. K. *Analysis of the response of planar polarization interferometer to molecular layer formation: fibrinogen adsorption on silicon nitride surface*, Biosensors and Bioelectronics **16** (2001) 381-390.
- § 2.3
- [146] Clark L.C. and Lyons C. *Electrode systems for monitoring in cardiovascular surgery*, Annals of the New York Academy of Sciences **102** (1962) 29-45.
- [147] Karube I. and Nomura Y. *Enzyme sensors for environmental analysis*, Journal of Molecular Catalysis B **10** (2000) 177-181.
- [148] Andreescu S. and Marty J.-L. *Twenty years research in cholinesterase biosensors: from basic research to practical applications*, Biomolecular Engineering **23** (2006) 1-15.
- [149] Bisenberger M., Brächle C. and Hampp N. *A triple-step potential waveform at enzyme multisensors with thick-film gold electrodes for detection of glucose and sucrose*, Sensors and Actuators B **28** (1995) 181-189.
- [150] Campanella L., Faveo G., Sammartino M. P. and Tomassetti M. *Further development of catalase, tyrosinase and glucose oxidase based organic phase enzyme electrode response as a function of organic solvent properties*, Talanta **46** (1998) 595-606.
- [151] Hämmerle M. and Hall E. A. H. *Electrochemical enzyme sensor for formaldehyde operating in the gas phase*, Biosensors and Bioelectronics **11** (1996) 239-246.
- [152] Guilbault G. G., Pravda M. and Kreuzer M. *Biosensors – 42 years and counting*, Analytical Letters **37** (2004) 14481-14496.
- [153] Evtugyn G. A., Budnikov H. C. and Nikolskaya E. B. *Sensitivity and selectivity of electrochemical enzyme sensors for inhibitor determination*, Talanta **46** (1998) 465-484.
- [154] Tran Minh Canh *Biosensors*, Chapman & Hall, London, 1993.
- [155] Stoytcheva M. *Electrochemical evaluation of the kinetic parameters of heterogeneous enzyme reaction in presence of metal ions*, Electroanalysis **14** (2002) 923-927.
- [156] Amine A., Mohammadia H., Bourais I. and Palleschi G. *Enzyme inhibition-based biosensors for food safety and environmental monitoring*, Biosensors and Bioelectronics **21** (2006) 1405-1423.

- [157] Kok F. N., Bozoglu F. and Hasirci V. *Construction of an acetylcholinesterase-choline oxidase biosensor for aldicarb determination*, Biosensors and Bioelectronics **17** (2002) 531-539.
- [158] Dzyadevych S. V., Arkhypova V. N., Soldatkin A. P., El'skaya A. P., Martelet A. V. and Jaffrezic-Renault C. *Enzyme biosensor for tomatine detection in tomatoes*, Analytical Letters **37** (2004) 1611-1624.
- [159] Sotiropoulou S. and Chaniotakis N. A. *Lowering the detection limit of the acetylcholinesterase biosensor using a nanoporous carbon matrix*, Analytica Chimica Acta **530** (2005) 199-204.
- [160] Ciucu A., Negulescu C. and Baldwin R. P. *Detection of pesticides using an amperometric biosensor based on ferrophthalocyanine chemically modified carbon paste electrode and immobilized bienzymatic system*, Biosensors and Bioelectronics **18** (2003) 303-310.
- [161] *The chemistry of organophosphorus pesticides, reactivity, synthesis, mode of action, toxicology*, Eds. Fest C. and Schmidt K.-J., Springer-Verlag Heidelberg, New York, 1973.
- [162] Marty J.-L., Garcia D. and Rouillon R. *Biosensors: potential in pesticide detection*, Trends in Analytical Chemistry **14** (1995) 329-333.
- [163] Stein K. and Schwedt G. *Comparison of immobilization methods for the development of an acetylcholinesterase biosensor*, Analytica Chimica Acta **272** (1993) 73-81.
- [164] Amine A., Mohammadia H., Bourais I. and Palleschi G. *Enzyme inhibition-based biosensors for food safety and environmental monitoring*, Biosensors and Bioelectronics **21** (2006) 1405-1423.
- [165] <http://www.charm.com/> (accessed 4 January 2007).
- [166] Evtugyn G. A., Budnikov H. C. and Nikolskaya E. B. *Influence of surfaceactive compounds on the response and sensitivity of cholinesterase biosensors for inhibitor determination*, Analyst **121** (1996) 1911-1915.
- [167] Palleschi G., Bernabei M., Cremisini C. and Mascini M. *Determination of organophosphorus insecticides with a choline electrochemical biosensor*, Sensors and Actuators B **7** (1992) 513-517.
- [168] Abad J. M., Pariente F., Hernández L., Abruña H. D. and Lorenzo E. *Determination of organophosphorus and carbamate pesticides using a piezoelectric biosensor*, Analytical Chemistry **70** (1998) 2848-2855.
- [169] Nabok A., Haron S. and Ray A. *Registration of heavy metal ions and pesticides with ATR planar waveguide enzyme sensors*, Applied Surface Science **238** (2004) 423-428.
- [170] Andres R. T. and Narayanaswamy R. *Fibre-optic pesticide biosensor based on covalently immobilized acetylcholinesterase and thymol blue*, Talanta **44** (1997) 1335-1352.
- [171] Choi J. W., Min J., Jung J. W., Hee-Woo Rhee and Lee W. H. *Fiber-optic biosensor for the detection of organophosphorus compounds using AChE-immobilized viologen LB films*, Thin Solid Films **327-329** (1998) 676-680.
- [172] Choi J. W., Kim Y. K., Lee I. H., Min J. and Lee W. H. *Optical organophosphorus biosensor consisting of acetylcholinesterase/viologen hetero Langmuir-Blodgett film*, Biosensors & Bioelectronics **16** (2001) 937-943.
- [173] Doong R. A. and Tsai H. C. *Immobilization and characterization of sol-gel-encapsulated acetylcholinesterase fiber-optic biosensor*, Analytica Chimica Acta **434** (2001) 239-246.
- [174] Andreescu S. and Marty J.-L. *Twenty years research in cholinesterase biosensors: From basic research to practical applications*, Biomolecular Engineering **23** (2006) 1-15.

- [175] Preininger C. and Wolfbeis O. S. *Disposable cuvette test with integrated sensor layer for enzymatic determination of heavy metals*, *Biosensors & Bioelectronics* **11** (1996) 981-990.
- [176] Nabok A. V., Ray A. K., Starodub N. F. and Dowker K. P. *Enzyme/indicator optodes for detection of heavy metal ions and pesticides*, *Proc. SPIE, Biochemical and Biomolecular Sensing* **4200** (2000) 32-41.
- [177] Benounis M., Jaffrezic-Renault N., Halouani H., Lamartine R. and Dumazet-Bonnamour I. *Detection of heavy metals by an optical fiber sensor with a sensitive cladding including a new chromogenic calix[4]arene molecule*, *Materials Science and Engineering C* **26** (2006) 364-368.
- [178] Malcik N., Oktar O., Ozser M. E., Caglar P., Bushby L., Vaughan A., Kuswandi B. and Narayanaswamy R. *Immobilised reagents for optical heavy metal ions sensing*, *Sensors and Actuators B* **53** (1998) 211-221.
- [179] Bachmann T. T. and Schmid R. D. *A disposable multielectrode biosensor for rapid simultaneous detection of the insecticides paraoxon and carbofuran at high resolution*, *Analytica Chimica Acta* **401** (1999) 95-103.
- [180] Arkhypova V. N., Dzyadevych S. V., Soldatkin A. P., El'skaya A. V., Jaffrezic-Renault N., Jaffrezic H. and Martelet C. *Multibiosensor based on enzyme inhibition analysis for determination of different toxic substances*, *Talanta* **55** (2001) 919-927.
- [181] Starodub N. F., Kanjuk N. I., Kukla A. L. and Shirshov Yu. M. *Multi-enzymatic electrochemical sensor: field measurements and their optimisation*, *Analytica Chimica Acta* **385** (1999) 461-466.
- [182] Kukla A. L., Kanjuk N. I., Starodub N. F. and Shirshov Yu. M. *Multienzyme electrochemical sensor array for determination of heavy metal ions*, *Sensors and Actuators B* **57** (1999) 213-218.
- [183] Haron S. *Planar waveguide enzyme sensors coated with nanocomposite membranes for water pollution monitoring*, Thesis for the degree of Doctor of Philosophy, Sheffield Hallam University, 2003.
- § 2.4
- [184] Akkoyun A. *Detection of low molecular weight molecules by using optical biosensors*, Thesis for the degree of Doctor of Natural Sciences, Technischen Universität Carolo-Wilhelmina zu Braunschweig, 2002.
- [185] Homola J. *Present and future of surface plasmon resonance*, *Analytical and Bioanalytical Chemistry* **377** (2003) 528-539.
- [186] Go Sakai, Kyoko Ogata, Taizo Uda, Norio Miura and Noboru Yamazoe *A surface plasmon resonance-based immunosensor for highly sensitive detection of morphine*, *Sensors and Actuators B* **49** (1998) 5-12.
- [187] Rodriguez-Mozaz S., Marco M., Lopez de Alda M. et al. *Biosensors for environmental applications: Future development trends*, *Pure and Applied Chemistry* **76** (2004) 723-752.
- [188] Minunni M. and Mascini M., *Detection of pesticide in drinking water using real-time biospecific interaction analysis (BIA)*, *Analytical Letters* **26** (1993) 1441-1460.
- [189] <http://www.tu-berlin.de/~oekotox/de/forschung/sandrine.html> (accessed 1 November 2006).
- [190] van der Gaag B., Spath S., Dietrich H., Stigter E., Boonzaaijer G., van Osenbruggen T. and Koopal K. *Biosensors and multiple mycotoxin analysis*, *Food Control* **14** (2003) 251-254.

- [191] Harris R. D., Luff B. J., Wilkinson J. S. et al. *Integrated optical surface plasmon resonance biosensor for pesticide analysis*, IEE Colloquium on Optical Techniques for Environmental Monitoring **182** (1995) 6.
- [192] Harris R. D., Luff B. J., Wilkinson J. S., Piehler J., Brecht A., Gauglitz G. and Abuknesha R. A. *Integrated optical surface plasmon resonance immunoprobe for simazine detection*, Biosensors & Bioelectronics **14** (1999) 377-386.
- [193] Vörös J., Ramsden J. J., Csúcs G., Szendro I., De Paul S. M., Textor M. and Spencer N. D. *Optical grating coupler biosensors*, Biomaterials **23** (2002) 3699-3710.
- [194] van Noort D., Welin-Klintström S., Arwin H., Zangoie S., Lundström I. and Mandenius C.-F. *Monitoring specific interaction of low molecular weight biomolecules on oxidized porous silicon using ellipsometry*, Biosensors and Bioelectronics **13** (1998) 439-449.
- [195] Skládal P., Deng A. and Kolář V. *Resonant mirror-based optical immunosensor: application for the measurement of atrazine in soil*, Analytica Chimica Acta **399** (1999) 29-36.
- [196] Schipper E. F., Rauchalles S., Kooyman R. P. H. et al. *The waveguide Mach-Zender interferometer as atrazine sensor*, Analytical Chemistry **70** (1998) 1192-1197.
- [197] Brecht A. and Gauglitz G. *Label free optical immunoprobes for pesticide detection*, Analytica Chimica Acta **347** (1997) 219-233.
- [198] Klotz A., Brecht A., Barzen C., Gauglitz G., Harris R. D., Quigley G. R., Wilkinson J. S. and Abuknesha R. A. *Immunofluorescence sensor for water analysis*, Sensors and Actuators B **51** (1998) 181-187.
- [199] <http://www.speclab.com/compound/c122349.htm> and <http://www.pesticideinfo.org> (accessed 31 October 2006).
- [200] <http://www2.gtz.de/uvp/publika/English/vol314.htm> and <http://www.pesticideinfo.org> (accessed 31 October 2006).
- [201] <http://www.cbwinfo.com/Biological/Toxins/T2.html#0002> (accessed 31 October 2006).
- [202] Hunter K. W., Brimfield A. A., Knower A. T., Powell J. A. and Feuerstein G. Z. *Reversal of intracellular toxicity of the trichothecene mycotoxin T-2 with monoclonal antibody*, The Journal of Pharmacology and Experimental Therapeutics **255** (1990) 1183-1187.
- [203] Cox C. *Nonylphenol and related chemicals*, Journal of Pesticide Reform **16** (1996) 15-20.
- [204] <http://www.mindfully.org/Plastic/Plasticizers/Nonylphenol-Migration.htm> (accessed 31 October 2006).
- [205] <http://www.chemindustry.com/chemicals/108893.html> and <http://www.pesticideinfo.org> (accessed 31 October 2006).
- [206] <http://apps.leg.wa.gov/WAC/default.aspx?cite=173-200-040> (accessed 31 October 2006).
- [207] <http://www.pesticideinfo.org> (accessed 31 October 2006).
- [208] [http://fisc.er.usgs.gov/Lake\\_Wales\\_Ridge/html/table\\_4.html](http://fisc.er.usgs.gov/Lake_Wales_Ridge/html/table_4.html) (accessed 31 October 2006).

# CHAPTER 3.

## EXPERIMENTAL METHODS

This chapter provides a brief description of experimental methodologies used in this study and it is divided into five sections.

Section 3.1 gives a short introduction to atomic force microscopy and scanning electron microscopy techniques as methods of morphological study. The procedure for ellipsometric data analysis including modelling and a fitting routine is given in section 3.2.

Section 3.3 provides experimental details for both dynamic and static spectroscopic ellipsometry measurements for the study of the *in situ* adsorption of bovine serum albumin (BSA) as a model protein into porous silicon (PS).

Section 3.4 covers the method of total internal reflection ellipsometry with a detailed description of the experimental set-up and protocol, analytes of interest, and the modeling and fitting routine.

Section 3.5 gives a detailed account of planar waveguide enzyme sensors array.

The principle of electrostatic self-assembly and introduction into kinetics of bio-reactions are described in brief in sections 3.6 and 3.7, respectively.

## 3.1 Methods of Morphology Study

### 3.1.1 Introduction to the scanning probe microscopy technique

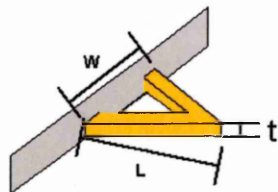
The atomic force microscope (AFM) was invented in 1986 by Binnig, Quate, and Gerber<sup>[1]</sup>. AFM, like all other scanning probe microscopes, utilizes a sharp probe moving over the surface of a sample in a raster scan. In the case of the AFM, the probe is a tip on the end of a cantilever, which bends in response to the force between the tip and the sample. Unlike traditional microscopes, scanned-probe systems do not use lenses, so the size of the probe determines the resolution limit.

#### a. Force between the tip and the sample

The AFM is, as the name suggests, based on interactive forces between the sample and the tip. When the tip is brought into proximity of a sample surface, forces between the tip and the sample lead to a deflection of the cantilever according to Hooke's law:

$$F = -kx, \quad (3.1)$$

where  $F$  is the force,  $k$  is the spring constant, and  $x$  cantilever deflection. The spring constant  $k$  (N/m) of the cantilever is strongly dependent on its physical dimensions (i.e., width –  $w$ , length –  $l$ , thickness –  $t$ ) and the elasticity of material (modulus of elasticity –  $E$ ). For instance, the spring constant for the triangular cantilever is approximately expressed by<sup>[2]</sup>:



$$k = \frac{Et^3 w}{4L^3} \quad (3.2)$$

The force most commonly associated with AFM is an interatomic force (van der Waals force). The relation between this force and distance is shown in Fig. 3.1-1. In the contact region the cantilever is held less than a few angstroms ( $10^{-10}$  m) from the sample surface and the inter-atomic force between the cantilever and the sample is repulsive. In the non-contact region, the cantilever is held in the order of tens to hundreds of angstroms from the sample surface and the interatomic force between the cantilever and sample is attractive.

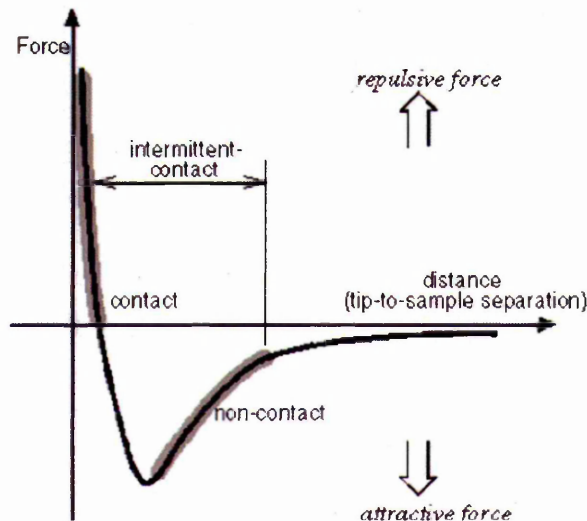


**Figure 3.1-1** Van de Waals force vs. distance (taken from Ref.<sup>[3]</sup>).

Different scanning modes operate in different regions of this curve: *Non-contact mode* is in the attractive region, *Contact mode* – in the repulsive region and *Tapping mode* fluctuates between the two.

*b. “Beam deflection” detection system*

Changes in the tip-sample interaction are monitored using an optical cantilever detection system, in which a laser beam is reflected back from the cantilever and collected by a position sensitive detector consisting of two closely spaced photodiodes connected to a differential amplifier. Angular displacement of the cantilever results in one photodiode collecting more light than the other photodiode, producing an output

signal (the difference between the photodiode signals is normalised by their sum) which is proportional to the deflection of the cantilever (see Fig. 3.1-2). The accuracy of the detection of cantilever deflections is less than  $1\text{\AA}$  (thermal noise limited). The long beam path (several centimetres) amplifies changes in the beam angle<sup>[4]</sup>.

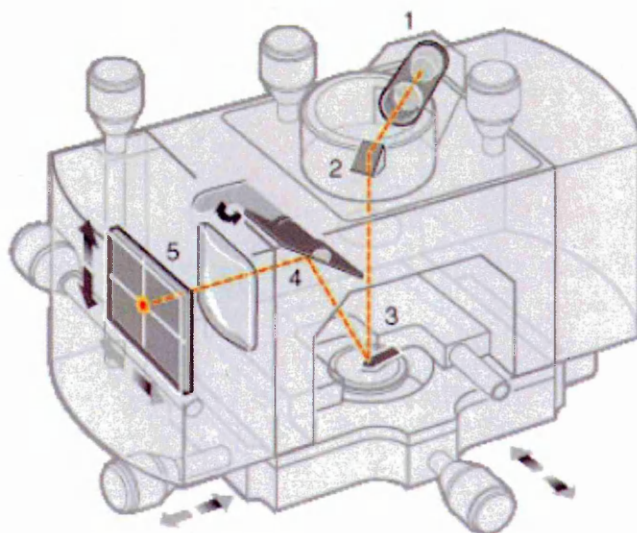


**Figure 3.1-2** NanoScope IIIa beam deflection detection system: 1 – laser; 2 – prism; 3 – cantilever; 4 – tilt mirror; 5 – photodetector (taken from Ref.<sup>[4]</sup>)

During scanning, a particular operating parameter is maintained at a constant level and images are generated through a feedback loop between the optical detection system and the piezoelectric scanners (see Fig. 3.1-3). The sample is scanned above a stationary probe tip (this is true for the NanoScope IIIa instrument, which was used in this study).

### *c. Contact mode AFM*

Contact mode AFM operates by scanning a tip attached to the end of a cantilever across the sample surface while monitoring the change in cantilever deflection with a split photodiode detector. The tip is in close contact with the surface, providing a repulsive regime of the inter-molecular force curve (see Figure 3.1-1).

A feedback loop maintains a constant deflection between the cantilever and the sample by moving the scanner vertically at each (X, Y) point to maintain a “setpoint”

deflection (see Fig. 3.1-3a). By maintaining a constant cantilever deflection, the force between the tip and sample (see Eq.(1)) remains constant. The data of vertical positions of the scanner at each (X, Y) point are stored in the computer to form the topographic image of the sample surface. AFM can operate in either a gaseous (air) or liquid environment.

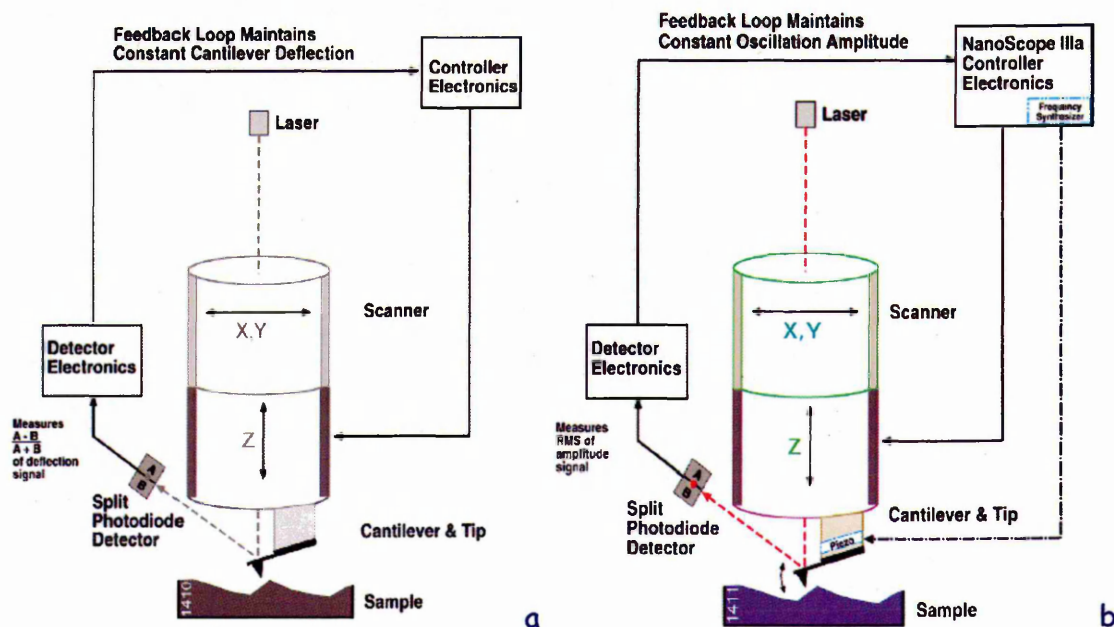


**Figure 3.1-3** A feedback loop of contact mode (a) and tapping mode AFM (b) (taken from Ref.<sup>[4]</sup>).

*Advantages* of contact mode AFM include firstly, the high scan speed and secondly, the possibility of scanning rough samples with extreme changes in vertical topography. The main *disadvantage* of contact mode AFM is that the tip may damage soft samples (i.e., biological samples, polymers, etc.) due to unwanted accidental touching of the sample surface (as a result of a large force between the tip and sample).

#### d. Tapping mode AFM

Tapping mode AFM operates by scanning a tip attached to the end of an oscillating cantilever across the sample surface. The cantilever is oscillated at or near its resonance frequency with the amplitude ranging typically from 20 nm to 100 nm. The

frequency of oscillation is in the range of 200–400 kHz, and it should be close to the resonant frequency of a cantilever.

The tip lightly “taps” the sample surface during scanning, contacting the surface at the bottom of this swing. The feedback loop maintains a constant oscillation amplitude by maintaining a constant tip–sample interaction during scanning (Figure 3.1-3b). Operation can take place in both gaseous and liquid environments<sup>[4]</sup>.

Tapping mode tends to be more applicable to general imaging in air, particularly for soft samples, as the resolution is similar (or even better) to contact mode, while the forces applied to the sample are lower and less damaging. In fact, the only real disadvantages of tapping mode relative to contact mode are that the scan speeds are slightly slower and the AFM operation is a bit more complex, but these disadvantages tend to be outweighed by the advantages<sup>[5]</sup>.

#### *e. Probes*

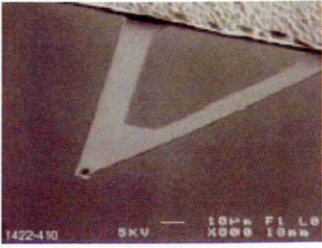
##### *Silicon nitride probes for contact mode AFM*

The contact mode AFM probes used in this research consist of a silicon cantilever integrated with a sharp silicon nitride tip on the end based on a gold-coated glass substrate.

For contact mode AFM imaging it is necessary to have a cantilever which is soft enough to be deflected by very small forces (i.e. small force constant) and has a high enough resonant frequency to not be susceptible to vibrational instabilities. This is accomplished by making the cantilever short, to provide a high resonant frequency, and thin, to provide a small force constant.

For the silicon nitride tips, there are four cantilevers with different geometries attached to each substrate, resulting in four different spring constants. The characteristics of the standard silicon nitride probes (model NP) used in this study are listed in Table 3.1-1.

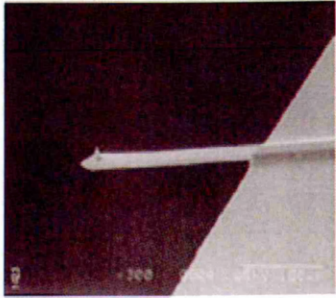
**Table 3.1-1** Characteristics of the silicon nitride probe for contact mode AFM (after Ref.<sup>[4]</sup>)

Spring constant, N/m	0.58 – 0.06	
Nominal tip radius of curvature, nm	20 – 60	
Cantilever lengths, µm	100 & 200	
Reflective coating	Gold	

*Silicon probes for tapping mode AFM*

Silicon probes are used primarily for tapping mode applications. The tip and cantilever are an integrated assembly of single crystal silicon, produced by etching techniques. Only one cantilever and tip are integrated with each substrate. These probes can be much stiffer than the silicon nitride probes, resulting in larger force constants and resonant frequencies. The characteristics of the Tapping Mode Etched Silicon Probes (Model TESP) are listed in Table 3.1-2:

**Table 3.1-2** Characteristics of the silicon probe for tapping mode AFM (after Ref.<sup>[4]</sup>)

Spring constant, N/m	20 – 100	
Resonant frequency, kHz	200 – 400	
Nominal tip radius of curvature, nm	5 – 10	
Cantilever lengths, µm	125	
Reflective coating	uncoated	

*f. AFM instrument*

The AFM instrument (NanoScope IIIa (see Fig.3.1-4a)) used in this research is situated in a "clean" room, and the microscope itself (Fig.3.1-5) rests on an anti-

vibration platform, which itself can be spring suspended on a tripod to reduce further the vibration noise as shown in Fig.3.1-4b.

The NanoScope IIIa instrument and its software give the opportunity to take images of the sample surface with nano-metre resolution and to determine their characteristics (i.e. sample features height, distributions, etc.). In addition, this software can analyse the sections, roughness, particle size, etc. and create pseudo 3-D images of the sample surface.

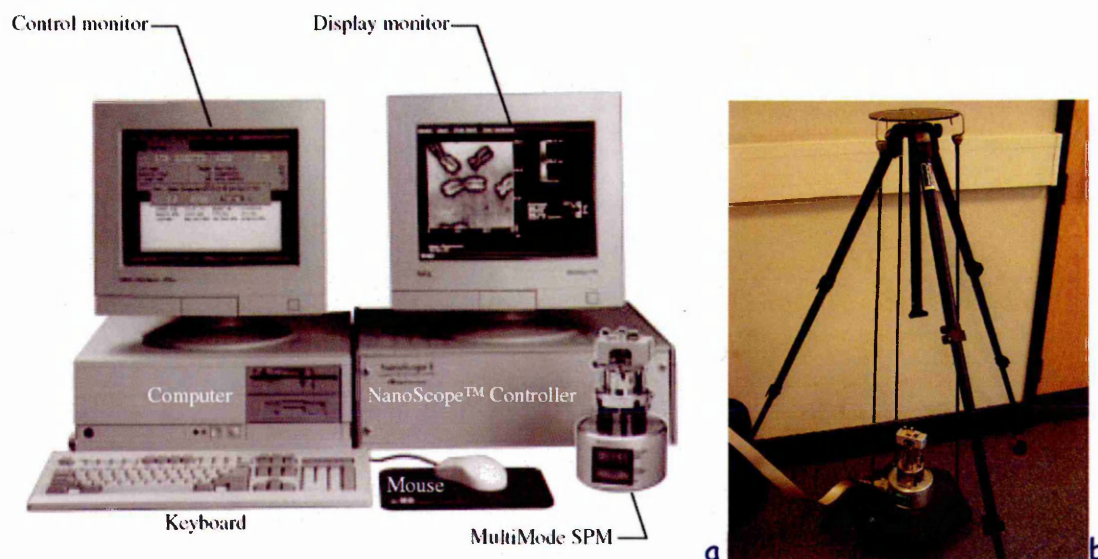


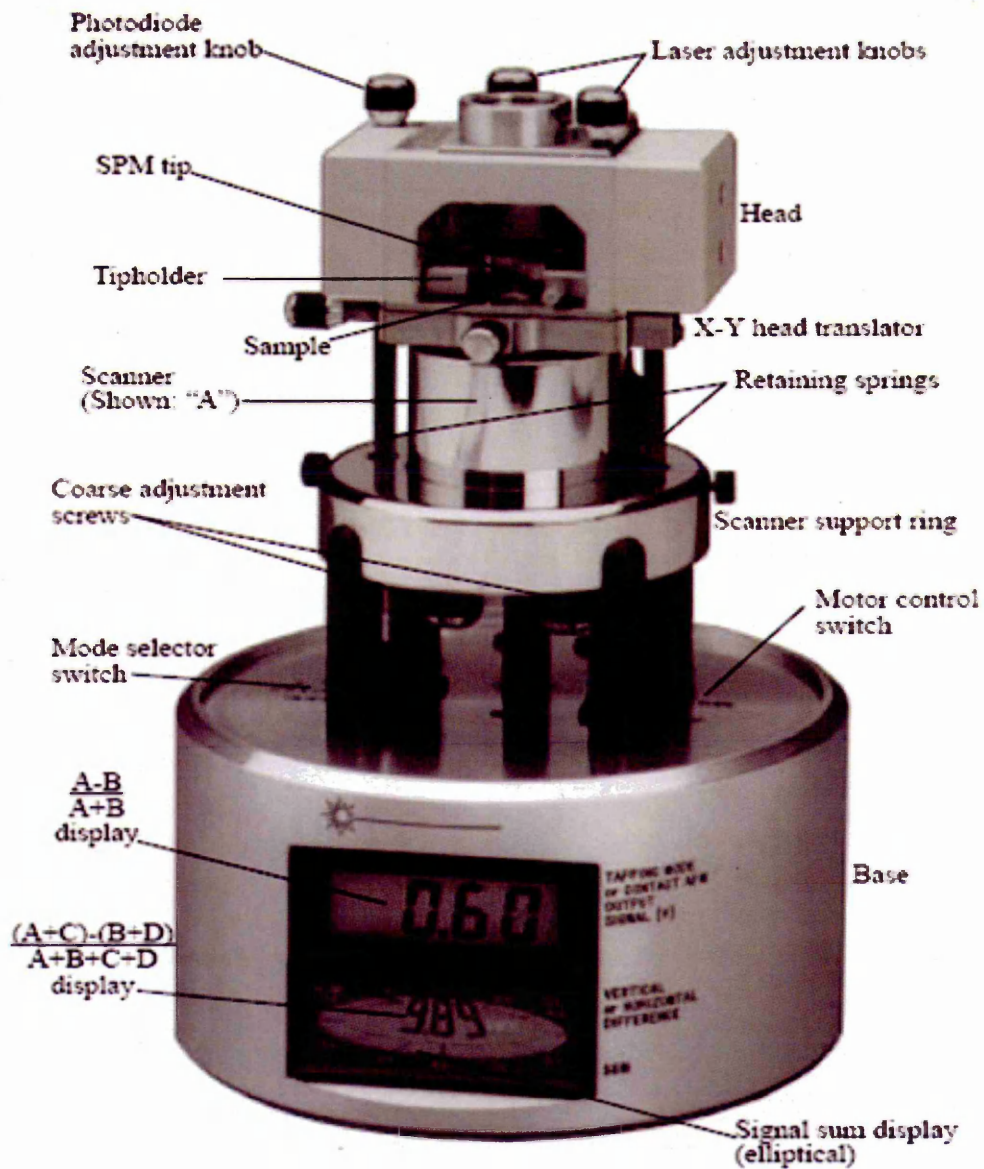
**Figure 3.1-4** NanoScope IIIa MultiMode™ SPM system components (a) and vibration isolation tripod (b).

### *g. Problems*

Some typical problems that may occur during an AFM scan:

- a particle can become attached to the tip and stamped across the sample; this can lead to loss of resolution and false changes in height;
- the tip can become split in two (or more) by wear; this leads to multiple images of details (shown by obvious pairs of details everywhere);
- the sample could be warmer or cooler than the holder; this causes a thermal drift of the sample relative to the tip during scanning and leads to distorting the shape of investigated features.

Scan times are in the range of 0.85 seconds per line, making for around 3.5 minutes per entire scan (apart from the special cases such as porous silicon samples or very rough samples requiring a much slower scan rate). The frequency can be increased making for shorter times, but the tip will begin to miss small details. The frequency can be decreased giving better resolution but the scanning will take a much longer time and the image is more likely to be effected by the thermal drift.



**Figures 3.1-5** NanoScope IIIa MultiMode™ scan probe microscope (taken from Ref.<sup>[4]</sup>).

### 3.1.2 Introduction to scanning electron microscopy technique

#### *a. Scanning Electron Microscope history*

The Scanning Electron Microscope (SEM) provides information regarding the surface structure. Electron microscopy is one of the traditional and well-established methods in surface science.

It is not completely clear who first proposed the principle of scanning the surface of a specimen with a finely focused electron beam to produce an image of the surface. The first published description appeared in 1935 in a paper by German physicist M. Knoll<sup>[6]</sup>. In 1942 Zworykin et al.<sup>[7]</sup> first described a true SEM with a resolution of 50 nm and a magnification of 8,000x<sup>[8]</sup>.

#### *b. Why was SEM used for the morphology study?*

There are a number of reasons why the SEM was used in this study. The first, and most obvious, is that it can give much more magnification than an optical microscope. The SEM has a maximum magnification of up to about 800,000x (for the Philips XL40 SEM instrument used).

Secondly, SEM itself is useful because it has great depth-of-focus. Most of the samples of interest (such as porous silicon) do not have flat surfaces, in fact at high magnification they often look like mountain landscapes. An optical microscope would be able to focus only on the peaks, or valleys, or some point in between. The SEM can have all of these features in focus at the same time, so it is possible to see and understand the true surface morphology. Finally, the images produced by the SEM are easy to interpret – most look like an aerial view of some landscape, illuminated by a low, late-afternoon sun. This means that a microscopic hole looks like a hole, a crack looks like a crack, etc.

The samples are put in the vacuum chamber of the microscope and a fine beam of high energy electrons is scanned across a small area. The scanning is done in a "raster" pattern, much like the way that a picture is built up on a TV screen<sup>[9]</sup>.

## c. SEM basics

A SEM consists of an electron-optical column, a vacuum system and electronics. All of the components of the SEM are usually housed in one unit. Figure 3.1-6 shows a scheme of SEM. An electron beam is produced at the top of the microscope by heating a tungsten filament (*1b*) with a diameter of around 0.1 mm. Optimum filament temperature for the thermo-ionic emission of electrons is around 2700 K. The accelerating voltage, generally between -500 V and -50,000 V DC, is applied to the Wehnelt cylinder grid (*1a*). Resistive self-biasing is usually used where an adjustable bias resistance connects the filament to the accelerating voltage. The biasing makes the filament slightly more positive than the Wehnelt; the anode (*1c*) is grounded<sup>[10]</sup>.

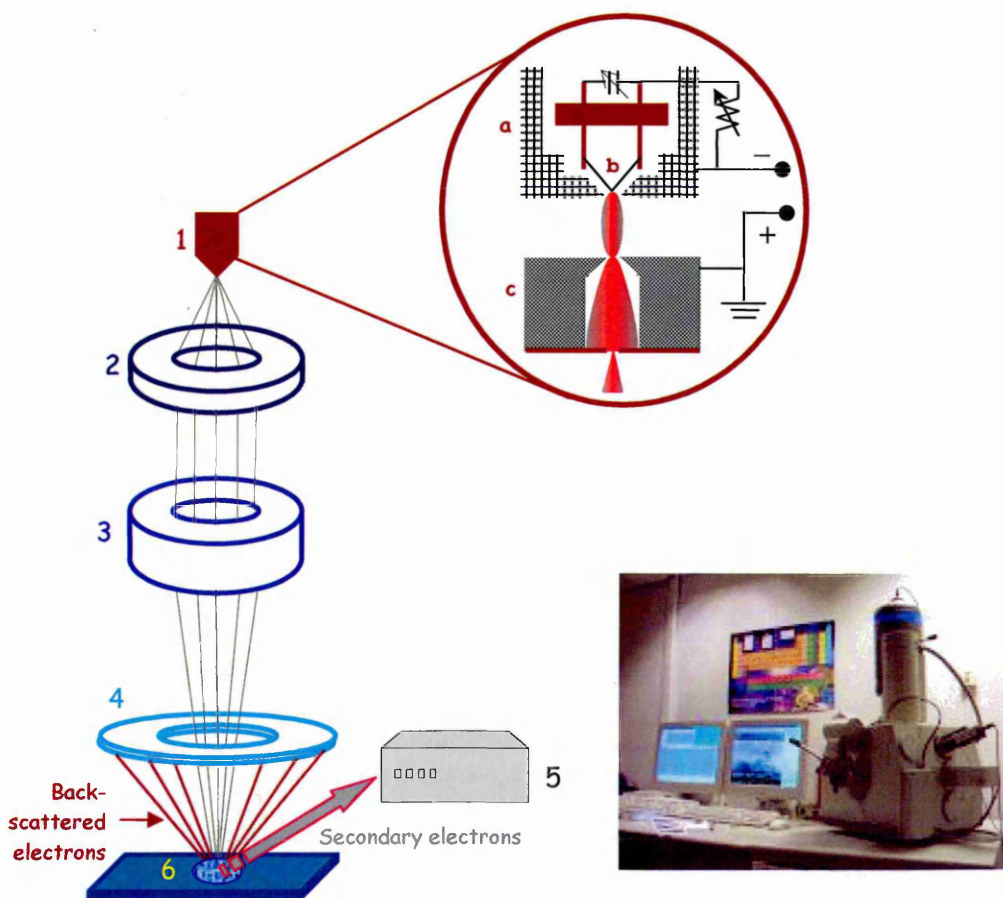


**Figure 3.1-6** The scheme of SEM: *1* – electron gun (consists of a tungsten filament (*b*), cathode – Wehnelt cylinder (*a*), and anode (*c*)); *2* – electromagnetic beam focusing system; *3* – electromagnetic (X,Y) scanner; *4* – backscattered electron detector; *5* – secondary electron detector; *6* – stage and specimen.

Without the Wehnelt cylinder and anode, electrons emitted from the filament would tend to stay in the area of the filament. This would form a “space charge” or a cloud of electrons whose mutual repulsion resisted any further emission from the filament. The anode would attract the electrons away from the filament – providing the primary acceleration for the electron beam. However, the current flow that would result would be very low and would be dependent on the accelerating voltage. By adding the grid, or Wehnelt cylinder, we have a way of controlling the space charge of the filament, shaping the beam and increasing the beam current<sup>[11]</sup>.

The electron beam follows a vertical path through the column of the microscope. It makes its way through electromagnetic lenses (2 and 3) which focus and direct the beam down towards the sample (6). Once it hits the sample, other electrons (backscattered or secondary electrons) are ejected from the sample. Detectors (4 and 5) collect the secondary or backscattered electrons and convert them into a signal that is sent to a viewing screen, producing an image<sup>[12]</sup>.

#### *d. Secondary and Backscattered electrons*

When electrons strike the specimen, several phenomena occur<sup>[13]</sup>:

1. Electrons on collision with a sample atom may interact with the electron shell and create a free electron, which leaves the sample with very low kinetic energy (~5 eV); the free electron is called a “*secondary electron*” (Fig. 3.1-7a). Each incident electron can produce several secondary electrons. Production of secondary electrons is topography related – only those near the surface (lying not “deeper” than 10 nm) can exit the sample;

2. Electrons colliding with the sample atom nuclei may be ‘backscattered’ to nearby 180 degrees (“elastic” process) (Fig. 3.1-7b). Production of *backscattered electrons* varies with atomic number – higher atomic number elements appear brighter (or scatter more effectively) than lower atomic number elements.

Secondary electrons indicate sample topography whereas backscattered electrons indicate specimen composition (Fig. 3.1-7c,d).

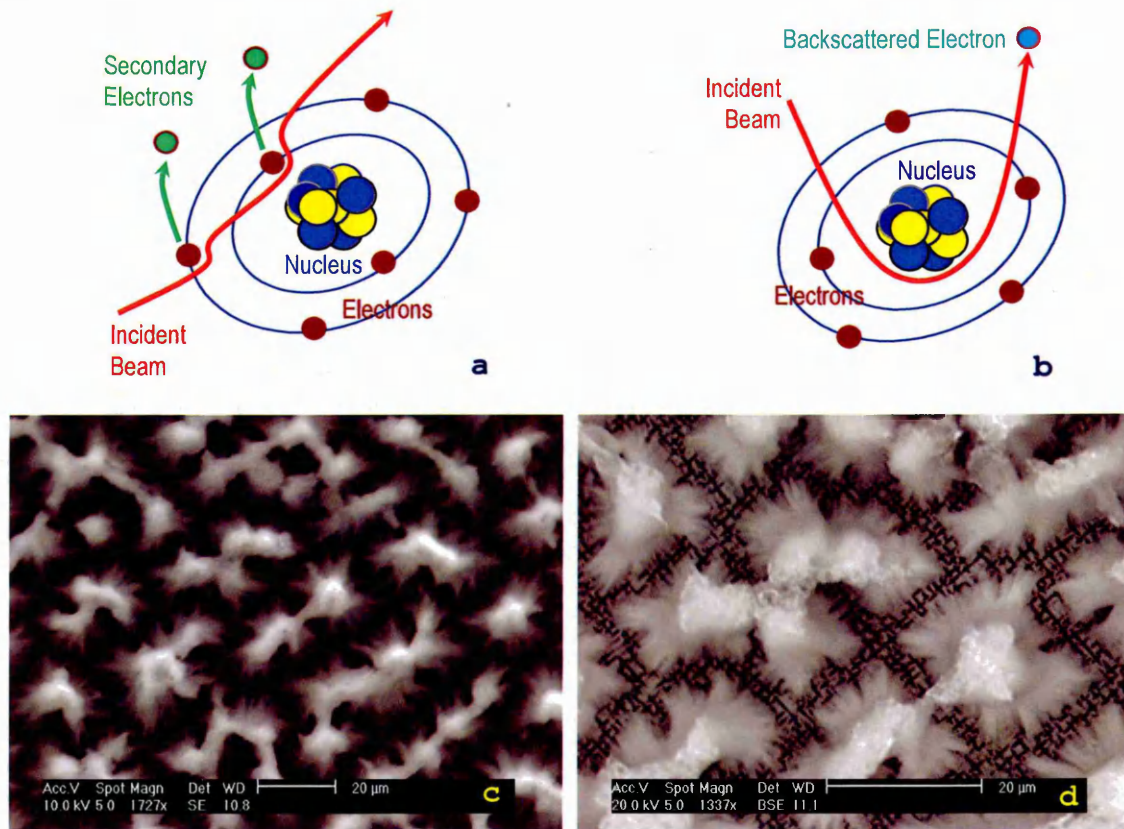


**Figure 3.1-7** SEM images of the same porous silicon sample formed by backscattered electrons (c) and secondary electrons (d).

SEM is often coupled with the X-ray analyser (energy dispersive X-ray spectroscopy (EDS)). The energetic electron beam-sample interactions generate X-rays that are characteristic of the elements present in the sample.

## 3.2 Ellipsometry Data Analysis Routine

### a. The M-2000V ellipsometer

The main scheme of ellipsometry is shown in Figure 3.2-1. The optical part comprises a light source, two polarising elements, called respectively polarizer and analyser, and a photodetector.

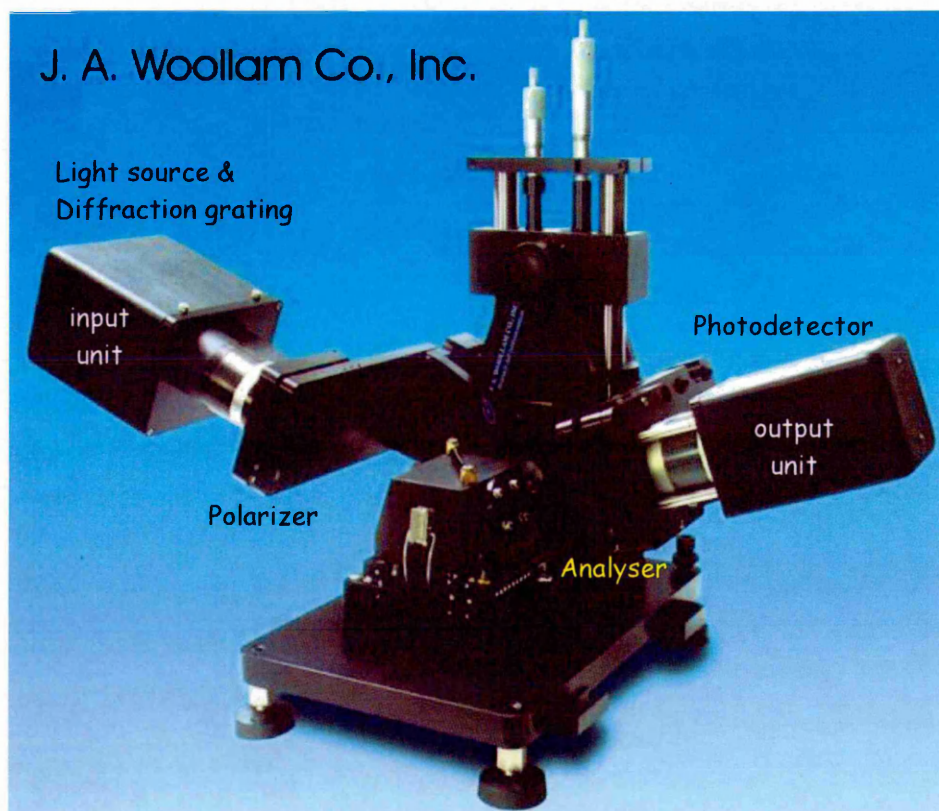


**Figure 3.2-1** The scheme of ellipsometry (after Ref.<sup>[14]</sup>).

The M-2000<sup>TM</sup>-V spectroscopic ellipsometer system used in this study is based on *advance diode array rotating compensator ellipsometer* technology from J. A. Woollam Co. The model “V” (for visible) ellipsometer uses a quartz tungsten halogen lamp (beam diameter from 2 mm to 5 mm and spectral range 370 – 1000 nm) and diffraction grating

based in one unit (referred to in Fig. 3.2-1 as "input unit") with the beam collimation optics, a fixed polarizer, and a compensator located on a continuously stepped motor.

The "output unit" consists of the stepper motor, which drives a stage which houses an analyser. There is also a four-quadrant detector (used for alignment of the system and sample) and a detector array.

The ellipsometer has a manually adjusted angle-of-incidence system (angles may vary from  $\sim 40^\circ$  to  $90^\circ$ ), which allows it to perform both *in situ* (dynamic) and *ex situ* (spectroscopic) measurements.

### *b. Ellipsometry data analysis routine*

Variable angle spectroscopic ellipsometry (VASE) performs the measurement of two positions of cross-polarization which can then be recalculated into two ellipsometric angles  $\Psi$  and  $\Delta$  as a function of both wavelength and angle of incidence<sup>[14]</sup>.  $\Psi$  and  $\Delta$  by themselves are not very useful in characterising a sample. Physical properties of the sample such as film thickness, optical constants and surface roughness are more informative. Ellipsometry does not directly measure these parameters; however, it measures functions of these parameters, namely  $\Psi$  and  $\Delta$ . Analytic expressions can be written for predicting  $\Psi$  and  $\Delta$  as functions of optical constants and the layer thickness.

Film thickness and optical constants can be extracted through a model based analysis exploiting electromagnetic theory (Fresnel reflection coefficients, Snell's law etc.)<sup>[15]</sup> (see §2.2.2). Figure 3.2-2 outlines this process.

Firstly, the experimental  $\Psi$  and  $\Delta$  data are collected within the spectral range at the desired angle of incidence. A model for the optical structure of the sample is then constructed. Secondly, the Fresnel equations (Eqs. 2.12 and 2.13, §2.2.2) along with the assumed model are used to predict the expected  $\Psi$  and  $\Delta$  values for each wavelength.

The third part of the process outlined in Figure 3.2-2 is to compare the measured  $\Psi$  and  $\Delta$  with the prediction of the model based on Fresnel equations, assuming the values of the optical constants and thicknesses. The analysis procedure is usually called *data fitting* because the adjustable model parameters are varied to find the best fit of the generated data

to the actual experimental data. The most common fit parameters are thicknesses ( $d$ ) and optical constants (e.g. refractive index  $n$  and extinction coefficient  $k$ ).

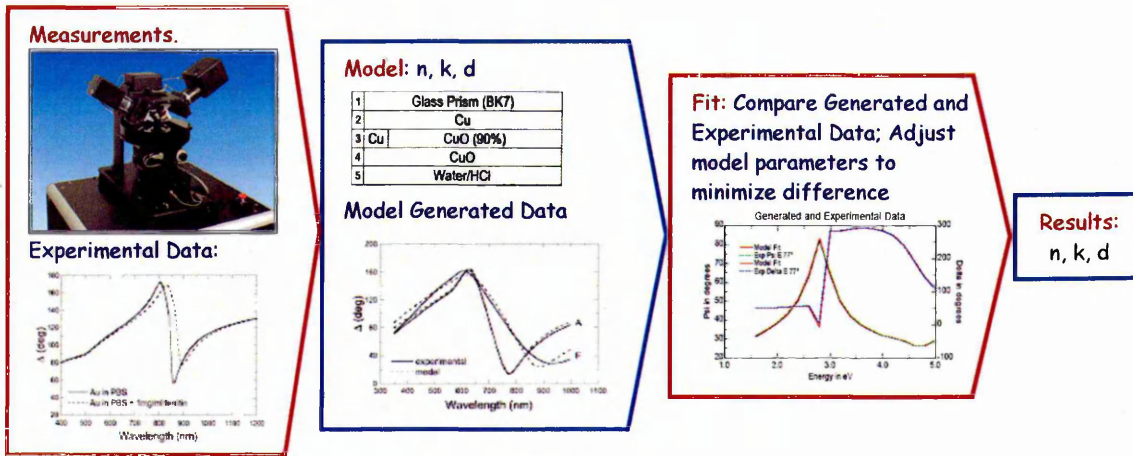


Figure 3.2-2 Data analysis procedure.

Various fitting algorithms have been introduced, but will not be described here, as they are well documented in Ref.<sup>[16]</sup>. The aim is to quickly determine the model which exhibits the difference between the measured and calculated  $\Psi$  and  $\Delta$  values.

The *mean squared error* (MSE) is used to quantify the difference between experimental and predicted data. The MSE can be normalized by the standard deviations on the experimental data, so the noisy data are weighted less heavily. A smaller MSE corresponds to a better model fit to data<sup>[15]</sup>. The MSE function commonly used is given as follows<sup>[17]</sup>:

$$MSE = \frac{1}{2N - M} \sum_{i=1}^N \left( \frac{\Psi_i^{Mod} - \Psi_i^{Exp}}{\sigma_{\Psi,i}^{Exp}} \right)^2 + \left( \frac{\Delta_i^{Mod} - \Delta_i^{Exp}}{\sigma_{\Delta,i}^{Exp}} \right)^2, \quad (3.3)$$

where  $N$  is the number of ( $\Psi$ ,  $\Delta$ ) pairs,  $M$  is the number of variable parameters in the model, and  $\sigma$  are the standard deviations on the experimental data points.

To minimise the MSE the method of iterative non-linear regression is used. Such regression analysis requires the correct model to achieve a good fit to the experimental data. If the model does not correctly represent the true sample structure, then good agreement between the experiment and model cannot be found, and the model needs to be revised. If the initial guess for a parameter value (thickness, for example) is too far from the

actual value, the regression algorithm can land on a secondary minimum in the MSE, thus giving wrong values for parameters  $d$ ,  $n$  and  $k$  (see Fig. 3.2-3).

In Figure 3.2-3, there are a few MSE minima shown, but only one “global” minimum gives the correct thickness. To ensure that the true “global” minimum MSE is found, the regression algorithm can be started at different initial parameter values.

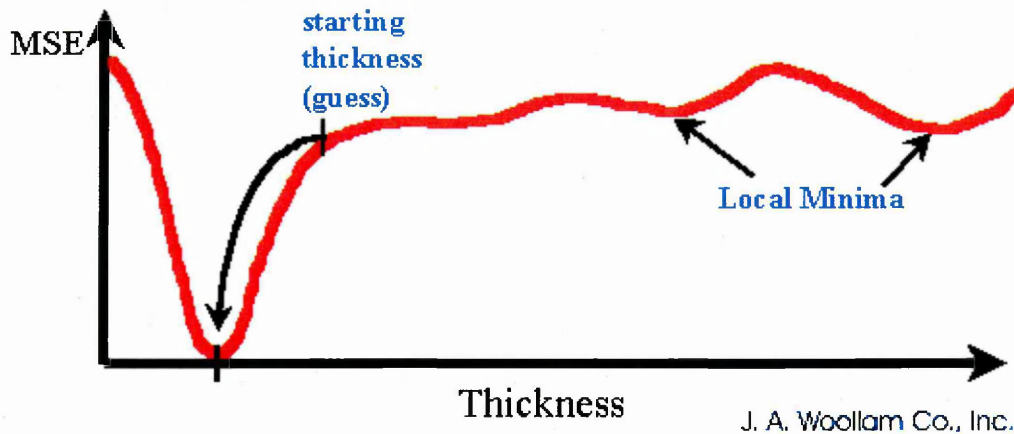


**Figure 3.2-3** Illustrations of secondary MSE minima (taken from Ref.<sup>[15]</sup>).

Ellipsometry has become a very popular instrument for characterisation of thin films and is a powerful analytical tool in chemical sensing and biosensing. However, its application is limited by the experimental difficulties of the light beam passing through the investigated medium. The variations of the medium refractive index can seriously affect the measurements (especially during the *in situ* investigation of the kinetics of chemical reactions). The cell design is quite complicated and requires the use of non-polarising transparent windows.

*c. Model layers used in this study*

*1. Bruggemann effective medium approximations model layer*

There are a number of models described in the literature for the calculation of the effective optical constants of a mixture of two or three materials, known as *effective medium approximations* (EMA). The usual interpretation of the EMA theory is that small

particles of one material are suspended in a matrix of the host material. The simplest EMA model is to simply linearly interpolate between the constituent optical constants, as shown in Eq.(3.4):

$$\tilde{\epsilon} = f_A \tilde{\epsilon}_A + f_B \tilde{\epsilon}_B + f_C \tilde{\epsilon}_C, \quad (3.4)$$

where  $\tilde{\epsilon}$  is the effective complex dielectric function of the mixture,  $f_A$ ,  $f_B$ , and  $f_C$  are the volume fractions (ranging from zero to one) of each constituent material;  $\tilde{\epsilon}_A$ ,  $\tilde{\epsilon}_B$  and  $\tilde{\epsilon}_C$  are the complex dielectric functions of the constituent materials. The Eq. (3.4) is true for three constituent EMA models (for two component EMA models  $f_C$  is fixed at zero). The linear interpolation EMA is not highly accurate, but is often used for graded layers to reduce calculation time.

The Bruggemann EMA makes the self-consistent choice of the host material complex dielectric function equal to the final effective complex dielectric function of the multi-constituent material. The Bruggemann EMA requires the numerical solution of the following equation, valid for three constituents, or for two constituents if  $f_C$  is fixed at zero:

$$f_A \frac{\tilde{\epsilon}_A - \tilde{\epsilon}}{\tilde{\epsilon}_A + 2\tilde{\epsilon}} + f_B \frac{\tilde{\epsilon}_B - \tilde{\epsilon}}{\tilde{\epsilon}_B + 2\tilde{\epsilon}} + f_C \frac{\tilde{\epsilon}_C - \tilde{\epsilon}}{\tilde{\epsilon}_C + 2\tilde{\epsilon}} = 0. \quad (3.5)$$

This is a complex equation and can yield an infinite number of solutions, such that the VASE software user must correctly choose the appropriate (physical and reasonable) solution.

## 2. *Cauchy model layer*

The most commonly used layer for the calculation of the optical parameters and thickness of the transparent dielectric materials is the Cauchy layer. Over the part of the spectral range for dielectrics and semiconductors, the index of refraction  $n$  and extinction coefficient  $k$  can be represented by a slowly varying function of the wavelength  $\lambda$  and exponential absorption tail, respectively:

$$n(\lambda) = A + \frac{B}{\lambda^2} + \frac{C}{\lambda^4}, \quad (3.6)$$

---

$$k(\lambda) = \alpha \exp\left(\beta \left(12400 \left(\frac{1}{\lambda} - \frac{1}{\gamma}\right)\right)\right) \quad (3.7)$$

The six parameters in this dispersion model are A, B, C, the extinction coefficient amplitude  $\alpha$ , the exponent factor  $\beta$ , and the band edge  $\gamma$ . Each of these parameters except for the band edge can be defined as a variable fit parameter.

### 3.3 Ellipsometric Study of Adsorption of Bovine Serum Albumin into Porous Silicon

The use of spectroscopic ellipsometry for studying porous silicon has been reported in literature (see chapter 2, section 2.1 and corresponding references). These studies have revealed many important aspects regarding the application of PS in biosensors, biochips and biomaterials for medical implants.

However, due to experimental difficulties of the ellipsometric measurements on PS, such as depolarisation and diffused scattering of the incident light, the majority of research work has been done on microporous PS samples with quite shallow (few micrometers deep) pores in contact with either vacuum or dry air<sup>[18]</sup>.

The adsorption of proteins was mostly studied *ex situ* with ellipsometric measurements performed on dry PS samples before and after the protein adsorption<sup>[19]</sup>. However, the *in situ* registration of adsorption of protein and further biochemical reactions is more promising for bio-sensing.

In this work, the adsorption of bovine serum albumin (BSA) as a common protein, into the PS layers, was studied *in situ* at solid/liquid interface with the method of spectroscopic ellipsometry and subsequent fitting to the Bruggemann effective medium approximations (EMA) model. The influence of polyelectrolytes on the protein adsorption into the porous silicon has also been investigated. The microstructure of PS was modelled using the EMA model.

#### 3.3.1 Experimental set-up for porous silicon formation

Porous silicon layers, investigated in this thesis, were prepared by a method of anodization of *p*-type and *n*-type <100> Si wafers of the resistivity in the range of 2 – 6.25 ( $\Omega\cdot\text{cm}$ ) in the electrolyte containing hydrofluoric acid (HF).

The electrolyte was prepared by adding 49% HF to the (1:1) ethanol/water mixture up to a desired concentration of about 20%. The anodization of the Si surfaces was carried out at positive DC bias applied to the Si electrode with a current density of about  $25 - 30 \text{ mA}\cdot\text{cm}^{-2}$ . The etching time was  $7 \pm 2$  minutes. The applied anodic current density and etching time were monitored, controlled, and kept at a particular constant level required during the process.

The experimental set-up used for the PS formation is sketched in Figure 3.3-1. The anodization cell is made of a highly acid-resistant polymer, namely polytetrafluoroethylene (PTFE or Teflon<sup>a</sup>). The silicon sample was sealed against the Teflon cell through a rubber O-ring, so that the front side of the silicon wafer was in contact with the electrolyte. The spiral *cathode* of the anodization cell is made of chemically inert metal platinum (Pt) immersed in the electrolyte and positioned about 2 cm from the silicon wafer. The Si surface itself serves as the *anode*.

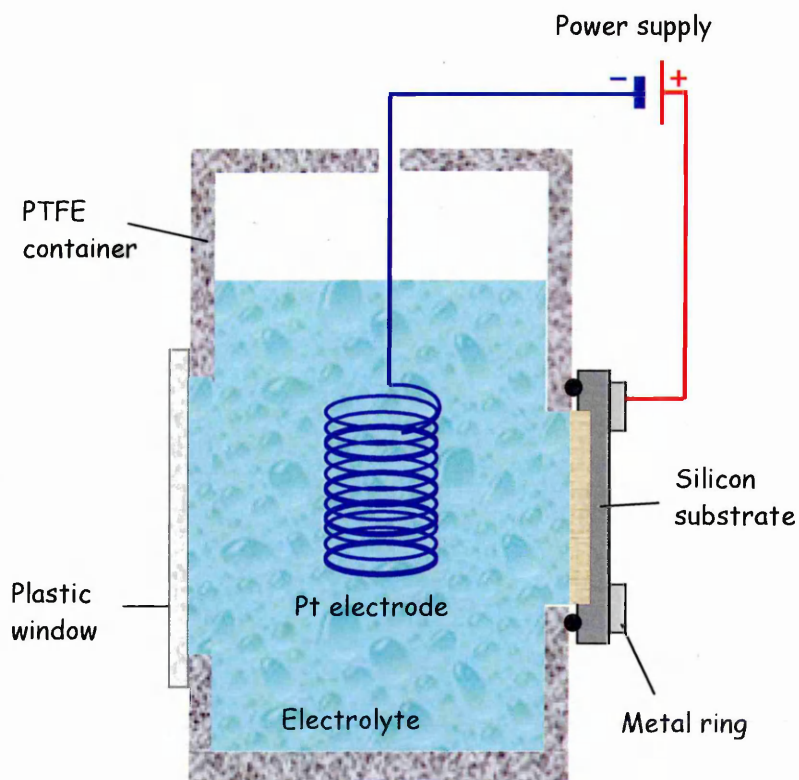


Figure 3.3-1 The set-up for the formation of porous silicon.

<sup>a</sup>Teflon is the trademarked name of polytetrafluoroethylene (PTFE).

In the case of n-type silicon, the holes necessary for pore formation were generated by illuminating the front side of the sample with a 300 W solar simulator lamp (Bentham 605, type IL 7S-X). In order to provide uniform electrical potential and thus homogeneous current density across the sample, the backside of the silicon wafers were coated with a thin layer of conductive silver paint. The electrical contact between the Si wafer and a power supply was provided via a metal ring.

Following anodization, the samples were rinsed with Millipore water for 10 min and then in a stop-solution (acetone or ethanol) for 5–7 min, rinsed again with Millipore water before being finally dried with nitrogen gas. The resulting PS samples had a circular shape with the area of about  $2.54\text{-cm}^2$ .

### *Methods for morphology study of porous silicon layers*

The morphology of PS samples was studied by SEM and AFM. The Philips XL40 SEM instrument was used in the secondary electron emission mode. A typical accelerating voltage was 10–15 kV.

The AFM study was carried out using the NanoScope IIIa instrument equipped with  $\text{Si}_3\text{N}_4$  tips of 4 nm radius. The AFM pictures of the PS samples were obtained in a tapping mode and at a slow scan rate of about  $0.1\text{--}0.2\text{ sec}^{-1}$ . The latter was chosen because of the high surface roughness of PS samples previously observed with the SEM on a larger scale.

The pore size was determined using the SEM and AFM data. The cross-section SEM images allowed the evaluation of the pore depth, and thus the thickness of the PS layers.

### 3.3.2 Cell design for ellipsometric measurements

The ellipsometric measurements were performed *in situ* in a specially designed cell using a rotating analyzer ellipsometer M2000-V (J. A. Woollam Co.) operating in the 370–1000 nm wavelength region. The cell of  $2.2\text{ cm}^3$  in volume, shown

schematically in Figure 3.3-2, has two transparent windows, made of standard microscopic glass slides (from Menzel-Glaser<sup>®</sup>), providing light incidence at a fixed angle of  $68.13^\circ$ .

Two plastic tubes (inlet and outlet) allowed the injection of different solutions into the cell. The samples were sealed against the cell through a rubber O-ring, so that the front side of the PS layer was in contact with the solution. The spectrum took  $\sim 2$  minutes to acquire.

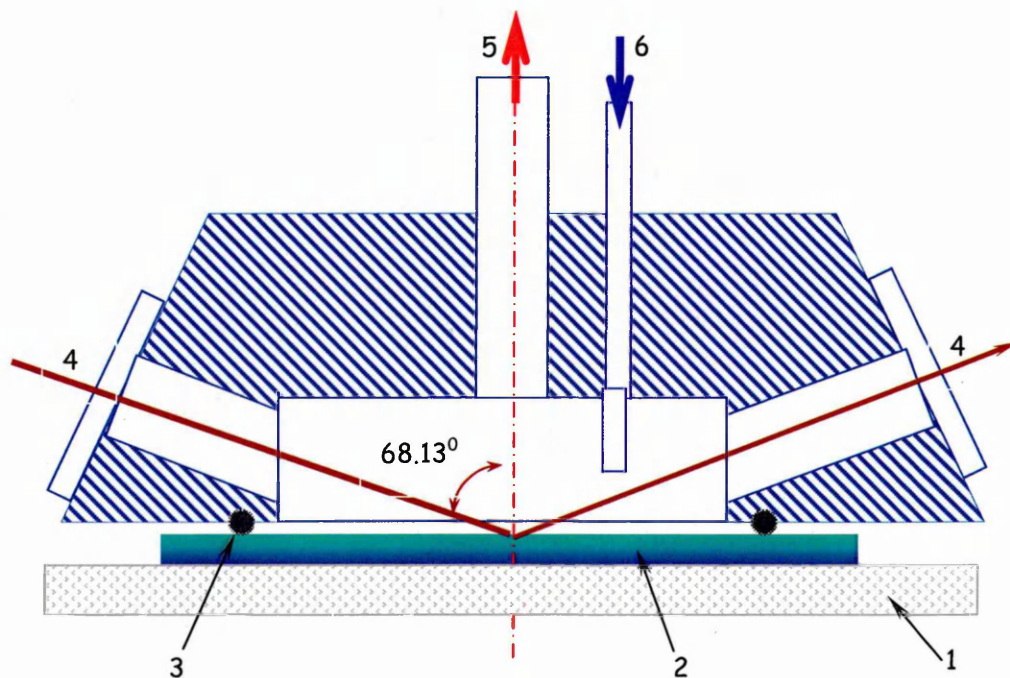


**Figure 3.3-2** Cross-section of the cell for ellipsometric measurements: *1* – glass holder; *2* – the sample; *3* – rubber O-ring; *4* – glass windows; *5* – outlet tube; *6* – inlet tube.

### 3.3.3 Chemicals

Chemicals used in this research for the ellipsometric study of the adsorption of BSA into PS are listed in Table 3.3-1. All chemicals were obtained from Sigma-Aldrich<sup>®</sup> and used as received without further purification.

A buffer solution was made of Trizma-base, with its pH adjusted by adding an appropriate amount of HCl (referred to as Trizma/HCl).

**Table 3.3-1** Chemicals used for ellipsometric study of the adsorption of BSA into PS.

<i>Reactive</i>	<i>Chemical formula</i>	<i>Molecular weight</i>	<i>Concentration and pH used</i>
<i>tris(hydroxymethyl)-aminomethane hydrochloride</i> Trizma-base buffer solution	$C_4H_{11}NO_3 HCl$ ;	121.1 g/mol	35 mM/l pH 7.5
<i>Bovine Serum Albumin (BSA)</i>		~66000 g/mol	1 mg/ml in Trizma/HCl buffer pH 8.0
<i>Poly(sodium 4-styrenesulfonate) (PSS)</i>	$[C_8H_7NaO_3S]_n$	Average MW ~77400 g/mol	2 mg/ml in Millipore water pH 5.5
<i>Poly(allylamine hydrochloride) (PAH)</i>	$[-CH_2CH(CH_2NH_2 \cdot HCl)-]_n$	Average MW ~70000 g/mol	2 mg/ml in Millipore water pH 4.0

### 3.3.4 Experimental procedure for ellipsometric study of the adsorption of BSA into PS

The ellipsometric study of adsorption of proteins in PS was carried out in two regimes:

1. *static* ellipsometric spectral measurements performed before and after adsorption of different species but always in the same aqueous environment, i.e. Trizma/HCl buffer solution;

2. *dynamic* measurements, in which the whole spectrum was registered *in situ* during the injection of different solutions into the cell.

The procedure for the *static* ellipsometric study of adsorption of BSA into the PS was as follows. Firstly, the cell was filled with the Trizma/HCl buffer solution, and the ellipsometric spectrum was registered. Then the cell was filled with BSA solution in Trizma/HCl buffer and kept there for five minutes. The cell was then flushed several times with Millipore water in order to remove the excess of protein and finally, filled again with the Trizma/HCl buffer solution; the ellipsometric spectrum was measured once more.

The adsorption of polyelectrolytes, namely *polyallylamine hydrochloride* (PAH) and *polysterylsulphonate sodium salt* (PSS), and their effect on the immobilisation of BSA were studied in the same way using 2 mg/ml aqueous solutions of PAH and PSS.

### 3.3.5 Influence of polyelectrolytes on BSA adsorption

The idea of stabilisation of the surface of PS by its chemical modification<sup>[20]</sup> was further developed here by using the adsorption of polyelectrolytes. Both types of polyelectrolytes, i.e. polycationic (PAH) and polyanionic (PSS), are supposed to form strong Coulomb interaction with the PS surface containing both OH<sup>-</sup> and H<sup>+</sup> groups as respective binding centres.

To study the influence of polyelectrolytes on BSA adsorption the following experimental sequence was chosen:

1. Ellipsometric spectral measurements of PS in Trizma/HCl buffer solution.
2. Adsorption of either PAH or PSS for 10 – 15 min by filling the cell with the corresponding polyelectrolyte solution followed by thorough flushing of the cell with Millipore water.
3. Filling the cell with Trizma/HCl buffer and ellipsometric spectral measurements.
4. Adsorption of BSA (as described earlier) followed by washing out of excessive non-specifically bound BSA.
5. Ellipsometric measurements in Trizma/HCl buffer.

### 3.3.6 Modelling and fitting routine

The analysis of experimental spectra of the ellipsometric angle  $\Delta$  was carried out by fitting the results to a five-layer model using WVASE32<sup>®</sup> software<sup>[21]</sup>. The model consists of an aqueous ambient and Si-substrate as top and bottom layers, respectively and three inner layers represented by the EMA model. The constant value of 1/3 was used as a default depolarization factor, as recommended in Ref.<sup>[21]</sup> for multilayer EMA models.

The mathematical accuracy of WVASE32<sup>®</sup> fitting is very high and exceeds the reasonable physical limits for the parameters obtained. In order to find the real accuracy the fitting was performed several times for every sample yielding slightly different values. Thus, the accuracy of thicknesses and material contents was found to be in the range of 5 – 7%.

Since the cell windows cause a constant phase shift between *s*- and *p*-components of polarized light, the experimental ellipsometric data were normalized by subtracting the  $\Delta(\lambda)$  spectra associated with glass windows. The latter was found for every sample by comparing two  $\Delta(\lambda)$  spectra measured in air: firstly, without the cell, secondly, in the cell.

### 3.4 Total Internal Reflection Ellipsometry Detection of Low Molecular Weight Environmental Toxins

The main goal of this part of the work was to develop an experimental procedure for the registration of low molecular weight environmental toxins, particularly *T-2 mycotoxin*<sup>a</sup>, which is regarded as an extremely hazardous compound and, therefore, potential bio-warfare agent. Because of the high toxicity of *T-2 mycotoxin*, it was first decided to develop an analysis routine using much less toxic analogues, such as commercial herbicides *simazine*<sup>b</sup> and *atrazine*<sup>c</sup>.

A traditional immune assay approach, which is based upon specific binding of the above toxins to respective antibodies, was chosen for the toxins' registration in conjunction with the optical technique of surface plasmon resonance (SPR). The method of SPR is very common for immune analyses, since specific binding of relatively large immune components (antibodies or antigens) causes a noticeable shift of the plasmon resonance. However, as has been mentioned in chapter 2.2, this optical technique struggles with the registration of low molecular weight compounds (in the range of several hundred atomic units).

Alternatively, a method of total internal reflection ellipsometry (TIRE) promises much higher sensitivity, which may be sufficient for the registration of relatively small molecules of *simazine*, *atrazine*, and *T-2 mycotoxin*.

This part of the work represents the descriptions of experimental procedures for the registration of *simazine* and *atrazine* using both SPR and TIRE methods. Later, the established measurements' routine will be extended towards the registration of *T-2 mycotoxin* with a more sensitive technique.

The method of TIRE has been applied for registration of the next analyte of interest *nonylphenol*<sup>d</sup>, a member of the group of alkylphenols. Alkylphenols are toxic, carcinogenic, and have recently been found to have oestrogen mimicking behavior; for

---

<sup>a</sup> molecular weight of *T-2 mycotoxin* is 466.6 g/mol

<sup>b</sup> molecular weight of *simazine* is 201.7 g/mol

<sup>c</sup> molecular weight of *atrazine* is 215.7 g/mol

<sup>d</sup> molecular weight of *nonylphenol* is 220.4 g/mol

these reasons their registration in natural water resources is of great importance nowadays.

Immobilization of antibodies was realized by means of electrostatic self-assembly, a method which proved to be very successful for different bio-molecules and was thus adopted in different research groups (see review article by Harada and Kataoka<sup>[22]</sup>, for instance).

### 3.4.1 Surface plasmon resonance: experimental set-up

A Kretschmann type SPR experimental set-up as shown in Fig.3.4-1 was exploited in the current study.

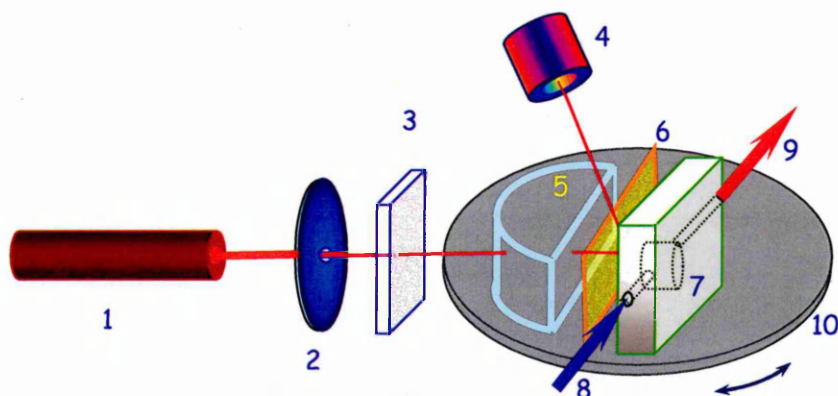


**Figure 3.4-1** A simplified scheme of the experimental set-up for SPR measurements: *1* – He-Ne laser; *2* – aperture; *3* – polarizer; *4* – photo-detector; *5* – semi-cylindrical lens; *6* – gold coated glass slide; *7* – flow reaction cell with inlet (*8*) and outlet (*9*) tubes. Elements *5* – *9* are placed on a rotating stage *10*.

The *p*-polarized HeNe laser beam ( $\lambda = 632.8 \text{ nm}$ ) traveled through a semi-cylindrical prism to incident on the gold coated glass slide attached to the back of the prism. The prism was brought into optical contact with the glass slide via an index-matching liquid. The thickness of the gold layer deposited on the glass slide was about 50 nm. The cell was attached to the gold coated glass slide via a rubber O-ring; it had input and output tubes enabling the injection of different liquids into the cell.

### 3.4.2 Total internal reflection ellipsometry: experimental set-up

The TIRE experimental set-up (shown in Fig. 3.4-2) was based on the spectroscopic ellipsometer M2000-V (J. A. Woollam Co.) exploiting the rotating compensator principle, and operating in the 370 – 1000 nm wavelength range. The addition was the prism, which allowed the coupling of the light beam into the thin metal film, deposited on the glass slide attached to it. Similarly to the SPR, a chromium/gold coated glass slide was brought into optical contact with the prism via an index matching fluid. The choice of the prism was dictated by the conditions of total internal reflection on the glass/medium interface; a  $68^\circ$  prism was used for the measurements in aqueous media.

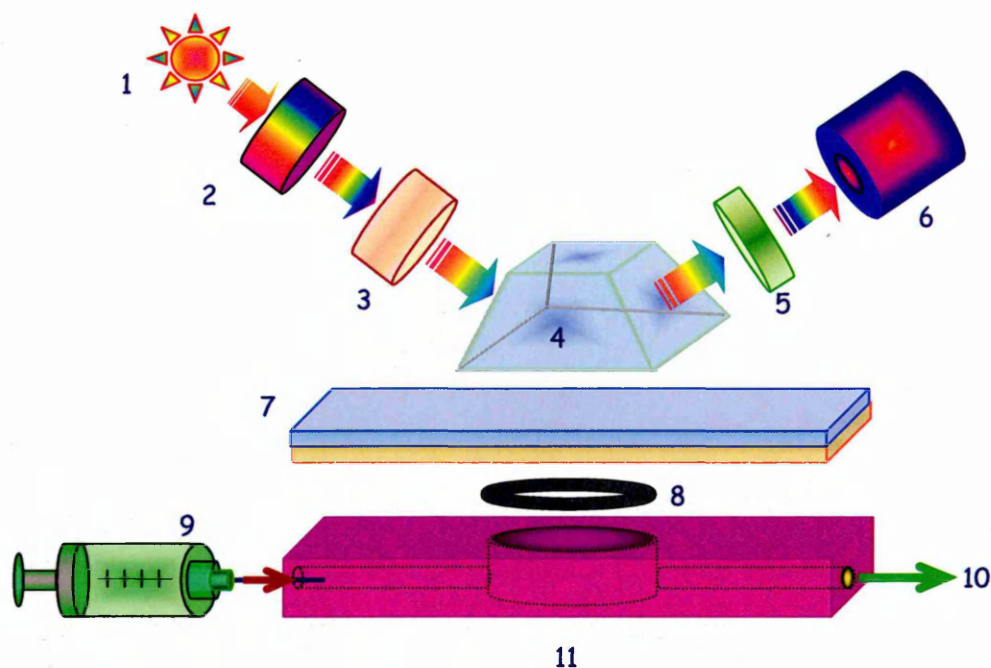


**Figure 3.4-2** The experimental setup for the total internal ellipsometric measurements: *1* – light source; *2* – diffraction grating; *3* – polarizer; *4* –  $68^\circ$  prism; *5* – analyser; *6* – photodetector; *7* – glass slide with chromium–gold coating; *8* – rubber O-ring; *9* – syringe serves as inlet tube; *10* – outlet tube; *11* – the cell.

The measurements were performed *in situ* in a specially designed cell having a volume of about  $1.5 \text{ cm}^3$ , attached at the bottom of a  $68^\circ$  trapezoidal glass prism to the chromium/gold-coated side of a glass slide. The cell was sealed to the slide via a rubber

O-ring and had input and output tubes enabling the injection of different liquids into the cell and, therefore, performing different chemical (bio-) reactions on the surface.

The substrates for TIRE measurements were prepared by the consecutive thermal evaporation of 3–5 nm of chromium and 25–30 nm of gold on clean microscopic glass slides without breaking the vacuum of  $10^{-6}$  Torr, as was recommended in Ref.<sup>[23]</sup>. The presence of the chromium layer improved the adhesion of gold film to the glass substrate.

### 3.4.3 Samples preparation

The following organic and bio-chemicals were used in the current study:

- 10 mM/l *Trizma-base/HCl buffer solution* (pH 7.56) was used for the preparation of solutions of all bio-chemicals except polyelectrolyte;
- 2 mg/ml solution of *poly(allylamine hydrochloride)* (PAH);
- *Protein A* (0.02 mg/ml) from *Staphylococcus aureus*;

All of the above chemicals were obtained from the Sigma–Aldrich®.

- *Antiserums* to *simazine* (*as-simazine*), *atrazine* (*as-atrazine*) and *nonylphenol* were acquired from the Institute of Biochemistry, Kiev (Ukraine);
- *Antibodies* to *T-2 mycotoxin*. Two types of antibodies to *T-2 mycotoxin* were used: *polyclonal antibodies* (poly-AB) acquired from the Institute of Biochemistry, Academy of Science of Ukraine, and *monoclonal antibodies* (mono-AB) purchased from Sigma–Aldrich® (monoclonal anti-T-2 toxin, clone T-2-50);
- The respective toxins, namely *simazine*, *atrazine* and *T-2 mycotoxin* were also obtained from the Institute of Biochemistry, Academy of Science of Ukraine. *Nonylphenol* was purchased from Sigma-Aldrich®.

Detailed information for analytes of interest is given in Table 2.4-2.

The specific reactions of binding *atrazine*, *simazine*, and *T-2 mycotoxin*, as well as previous stages of adsorption, were studied *in situ* with both SPR and TIRE methods. The specific reaction of binding *nonylphenol* was studied *in situ* with the method of TIRE only.

### 3.4.4 Measurements routine

The measurements routines for the SPR and TIRE techniques were absolutely identical; for that reason, only the experimental procedure for TIRE measurements will be given in detail below.

In TIRE experiments all the steps of adsorption were performed in the cell by injecting the solutions required in the following sequence with the syringe:

*Trizma/HCl buffer solution* → *PAH* → *protein A* → *antibodies* → *toxins*.

The TIRE measurements were carried out after each adsorption step, and always in the same aqueous environment, i.e. *Trizma/HCl* buffer solution (pH 7.5). Intermediate washing in *Trizma-base/HCl* buffer water was carried out after each adsorption step, apart from that after adsorption of *PAH* when Millipore water was used.

The incubation time of 15 min was used for the majority of the adsorption steps, and TIRE spectra were recorded after each step of adsorption in the cell filled with 10 mM of *Trizma-base/HCl* buffer solution.

The following routine was used for adsorption of bio-chemicals on the surface of chromium/gold- (Cr/Au) and pure gold- coated glass slides for TIRE and SPR experiments, respectively.

1. The cell was filled with *Trizma/HCl* buffer solution, and the initial ellipsometric spectrum was measured.
2. A layer of *PAH* was electrostatically adsorbed on the surface of the Cr/Au coated glass slide from its 2 mg/ml solution in Millipore water. The sample was kept in the above solution for 15 min and then rinsed several times with Millipore water.
3. A layer of *protein A* was electrostatically adsorbed on the *PAH* layer. Molecules of *protein A* were used as intermediate agents' for the orientation of antibodies with their binding sites towards the solution, as previously was described by Starodub et al.<sup>[24]</sup>.
4. A layer of respective *antibodies* to the toxin (see Table 3.4-1) was deposited on top of the *protein A* layer. Typical incubation time was 15 min.

5. Then the coating was exposed to solutions with different concentrations of the respective *toxin* (see Table 3.4-1).

**Table 3.4-1** Toxins, antibodies and their concentrations used for TIRE measurements.

<i>Toxin</i>	<i>Concentration</i>	<i>Antibody</i>	<i>Concentration</i>
<i>simazine</i>	0.002 mg/ml	<i>as-simazine</i>	0.02 mg/ml
<i>atrazine</i>	0.001 mg/ml	<i>as-atrazine</i>	0.0175 – 0.02 mg/ml
<i>T-2 mycotoxin</i>	0.15 ng/ml; 1.5 ng/ml; 7.5 ng/ml; 30 ng/ml; 150 ng/ml; 600 ng/ml; 1500 ng/ml; 6000 ng/ml	<i>polyclonal</i> and <i>monoclonal</i> antibodies	0.02 mg/ml 0.025 mg/ml
<i>nonylphenol</i>	1.2 ng/ml; 3.7 ng/ml; 7.5 ng/ml; 15 ng/ml; 20 ng/ml; 30 ng/ml 63 ng/ml; 100 ng/ml; 125 ng/ml; 200 ng/ml; 250 ng/ml; 1000 ng/ml	<i>nonylphenol</i> <i>antiserum</i>	0.025 mg/ml

*Simazine* and *atrazine* were diluted in 20 mM Trizma/HCl buffer solution (pH 7.45 – 7.56). The initial solution of *T-2 mycotoxin* in methanol was diluted with 10 mM Trizma/HCl buffer (pH 7.5) to obtain desired concentrations from 0.15 ng/ml to 6000 ng/ml. In order to wash out non-specifically bound *T-2 mycotoxin*, samples for TIRE measurements were washed with a 30% methanol/water mixture and then in Trizma/HCl buffer solution.

The initial *nonylphenol* solution in acetonitril was diluted with 10 mM Trizma/HCl buffer (pH 7.56) to obtain different concentrations from 1.2 to 1000 ng/ml. In order to wash out non-specifically bound *nonylphenol* molecules, samples were washed with 30% acetonitril/water mixture and then in buffer solution for TIRE measurements.

### 3.4.5 Kinetics measurements

Not only the resulting shift in the ellipsometric spectra  $\Psi(\lambda)$  and  $\Delta(\lambda)$  but also the time evolution, i.e. kinetics of  $\Psi$  and  $\Delta$ , provide important information. For instance, analysis of the kinetics allows calculation of the adsorption and desorption coefficients as well as the association constant of the reaction.

The kinetics of binding of *nonylphenol* and *T-2 mycotoxin* to respective antibodies were studied by measuring TIRE spectra every 1 – 20 seconds (depending on the duration of the kinetics scan) during the exposure to *nonylphenol* (or *T-2 mycotoxin*) solution (typically for 15 – 20 min). Then time dependences of either  $\Psi$  or  $\Delta$  can be obtained at selected wavelengths. Typically, the time dependence of  $\Psi$  was used, since  $\Psi(\lambda)$  spectra give a wider linear range as compared to  $\Delta(\lambda)$  spectra.

Such measurements were repeated for different concentrations of *nonylphenol* and *T-2 mycotoxin*. The analysis of binding kinetics was done following the procedure described in chapter 2, section 2.5.

### 3.4.6 Samples for AFM

Several samples (listed below) were prepared for the AFM study of *T-2 mycotoxin* binding following a similar routine to the one described in detail above. Monoclonal antibodies to *T-2 mycotoxin* were immobilized on the surface of Cr/Au coated glass slides via the layers of PAH and *protein A*. Then *T-2 mycotoxin* molecules were specifically bound from its 500 ng/ml solution in Trizma/HCl buffer followed by washing out the non-specifically bound *T-2 mycotoxin* molecules in 10% methanol, rinsing in Millipore water, and drying with nitrogen gas. AFM measurements were carried out on different samples after each adsorption step:

- sample №1 bare Cr/Au surface deposited on glass slide.
- sample №2 *protein A*.
- sample №3 PAH + *protein A*.
- sample №4 PAH + *protein A* + monoclonal antibodies to *T-2 mycotoxin* (mono-AB).

sample №5 PAH + *protein A* + mono-AB + *T-2 mycotoxin*.

The same procedure was applied for samples prepared for the AFM study of *nonylphenol* binding. The antiserum to *nonylphenol* was immobilized on the surface of Cr/Au coated glass slides via the layer of PAH and *protein A*. Then *nonylphenol* molecules were specifically bound from its 20 ng/ml solution in Trizma/HCl buffer solution followed by washing out the non-specifically bound *nonylphenol* molecules in 10% acetonitril, rinsing in Millipore water, and drying with nitrogen gas. AFM measurements were carried out on different samples after each adsorption step:

sample №6 PAH + *protein A* + antiserum to *nonylphenol*.

sample №7 PAH + *protein A* + antiserum to *nonylphenol* + *nonylphenol*.

AFM images of adsorbed layers were taken using the Nanoscope IIIa instrument operating in tapping mode with the oscillation frequency in the range of 280 – 310 kHz and the scan rate of about 0.85 Hz. The tip radius was less than 7 nm (probe type was TAP300/RTESP, Veeco). The main focus of the AFM study was on observation of general features and mean roughness of the samples.

### 3.4.7 Real samples

The method of TIRE was applied for the detection and quantification of the *T-2 mycotoxin* in food samples. Eight samples, namely: fresh<sup>a</sup> and mouldy bread; stale and mouldy buckwheat; mouldy fodder and maize; and fresh and stale muesli were immersed for 24 hours in 25% acetonitril solution (5 g of sample in 25 ml of acetonitril : water mixture). The following routine was used for detection of the *T-2 mycotoxin* in the above extracts:

1. The cell was filled with *Trizma/HCl buffer* solution and the initial ellipsometric spectrum was measured.

---

<sup>a</sup> “Wholemeal” bread obtained from Tesco supermarket. The sample preparation date was the 3 days after the “best before” date.

2. A layer of *PAH* was electrostatically adsorbed on the surface of the Cr/Au slide from its 2 mg/ml solution in Millipore water.
3. A layer of *protein A* was electrostatically adsorbed on the PAH layer.
4. A layer of *monoclonal antibodies* to *T-2 mycotoxin* was deposited on top of the *protein A* layer.
5. Then the coating was exposed to solutions (25% acetonitril + 75% Trizma/HCl buffer) with different food extracts.

The incubation time of 15 min was used for all adsorption steps, and TIRE spectra were recorded after each step of adsorption in the cell filled with 10 mM Trizma-base/HCl buffer solution with pH  $7.5 \pm 0.1$ . In addition, after depositions of the food extract the cell was rinsed with 25% acetonitril in order to wash out non-specifically bound *T-2 mycotoxin*.

## 3.5 Electrostatic Self-Assembly Technique for Protein Immobilisation

### *a. Introduction to the electrostatic self-assembly technique*

In biosensors, the biological component has to be properly deposited onto the transducer. This process is known as immobilization<sup>[25]</sup>. Several well established methods of immobilization of proteins<sup>[26, 27]</sup> are widely exploited, such as physical adsorption, covalent bindings<sup>[28]</sup>, entrapment<sup>a[29]</sup> and a recently developed electrostatic self-assembly<sup>[30, 31, 32]</sup> technique (also known as layer-by-layer assembly).

The purpose of any immobilization method is to retain maximum activity of the biological component on the surface of the transducer. The selection of an appropriate immobilization method depends on the nature of the biological element, the type of the transducer used, the properties of the analyte and the operating conditions of the biosensor<sup>[33]</sup>.

The electrostatic self-assembly (ESA) technique is based on consecutive adsorption steps of oppositely charged polyelectrolytes. It leads to the formation of multilayer assemblies on a solid surface. The ESA deposition has been shown to be a simple and versatile method for assembling thin films<sup>[34, 35, 36]</sup>. By using the ESA technique, the multilayer films with well defined thickness, composition, and structure can be deposited onto the substrates, and the thickness of ESA films can be controlled with nanoscale precision<sup>[37]</sup>.

Information about the structure of a multilayer film constructed by using the ESA technique can be gathered by various measurement methods such as quartz crystal microbalance (QCM), reflection spectroscopy, surface plasmon resonance (SPR), atom force microscopy (AFM), scan electron microscopy (SEM), ellipsometry<sup>[38, 39, 40]</sup>, and planar waveguide<sup>[41]</sup>. A mercury probe technique was employed by Nabok and co-workers<sup>[42]</sup> for studying the electrical characteristics of polyelectrolyte self-assembled films.

---

<sup>a</sup> In this method the biomaterial is mixed with a monomer solution, which is then polymerised to a gel, trapping the biomaterial

### b. Formation of ESA films

Polyelectrolytes are polymers whose repeating units bear either cationic or anionic groups. Polyelectrolyte properties are similar to both electrolytes (salts) and polymers (high molecular weight compounds). Like salts, their solutions are electrically conductive. Like polymers, their solutions are often viscous<sup>[43]</sup>.

Polyelectrolytes dissociate in water into polymer chains containing ionic groups and counterions. They form as polycation or polyanion solutions, depending upon the charge of the ionic group. Attraction of different charges between the polycation (positive) and polyanion (negative) become a driving force for polymer film formation through the ESA technique<sup>[44]</sup>. Electrostatic attraction allows the formation of multilayered films on a substrate surface by sequential dipping of the electrical charged substrate into the polyanion and polycation solutions. The four step basic sequence for the polyelectrolyte layer ([polyanion/polycation]<sub>n</sub>) deposition is illustrated by Fig. 3.5-1.

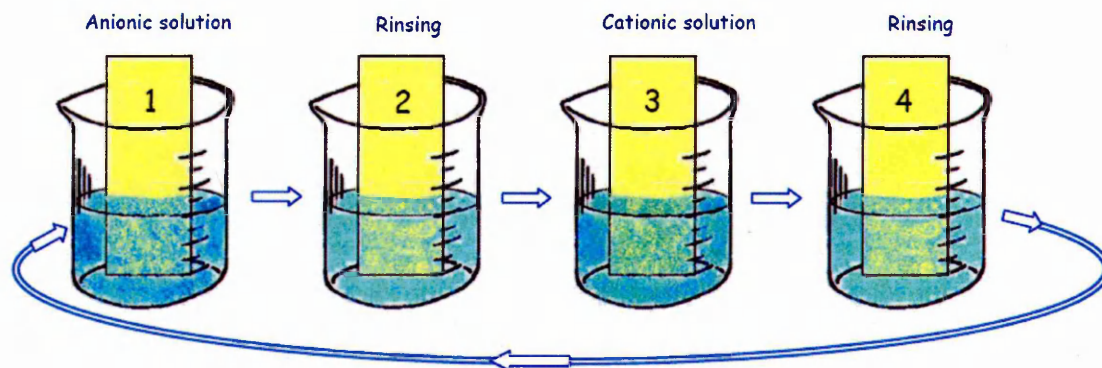


**Figure 3.5-1** Basic sequence of the ESA technique.

- Step 1:* Immersing a positively charged glass substrate in a beaker containing a polyanion solution;
- Step 2:* Rinsing in deionised water or buffer solution;
- Step 3:* Immersing the substrate in a beaker containing a polycation solution;
- Step 4:* Rinsing in deionised water or buffer solution;

It is important to rinse with water between two consecutive polyelectrolyte adsorptions in order to remove the non-adsorbed polymer molecules, which are loosely attached to the pre-adsorbed polymer layer.

The polyelectrolyte deposition process can be divided into two stages. During the first stage, lasting only a few seconds, the positively charged ionic groups of the polymer interact electrostatically with the substrate, leaving a number of positive ions available for further binding. The remaining adsorption sites are filled during the second stage of the process.

As has been mentioned above, the ESA technique has been successfully used for incorporation of biomolecules such as enzymes, antibodies, DNA etc. into the polymer matrix. Biomolecules are ideal for ESA deposition because their natural electric charge can be controlled by the pH of a buffer solution beyond the isoelectric point of the biomolecules. This technique provides a very natural environment for the biomolecules because the immobilization process is performed in a mild condition, and does not involve any modification of the biomolecule's structures.

### *c. Advantages and disadvantages of the ESA technique*

The ESA has some advantages over other popular wet deposition processes, such as spin coating or Langmuir-Blodgett (LB) methods, in the development of thin composite films. Spin coating is a very simple and fast technique, which forms ultra thin films by dispersing solutions onto rotating substrates. However, the spin coating technique cannot control the molecular order and the thickness of the films.

In the case of the LB technique, ultra thin films are formed by transferring a monolayer of ordered amphiphilic molecules from the water surface onto a solid substrate. The LB technique has high accuracy in controlling the film thickness, but it needs special instrumentation. The materials suitable for the LB preparation are usually limited to water insoluble components having high purity and surfactant-like properties<sup>[44]</sup>. The layers in LB films are found to be more ordered than those in ESA films<sup>[45]</sup>. Another drawback of the ESA technique is low deposition speed.

The ESA technique allows the fabrication of well defined layer-by-layer structures of ultra-thin films, without requiring complicated and expensive equipment.

The adsorption processes are independent of the substrate size and topology. The ESA technique also does not require a very high purity of the solution to have a satisfactory multilayer deposition<sup>[44]</sup>.

The benefit of the ESA technique includes a wide range of suitable components that can be used. Enzymes<sup>[46, 47, 48]</sup>, antibodies<sup>[49, 50, 51, 52]</sup>, DNA and nanoparticles<sup>[53, 54, 55]</sup> can all be assembled alternately with the oppositely-charged polyions.

Moreover, the ESA films are mechanically stable due to strong Coulomb interaction, both between polymer layers and between the first layer and solid substrate. Another advantage of the ESA is a wide range of substrates that can be used to deposit the ESA multilayer films, for example, quartz, glass, gold<sup>[51]</sup> or silicon.

Taking into account all these advantages the ESA technique has been chosen for immobilization of biomolecules on the solid substrate in this thesis.

#### *d. ESA films containing organic macromolecules*

A composite film can be formed with the ESA technique, since it is possible to incorporate into the same polymer matrix both active biomolecules and chromophore molecules containing ionic groups having transducing characteristics. Preferably, the chromophore molecule must contain more than one ionic group in a three-dimensional configuration. It allows its' binding on top of the polyion layer, leaving some groups for electrostatic binding of the next polyion layer. This composite ESA film can serve as a sensing membrane, combining functions of molecular recognition and transduction, which is suitable for enzyme or immune sensors<sup>[56]</sup>.

#### *e. Embedding of biomolecules into ESA films*

Protein molecules are known to have both negatively charged carboxylic acid groups ( $-COO^-$ ) and positively charged amino groups ( $-NH_3^+$ ) in their structure. The electrostatic balance of protein molecules depends on the pH of the buffer solution. At the isoelectric point, the balance is achieved, and this results in a net zero electric charge of protein molecules. Below this point (i.e. at acidic pH), proteins are positively charged;

above it (i.e. at alkaline pH), negatively charged. Because of the three-dimensional globular structure of proteins, they automatically fulfil the main suitability criterion for ESA deposition<sup>[56]</sup>. A typical structure of ESA films containing proteins is shown schematically in Fig. 3.5-2.

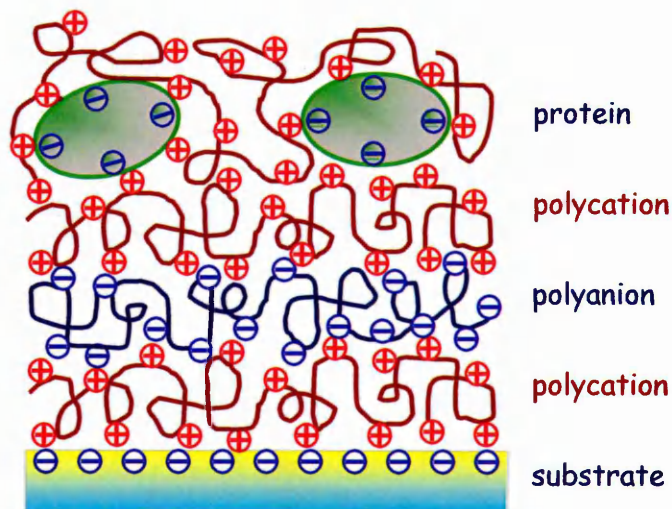


**Figure 3.5-2** The incorporation of proteins into the ESA films (adapted from Ref.<sup>[56]</sup>).

Biomolecules and specific conditions of their ESA deposition are summarised in Table 3.5-1.

**Table 3.5-1** Experimental data for ESA deposition of biomolecules.

<i>Biomolecule</i>	<i>Isoelectric point</i>	<i>pH for ESA deposition</i>	<i>Electric charge</i>
<i>Bovine serum albumin</i>	5.4 <sup>[57]</sup>	8.0	–
<i>Cytochrome</i>	10.1 <sup>[56]</sup>	4.5	+
<i>Urease</i>	5.1 <sup>[58]</sup>	8.2	–
<i>Cholinesterase</i>	3.99 <sup>[59]</sup>	8.0	–
<i>Protein A</i>	5.7 <sup>[60]</sup>	8.2	–
<i>Immunoglobulin</i>	6.8 <sup>[56]</sup>	7.5	–

## 3.6 Portable Planar Waveguide Enzyme Sensor Array

The proposed planar waveguide enzyme sensor array is based on two key elements: a *planar waveguide transducer* and a *composite sensing membrane* containing chromophore molecules and enzymes immobilized on nylon membranes. If the substratum is delivered to the system, the reaction of the substratum decomposition catalyzed by the enzyme takes place on the nylon membrane. The reaction is accompanied with pH changes in the local vicinity which in turn affect the absorption spectrum of the chromophore molecules. This could be registered with the sensitive planar waveguide transducer.

### 3.6.1 Planar waveguide transducer

The planar waveguides used in this study (see Fig.3.6-1) consist of a silicon nitride ( $\text{Si}_3\text{N}_4$ ) core layer with a thickness of  $d_2 = 190 \pm 10 \text{ nm}$  sandwiched between two thick silicon dioxide ( $\text{SiO}_2$ ) layers  $d_1 = 1500 \pm 100 \text{ nm}$ . The refractive indices are  $n_1 = 1.46$  and  $n_2 = 2.05$  for the  $\text{SiO}_2$  and  $\text{Si}_3\text{N}_4$  layers, respectively.

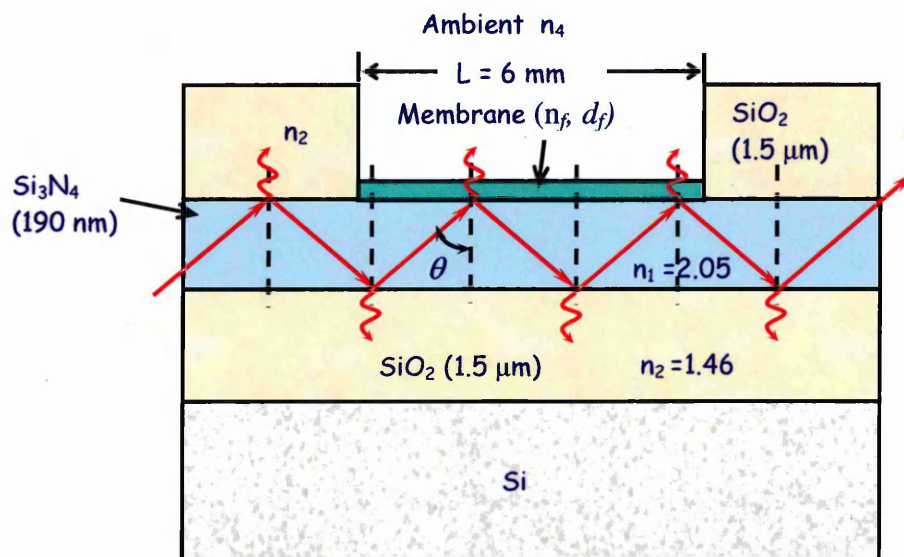


**Figure 3.6-1** Schematic diagram of light propagation through the planar waveguide (taken from Ref.<sup>[61]</sup>).

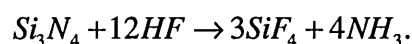
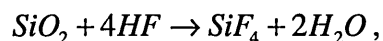
The above parameters for core and cladding layers were chosen to provide a single mode light propagation<sup>[62]</sup> at the wavelength of 633 nm from a HeNe laser.

A large difference in refractive indices of the Si<sub>3</sub>N<sub>4</sub> core and SiO<sub>2</sub> cladding layers in the waveguide causes the light to propagate through the waveguide at angles close to the critical angle ( $\theta_c \approx 47^\circ$ ) and thus provides a large number of reflections. The light intensity attenuation is still negligible if both core and cladding layers are transparent. However, the presence of light absorbing molecules in the cladding may cause the attenuation of the light intensity at every reflection due to the evanescent wave penetrating into the cladding. Because of a large number of reflections, the Si<sub>3</sub>N<sub>4</sub>/SiO<sub>2</sub> planar waveguide is exploited in this study as sensitive tool for the registration of small changes in the absorption coefficient. Earlier experiments showed an increase in sensitivity of up to 10<sup>3</sup> times in comparison to conventional UV-Vis spectroscopy<sup>[61]</sup>.

### 3.6.2 Formation of the sensing windows

Three sensing windows of 4 mm×6 mm in size, which were formed in the top SiO<sub>2</sub> layer using a wet etching technique exposed the surface of the Si<sub>3</sub>N<sub>4</sub> layer to the environment. The etching solution was prepared by adding 49% hydrofluoric acid (HF) to water up to a desired concentration of about 5%. Etching time was about 3 min as shown in Figure 3.6-2.

Calibration of the etching time was done by performing ellipsometric measurements after a certain etching time. The obtained thickness vs. time dependence showed that the top SiO<sub>2</sub> layer was etched at the rate of 530 nm/min. During the first 3 min the SiO<sub>2</sub> layer was etched completely, exposing the Si<sub>3</sub>N<sub>4</sub> layer. A small exceeding of the required etching time is not critical because the etching rate of Si<sub>3</sub>N<sub>4</sub> is much slower (0.99 nm/min) than that of SiO<sub>2</sub>. The etching chemistry of silicon dioxide and silicon nitride are given below:



In addition, due to the etching process, the Si<sub>3</sub>N<sub>4</sub> surface became positively charged because of the presence of Si-NH<sub>3</sub> groups. This positive charge was required

for the ESA deposition of the sensing membrane to start with a compound, which has a negative surface charge. The etching of the  $\text{Si}_3\text{N}_4$  layer in 5% HF acid for a few (~5 – 7) seconds was used time to time to "refresh" e.g. enhance the surface charge before ESA deposition.

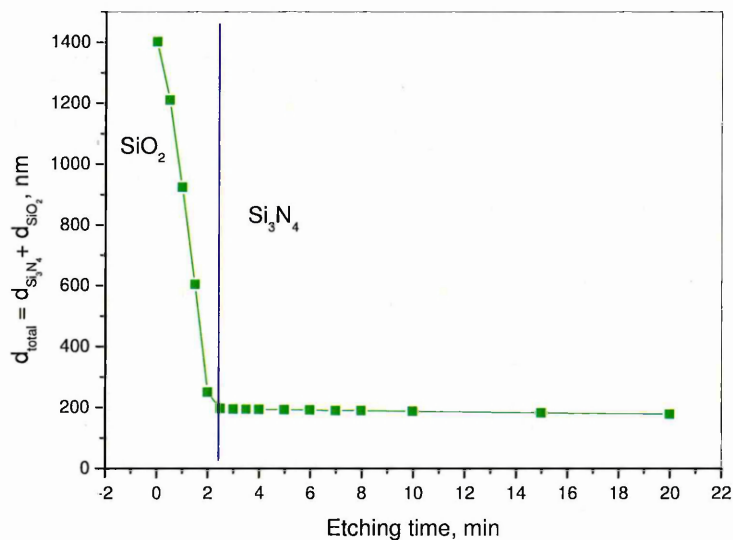


**Figure 3.6-2** Etching kinetics of the  $\text{SiO}_2/\text{Si}_3\text{N}_4$  layers.

### 3.6.3 Formation of the sensing layer using ESA technique

The three sensing windows were coated with a sensitive membrane with a refractive index of about  $n_f = 1.4$ , which is typical for organic films. The freshly etched (or "refreshed")  $\text{Si}_3\text{N}_4$  surface was first covered with the *polyanionic* polyelectrolyte. After that the sensitive film was deposited by consecutive electrostatic adsorption of layers of polycations and pH sensitive chromophore molecules.

Typically 3 – 4 bilayers of chromophore–polycation were deposited. Enzymes were immobilized on the surface of the nylon membranes from their 1 mM solution in Trizma/HCl buffer with pH 8.5.

### a. Chemicals

The polymers, namely *poly(allylamine hydrochloride)* (PAH) and *poly(styrenesulfonate) sodium salt* (PSS), were, respectively, used as polycations and polyanions for ESA deposition.

PAH is fully ionized at a pH lower than 7.0<sup>[63]</sup>. PAH has a *positive* surface charge, associated with  $NH_3^+$  groups (see Table 3.3-1). The advantage of using PAH was that its charge is located at the far end of the side chain, which was easily accessible for the compensation by other ionic molecules. It has a pH of 4.0 when diluted to a concentration of 2 g/l in ultra-pure water.

PSS has a *negative* surface charge, delivered from  $SO_3^-$  groups (see Table 3.3-1). It has a pH about of 5.5 when diluted to a concentration of 2 g/l in ultra-pure water.

These concentrations (2 g/l) for both PAH and PSS were considered to be suitable to provide enough charge for ESA deposition, as was confirmed by Lvov et al.<sup>[64]</sup>. Both polyelectrolytes were purchased from Sigma-Aldrich®.

Ultra-pure (or Millipore) water (type III laboratory-grade) was obtained by using the RiOs™ water purification system (Millipore Corp, Billerica, MA). The resistance of Millipore water is  $\geq 18$  M $\Omega$ . Information about purification of water based on technical data for the RiOs™ system<sup>[65]</sup> is given in Table 3.6-1.

**Table 3.6-1** Purification of the water by RiOs™ system (after Ref.<sup>[65]</sup>).

<i>Contaminant</i>	<i>Rejection</i>	<i>Passage</i>
Ions, %	~ 99	~ 1
Organics, %	$\geq 99$	$\leq 1$
Particles, %	$\geq 99$	$\leq 1$
Microorganism, %	$\geq 99$	$\leq 1$

*Cyclotetrachromotropylene* (CTCT) was chosen as an organic indicator for the enzyme sensor because of its ability to change the absorption spectrum over a wide range of pH from pH 3 to 13<sup>[66]</sup>. As shown in Figure 3.6-3, CTCT has four  $SO_3^-Na^+$

groups providing negative surface charges in 3D configuration required for the ESA deposition. The peculiarities of the structure of CTCT allow it to form complexes with some metal ions and pesticides<sup>[66]</sup>.

The CTCT used in this study was synthesized and kindly provided by Dr. Frank Davis (Cranfield University, UK). The molecular weight of CTCT is 1497.05 g/mole and the pH was 4.4 when diluted to  $10^{-4}$  M in ultra-pure water. The concentration of CTCT used for the sensing membrane preparation was 1 mg/ml, which was equivalent to  $\sim 10^{-4}$  M. A similar concentration of CTCT was used by Nabok et al.<sup>[67]</sup> to prepare multilayered PAH/CTCT membranes.

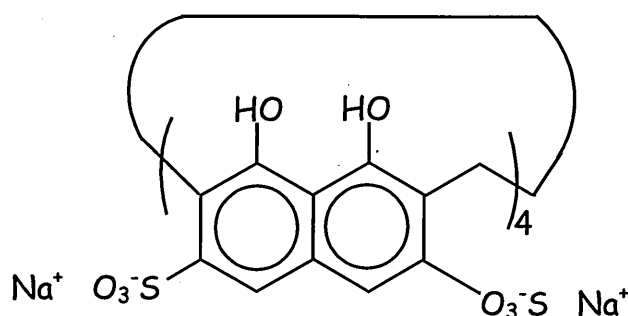


**Figure 3.6-3** Chemical structure of *cyclotetrachromotrylene* (CTCT) (after Ref.<sup>[67]</sup>).

Three types of *enzymes* were tested as sensitive elements in the nanocomposite membrane, namely *urease*, *acetylcholine esterase* (AChE) and *butyrylcholine esterase* (BChE).

Enzyme molecules (as any other proteins) are known to have both negatively charged carboxylic acid groups and positively charged amino groups in their structure. The electrostatic balance between these groups depends on the pH of the buffer solution in which the enzyme is kept. The enzyme molecule was electrically neutral at the isoelectric point, where the electrostatic balance was achieved. In this study, the enzymes *urease* and *AChE* had their isoelectric points of about pH 5, while the isoelectric point of *BChE* was pH 7. Therefore, these compounds were dissolved in 1 mM Trizma/HCl buffer solutions at pH 8.5 to make them negatively charged. This was necessary for the ESA deposition on the positively charged PAH layer.

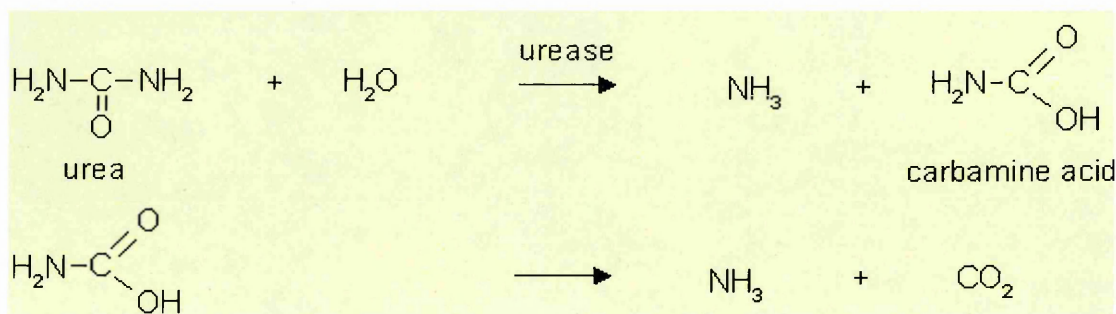
Concentrations of enzymes equivalent to 100 units of activity as recommended by Lvov et al.<sup>[64]</sup> were chosen (see Table 3.6-2).

Typically one unit of enzyme was sufficient to catalyze 1  $\mu$ mole of the respective substratum per minute under standard conditions. The reactions catalyzed by these enzymes are given below. pH changes will occur due to the production of acidic or alkaline compounds during the enzyme reaction.

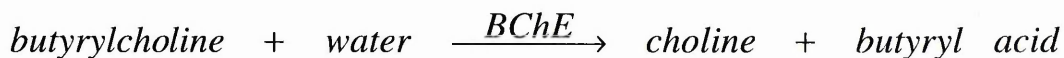
**Table 3.6-2** Concentrations of enzymes equivalent to 100 units of activity.

<i>Enzyme</i>	<i>Weight activity, units/mg</i>	<i>Concentration, mg/ml</i>
<i>Urease from Canavalia ensiformis (Jack bean)</i>	29.5	3.39
<i>Acetylcholine esterase (AChE) from Electric Eel</i>	1670 1052	0.06 0.095
<i>Butyrylcholine esterase (BChE) from Horse Serum</i>	1100 1012.8	0.091 0.099

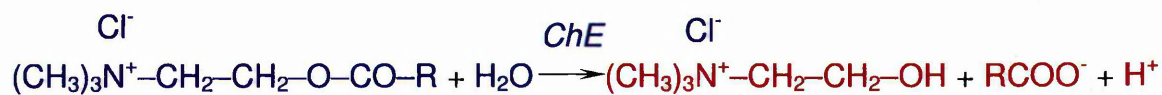
For instance, *Urease* is an enzyme that catalyzes the hydrolysis of *urea* to form *ammonia* and *carbamine acid*. The latter compound spontaneously decomposes to generate a second molecule of ammonia ( $\text{NH}_3$ ) and carbon dioxide ( $\text{CO}_2$ )<sup>[68]</sup>:



*Cholinesterase* (ChE) hydrolyzes its natural substrate (acetylcholine for *AChE* and butyrylcholine for *BChE*) to *choline* and *acetate*<sup>[69]</sup>:



or



R = CH<sub>3</sub> : *acetylcholine*

R = (CH<sub>2</sub>)<sub>2</sub>CH<sub>3</sub> : *butyrylcholine*

Chemical formulas, molecular weights and concentrations of substrata used in this study are listed in Table 3.6-3. All substrata were dissolved in 1 mM Trizma/HCl buffer solutions at pH 7.5 as recommended in Ref.<sup>[61]</sup>.

**Table 3.6-3** Chemical formulas, molecular weights and concentrations of substrata.

<i>Substratum</i>	<i>Chemical formula</i>	<i>Molecular weight</i>	<i>Concentration</i>	<i>Corresponding enzyme</i>
<i>Urea</i>	(NH <sub>2</sub> ) <sub>2</sub> CO	60.07 g/mol	100 mM	Urease
<i>Butyrylcholine</i> [chloride] (BCh)	C <sub>9</sub> H <sub>20</sub> NO <sub>2</sub> <sup>+</sup> ·(Cl <sup>-</sup> )	174.26 g/mol	10 mM	BChE
<i>Acetylcholine</i> [chloride] (ACh)	C <sub>7</sub> H <sub>16</sub> NO <sub>2</sub> <sup>+</sup> ·(Cl <sup>-</sup> )	146.21 g/mol	10 mM	AChE

### *b. Enzyme adsorption on nylon membranes*

A novel (relatively to the research made in 2001 – 2004 by S. Haron<sup>[70]</sup>) approach in the immobilization of enzymes was exploited in this study. Enzymes were immobilized on disposable nylon membranes which reduce the cost of the biosensor device significantly. Moreover, they provide better resistance to temperature and longer stability than free enzymes. However, the main disadvantage of the immobilization process is the lower specific activity of the immobilized enzymes compared to that exhibited by the same amount of free enzymes<sup>[71]</sup>.

Fibrous materials, such as *nylon membrane*, are among the most suitable solid supports for immobilization of enzymes due to their porous structure, providing the quantity and the accessibility of the active sites necessary for high reaction rates and conversions.

Enzymes were adsorbed on 6×3.5 mm pieces of BioBond™-Plus nylon membrane obtained from Sigma-Aldrich. Adsorption of enzymes was carried out by immersing the membranes into 1 mM Trizma/HCl buffer solution (pH 8.4 ± 0.1) containing enzyme. The enzyme concentration was between ~0.1 mg/ml and ~3.4 mg/ml (see Table 3.6-2) and the adsorption was conducted at room temperature for 4 hours. After that, the enzyme-adsorbed membranes were washed in the 1 mM Trizma/HCl buffer having pH 7.5 ± 0.1, and then dried at room temperature. The lifetime of the enzymes adsorbed on such membrane is about 30 – 45 days<sup>a</sup>.

### c. *Pollutants and their preparations*

The following metal salts and pesticides were used to study the response of the planar waveguide enzyme sensors array to different concentrations of pollutants: *cadmium chloride* (CdCl<sub>2</sub>), *nickel chloride* (NiCl<sub>2</sub>), *lead nitrate* (Pb(NO<sub>3</sub>)<sub>2</sub>), *imidacloprid*, and *2,2-dichlorovinyl dimethyl phosphate* (DVDP or *dichlorvos*). All compounds are highly soluble in water. The metal salts are dissociated on cations (Cd<sup>2+</sup>, Ni<sup>2+</sup>, Pb<sup>2+</sup>) and anions ((NO<sub>3</sub>)<sup>2-</sup>, Cl<sup>2-</sup>). Previous research<sup>[70]</sup> proved that both chloride and nitrate anions exhibit practically no effect on the sensing membrane, particularly on the activity of immobilized enzymes. Different pesticides were chosen in order to investigate the sensitivity of the enzyme sensors to pollutants of different toxicity.

The pollutant solutions were prepared by multiple dilution of the sample solution in Millipore water to achieve concentrations in the range from 100 ppm down to 0.1 ppb. The dilution process began with the preparation of sample solutions at a concentration of 100 ppm by dissolving 1 mg of the respective compounds in 10 ml of Millipore water. Stirring at room temperature was used to obtain a homogeneous mixture of the sample solutions.

---

<sup>a</sup> Membranes with adsorbed enzymes must be stored in the fridge at 4-8 °C

The method of planar waveguide was applied to analyse the samples of tap water taken from the different places in Sheffield, UK as well as from Odessa, Ukraine.

### 3.6.4 ESA deposition process

All steps of ESA deposition were performed either in the multi-channel cell by injecting the solutions required with the syringe or by dipping the planar waveguide (see Figure 3.6-4) into beakers, containing the required polyelectrolyte solutions in the following sequence:  $PSS \rightarrow (PAH \rightarrow CTCT)_n$  (where  $n$  is the number of layers).

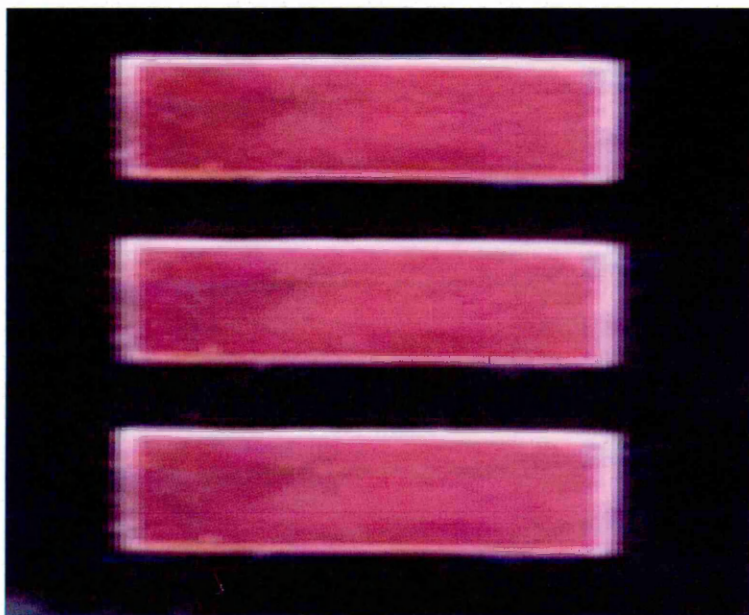


**Figure 3.6-4** Planar waveguide with three sensing windows (top view).

Intermediate thorough washing with Millipore water was carried out after each adsorption step in order to flush out the remaining unbound polymer. The incubation time of 12 – 20 min was used for the majority of adsorption steps.

The deposition process can be monitored by recording the light intensity in each channel, as shown in Fig. 3.6-5.

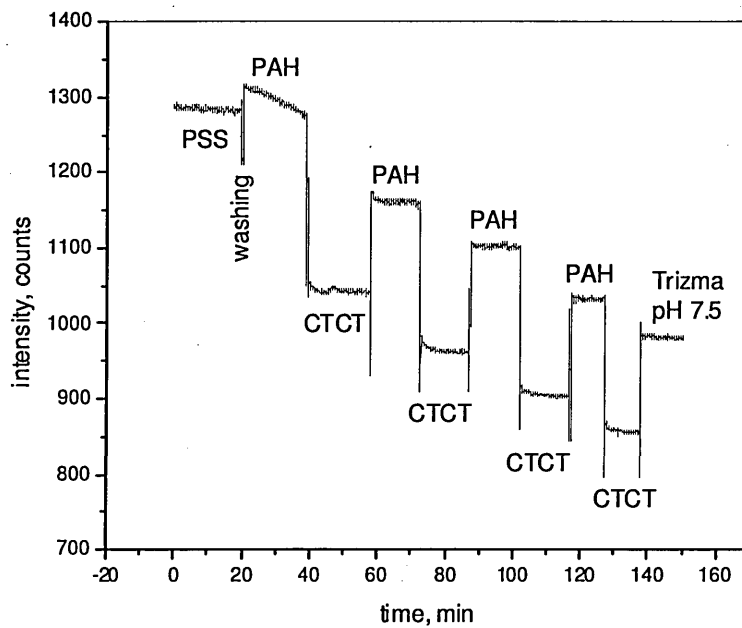


**Figure 3.6-5** Monitoring of the sequential electrostatic deposition of PSS-(PAH-CTCT)<sub>4</sub> layers.

### 3.6.5 Experimental set-up for a multichannel enzyme sensor array

All experiments i.e. enzyme reactions, effect of pollutants, as well as the process of electrostatic polyelectrolyte deposition, were studied *in situ* using a portable sensor array set-up, shown schematically in Figure 3.6-6a. It consisted of a fan-beam laser diode (Coherent) which produces a narrow line beam of 630 nm in wavelength. Then, a semi-cylindrical lens was used to focus the beam into a narrow horizontal line with a thickness of about 0.5 mm on the edge of the planar waveguide with three sensing windows etched in the top Si<sub>3</sub>N<sub>4</sub> layer to form three channels.

The assembly of the waveguide on the holder with the three-channel cell attached is placed right in front<sup>a</sup> of the CCD array photo-detector in order to avoid any light intensity loss. Otherwise, scattering of the light coming out from the waveguide

<sup>a</sup> The gap between the cell and CCD array photo-detector is less than 1.5 mm.

causes both significant losses in the light intensity and smearing (and even overlapping) of the images of individual channels.

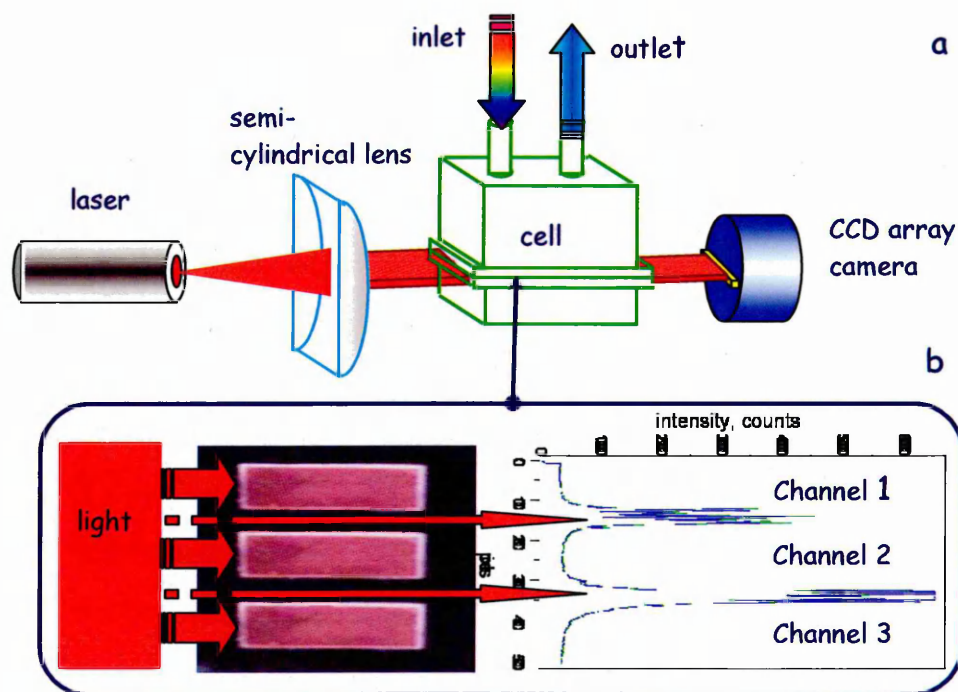


**Figure 3.6-6** a – Schematic diagram of portable sensors array device; b – Typical CCD array image of the light coming out from the waveguide.

A reaction cell (made from black plastic) with a volume of  $1.5 \text{ cm}^3$  was tightly sealed with a rubber seal having three slots, which form three waveguiding channels, and was placed on top of the planar waveguide. This cell, shown enlarged in Fig. 3.6-7, contains three channels connected parallel to each other; to provide a continuous and low-mixable flow of liquid through the cell with inlet and outlet tubes. The multi-channel sensor cell is designed to accommodate replaceable nylon membranes containing the immobilised enzymes. This facilitates easy low-cost replacement of the sensitive elements. The above cell was assembled on a specially designed holder. All parts were manufactured in the SHU engineering workshop.

The experimental set-up was enclosed in a  $20 \times 25 \times 45 \text{ cm}$  metal case (see Figs. 3.6-8a and 3.6-8b) which improved its light screening and reduced the noise level. The Hamamatsu (model C7557, type S7010-0906) multi-channel detector head with front side CCD was connected to a PC via a SCSI card.

Typical CCD array image of the light coming out from the waveguide is shown in Fig. 3.6-6b. The three sections of low light intensity correspond to the etched sensing windows in the waveguide and thus constitute three channels.

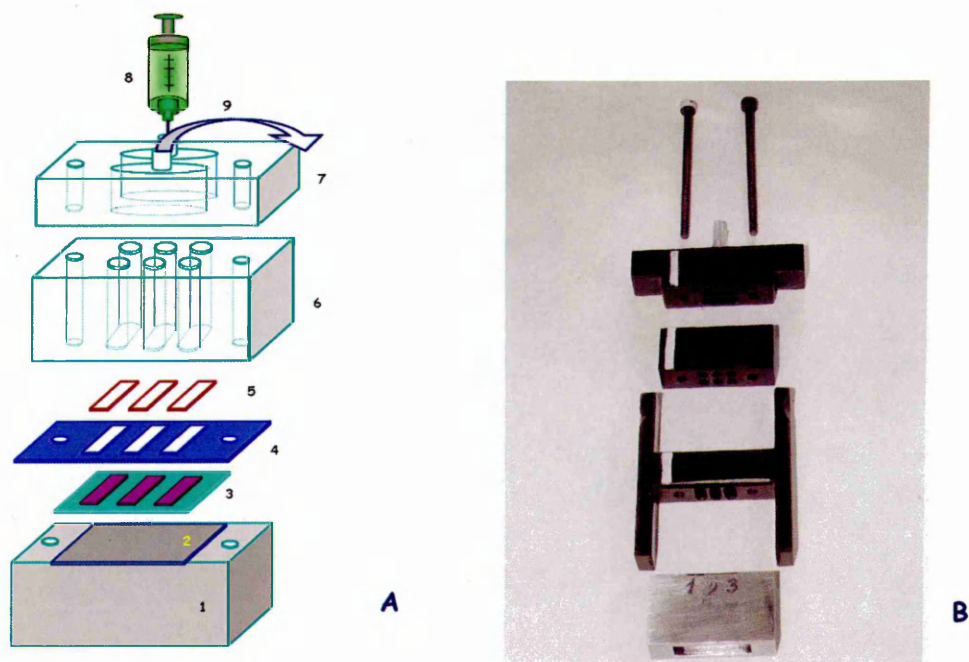


**Figure 3.6-7** Exploded drawing (A) and picture (B) of the flow reaction cell. 1 – steel holder; 2 – rubber base for planar waveguide; 3 – planar waveguide; 4 – rubber frame; 5 – disposable nylon membranes with adsorbed enzymes; 6 – three-channel reaction cell; 7 – cell's lid with inlet (8) and outlet (9) tubes.

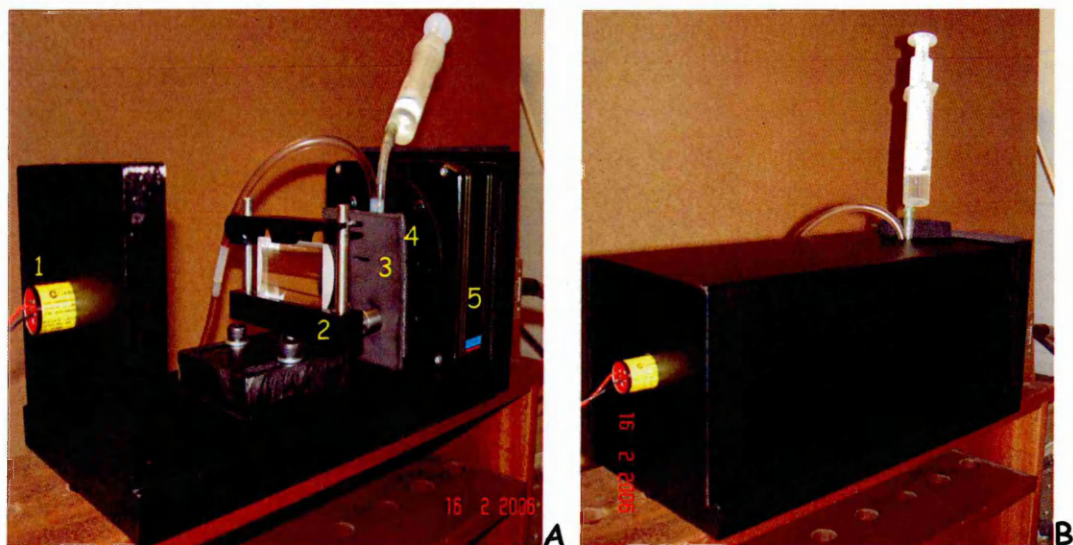


**Figure 3.6-8** Portable planar waveguide enzyme sensors array device. A – open unit: 1 – laser; 2 – semi-cylindrical prism; 3 – aperture; 4 – reaction flow cell; 5 – CCD array camera; B – unit assembled.

### 3.6.6 Measurements procedure for pollutants registration

The measurement procedure for pollutants registration was as follows. Disposable nylon membranes with the immobilized enzymes (namely, Urease, AChE, and BChE) were placed into the corresponding channels of the reactions cell. The channels of the reaction cell were positioned above the sensing windows on the top of the planar waveguide. The sensing windows of the planar waveguide were covered with composite sensing membrane containing PSS-(PAH-CTCT)<sub>4</sub> layers deposited earlier by the ESA method (the lifetime of this reusable membrane is at least 3 weeks).

The substrata used in this study were dissolved in mildly concentrated (1 mM) Trizma/HCl buffer solution (pH 7.5 ± 0.1) to standardise the pH at the start of the enzyme reactions. The buffer solution was also injected into the reaction cell before each measurement to stabilize the sensor response in neutral conditions.

The routine began with the registration of the sensor response to enzyme reactions in the corresponding substratum solution (or mixture of the substrata). Then, a sample solution containing only one pollutant (or mixture of two pollutants) was injected into the reaction cell and held there for 10 – 12 minutes.

After this inactivation process, the response to the enzyme reaction was recorded again under similar conditions as before. The reaction cell was rinsed with the 1 mM Trizma/HCl buffer solution after each step of the measurements.

Since each data recording started at a different background level of the sensor signal, the absolute response ( $\Delta I$ ) was defined as a difference between the initial ( $I_b$ ) and final (after saturation) ( $I_f$ ) values of the output signal:

$$\Delta I = |I_b - I_f|. \quad (3.8)$$

Thus, the relative response of the sensor (also called *residual activity* of the enzyme) can be calculated as,

$$\Delta R = \frac{\Delta I_i}{\Delta I_0} \times 100\%, \quad (3.9)$$

where  $\Delta I_0$  and  $\Delta I_i$  are the response value of the initial enzyme reaction and that after the inhibition process, respectively.

### 3.6.7 Software description

The original Hamamatsu software designed to record images with CCD array was modified to the required experimental task:

1. To measure a series of line-images of the waveguide edge after certain (variable) time intervals and store the obtained images. A typical “line” image is given in Fig. 3.6-9.
2. To select three sections of every image corresponding to three channels, and to store three values of the average light intensity in each channel. The resulting data file consisted of four columns: one was the time, the other three gave corresponding average light intensities in each channel.
3. To register initial and final (after a certain time) average light intensities in each channel.

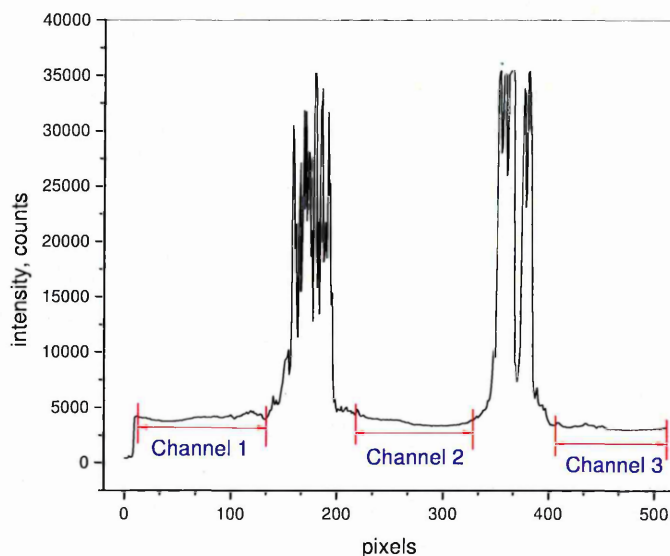


**Fig. 3.6-9** Typical “line” image.

A more detailed description of the software as well as the full text of the program developed is given in Appendix A.

### 3.6.8 Analysis of pollutants using an Artificial Neural Network algorithm

The response of the sensor array to different pollutants was analysed with the *artificial neural network* (ANN). ANN is a program, which is based on virtual “nerve cells” called *neurons*. These neurons are connected between each other in multiple ways to build up networks. Such networks have the capacity to learn, memorise and create relationships amongst the data sets. A brief introduction to the ANN basic is given in Appendix C.

One of the applications of ANN is as a tool for multi-component analysis particularly suitable for chemical- and biosensing purposes. ANN has been proven as a powerful analytical tool capable of recognising both the quantitative and qualitative composition of solutions. ANN has been successfully exploited for the determination of pesticides using enzyme sensors and immunosensors<sup>[72,73]</sup>, for the quantification of metals and inorganic pollutants in groundwater<sup>[74]</sup>, and for the determination of phenolic compounds<sup>[75]</sup>.

In this study, the ANN was employed as a pattern recognition tool for data analysis of the developed enzyme sensors array. MATLAB software (version 6.1, MathWorks Inc., Natick, MA) was used for the ANN modelling, using the supplied functions and algorithms in the MATLAB Neural Network Toolbox (version 4.0, MathWorks Inc., Natick, MA) as part of MATLAB.

Prior to ANN processing, the experimental results from the repeated measurements were divided into two data sets, which were used for the *training* and *testing* of the network models. The training was performed for 20000 repetitions (“epochs”) with the mean squared error (MSE) goal set to  $1 \cdot 10^{-10}$ . For qualitative and quantitative analysis, eight separate network models were produced and trained.

One of the neural networks was used to classify the pollutants. This contained seven neurons in the *hidden* layer, as illustrated in Figure 3.6-10.

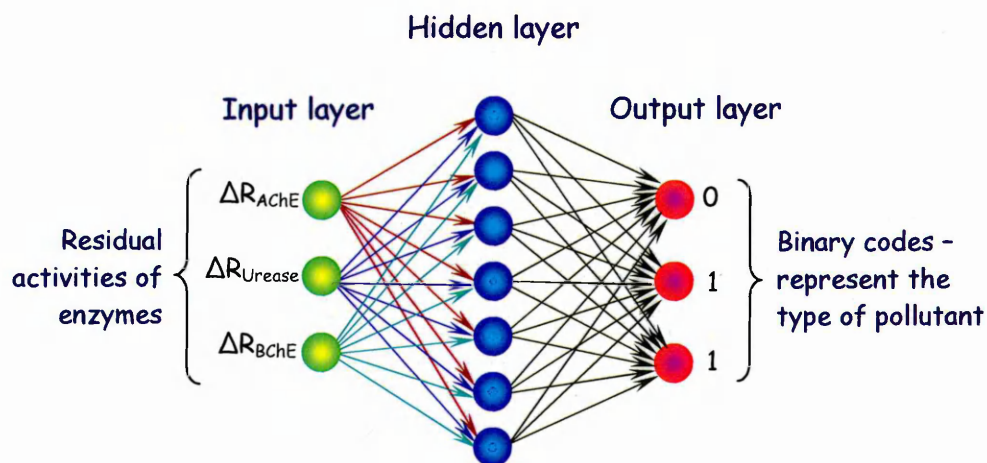


**Figure 3.6-10** Neural network architecture for classifying the pollutants.

The number of neurons in the *input* layer was set to three, equal to the number of channels in the sensors array. Three neurons in the *output* layer were used to describe a three-digit binary code, representing the type of pollutants (see Table 3.6-4).

**Table 3.6-4** Binary codes for representing the type of pollutants.

<i>Pollutant</i>	<i>Binary code</i>		
DVDP	0	0	0
Pb <sup>2+</sup>	0	0	1
Cd <sup>2+</sup>	1	0	0
Imidacloprid	0	1	1
Ni <sup>2+</sup>	1	0	1
Mixture-1	1	1	0
Mixture-2	1	1	1

The other seven network models were designed to quantify each pollutant (cadmium, lead, nickel, imidacloprid, and DVDP) and two binary mixtures (Mixture-1 and Mixture-2). The topology of these network models consisted of three and one neuron in the input and output layer, respectively. The number of neurons in the hidden layer was five (see Figure 3.6-11). All network models were developed by Dr. A. Holloway.

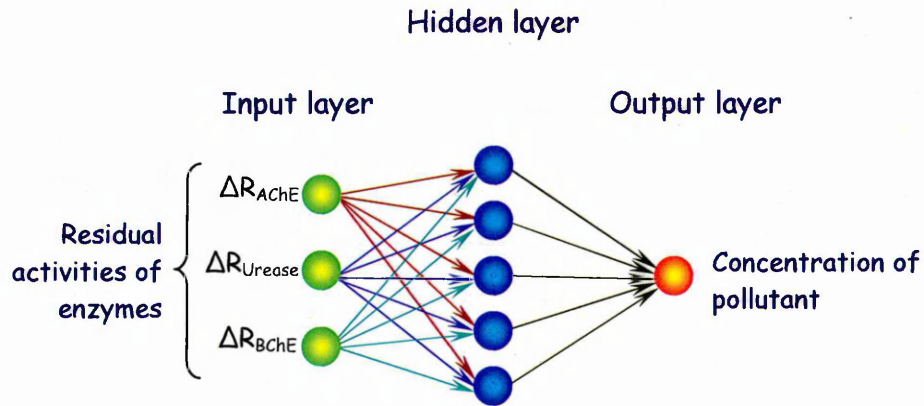


**Figure 3.6-11** Neural network architecture for quantifying pollutants.

## 3.7 Kinetics of Bio-reactions

### a. Affinity

As has been mentioned in the Introduction, immunosensors transduce antigen – antibody interactions directly into physical signals<sup>[76]</sup>. The antibody or immunoglobulin is usually described as a Y-shaped molecule with two identical binding sites for the antigen (Fig. 3.7-1). Each antibody recognizes a specific antigen unique to its target. The strength with which an antibody molecule binds an antigenic determinant is called its *affinity*.

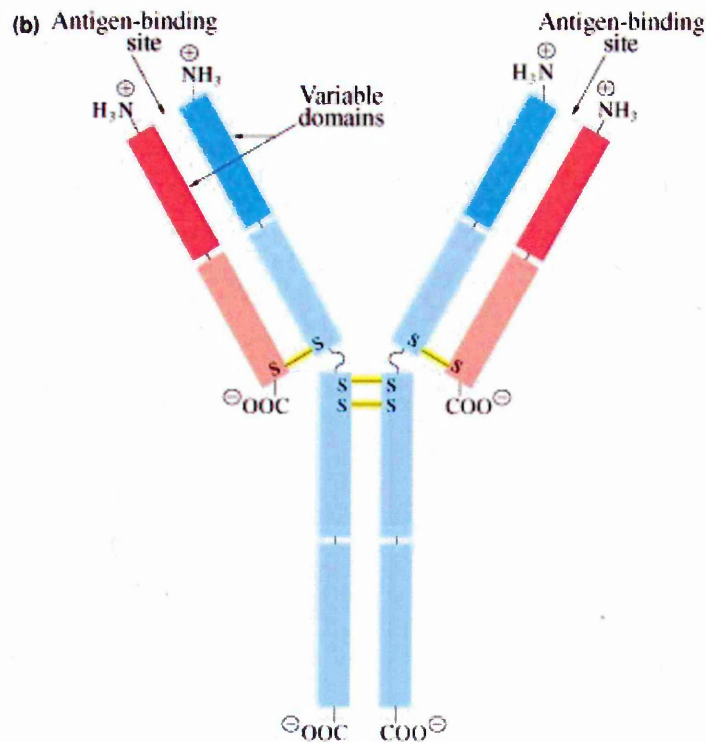


**Figure 3.7-1** Scheme for a typical antibody (taken from the Ref.<sup>[77]</sup>).

The antibody (*Ab*) can be considered as a molecular recognition complex which binds reversibly with a specific antigen (*Ag*). The binding reaction may be represented as follows:



*b. Kinetics*

Affinity can be quantified by determining an *association constant*  $K_A$ :

$$K_A = \frac{[AgAb]}{[Ag][Ab]}, \quad (3.11)$$

where the terms in brackets represent the concentration of antibody-antigen complexes  $[AgAb]$ , unbound antibody  $[Ab]$ , and unbound ("free") antigen  $[Ag]$ . Values of  $K_A$  are in a range from about  $10^4$  to  $10^{12}$  litres/mole. Immunoglobulins with  $K_A < 10^4$  for a particular antigen would be ineffective as antibodies against the antigen<sup>[78]</sup>. The association constant  $K_A$  is related to the *dissociation constant*  $K_D$  as

$$K_A = \frac{1}{K_D} \quad (3.12)$$

The magnitude of  $K_D$  describes the affinity, or 'tightness', of the  $Ab-Ag$  binding. The closer  $K_D$  is to zero, the higher is the affinity that characterizes the complex.

Introducing the total concentration of antibody sites

$$[Ab]_t = [Ab] + [AbAg], \quad (3.13)$$

the Eq. (3.11) can be rewritten:

$$[AbAg] = \frac{K_A [Ab]_t [Ag]}{1 + K_A [Ag]}. \quad (3.14)$$

Figure 3.7-2 shows a saturation binding curve of  $[AbAg]$  versus free antigen  $[Ag]$ :

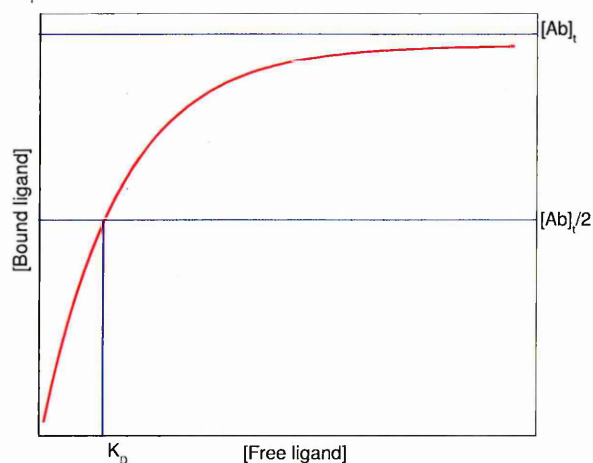


**Figure 3.7-2** Saturation binding curve.

The curve illustrates the effect of an increase in free antigen concentration  $[Ag]$  on the concentration of  $[AbAg]$  complex at a constant antibody concentration  $[Ab]_t$ . When  $K_A[Ag] \ll 1$ , there is a near linear relationship between  $[AbAg]$  and  $[Ag]$ . The complex concentration  $[AbAg]$  asymptotically approaches the plateau denoting total antibody concentration  $[Ab]_t$ . The antibody saturation, i.e.  $[AbAg]/[Ab]_t$ , is given by

$$\frac{[AbAg]}{[Ab]_t} = \frac{K_A[Ag]}{1 + K_A[Ag]} \quad (3.15)$$

When  $[Ag] = 1/K_A$  (that is  $K_D$ ), then 50% of the antibody bindings sites are saturated. By plotting the ratio between bound and free antigen concentration ( $[AbAg]/[Ag]$ ) versus bound antigen concentration  $[AbAg]$ , a straight line is obtained (Fig. 3.7-3). The slope equals  $-K_A$  and the intercept on the ordinate gives the concentration of antibody binding sites ( $[Ab]_t$ )<sup>[79]</sup>.

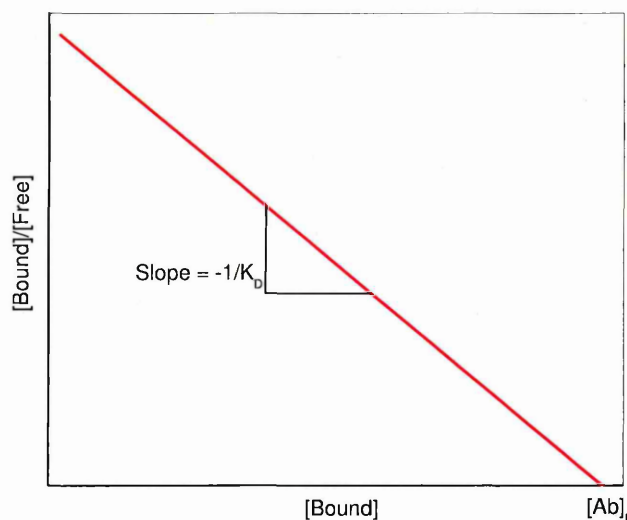


**Figure 3.7-3** Plot for determination of dissociation constant  $K_D$  and  $[Ab]_t$ .

The affinity can also be expressed as the ratio between the kinetic constants of the interaction:

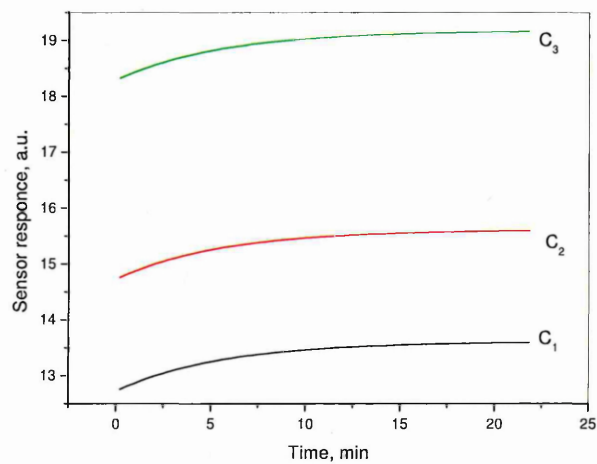
$$K_D = \frac{k_d}{k_a} \quad (3.16)$$

where  $k_a \left[ \frac{l}{M \cdot s} \right]$  is the *association rate constant* and  $k_d \left[ \frac{1}{s} \right]$  is the *dissociation rate constant*, describing the rate of formation and decay of the complex, respectively. Thus

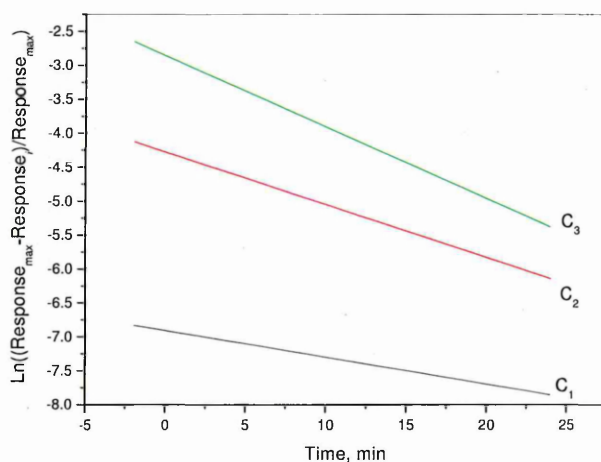
$$\frac{d[AbAg]}{dt} = k_a [Ab][Ag] - k_d [AbAg] \quad (3.17)$$

describes the complex formation as a function of time.

The antigen – antibody (or antigen – analyte) interaction can be monitored by observing changes in the biosensor response<sup>[80]</sup> (the typical experimental graph is shown in Fig. 3.7-4a). These measurements can be repeated for different concentration of analyte.



a



b

**Figure 3.7-4** Typical kinetics of sensor responses in the course of antibody-antigen binding for different concentrations of analyte C.

The signal can be expressed by the equation as follows:

$$\frac{dR}{dt} = k_a C(R_{\max} - R) - k_d R, \quad (3.18)$$

where  $\frac{dR}{dt}$  is the rate of change of the sensor signal,  $k_a$  is the association rate constant,  $C$  is the concentration of the analyte,  $R_{\max}$  is the maximum response corresponding to a saturation of binding sites,  $R$  is the amount of bound antibody measured as the biosensor response at time  $t$ , and  $k_d$  is the dissociation rate constant. The integrated form of the Eq. (3.18) is:

$$R = \frac{k_a \cdot C \cdot R_{\max}}{k_a \cdot C + k_d} \{1 - \exp[-(C \cdot k_a + k_d)t]\}. \quad (3.19)$$

Experimental kinetic curves for different concentrations of analyte plotted in semi-logarithmic scale ( $\ln R(t)$ ) yield linear dependence with the slope  $S$  (Fig. 3.7-4b):

$$S = C \cdot k_a + k_d. \quad (3.20)$$

A linear plot of  $S$  against different analyte concentrations  $C$  gives a straight line with a slope  $k_a$  and a y-intercept  $k_d$  (Fig.3.7-5). The association constant  $K_A$  can be calculated from  $\frac{k_a}{k_d}$ .

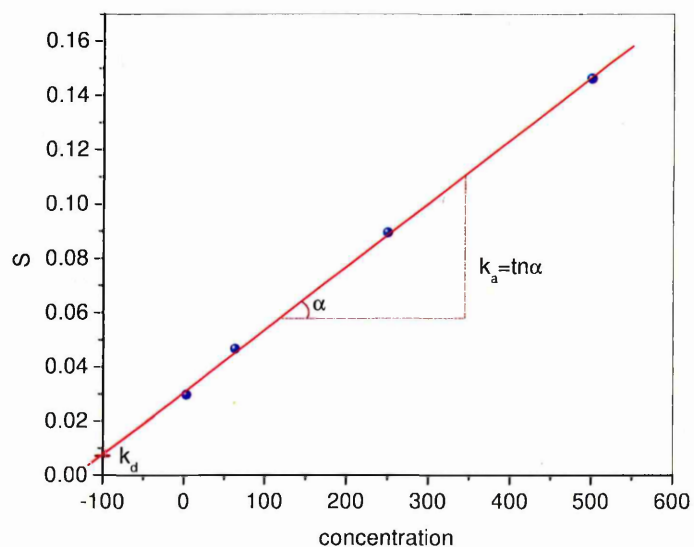


**Figure 3.7-5** Graph for calculation of the association constant  $K_A$  (detailed in the text).

## 3.8 Summary

This chapter introduces experimental methodologies. Detailed descriptions of experimental routines and sample preparation procedures used in this study are given here.

Porous silicon (PS) matrix can be used to study molecular adsorption and to perform different biological reactions. The high sensitivity of ellipsometry to refractive index changes can be beneficiary in conjunction with PS. For this reason, the spectroscopic ellipsometry method has been chosen to study the adsorption of biomolecules (namely, bovine serum albumin as a common protein) into PS.

The recently proposed method of total internal reflection ellipsometry (TIRE) combines the advantages of the spectroscopic ellipsometry and the Kretschmann type SPR. Spectral changes caused by adsorption of low molecular weight molecules (such as atrazine, simazine, mycotoxin, and nonylphenol) can be registered. Since the sensitivity of TIRE is several times higher than that of both SPR and conventional ellipsometry, this method has been proposed for the detection and quantification of low molecular weight environmental toxins.

A concept of optical biosensors based on planar waveguides was developed further in this project. This development included improvements to the existing system allowing greater portability combined with simplicity. The set-up developed was based on a CCD array camera. The cell/system design allowed registration of enzyme reactions in all cell channels simultaneously. The use of disposable nylon membranes with adsorbed enzymes is considered. Pattern recognition algorithm is exploit using artificial neural network software to identify and quantify pollutants in water samples.

A description of the electrostatic self-assembly (ESA) technique for immobilization of biomolecules on a substrate was given. The application of the ESA technique to form multi-function sensing membranes was reviewed. The ESA method proved to be suitable for the formation of composite membranes for optical biosensors.

Finally, the basic principle of the kinetics of bio-reactions was given.

## References

### §3.1

- [1] Binnig G., Quate C. F. and Gerber C. *Atomic force microscope*, Physical Review Letters **56** (1986) 930-933.
- [2] <http://invsee.asu.edu/nmodules/spmmod/senses.html> (accessed 18 January 2007).
- [3] <http://uweb.txstate.edu/~ab35/manuals/AFMmanuals/AFMLabManual.pdf> (accessed 19 January 2007).
- [4] *Scanning Probe Microscopy Training Notebook v.3.0*, Digital Instruments & Veeco Metrology Group, 2000.
- [5] [http://www.bfrl.nist.gov/nanoscience/BFRL\\_AFM.htm](http://www.bfrl.nist.gov/nanoscience/BFRL_AFM.htm) (accessed 19 January 2007).
- [6] Knoll M. *Aufladepotential und Sekundaremission elektronenbestrahlter Körper*. Z. Tech. Phys. **16** (1935) 467-475.
- [7] Zworykin V., Hiller J. and Snyder R. *A scanning electron microscope*. ASTM Bulletin **117** (1942) 15-23.
- [8] Smith K. C. A. *Charles Oatley: pioneer of scanning electron microscopy*, Annual Conference of the Electron Microscope Group of the Institute of Physics: EMAG-97.
- [9] <http://www.shu.ac.uk/research/meri/sem.htm> (accessed 19 January 2007).
- [10] <http://www.sem.com/analytic/sem.htm> (accessed 19 January 2007).
- [11] <http://www.fei.com/Resources/StudentLearning/tabid/91/Default.aspx> (accessed 19 January 2007).
- [12] <http://www.sem.com/analytic/sem.htm> (accessed 19 January 2007).
- [13] <http://mse/iastate.edu/microscopy> (accessed 10 November 2005).

### §3.2

- [14] [http://www.jawoollam.com/tutorial\\_faq.html](http://www.jawoollam.com/tutorial_faq.html) (accessed 1 February 2007).
- [15] Woollam J. A., Johs B., Herzinger C. M., Hilfiker J., Synowicki R. and Bungay C. L. *Overview of variable angle spectroscopic ellipsometry (VASE), Part I: Basic theory and typical applications*, Critical Reviews of Optical Science and Technology CR **72** (1999) 3-28.
- [16] Press W. H., Teukolsky S. A., Vetterling W. T. and Flannery B. P. *Numerical recipes in C*, Cambridge University Press, Cambridge, 1988.
- [17] *Guide to Using WVASE®*, J. A. Woollam Co. Inc., 2003.

### §3.3

- [18] Fried M., Lohner T., Polgár O., Vázsonyi É., Bársony I., Piel J. P. and Stehle J. L. *Characterization of different porous silicon structures by spectroscopic ellipsometry*, Thin Solid Films **276** (1996) 223-227.

- [19] Karlsson L. M., Tengvall P., Lundström I. and Arwin H. *Penetration and loading of human serum albumin in porous silicon layers with different pore sizes and thicknesses*, Journal of Colloid and Interface Science **266** (2003) 40-47.
- [20] Boukherroub R., Wayner D., Lockwood D. et al. *Passivated luminescent porous silicon*, Journal of the Electrochemical Society **148** (2001) 91-96.
- [21] *Guide to Using WVASE<sup>®</sup>*, J. A. Woollam Co. Inc., 2003.

### §3.4

- [22] Harada A. and Kataoka K. *Supramolecular assemblies of block copolymers in aqueous media as nanocontainers relevant to biological applications*, Progress in Polymer Science **31** (2006) 949-982.
- [23] Westphal P. and Bornmann A. *Biomolecular detection by surface plasmon enhanced ellipsometry*, Sensors and Actuators B **84** (2002) 278-282.
- [24] Starodub N. F., Nabok A. V. and Starodub V. M. *Immobilization of biocomponents for immune optical sensors*, Ukrainian Bio-Chemical Journal **73** (2001) 55-64.

### §3.5

- [25] Eiggins B. *Biosensors: an introduction*, John Wiley & Sons, Chichester, England, 1996.
- [26] Turková J. *Oriented immobilization of biologically active proteins as a tool for revealing protein interactions and function*, Journal of Chromatography B **722** (1999) 11-31.
- [27] Cao L. *Immobilised enzymes: science or art?* Current Opinion in Chemical Biology **9** (2005) 217-226.
- [28] Bilitewski U. *Protein-sensing assay formats and devices*, Analytica Chimica Acta **568** (2006) 232-247.
- [29] Cosnier S. *Biomolecule immobilization on electrode surfaces by entrapment or attachment to electrochemically polymerized films. A review*, Biosensors and Bioelectronics **14** (1999) 443-456.
- [30] Decher G., Hong J. D. and Schmitt J. *Buildup of ultrathin multilayer films by a self-assembly process: III. Consecutively alternating adsorption of anionic and cationic polyelectrolytes on charged surfaces*, Thin Solid Films **210-211** (1992) 831-835.
- [31] Decher G., Lvov Y. and Schmitt J. *Proof of multilayer structural organization in self-assembled polycation-polyanion molecular films*, Thin Solid Films **244** (1994) 772-777.
- [32] Lvov Y., Decher G. and Moehwald H. *Assembly, structural characterization, and thermal behavior of layer-by-layer deposited ultrathin films of poly(vinyl sulfate) and poly(allylamine)*, Langmuir **9** (1993) 481-486.
- [33] Mello L. D. and Kubota L. T. *Review of the use biosensors as analytical tools in the food and drink industries*, Food Chemistry **77** (2002) 237-256.
- [34] Sastry M., Rao M. and Ganesh K. N. *Electrostatic assembly of nanoparticles and biomacromolecules*, Accounts of Chemical Research **35** (2002) 847-855.
- [35] Sukhorukov G. B., Möhwald H., Decher G. and Lvov Y. M. *Assembly of polyelectrolyte multilayer films by consecutively alternating adsorption of polynucleotides and polycations*, Thin Solid Films **284-285** (1996) 220-223.

- [36] Zhang X. and Shen J. C. *Self-assembled ultrathin films: from layered nanoarchitectures to functional assemblies*, *Advanced Materials* **11-13** (1999)1139-1143.
- [37] Decher G. *Fuzzy nanoassemblies: toward layered polymeric multicomposites*, *Science* **277** (1997) 1232-1237.
- [38] Forzani E. S., Otero M., Pérez M. A., Teijelo M. L. and Calvo E. J. *The structure of layer-by-layer self-assembled glucose oxidase and Os(Bpy)<sub>2</sub>ClPyCH<sub>2</sub>NH-poly(allylamine) multilayers: ellipsometric and quartz crystal microbalance studies*, *Langmuir* **18** (2002) 4020-4029.
- [39] Lvov Y., Ariga K., Onda M., Ichinose I. and Kunitake T. *A careful examination of the adsorption step in the alternate layer-by-layer assembly of linear polyanion and polycation*, *Colloids and Surfaces A* **146** (1999) 337-346.
- [40] Caruso F., Niikura K., Furlong D. N. and Okahata Y. *1. Ultrathin multilayer polyelectrolyte films on gold: Construction and thickness determination*, *Langmuir* **13** (1997) 3422-3426.
- [41] Ramsden J. J., Lvov Yu. M. and Decher G. *Determination of optical constants of molecular films assembled via alternate polyion adsorption*, *Thin Solid Films* **254** (1995) 246-251.
- [42] Nabok A. V., Hassan A. K., Ray A. K. and Toldi G. N. *Electrical study of polyelectrolyte self-assembled films using mercury probe*, *Materials Science and Engineering C* **22** (2002) 387-391.
- [43] Ariga K., Lvov Y. and Kunitake T. *Assembling alternate dye-polyion molecular films by electrostatic layer-by-layer adsorption*, *Journal of American Chemical Society* **119** (1997) 2224-2231.
- [44] Lvov Y. M. and Decher G. *Assembly of multilayer ordered films by alternating adsorption of oppositely charged macromolecules*, *Crystallography Reports* **39** (1994) 628-647.
- [45] Lvov Y., Ariga K., Ichinose I. and Kunitake T. *Assembly of multicomponent protein films by means of electrostatic layer-by-layer adsorption*, *Journal of American Chemical Society* **117** (1995) 6117-6123.
- [46] Nabok A. V., Ray A. K., Starodub N. F. and Dowker K. P. *Enzyme/indicator optrodes for detection of heavy metal ions and pesticides*, *Proceedings SPIE – Biochemical and Biomolecular Sensing* **4200** (2000) 32-41.
- [47] Ai H., Jones S. A. and Lvov Y. M. *Biomedical applications of electrostatic layer-by-layer nano-assembly of polymers, enzymes, and nanoparticles*, *Cell Biochemistry and Biophysics* **39** (2003) 23-43.
- [48] Ladam G., Schaaf P., Decher G., Voegel J.-C. and Cuisinier F. J. G. *Protein adsorption onto auto-assembled polyelectrolyte films*, *Biomolecular Engineering* **19** (2002) 273-280.
- [49] Starodub N. F., Pirogova L. V., Demchenko A. and Nabok A. V. *Antibody immobilisation on the metal and silicon surfaces. The use of self-assembled layers and specific receptors*, *Bioelectrochemistry* **66** (2005) 111-115.
- [50] Cassier T., Lowack K. and Decher G. *Layer-by-layer assembled protein/polymer hybrid films: nanoconstruction via specific recognition*, *Supramolecular Science* **5** (1998) 309-315.
- [51] Caruso F., Niikura K., Furlong D. N. and Okahata Y. *1. Ultrathin multilayer polyelectrolyte films on gold: Construction and thickness determination*, *Langmuir* **13** (1997) 3422-3426.
- [52] Minshi An, Jong-Dal Hong, Kyung-Sang Cho, Sun-Mi Yoon, Eun-Sung Lee, Byung Ki Kim, Jae-Young Choi *Spin-coating electrostatic self-assembly: Fabrication method for CdSe nanoparticle monolayer*, *Bulletin of the Korean Chemical Society* **27** (2006) 1119-1120.

- [53] Liu H. A., Zhai J. and Jiang L. *The research progress in self-assembly of nano-materials*, Chinese Journal of Inorganic Chemistry **22** (2006) 585-597.
- [54] Hao Konga, Ping Luoa, Chao Gao and Deyue Yan *Polyelectrolyte-functionalized multiwalled carbon nanotubes: preparation, characterization and layer-by-layer self-assembly*, Polymer **46** (2005) 2472-2485.
- [55] De Gennes P.-G. *Scaling concepts in polymer physics*, Cornell University Press, 1979.
- [56] Nabok A. *Organic and inorganic nanostructures*, Artech House, Boston – London, USA, 2005.
- [57] Qinghong Shi, Ying Zhou and Yan Sun *Influence of pH and ionic strength on the steric mass-action model parameters around the isoelectric point of protein*, Biotechnology Progress **21** (2005) 516-523.
- [58] Abdel Magid H. M and El Mahi Y. *In vitro effects of urease inhibitors on rate of urea hydrolysis in soils*, Nutrient Cycling in Agroecosystems **8** (1986) 203-212.
- [59] Das P. K. and Liddell J. *Purification and properties of human serum cholinesterase*, Biochemical Journal **116** (1970) 875-881.
- [60] Salerno M. B., Rothstein S., Nwachukwu C., Shelbi H., Velegol D. and Logan B. E. *Differences between chemisorbed and physisorbed biomolecules on particle deposition to hydrophobic surfaces*, Environmental Science and Technology **39** (2005) 6371-6377.
- §3.6
- [61] Nabok A., Haron S. and Ray A. *Registration of heavy metal ions and pesticides with ATR planar waveguide enzyme sensors*, Applied Surface Science **238** (2004) 423-428.
- [62] Shirshov Yu. M., Svechnikov S. V., Kiyanovskii A. P., Ushenin Yu.V., Venger E. F., Samoylov A. V. and Merker R. *A sensor based on the planar-polarization interferometer*, Sensors and Actuators A **68** (1998) 384-387.
- [63] Mendelsohn J. D., Barrett C. J., Chan V. V., Pal A. J., Mayes A. M. and Rubner M. F. *Fabrication of microporous thin films from polyelectrolyte multilayers*, Langmuir **16** (2000) 5017-5023.
- [64] Lvov Yu., Ariga K. and Kunitake T. *Assembly of multicomponent protein films by means of electrostatic layer-by-layer adsorption*, Journal of American Chemical Society **117** (1995) 6117-6123.
- [65] <http://www.millipore.com/catalogue.nsf/docs/C7665> (accessed 7 February 2007).
- [66] Poh B.-L. and Lim P. *Complexations of metal cations with cyclotetrachromotrolylene in water and methanol*, Tetrahedron **46** (1990) 4379-4386.
- [67] Nabok A. V., Ray A. K., Starodub N. F. and Dowker K. P. *Enzyme/indicator optodes for detection of heavy metal ions and pesticides*, Proceedings of SPIE – Biochemical and Biomolecular Sensing **4200** (2000) 32-41.
- [68] [http://www.uni-regensburg.de/Fakultaeten/nat\\_Fak\\_IV/Organische\\_Chemie/Didaktik/Keusch/D-Urease-e.htm](http://www.uni-regensburg.de/Fakultaeten/nat_Fak_IV/Organische_Chemie/Didaktik/Keusch/D-Urease-e.htm) (accessed 6 March 07).
- [69] Andreescu S. and Marty J.-L. *Twenty years research in cholinesterase biosensors: from basic research to practical applications*, Biomolecular Engineering **23** (2006) 1-15.

- [70] Haron S. *Planar waveguide enzyme sensors coated with nanocomposite membranes for water pollution monitoring*, Thesis for the degree of Doctor of Philosophy, Sheffield Hallam University, 2005.
- [71] El-Sherif H., Martelli P. L., Casadio R., Portaccio M., Bencivenga U. and Mita D. G. *Urease immobilisation on chemically grafted nylon membranes: Part I: Isothermal characterisation*, *Journal of Molecular Catalysis B* **14** (2001) 15-29.
- [72] Bachmann T. T., Leca B., Vilatt F., Marty J.-L., Fournier D. and Schmid R. D. *Improved multianalyte detection of organophosphates and carbamates with disposable multielectrode biosensors using recombinant mutants of *Drosophila acetylcholinesterase* and artificial neural networks*, *Biosensors and Bioelectronics* **15** (2000) 193-201.
- [73] Reder S., Dieterle F., Jansen H., Alcock S. and Gauglitz G. *Multi-analyte assay for triazines using cross-reactive antibodies and neural networks*, *Biosensors and Bioelectronics* **19** (2003) 447-455.
- [74] Rudnitskaya A., Ehlert A., Legin A., Vlasov Yu. and Büttgenbach S. *Multisensor system on the basis of an array of non-specific chemical sensors and artificial neural networks for determination of inorganic pollutants in a model groundwater*, *Talanta* **55** (2001) 425-431.
- [75] Gutés A., Céspedes F., Alegret S. and del Valle M. *Determination of phenolic compounds by a polyphenol oxidase amperometric biosensor and artificial neural network analysis*, *Biosensors and Bioelectronics* **20** (2005) 1668-1673.

### §3.7

- [76] Tran Minh C. *Biosensors*, Chapman & Hall, 1993.
- [77] <http://chemistry.umeche.maine.edu/CHY431/Chorismate5.html> (accessed 29 October 2006).
- [78] Hall E. *Biosensors*, Open University Press, Milton Keynes, 1990.
- [79] Eggins B. *Biosensors: an introduction*, Wiley & Teubner, Stuttgart, 1996.
- [80] Xia Liu, Jingyan Wei, Daqian Song, Ziwei Zhang, Hanqi Zhang and Guimin Luo *Determination of affinities and antigenic epitopes of bovine cardiac troponin I (cTnI) with monoclonal antibodies by surface plasmon resonance biosensor*, *Analytical Biochemistry* **314** (2003) 301-309.

# *CHAPTER 4.*

## **RESULTS and DISCUSSIONS**

The experimental results and data analysis are presented and discussed here.

## 4.1 Protein Adsorption into Porous Silicon: Ellipsometric Study

### 4.1.1 Characterisation of porous silicon layers

The porous layers were characterized with respect to the pore size, porous layer thickness, and porosity using scanning electron microscopy (SEM), atomic force microscopy (AFM), and variable angle spectroscopic ellipsometry.

The SEM images in Figure 4.1-1 show a “net-like” structure of the PS surface with flat islands separated by deep trenches. The AFM image zoomed in on the flat top of the island shows a nanoporous sponge-like structure (see Figs. 4.1-2a and 4.1-2b).

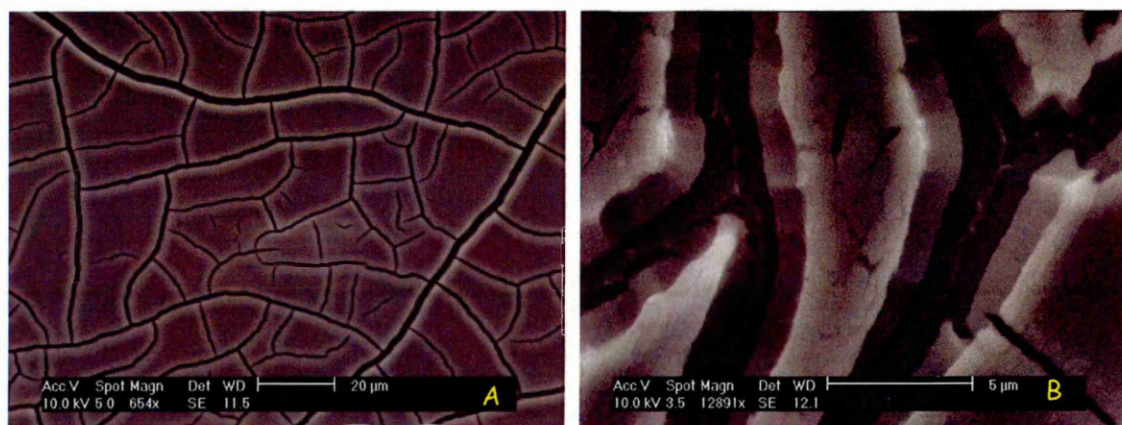


**Figure 4.1-1** SEM images of porous silicon (plane view): **A** – scan size 20  $\mu\text{m}$ ; **B** – a zoomed in image of the sample (scan size 5  $\mu\text{m}$ )

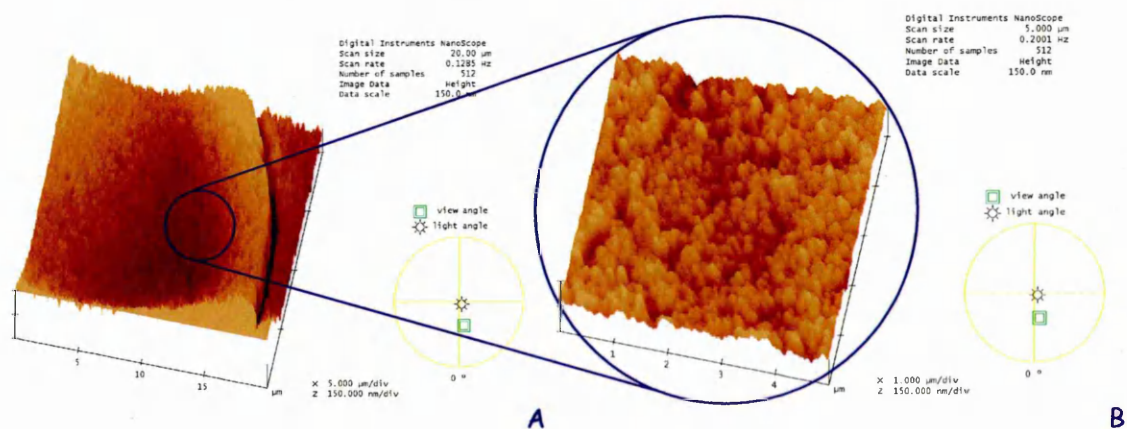


**Figure 4.1-2** Pseudo 3-D AFM images of porous silicon: **A** – scan size 20  $\mu\text{m}$ ; **B** – a zoomed in image of the sample (scan size 5  $\mu\text{m}$ ).

The pore sizes in the range of 30–100 nm were evaluated from these images. The cross-section SEM image, presented in Fig. 4.1-3, allows the estimation of the pore depth and thus the total PS layer thickness in the range of 1  $\mu\text{m}$ .

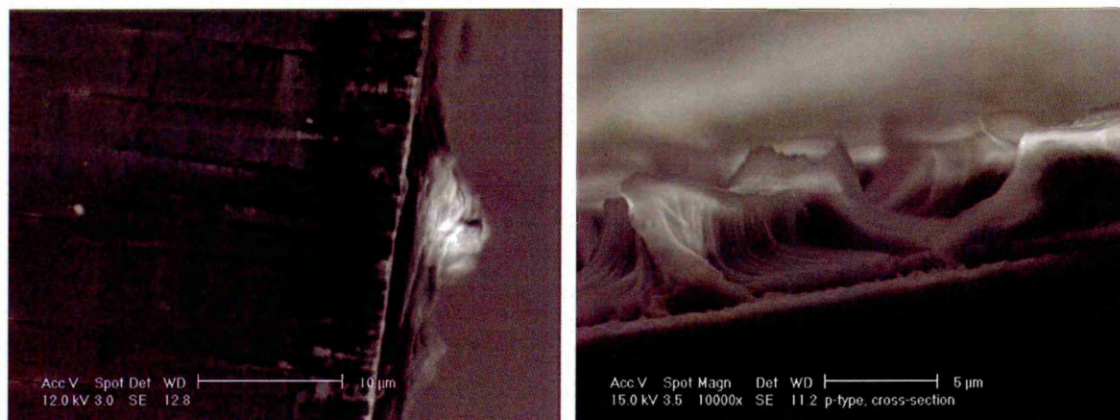


**Figure 4.1-3** SEM images of cleaved PS/Si samples (cross-section view).

Mean values of the pore size and depth are summarised in the Table 4.1-1.

**Table 4.1-1** Pore size and depth for PS samples (based on SEM and AFM data).

<i>Morphology features</i>	<i>Pore size</i>	<i>Pore depth</i>
“Trenches”	0.22 $\mu\text{m}$ – 8.20 $\mu\text{m}$	0.50 $\mu\text{m}$ – 1.53 $\mu\text{m}$
“Sponge”	30 – 100 nm	20 – 150 nm

Figure 4.1-4 shows typical ellipsometric spectra  $\Delta(\lambda)$  and  $\Psi(\lambda)$  measured at an angle of incidence of  $68^\circ$  of a porous layer with a porosity of 68% and a thickness of 0.85  $\mu\text{m}$ .

Analysis of the experimental data using WVASE32<sup>®</sup> software yields the following five level model with three effective medium approximation (EMA) sub-layers for porous silicon:

1. Si substrate/ 2. EMA/ 3. EMA/ 4. EMA/ 5. Ambient.

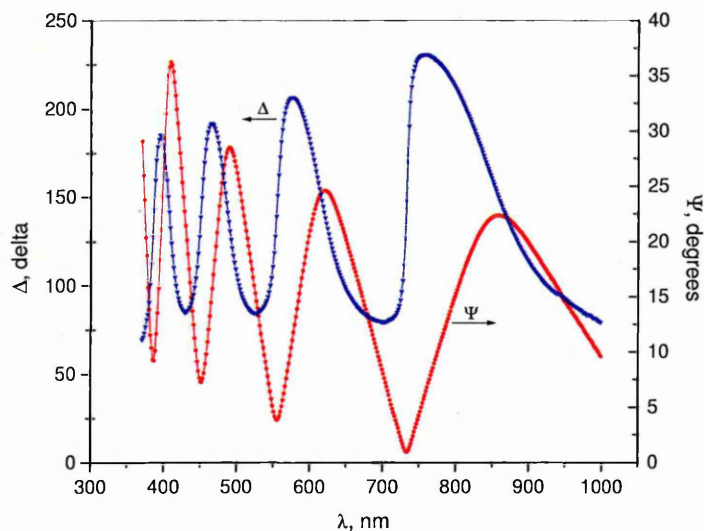


**Figure 4.1-4** Typical ellipsometric spectra  $\Delta(\lambda)$  and  $\Psi(\lambda)$  of porous silicon samples without any adsorbent.

Each EMA sub-layer consists of silicon and voids filled with the aqueous ambient (Trizma/HCl buffer) with a refractive index of  $n = 1.33$  at  $\lambda = 633$  nm. The parameters of each layer are shown in Figure 4.1-5.

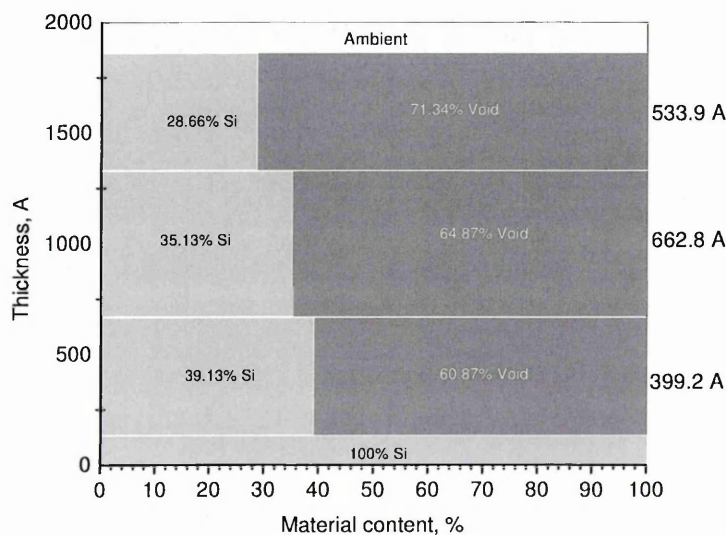


**Figure 4.1-5** Five-layer model (with three EMA sub-layers) of PS sample with pores filled with Trizma/HCl buffer solution. The numbers to the right are the thickness of the sub-layers.

For every sample, the obtained values of the thickness of each EMA layer were kept fixed in further data fitting after adsorption. The result of fitting is mathematically unique. This was established by performing fitting started from different initial sets of parameters.

It should be noted that no reasonable fitting can be obtained either with a single layer or two-layer EMA model. The three-layer model is the most likely mathematical representation of a complex structure of porous silicon containing features in both micro- and nano- meter scales. The total thickness of the PS layer correlates well with the SEM data.

The porosity was found to decrease towards the bulk Si layer, which corresponds well to the PS structure, observed with SEM and AFM as well as to the results obtained by other research groups. The porosity of the PS layers was also determined independently with the gravimetric method<sup>[1]</sup>:

$$p = \frac{\Delta P}{2 \cdot \rho \cdot d \cdot S} \times 100\% , \quad (4.1)$$

where  $\Delta P$  is changes in the sample weight before and after etching;  $\rho$  is the density of the material (Si);  $d$  is PS layer thickness;  $S$  is area of the specimen. This estimation yields porosity values in the range of 56 – 77% (for different samples) with the accuracy of about 10%.

#### 4.1.2 Adsorption of BSA: static ellipsometric study

Figure 4.1-6a shows typical ellipsometric  $\Psi(\lambda)$  and  $\Delta(\lambda)$  spectra before and after adsorption of BSA into the PS layer. The observed spectral shift towards longer wavelengths is believed to be caused by adsorption of BSA. Because the BSA layer has a different refractive index to silicon a three-component EMA model with silicon, protein, and void should be used in the modelling.

This concept was confirmed by fitting the experimental results to a five-layer model: Si substrate/ 1.EMA/ 2.EMA/ 3.EMA/ Ambient. An extra component appeared in all three EMA sub-layers (see Figure 4.1-6b). For the data recorded after protein adsorption, the silicon parameters were fixed to the values found without protein.

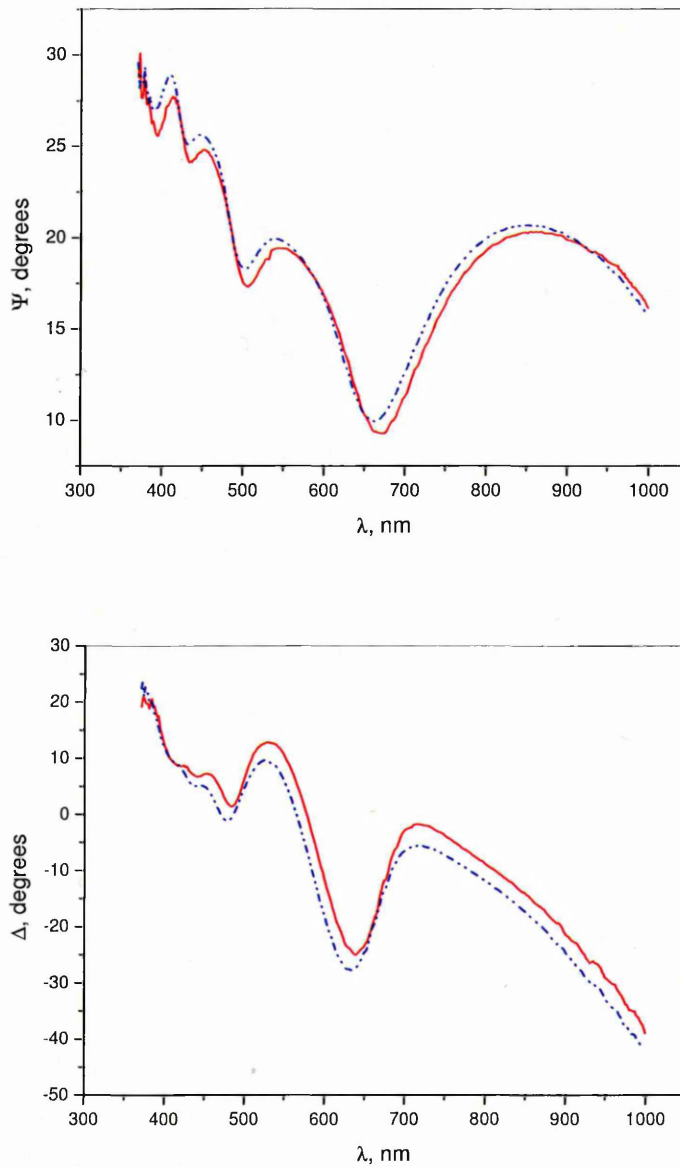


**Figure 4.1-6a** Ellipsometric  $\Psi(\lambda)$  and  $\Delta(\lambda)$  spectra before (dot) and after (line) BSA adsorption into the PS layer.

A Cauchy dispersion function was deployed for fitting the additional adsorbed layer<sup>[2]</sup>:

$$n(\lambda) = A_n + \frac{B_n}{\lambda^2} + \frac{C_n}{\lambda^4}, \quad (4.2)$$

where the values  $A_n = 1.396$ ,  $B_n = 0.01$  and  $C_n = 0$  were fixed during fitting as well as a zero value for the extinction coefficient ( $k$ ). This gives a value of refractive index  $n$  of 1.42 at  $\lambda = 633$  nm, which is typical for proteins and polyelectrolytes.

The percentage of the adsorbed BSA layer was evaluated and presented on the diagram in Figure 4.1-6b. Small variations of  $\pm 0.005$  of the parameter  $A_n$  did not cause significant changes in the results. It is logical that the presence of the adsorbed layer of BSA has just slightly altered the porosity of the PS. Yet, the fact that the upper PS layers contain more BSA than the layers below is physically likely.

The general observation is that the BSA molecules are located throughout the porous layer but with the larger volume fraction closer to the surface.

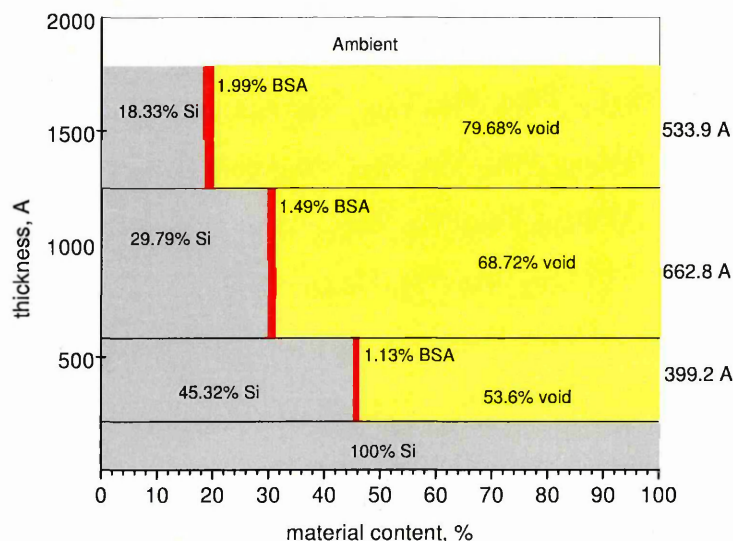


**Figure 4.1-6b** Five-layer model of a PS sample after BSA adsorption.

### 4.1.3 Influence of polyelectrolytes on BSA adsorption

The idea of stabilisation of the surface of PS by its chemical modification<sup>[3]</sup> was further developed here by using the adsorption of polyelectrolytes. Both types of polyelectrolytes, i.e. polycationic (PAH) and polyanionic (PSS), are supposed to form strong Coulomb interaction with the PS surface containing both  $\text{OH}^-$  and  $\text{H}^+$  groups as respective binding centres.

Ellipsometric  $\Delta(\lambda)$  and  $\Psi(\lambda)$  spectra measured on fresh PS samples (dot) and after adsorption of PSS/BSA or PAH/BSA into the PS layer (line) are shown in Figures

4.1-7a and 4.1-8a, respectively. It should be noted that adsorption of either PAH or PSS alone does not significantly change the ellipsometric spectra, because of a very small thickness of adsorbed polyelectrolyte monolayers.

Similarly, the results in Fig. 4.1-6a, both graphs in Figs. 4.1-7a and 4.1-8a showed a shift towards longer wavelengths after adsorption of BSA. However, this time the shift is larger, which indicates more effective adsorption of BSA on top of intermediate PAH (or PSS) layers. The models for BSA adsorbed on PSS and PAH layers, shown in Figs. 4.1-7b and 4.1-8b respectively, demonstrated that the amount of immobilised BSA is much larger in comparison with that on bare PS (Fig. 4.1-6b), which is a result of electrostatic binding between polyelectrolytes and BSA molecules.

The total amount of BSA adsorbed on PAH was higher than that on PSS. This is quite understandable, since BSA was deposited from the Trizma/HCl buffer solution having pH 7.35, which is higher than the BSA iso-electric point (pH 4.9). In these conditions BSA is negatively charged due to the dominance of acidic groups over amine groups, so that electrostatic binding is more likely on the cationic PAH layers than on anionic PSS layers.

In all cases the distribution of the amount of adsorbed BSA is controlled by the permeation of the adsorbate (polyelectrolytes and BSA) and follows the porosity of PS, i.e. lower PS layers having low porosity contain less BSA and vice versa as the more porous top PS layer contains more BSA.

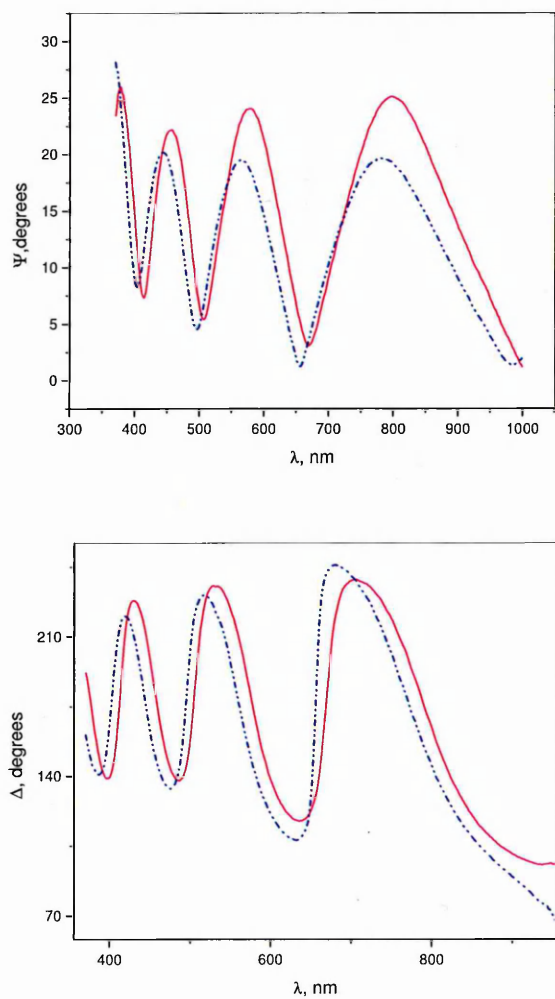


**Figure 4.1-7a** Ellipsometric  $\Psi(\lambda)$  spectra before (dot) and after (line) adsorption of PSS/BSA into the PS layer.

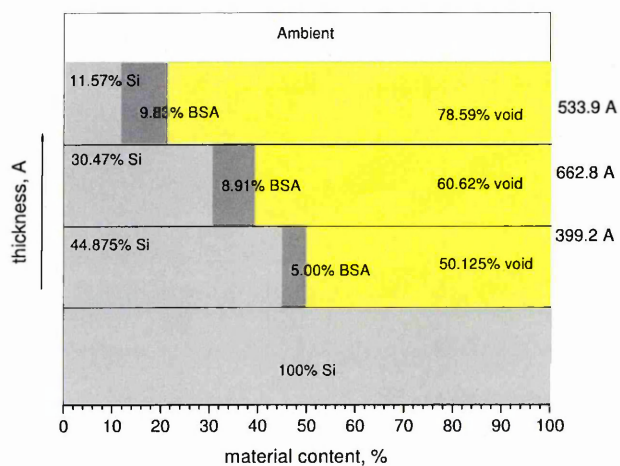


**Figure 4.1-7b** Five-layer model for BSA adsorbed on the PSS layer.

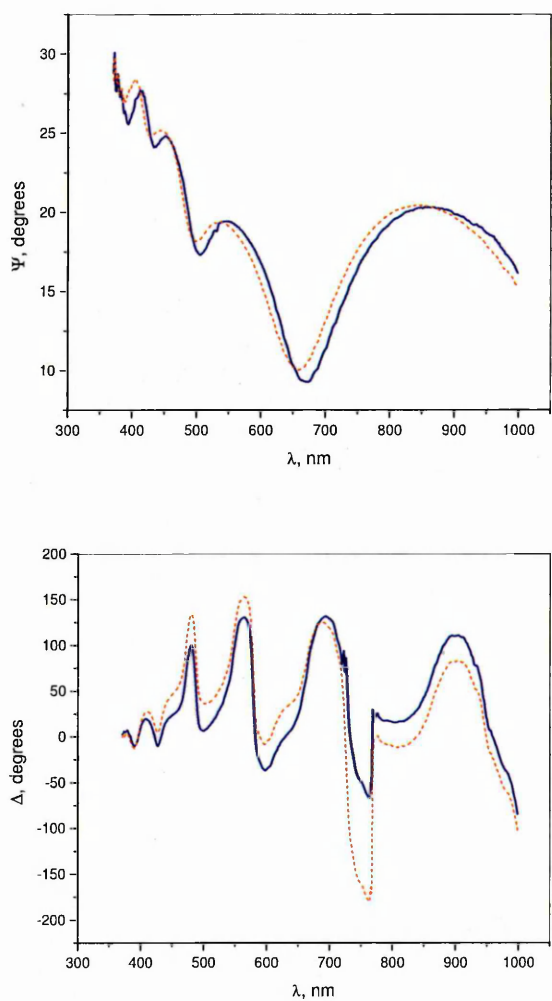


**Figure 4.1-8a** Ellipsometric  $\Psi(\lambda)$  spectra before (dot) and after (line) adsorption of PAH/BSA into the PS layer.

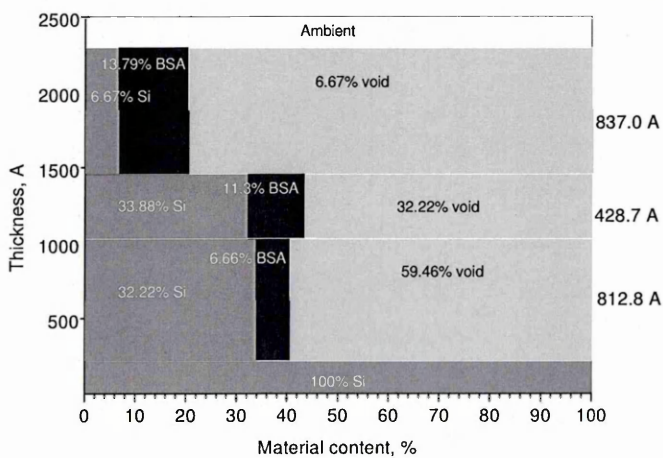


**Figure 4.1-8b** Five-layer model for BSA adsorbed on the PAH layer.

#### 4.1.4 Adsorption of BSA: dynamic study

The kinetics of BSA adsorption into porous silicon were also studied *in situ* by performing ellipsometric spectral measurements continuously. Fig. 4.1-9 shows  $\Delta$  as a function of time during adsorption of BSA into the PS substrate at the wavelength of 700 nm.

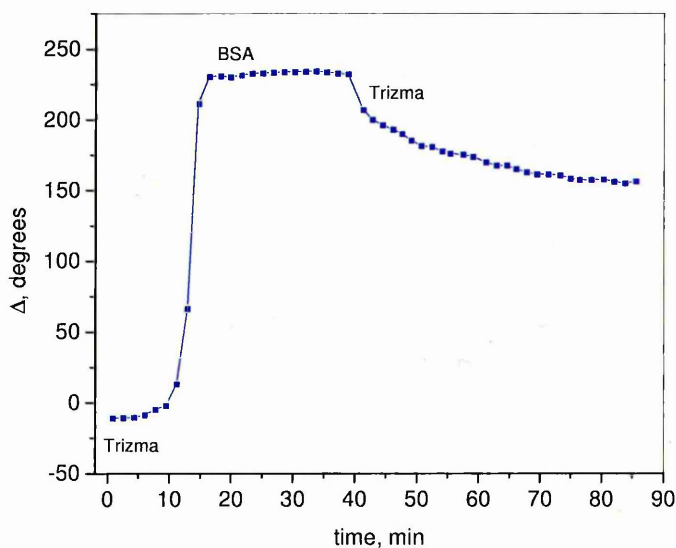


**Figure 4.1-9** Kinetics of adsorption of the BSA into the PS substrate measured by *in situ* ellipsometry at a wavelength of 700 nm.

It can be seen that, the injection of BSA into the cell causes quite a substantial increase in  $\Delta$  value. It should be taken into account that refractive indices of pure Trizma buffer and buffer solution containing BSA might be slightly different, which may cause a false ellipsometric response.

The whole process of adsorption lasts no more than 10 minutes. Flushing the cell with pure Trizma buffer solution results in a sharp drop of the signal, most likely caused by changes of the refractive index, followed by a slow reduction and final stabilisation of  $\Delta$  in the course of washing out weakly bound excessive BSA molecules. It is believed that the difference between initial and final values of  $\Delta$  represents a true response due to the adsorption of BSA.

The influence of intermediate layers of polyelectrolytes on adsorption of BSA was studied with kinetic ellipsometry measurements. The results for BSA adsorption on PSS and PAH layers are shown in Figs. 4.1-10 and 4.1-11, respectively. In contrast to the results in Fig. 4.1-9, the signal goes down at every consecutive injection of solutions. The spikes between injections are caused by the presence of air in the cell during changes of the solution and flushing the cell with Millipore water. Comparison of the initial and final stages of adsorption on these two graphs shows that the changes in  $\Delta$  for adsorption of BSA on PSS are larger than those for adsorption of BSA on PAH.

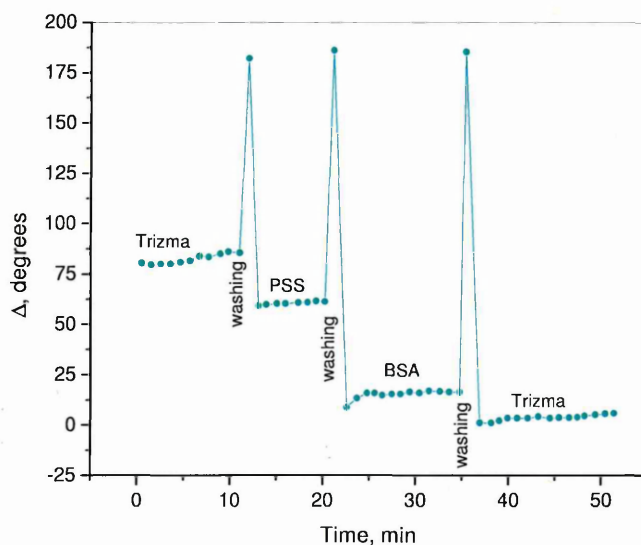


**Figure 4.1-10** Kinetics of adsorption of the PSS/BSA into the PS substrate measured by *in situ* ellipsometry at a wavelength of 700 nm.

Interpretation of the kinetic spectroscopic ellipsometry measurements is quite difficult. Apart from the above mentioned side effect of the refractive index of the environment, the response depends very much on the shape of the  $\Delta(\lambda)$  or  $\Psi(\lambda)$  spectra and the choice of the wavelength.

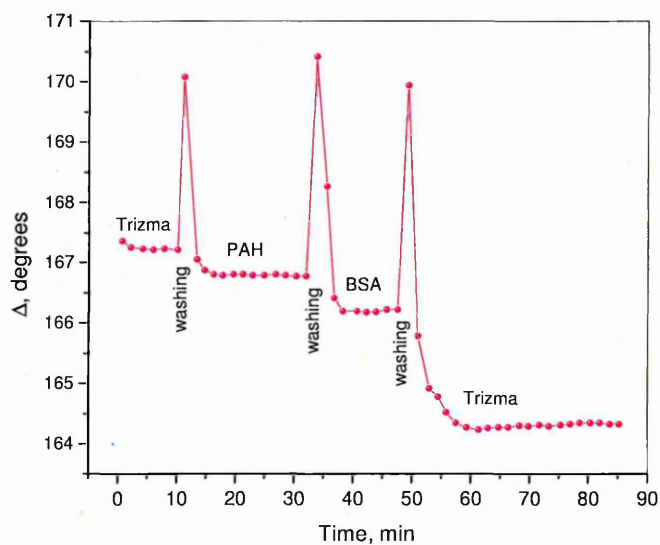


**Figure 4.1-11** Kinetics of adsorption of the PAH/BSA into the PS substrate measured *in situ* at a wavelength of 700 nm.

A schematic diagram in Fig. 4.1-12 demonstrates clearly that depending on the choice of the wavelength, the value of  $\Delta$  or  $\Psi$  may rise (1), fall (2) or even remain intact (3) in the course of adsorption. From this point of view, static spectroscopic ellipsometry measurements together with proper fitting provide more reliable information on adsorption of proteins.

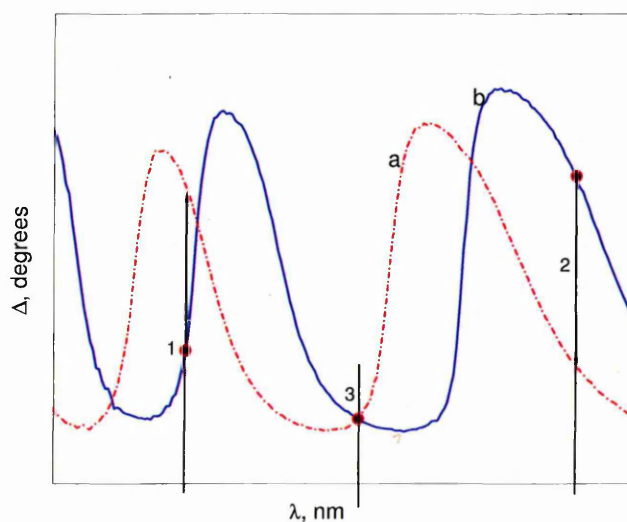


**Figure 4.1-12** Effect of the choice of  $\lambda$  on the kinetic ellipsometric measurement: **a** – initial  $\Delta(\lambda)$  spectrum; **b** – post-adsorption spectrum.

## 4.2 Registration of Low Molecular Weight Environmental Toxins with the Method of Total Internal Reflection Ellipsometry

Typical TIRE spectra of  $\Psi(\lambda)$  and  $\Delta(\lambda)$  measured on bare chromium-gold coated slides are shown in Figure 4.2-1. The  $\Psi(\lambda)$  spectrum, representing an amplitude ratio of  $p$ - and  $s$ - components of polarized light ( $\tan \Psi = A_p / A_s$ ) resembled very much the SPR curve. While the  $\Delta(\lambda)$  spectrum, representing the phase shift between  $p$ - and  $s$ - components ( $\Delta = \varphi_p - \varphi_s$ ), appeared in Fig. 4.2-1 as a nearly vertical drop in  $\Delta$  (from  $270^\circ$  down to  $-90^\circ$ ) which is a new quantity that does not exist in the SPR method. Because of the high sensitivity of  $\Delta(\lambda)$  spectra to molecular adsorption, they were exploited in the current work to study the specific binding of toxins.

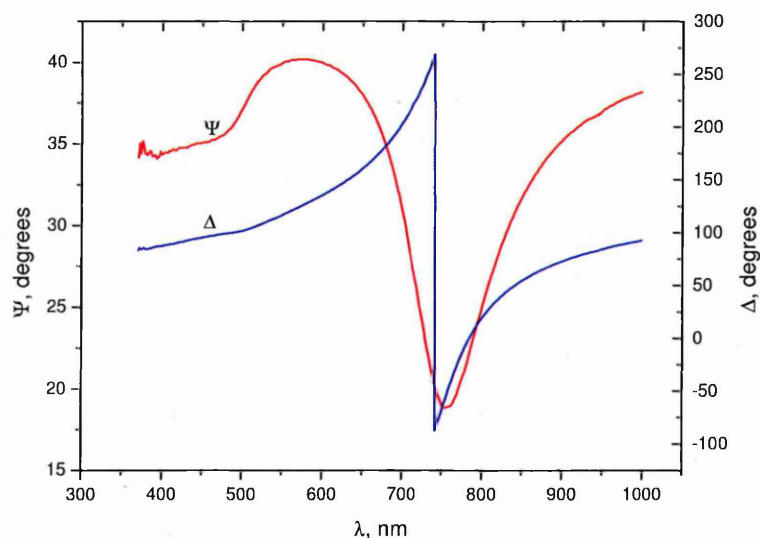
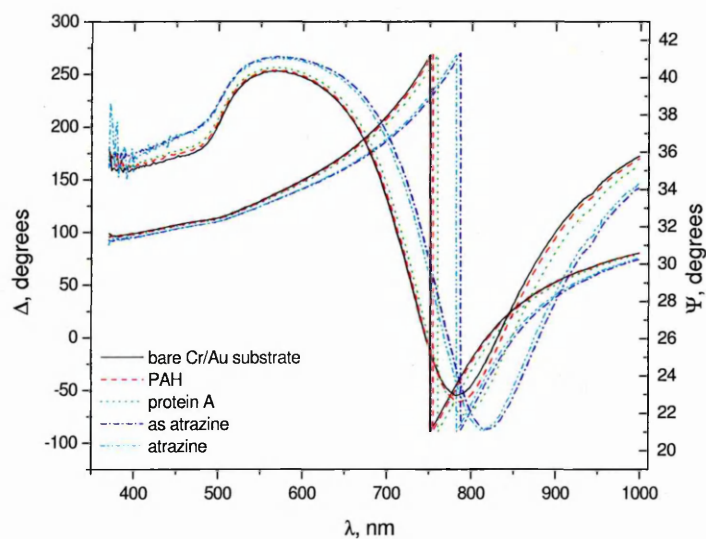


**Figure 4.2-1** Typical spectra of  $\Psi(\lambda)$  and  $\Delta(\lambda)$  obtained by the TIRE method.

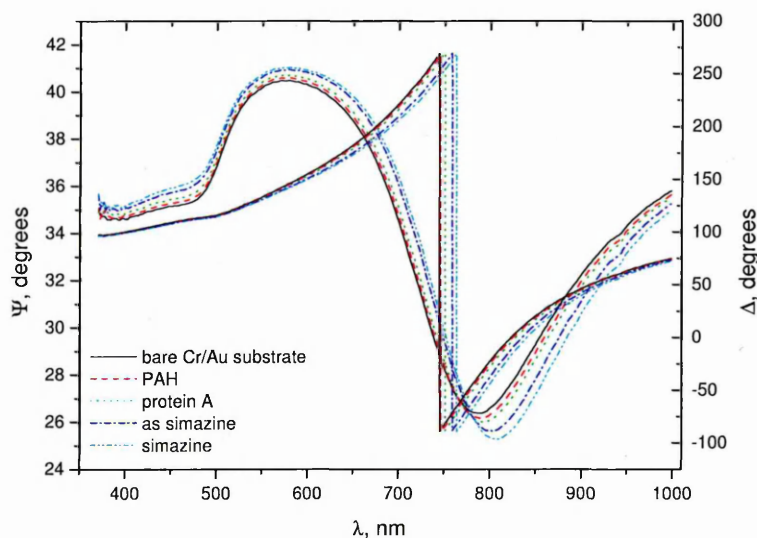
### 4.2.1 Simazine and atrazine registration

Typical transformations of TIRE spectra in the course of the adsorption sequences for *atrazine* and *simazine* are shown in Figure 4.2-2. All stages of adsorption

are well-resolved, with the spectral shift corresponding to the size of adsorbed molecules. For example, the largest shift of  $\Delta(\lambda)$  spectra is caused by adsorption of quite large antiserum to *atrazine* (as-*atrazine*) molecules.



a



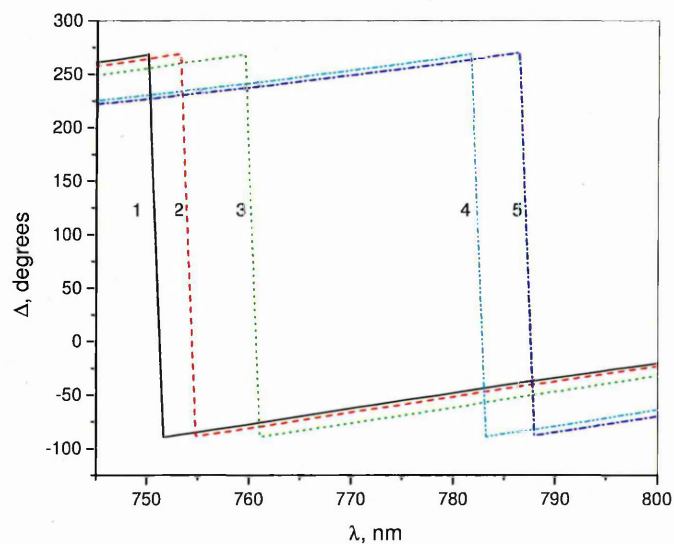
b

**Figure 4.2-2** A typical set of  $\Psi(\lambda)$  and  $\Delta(\lambda)$  TIRE spectra corresponding to the following sequence of adsorptions: **a** – bare Cr/Au substrate /PAH/ as-*atrazine*/*atrazine*; **b** – bare Cr/Au substrate /PAH/ as-*simazine*/*simazine*.

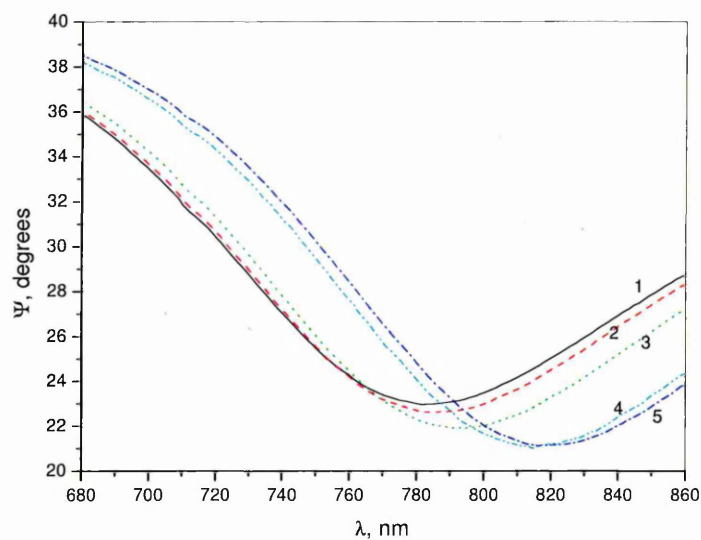
The enlargement of a section of  $\Psi(\lambda)$  and  $\Delta(\lambda)$  spectra (given in Fig. 4.2-3), shows a larger shift of  $\Delta(\lambda)$  curves as compared to  $\Psi(\lambda)$  in response to adsorption of as-

*atrazine* and specific binding of *atrazine*. Further analysis and fitting of TIRE data were performed using  $\Delta(\lambda)$  spectra.

Similar results were obtained for *simazine* (see Figure 4.1-4).

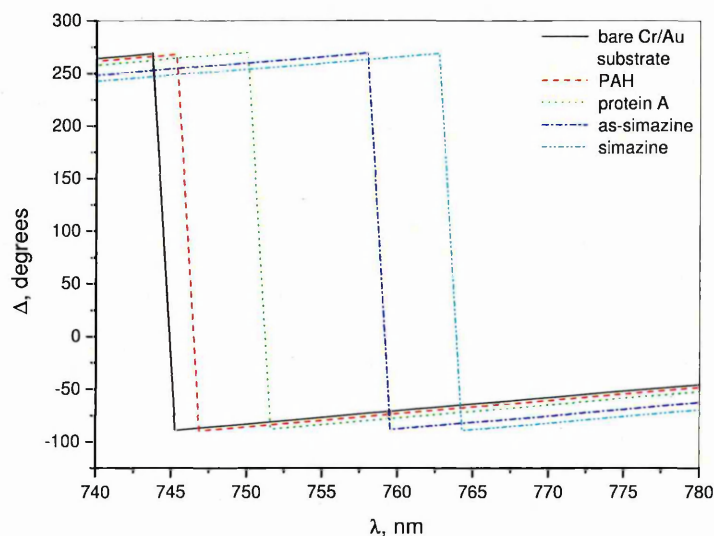


**a**

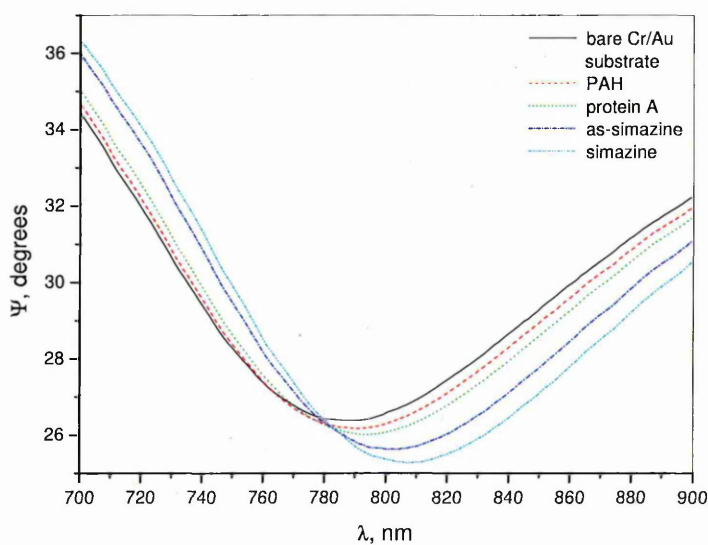


**b**

**Figure 4.2-3** Enlargement of a section of  $\Delta(\lambda)$  (a) and  $\Psi(\lambda)$  (b) TIRE spectra. Numbers near the spectra correspond to the following sequence of adsorptions 1 – bare Cr/Au substrate, 2 – PAH, 3 – protein A, 4 – antiserum to *atrazine*, and 5 – *atrazine*.



a



b

**Figure 4.2-4** Enlargement of a section of  $\Delta(\lambda)$  (a) and  $\Psi(\lambda)$  (b) TIRE spectra corresponding to the following sequence of adsorptions: bare Cr/Au substrate /PAH /as-simazine /simazine.

The adsorption of quite small *atrazine* molecules, with a molecular weight of 215.7 g/mol, resulted in a noticeable spectral shift. In contrast to that, SPR measurements performed on the same samples, and following a similar sequence of absorptions, gave much smaller, almost unnoticeable, shifts of SPR curves, as illustrated

by Fig. 4.2-5. This provided strong evidence of the high sensitivity of the TIRE method as compared to the conventional Kretschmann SPR technique.

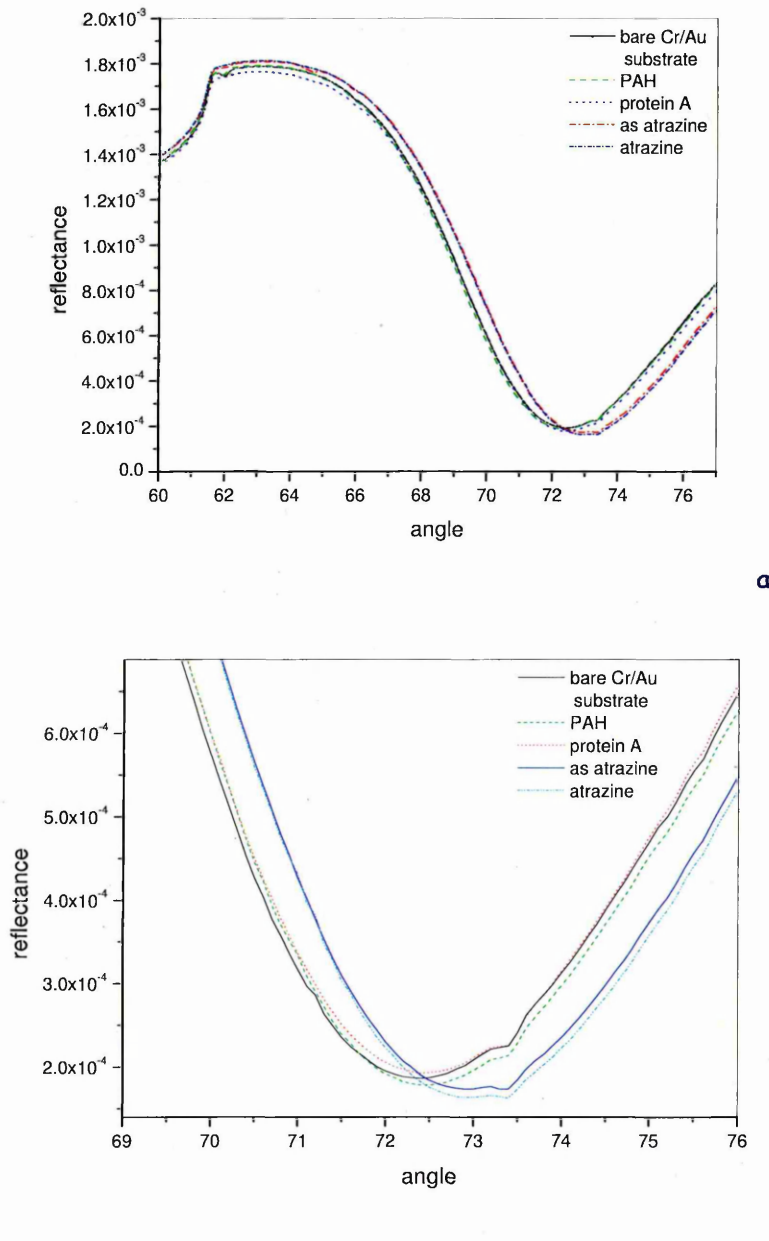


**Figure 4.2-5** A set of SPR curves corresponding to the following sequence of adsorptions: **a** – initial Cr/Au substrate/PAH/as-atrazine/atrazine; **b** – enlargement of a section of the SPR spectra.

Fitting of the experimental spectra of  $\Psi(\lambda)$  and  $\Delta(\lambda)$  was carried out using a four-layer model: aqueous Trizma/HCl buffer solution – Cauchy layer – Cr/Au substrate – BK7 glass. A Cauchy dispersion function (Eq. 3-6, §3.2) was deployed for the fitting of

the adsorbed organic and biomaterial layers. The values  $A_n = 1.396$ ,  $B_n = 0.01$  and  $C_n = 0$  were fixed during the fitting. This gave the value of the refractive index of 1.42 at  $\lambda = 633$  nm, which is typical for proteins and polyelectrolytes.

The obtained thicknesses of the chromium/gold layer and all of the Cauchy layers are summarised in Table 4.2-1. The fitting was performed several times for every sample yielding slightly different values. Thus, the accuracy of the obtained thickness values was found to be in the range of 1 – 3%. The data presented in Table 4.2-1 show a consistent increase in the thickness of layers following the adsorption sequence. In the final step, the changes in thickness due to binding of toxins were found to be of 4.71 nm and 5.77 nm for *atrazine* and *simazine*, respectively.

**Table 4.2-1** Results of the TIRE data fitting.

<i>layer content</i>	<i>Cr/Au substrate</i>	<i>PAH</i>	<i>protein A</i>	<i>antiserum to atrazine</i>	<i>atrazine</i>
<i>thickness, nm</i>					
$d_{Cr/Au}$	30.309±0.168	–	–	–	–
$d_{Cauchy}$	–	4.303±0.043	7.721±0.012	9.204±0.184	13.915±0.313
$\delta d_{Cauchy}$	–	–	–	–	4.711

<i>layer content</i>	<i>Cr/Au substrate</i>	<i>PAH</i>	<i>protein A</i>	<i>antiserum to simazine</i>	<i>simazine</i>
<i>thickness, nm</i>					
$d_{Cr/Au}$	29.077±0.365	–	–	–	–
$d_{Cauchy}$	–	3.255±0.033	8.582±0.150	12.207±0.214	17.981±0.794
$\delta d_{Cauchy}$	–	–	–	–	5.774

The results of the fitting of the SPR data are presented in Table 4.2-2. A noticeable change in thickness of 2.731 nm due to binding of *atrazine* was registered. The obtained value does not accord with that given in Table 4.2-1 (4.711 compared to 2.83), possibly because of the lower sensitivity of SPR measurements and difficulties in fitting SPR data.

**Table 4.2-2** Results of the SPR data fitting.

	<i>Cr/Au</i> <i>substrate</i>	<i>PAH</i>	<i>protein A</i>	<i>antiserum to</i> <i>atrazine</i>	<i>atrazine</i>
<i>Cr/Au</i>	$n = 0.251$	$n = 0.263$	$n = 0.260$	$n = 0.267$	$n = 0.286$
<i>substrate</i>	$k = 3.282$	$k = 3.312$	$k = 3.313$	$k = 3.336$	$k = 3.400$
	$d^a = 36.013$	$d = 35.475$	$d = 35.655$	$d = 35.303$	$d = 34.486$
<i>Organic</i>	$n = 1.4$	$n = 1.4$	$n = 1.4$	$n = 1.4$	$n = 1.4$
<i>film</i>	$d = 0.422$	$d = 1.952$	$d = 2.973$	$d = 6.918$	$d = 9.748$
<i>MSE</i>	3.845	3.509	4.256	4.003	3.790
$\delta d, nm$	–	–	–	–	2.83

Preliminary experiments with *simazine* and *atrazine* proved the feasibility of the TIRE method, which could be applied for the registration of *T-2 mycotoxin* which has a larger molecular weight than *simazine* or *atrazine*.

## 4.2.2 T-2 mycotoxin registration

### 4.2.2.1 TIRE and SPR measurements

A typical set of TIRE  $\Delta(\lambda)$  spectra in the course of consecutive adsorption steps of PAH, protein A and *T-2 mycotoxin* antibodies (polyclonal or monoclonal<sup>b</sup>), as well as consecutive binding steps of *T-2 mycotoxin* of increasing concentrations (in the range of 0.15 ng/ml – 1500 ng/ml) are shown in Fig. 4.2-6.

All stages of adsorption are well resolved, with the spectral shift corresponding to the size of adsorbed molecules. For example, the largest shift of  $\Delta(\lambda)$  spectra is caused by the adsorption of large monoclonal antibody molecules. The adsorption of quite small *T-2 mycotoxin* molecules in the lowest concentration of 0.15 ng/ml resulted in a noticeable spectral shift.

<sup>a</sup> The values of  $d$  are given in *nm*.

<sup>b</sup> Henceforth referred as mono- or poly- AB, correspondingly.

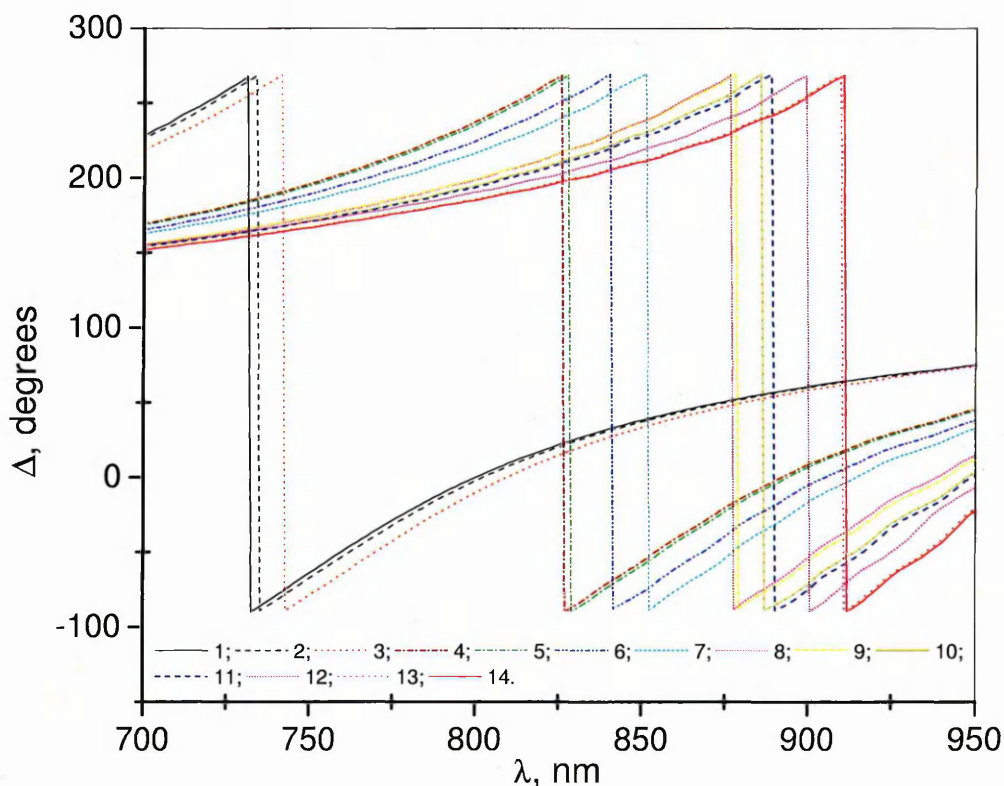


**Figure 4.2-6** A typical set of  $\Delta(\lambda)$  spectra for an initial bare Cr/Au surface (1), after the consecutive adsorption steps of PAH (2), protein A (3), monoclonal antibodies (4), and after binding of *T-2 mycotoxin* from solutions of different concentrations in ng/ml: 0.15 (5), 1.5 (6), 7.5 (7), 15 (8), 75 (9), 150 (10), 300 (11), 600 (12), 1200 (13), and 1500 (14).

A gradual shift of the  $\Delta(\lambda)$  spectra was observed in the course of *T-2 mycotoxin* binding. Such experiments were repeated several times using both poly- and mono-AB. The set of  $\Psi(\lambda)$  spectra (shown in Fig. 4.2-7) corresponding to the same sequence of adsorptions gave a much smaller spectral shift, which is in line with theoretical predictions (see Refs.<sup>[4, 5]</sup>).

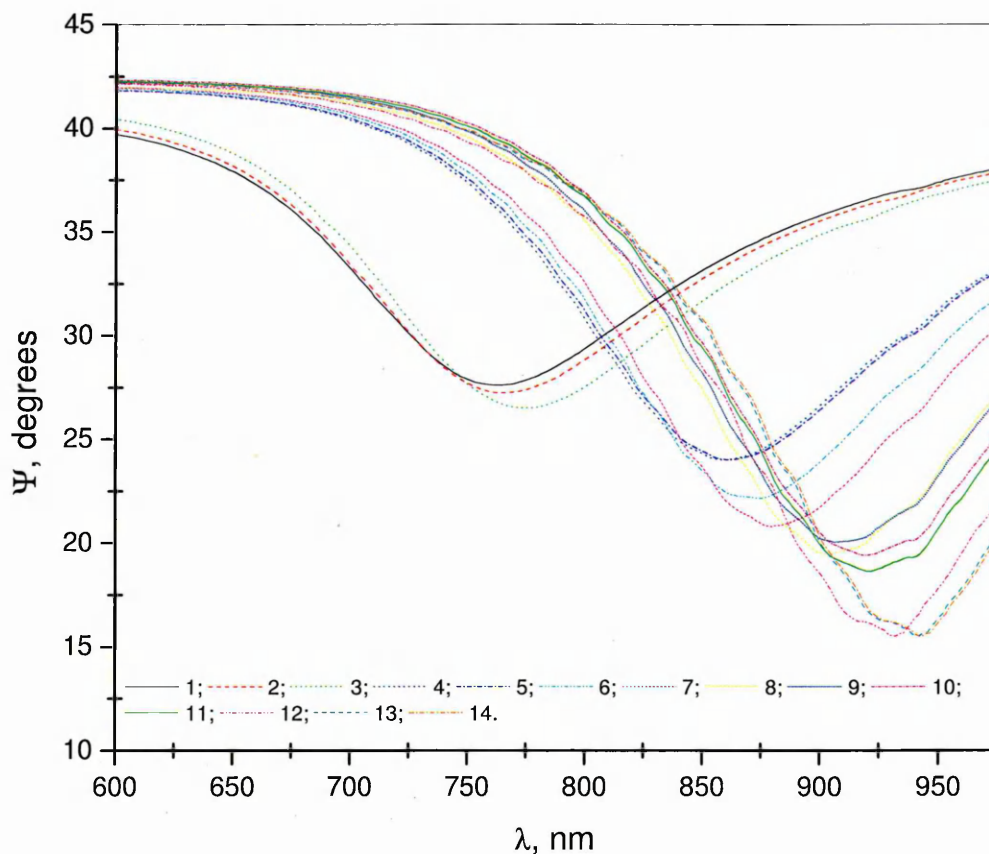


**Figure 4.2-7** A typical set of  $\Psi(\lambda)$  spectra for the initial bare Cr/Au surface (1), after consecutive adsorption steps of PAH (2), protein A (3), monoclonal antibodies (4), and after binding of *T-2 mycotoxin* from solutions of different concentrations in ng/ml: 0.15 (5), 1.5 (6), 7.5 (7), 15 (8), 75 (9), 150 (10), 300 (11), 600 (12), 1200 (13), and 1500 (14).

This was the case for SPR measurements performed on the same samples, following a similar sequence of adsorptions (see Fig. 4.2-8), which did not show a significant response to low molecular weight molecules, such as *simazine* and *atrazine*. The results of the fitting of the SPR data are presented in Table 4.2-3. A noticeable change in thickness of 2.731 nm due to the binding of *T-2 mycotoxin* (at a concentration of 600 ng/ml) was registered.

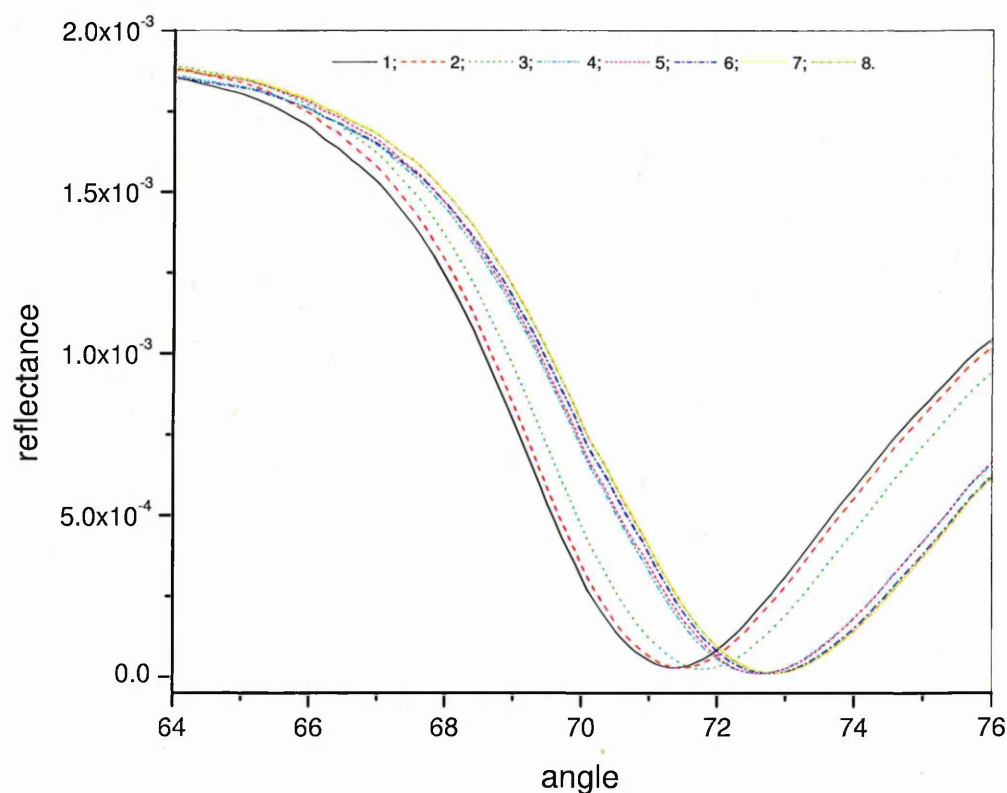


**Figure 4.2-8** A set of SPR curves corresponding to the following sequence of adsorptions: initial bare Au surface (1), after consecutive adsorption steps of PAH (2), protein A (3), polyclonal antibodies (4), and after binding of *T-2 mycotoxin* from solutions of different concentrations in ng/ml: 15 (5), 30 (6), 75 (7) and 600 (8).

**Table 4.2-3** Results of the SPR data fitting for *T-2 mycotoxin*.

	<i>Cr/Au</i> substrate	<i>PAH</i>	<i>protein A</i>	<i>polyclonal</i> <i>antibody</i>	<i>T-2 mycotoxin</i> , <i>c = 600 ng/ml</i>
<i>Cr/Au</i> substrate	$n = 0.228$	$n = 0.2399$	$n = 0.245$	$n = 0.227$	$n = 0.235$
	$k = 3.397$	$k = 3.488$	$k = 3.4699$	$k = 3.286$	$k = 3.338$
	$d^a = 34.599$	$d = 33.845$	$d = 33.671$	$d = 35.924$	$d = 35.267$
<i>Organic</i> <i>film</i>	–	$n = 1.404$	$n = 1.410$	$n = 1.410$	$n = 1.410$
	–	$d = 4.654$	$d = 2.936$	$d = 12.143$	$d = 14.874$
<i>MSE</i>	0.810	3.046	4.157	1.617	1.697
$\delta d$ , nm	–	–	–	–	2.731

<sup>a</sup> The values of  $d$  are given in nm.

TIRE fitting of the experimental  $\Psi(\lambda)$  and  $\Delta(\lambda)$  spectra to the four layer model (BK7 glass – Cr/Au layer – Cauchy layer – Ambient (i.e. aqueous buffer solution)) was carried out with dedicated WVASE32<sup>®</sup> software.

Firstly, the optical parameters (thickness  $d$ , refractive index  $n$  and extinction coefficient  $k$ ) of the Cr/Au layer were found by fitting the respective  $\Psi(\lambda)$  and  $\Delta(\lambda)$  data for the bare Cr/Au coating. Then, the parameters of organic layers were determined by fitting respective  $\Delta(\lambda)$  spectra<sup>a</sup>, while the parameters for the Cr/Au layers were fixed. The Cauchy dispersion function was used to describe the adsorbed organic and bio-layers. The parameters of all of the layers obtained by fitting are given in Table 4.2-4. The values of  $n$  and  $k$  are given at wavelength  $\lambda = 633$  nm, although the fitting was performed across the whole spectral range.

**Table 4.2-4** Parameters of the four-layer model in TIRE fitting.

<i>N<sub>o</sub></i>	<i>layer content</i>	<i>layer parameters</i>	<i>comments</i>
–	AMBIENT – glass BK7	$n = 1.515$ $k = 0$	$n$ and $k$ were fixed during the fitting
2.	Chromium-gold substrate	$n = 0.359 \pm 0.078$ $k = 2.857 \pm 0.114$ $d = 29.8 \pm 2.6$ nm	
1.	Cauchy	$n = 1.42$ $k = 0$ $A_n = 1.396$ $B_n = 0.01$ $C_n = 0$ $d$ , nm	$n$ , $k$ , $A_n$ , $B_n$ , and $C_n$ were fixed during the fitting; $d$ was the subject of fitting depending on the type of adsorption layer and <i>T-2 mycotoxin</i> concentration (see Table 4.2-5 and Fig. 4.2-9)
0.	Trizma/HCl buffer solution	$n = 1.3326$ $k = 0$	$n$ and $k$ were fixed during the fitting

<sup>a</sup> Because of a limited sensitivity of both  $\Psi(\lambda)$  TIRE spectra and SPR curves, further experimental analysis was carried out using  $\Delta(\lambda)$  TIRE spectra.

Since simultaneous evaluation of the thickness and refractive index of thin transparent films is theoretically impossible in ellipsometry<sup>[6]</sup>, it was assumed that refractive indices of all organic and bio-organic layers were the same and equal to 1.42 at wavelength  $\lambda = 633$  nm, so that all changes in adsorption layer were related to changes in thickness. Such an assumption is not strictly correct but is reasonable, so that all of the changes in the adsorption layer will be associated with the thickness. Following this assumption, the parameters  $A_n$ ,  $B_n$  and  $C_n$  of the Cauchy layer were fixed during fitting.

The fitting yields the following values of thickness:  $1.2 \pm 0.18$  nm for the PAH layer;  $4.23 \pm 1.06$  nm for the protein A layer;  $8.55 \pm 1.71$  and  $7.54 \pm 1.22$  nm for the layers of poly- and mono-AB, respectively. Changes in the film thickness ( $\delta d$  in nm) caused by binding of *T-2 mycotoxin* from its solutions of different concentrations are shown in Fig. 4.2-9 and Table 4.2-5.

The main changes in the film thickness occurred at the concentrations of *T-2 mycotoxin* in the range of 10 – 200 ng/ml, when poly-AB was used, while a much sharper increase of the response was observed in the case of using mono-AB.

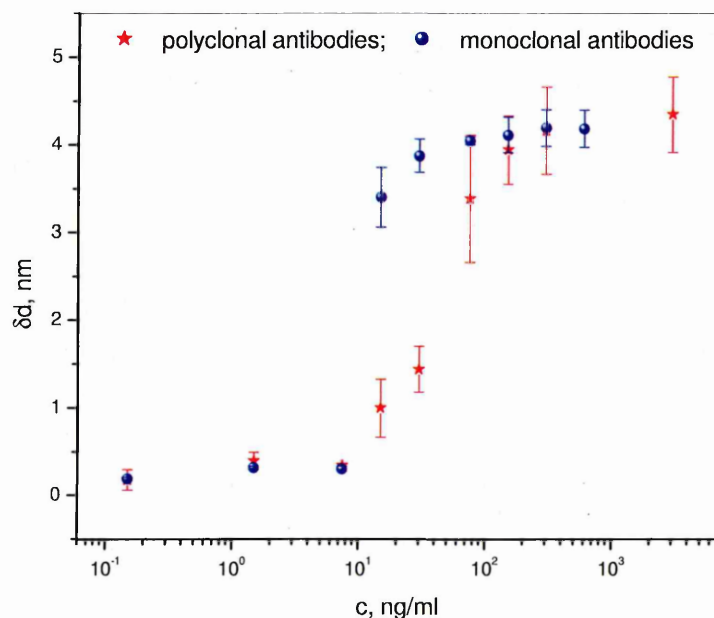


**Figure 4.2-9** Changes in the adsorption layer thickness  $\delta d$  caused by *T-2 mycotoxin* binding vs. *T-2 mycotoxin* concentration in solution. The data for both polyclonal and monoclonal antibodies are presented.

At higher concentrations of *T-2 mycotoxin*, the saturation of the response observed can be caused by the saturation of antibody binding sites with *T-2* molecules. The minimal registered concentration of *T-2 mycotoxin* was 0.15 ng/ml. The values of  $\delta d = 4 - 5$  nm at saturation are larger than the size of *T-2* molecules, which could be explained by non-specific adsorption of *T-2 mycotoxin*, adsorption of molecules of solvent (methanol, ethanol, acetonitril), or the binding of large aggregates (micelles) of *T-2 mycotoxin* molecules.

**Table 4.2-5** Changes in the adsorption layer thickness  $\delta d$  caused by *T-2 mycotoxin* binding depending on the *T-2 mycotoxin* concentration in solution.

<i>T-2 mycotoxin</i> concentration, ng/ml	$\delta d$ , nm (polyclonal antibodies)	$\delta d$ , nm (monoclonal antibodies)
0.15	$0.170 \pm 0.012$	$0.186 \pm 0.02$
1.5	$0.233 \pm 0.1$	$0.314 \pm 0.016$
7.5	$0.336 \pm 0.01$	$0.301 \pm 0.03$
15	$0.992 \pm 0.3$	$3.400 \pm 0.34$
30	$1.438 \pm 0.264$	$3.875 \pm 0.19$
75	$3.381 \pm 0.727$	$4.045 \pm 0.044$
150	$3.941 \pm 0.1$	$4.111 \pm 0.205$
300	$4.16 \pm 0.5$	$4.191 \pm 0.21$
3000	$4.643 \pm 0.1$	$4.182 \pm 0.21$
60000	$5.073 \pm 0.258$	—

#### 4.2.2.2 TIRE kinetics measurements

The study of the kinetics of antibody–toxin binding was carried out by measuring a series of TIRE spectra during exposure to a *T-2 mycotoxin* solution for a certain period of time (usually 10 – 20 min). Then the time dependences of either  $\Psi$  or  $\Delta$  could be obtained at a selected wavelength. Typically, the time dependence of  $\Psi$  was used, and the wavelength was chosen on the linear part of the  $\Psi(\lambda)$  spectra (marked on the graph with two crosses) closest to the SPR minimum, as shown in Fig. 4.2-10.

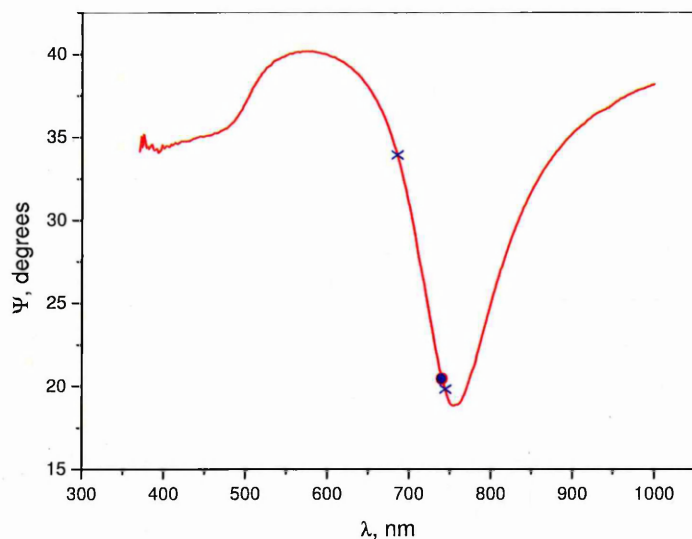


**Figure 4.2-10** The choice of wavelength (the dot) on the  $\Psi(\lambda)$  spectrum for kinetics measurements. Crosses indicate the linear range on the  $\Psi(\lambda)$  spectra.

This provided a wide linear dynamic range for kinetics measurements. These measurements were repeated for different concentrations of *T-2 mycotoxin*, and typical results are presented in Fig. 4.2-11.

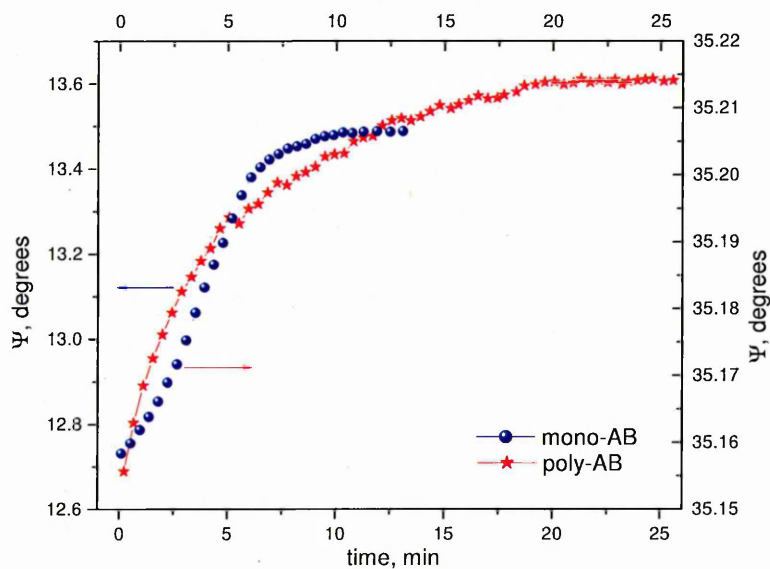


**Figure 4.2-11** Typical kinetics of the response in the course of binding *T-2 mycotoxin* to monoclonal antibodies and polyclonal antibodies at a wavelength of 700 nm.

An increase in the  $\Psi$  value followed by its saturation is observed for both polyclonal and monoclonal antibodies. However, the binding reaction is happening faster on mono-AB (~10 min) compared to poly-AB (17 – 20 min) (see Fig. 4.2-11).

As shown in §3.7, the analysis of binding kinetics can be performed using the following integral equation for the sensor response<sup>[7]</sup>:

$$R = \frac{k_a \cdot C \cdot R_{\max}}{k_a \cdot C + k_d} \{1 - \exp[-(C \cdot k_a + k_d)t]\}, \quad (4.3)$$

where  $R$  is the response of a sensor (changes in  $\Psi$  in our case) and  $R_{\max}$  is the maximal response corresponding to the saturation of binding sites;  $k_a$  and  $k_d$  are, respectively, coefficients of adsorption and desorption; and  $C$  is the concentration of *T-2 mycotoxin* in solution.

Following the procedure described by Liu et al.<sup>[7]</sup> and §3.7, the experimental kinetic curves for every concentration  $C$  were plotted in semi-logarithmic scale ( $\ln\Psi(t)$ ) and yielded a linear dependence with the slope:

$$S = k_a C + k_d. \quad (4.4)$$

The obtained dependencies of  $S(C)$  for mono- and poly-AB are shown in Fig. 4.2-12.

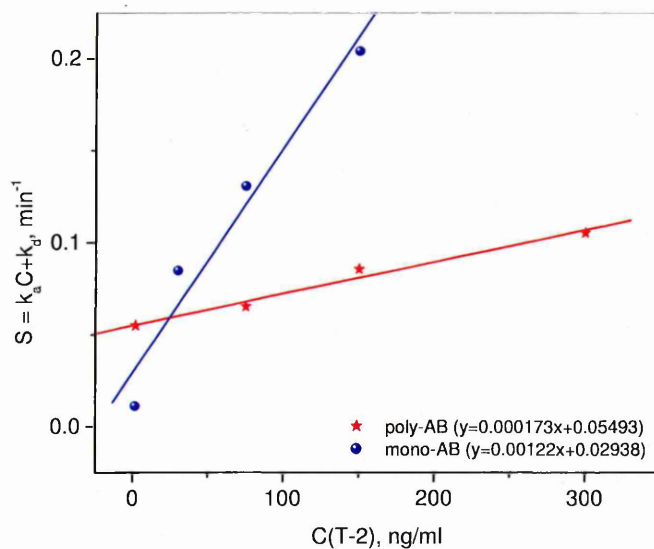


**Figure 4.2-12** Experimental points and fitting graphs (with equations) of  $S=k_a C+k_d$  vs. concentration ( $C$ ) of *T-2 mycotoxin* for mono-AB and poly-AB.

The values of  $k_a$  and  $k_d$  can be obtained, respectively, from the slope and intercept of the linear graphs  $S(C)$  in Fig. 4.2-12. They are shown in the form of linear equations near respective data, and also summarized in Table 4.2-6 along with the association constant  $K_A$ , which is defined as a ratio of adsorption and desorption coefficients  $K_A = k_a / k_d$ .

**Table 4.2-6** Parameters of *T-2 mycotoxin* binding kinetics.

	$k_a$ ( $\text{mol}^{-1} \cdot \text{l} \cdot \text{s}^{-1}$ )	$k_d$ ( $\text{s}^{-1}$ )	$K_A$ ( $\text{mol}^{-1} \cdot \text{l}$ )
poly-AB	$1.555 \cdot 10^3$	$9.15 \cdot 10^{-4}$	$1.7 \cdot 10^6$
mono-AB	$9.33 \cdot 10^3$	$4.9 \cdot 10^{-4}$	$1.9 \cdot 10^7$

The obtained values for the association constant  $K_A$  are typical for highly specific affinity reactions, such as antibody–antigen binding (see, for example, Ref.<sup>[7]</sup>). The much higher  $K_A$  value for mono-AB is possibly caused by higher specificity of *T-2 mycotoxin* monoclonal antibodies, as compared to polyclonal ones.

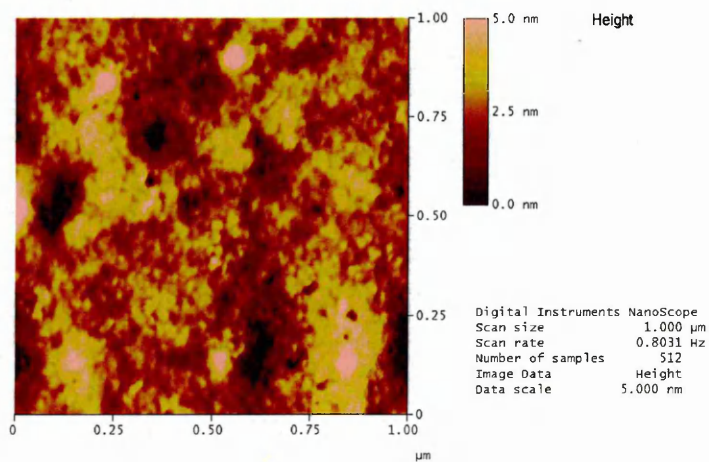
#### 4.2.2.3 AFM analysis of samples

The formation of large aggregates of *T-2 mycotoxin* (associated with anomalously large thicknesses of adsorbed layers, see §4.2.2.2) on the surface was directly observed with AFM.

The tapping mode AFM study revealed a repeatable grainy structure which appears in Fig. 4.2-13b after binding *T-2 mycotoxin* molecules. A more or less flat layer (with mean roughness<sup>a</sup>  $R_a = 0.935 \pm 0.137$  nm) of immobilized mono-AB antibodies in Fig. 4.2-13a transforms into a layer with a plainly distinguishable grainy structure and rougher surface (with mean roughness  $R_a = 3.046 \pm 0.430$  nm) in Fig. 4.2-13b after binding *T-2 mycotoxin* molecules from their 500 ng/ml solution.

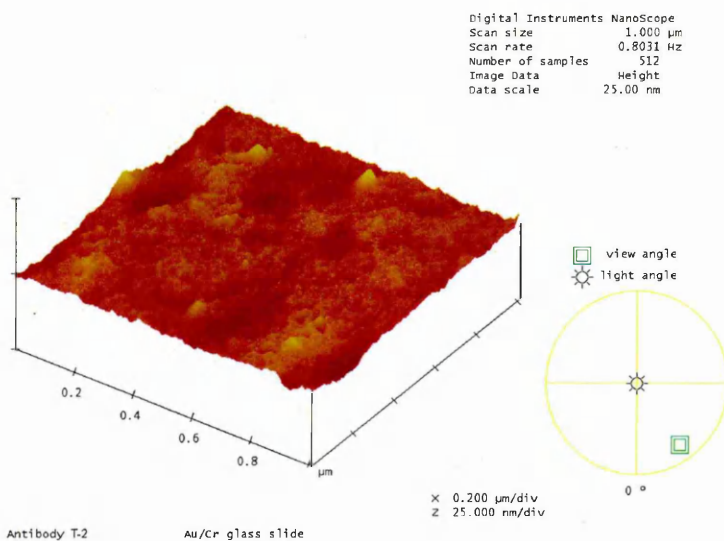
As can be seen from the AFM images, the observed small grains of ~30 nm are clustered on the surface to form larger aggregates of ~300 nm (see Fig. 4.2-14).

<sup>a</sup> Detailed information (including the definitions used) about AFM image analysis is given in Appendix D.



Antibody T-2 Au/Cr glass slide

a<sub>1</sub>

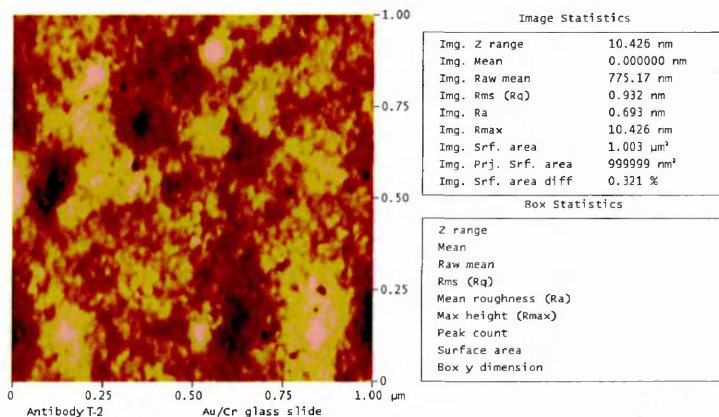


Antibody T-2 Au/Cr glass slide

a<sub>2</sub>

Peak Surface Area Summit Zero Crossing Stopband Execute Cursor

Roughness Analysis



Peak Off Summit Off Zero Cross. Off Box Cursor

a<sub>3</sub>

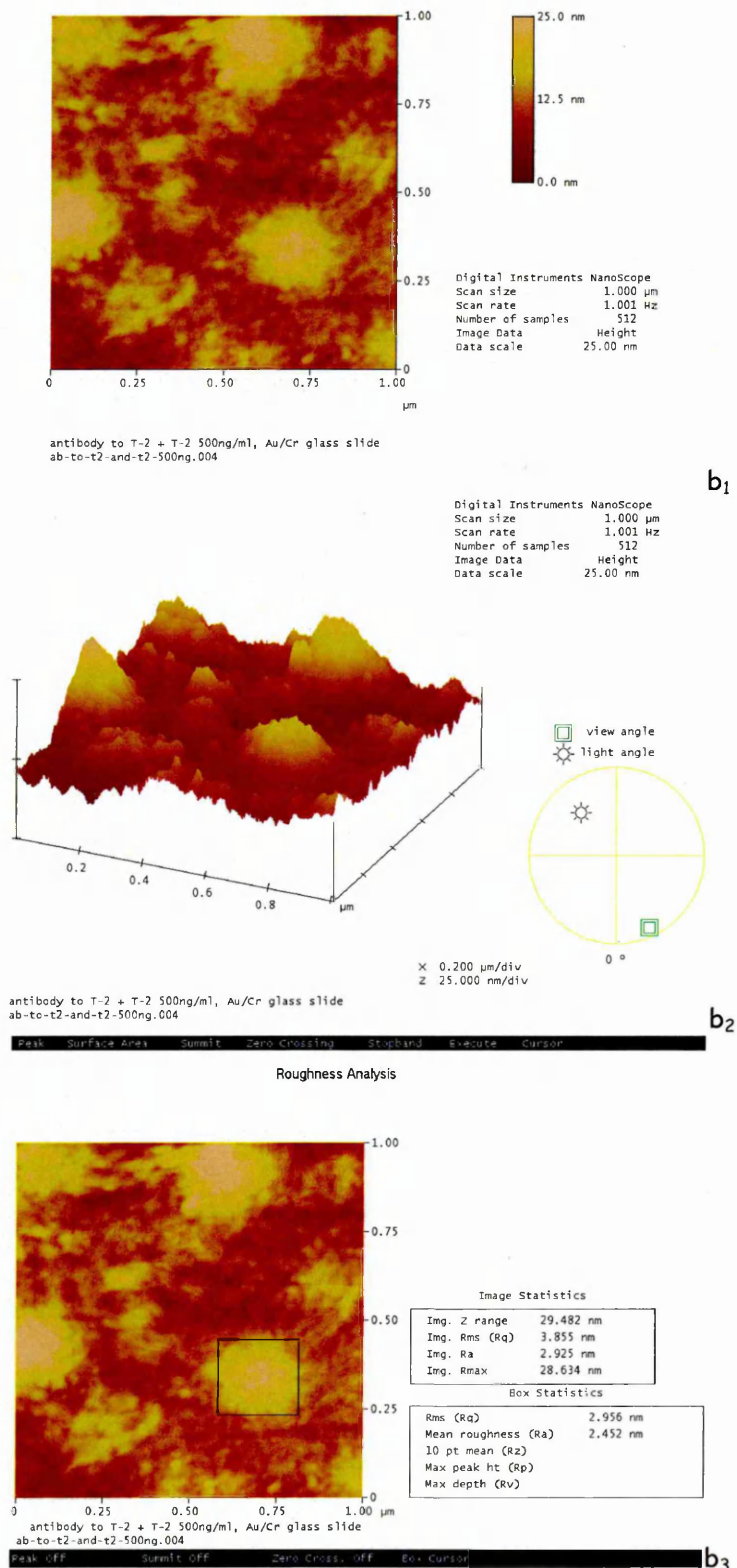
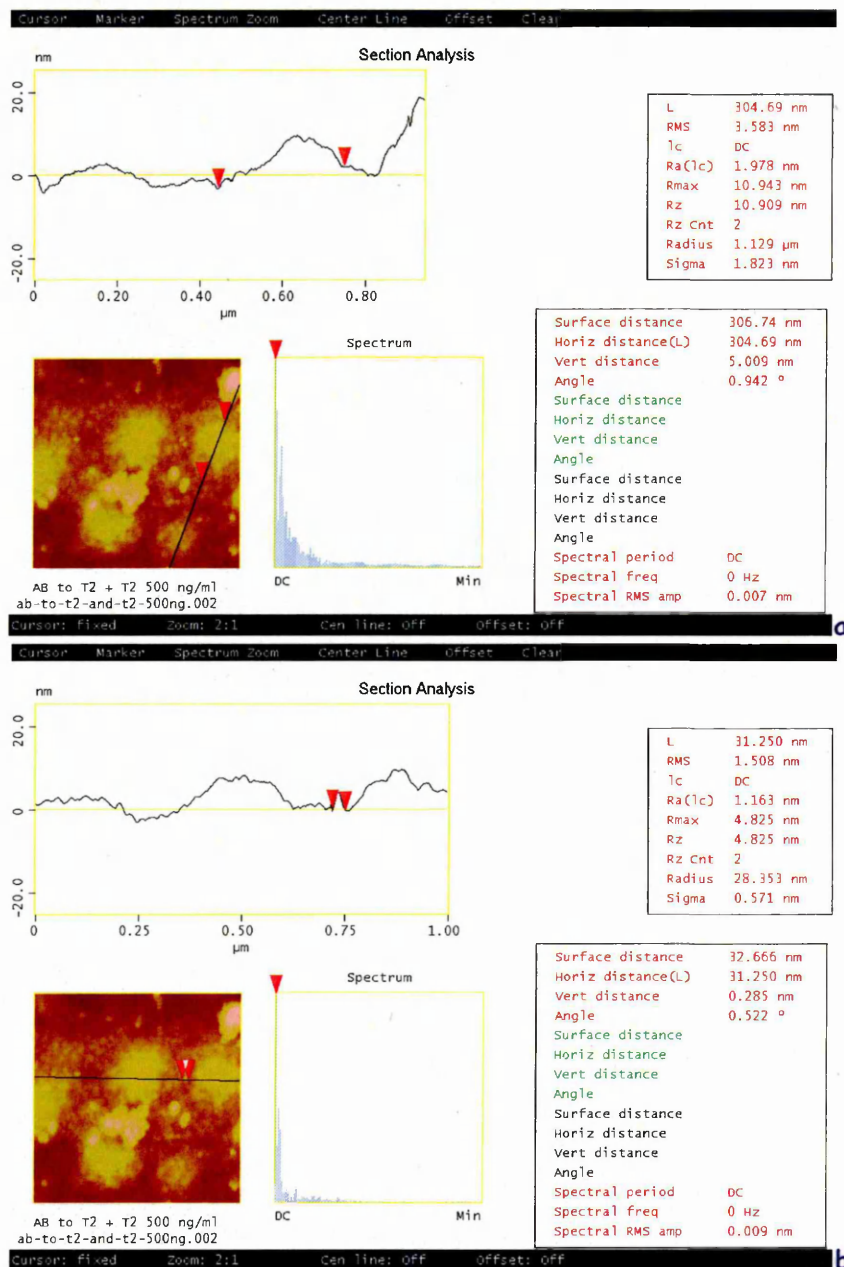


**Figure 4.2-13** AFM tapping mode images (height, pseudo-3D, and roughness) of the layer of immobilized monoclonal antibodies to *T-2 mycotoxin* (**a<sub>1</sub> – a<sub>3</sub>**), and the same layer after binding *T-2 mycotoxin* molecules (**b<sub>1</sub> – b<sub>3</sub>**).

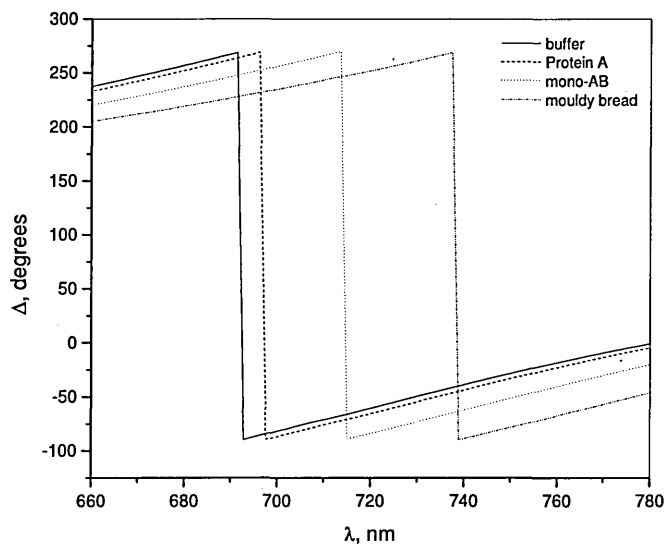


#### 4.2.2.4 Real samples

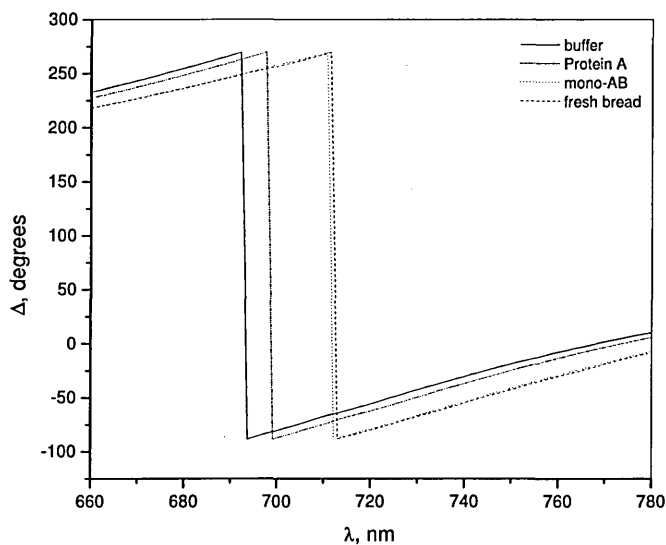
The main purpose of this part of the study was to investigate the possible occurrence of mycotoxin in animal feeds and human food. This study was divided into two parts: firstly, the detection of the presence of mycotoxin in the samples, and

secondly, the quantification of the amount of mycotoxin in these samples (a detailed description of the sample preparation routine was given in §3.4.7).

The results revealed that all of the samples except one (namely, “fresh” muesli) were contaminated with mycotoxin to a greater or lesser extent (see Figs. 4.2-15 and 4.2-16). Even the “fresh bread” sample showed a small but noticeable shift in the  $\Delta(\lambda)$  TIRE spectrum (see Fig.4.2-15b).



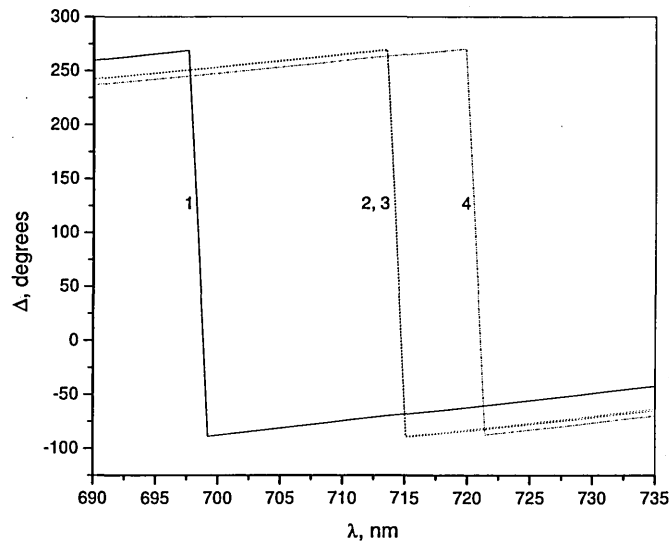
a



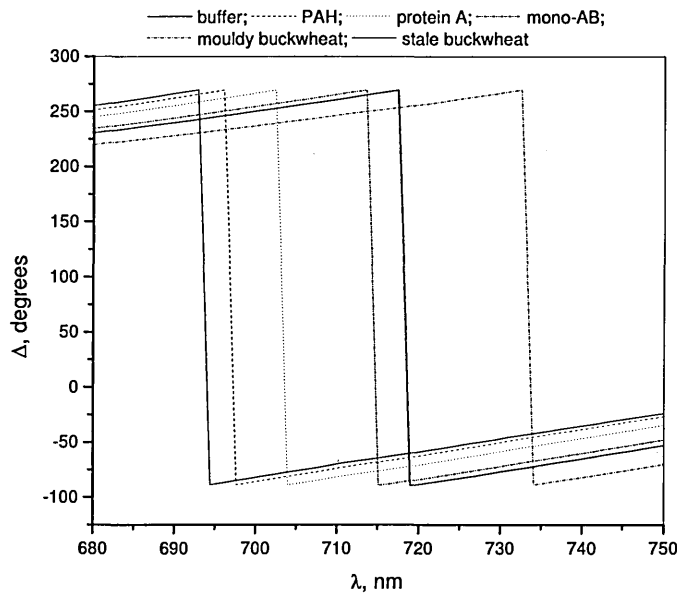
b

**Figure 4.2-15**

A typical set of  $\Delta(\lambda)$  TIRE spectra for the initial bare Cr/Au surface (*buffer*), after consecutive adsorption steps of protein A, monoclonal antibodies, and after binding of *T-2 mycotoxin* from its solutions in mouldy bread (a) and fresh bread (b) samples.



**a**



**b**

**Figure 4.2-16** **a** – a set of  $\Delta(\lambda)$  TIRE spectra for the initial bare Cr/Au surface (1) after adsorption of monoclonal antibodies (2) and after binding of *T-2 mycotoxin* from its solutions in “fresh” (3) and “stale” (4) muesli samples;  
**b** – a set of  $\Delta(\lambda)$  spectra for the initial bare Cr/Au surface (*buffer*), after consecutive adsorption steps of protein A, PAH, monoclonal antibodies, and after binding of *T-2 mycotoxin* from its solutions in “stale” and mouldy buckwheat samples .

All samples contaminated with mould contained a significant amount of mycotoxin (Table 4.2-7). The amount of mycotoxin was determined by the

superposition of experimental points on the calibration curve for monoclonal antibodies as shown in Fig.4.2-17.

**Table 4.2-7** Detection and quantification of the *T-2 mycotoxin* in the food samples.

<i>sample</i>	$\delta d, nm$	<i>concentration of T-2 mycotoxin in the sample</i>
mouldy fodder	4.900	more than 600 ng/ml
stale bread	0.031	less than 1.5 ng/ml
mouldy bread	4.391	more than 600 ng/ml
mouldy maize	4.369	more than 600 ng/ml
fresh muesli	0.000	none
stale muesli	0.298	less than 1.5 ng/ml
stale buckwheat	1.199	more than 7.5 but less than 15 ng/ml
mouldy buckwheat	5.274	more than 600 ng/ml

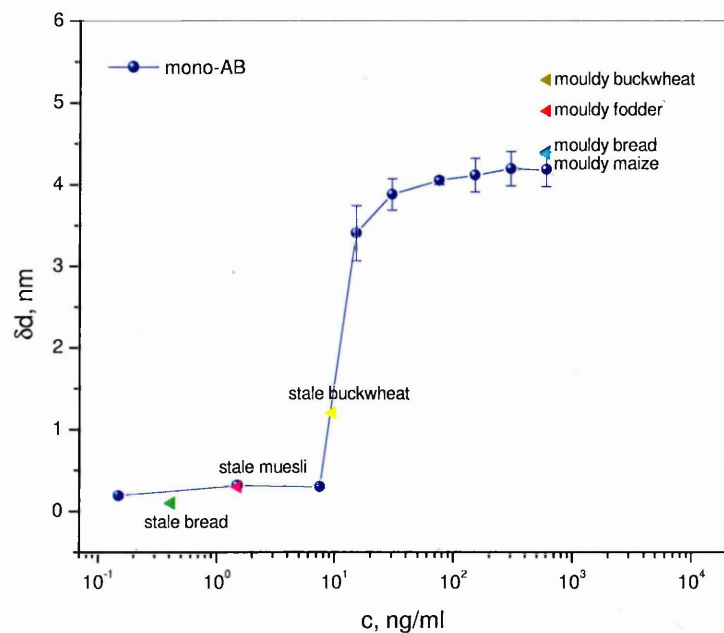
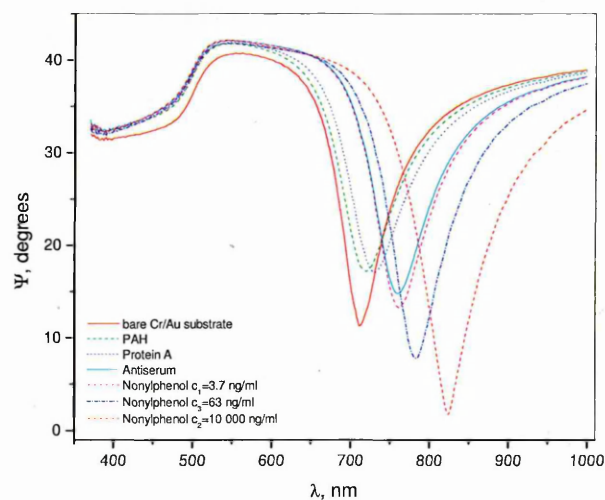


**Figure 4.2-17** Changes in the adsorption layer thickness  $\delta d$  caused by *T-2 mycotoxin* binding vs. *T-2 mycotoxin* concentration in real food samples.

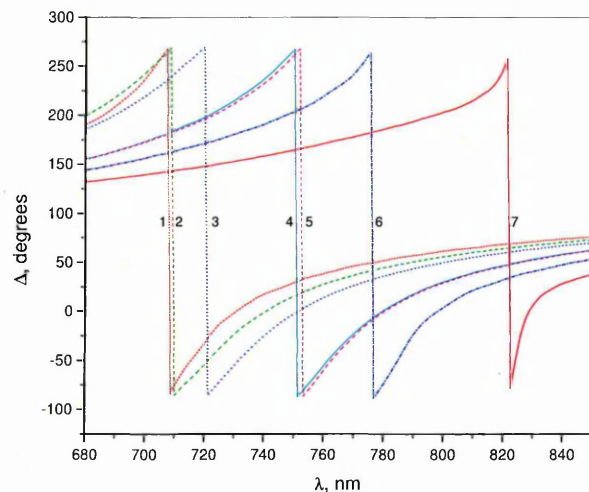
## 4.2.3 Nonylphenol registration

### 4.2.3.1 TIRE measurements

A typical set of TIRE  $\Psi(\lambda)$  and  $\Delta(\lambda)$  spectra in the course of consecutive adsorption steps of PAH, protein A, antibodies to *nonylphenol*, and binding of *nonylphenol* from its 3.7, 63 and 10000 ng/ml solutions is shown in Figure 4.2-18.



a



b

**Figure 4.2-18**

A typical set of  $\Psi(\lambda)$  and  $\Delta(\lambda)$  TIRE spectra corresponding to the following sequence of adsorption steps: initial spectrum of Cr/Au layer (1), after adsorption of PAH layer (2), after deposition of protein A (3), after deposition of *nonylphenol* antiserum (4), after binding of *nonylphenol* from its solutions of 3.7 ng/ml (5), 63 ng/ml (6), and 10000 ng/ml (7).

The spectral shift ( $\delta\lambda$ , nm), caused by *nonylphenol* binding, depends on the concentration of *nonylphenol*, as shown in Figure 4.2-19. It is intriguing that binding of quite small molecules of *nonylphenol* with a molecular weight of  $MW = 220.39$  g/mol shows a substantial spectral shift of about 45 nm at saturation. This effect is similar (and even more pronounced) to that described above upon binding of *T-2 mycotoxin* molecules.

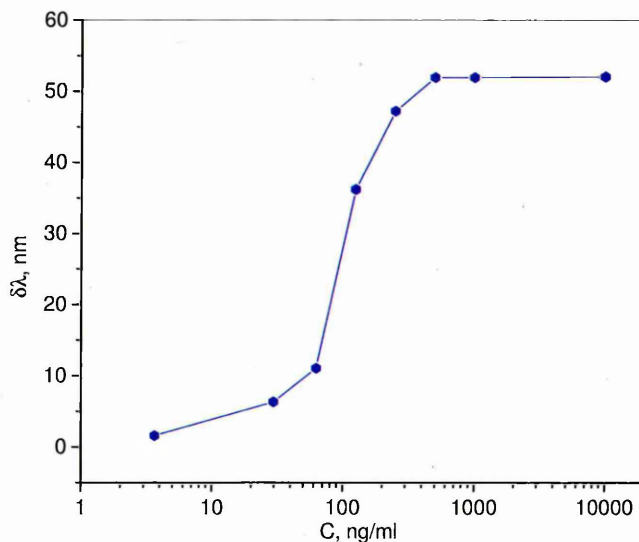


**Figure 4.2-19** A typical dependence of the spectral shift  $\delta\lambda$  on the concentration of *nonylphenol*.

The values of the thickness of the adsorbed layer were obtained by the fitting of the experimental  $\Psi(\lambda)$  and  $\Delta(\lambda)$  spectra to the four-layer model (BK7 glass – Cr/Au layer – Cauchy layer – aqueous buffer solution), which was carried out using the dedicated WVASE32<sup>®</sup> software. The fitting procedure was identical to that described earlier (see §4.2.2.2).

The parameters of all layers obtained by fitting are given in Table 4.2-8. The values of  $n$  and  $k$  are given at a wavelength of  $\lambda = 633$  nm, although the fitting was performed across the whole spectral range. The effective optical parameters of the Cr/Au coating were different in the two series of samples studied.

Changes in the film thickness ( $\delta d$ ) caused by the binding of *T-2 mycotoxin* from its solutions of different concentrations are shown in Fig.4.2-20 and Table 4.2-9.

**Table 4.2-8** Parameters of the four-layer model in TIRE fitting<sup>a</sup>.

№	layer content	layer parameters	
		series 1	series 2
–	AMBIENT – glass BK7	$n^* = 1.515; k^* = 0$	
2.	Chromium- gold substrate	$n = 0.263 \pm 0.014$ $k = 3.202 \pm 0.061$ $d = 27.69 \pm 0.74$ nm	$n = 0.328 \pm 0.014$ $k = 2.999 \pm 0.053$ $d = 36.38 \pm 1.51$ nm
1.	Cauchy layers:	$n^* = 1.42; k^* = 0$ $A_n^* = 1.396; B_n^* = 0.01; C_n^* = 0$ $d$ is the subject of fitting depending on the type of adsorption layer and <i>nonylphenol</i> concentration	
	<i>PAH</i>	$d = 0.94 \pm 0.58$ nm	$d = 1.57 \pm 0.54$ nm
	<i>protein A</i>	$d = 2.97 \pm 1.40$ nm	$d = 5.04 \pm 1.73$ nm
	<i>nonylphenol</i> <i>antiserum</i>	$d = 16.27 \pm 5.12$ nm	$d = 22.90 \pm 6.07$ nm
	<i>nonylphenol</i>	The results are shown on the graph in Fig.4.2-20 and Table 4.2-9	
0.	Trizma/HCl buffer solution	$n^* = 1.3326$ $k^* = 0$	

Similar to earlier observations on *T-2 mycotoxin*, the main changes in the film thickness occur at the concentrations of *nonylphenol* in the range of 20 – 200 ng/ml. The saturation of the response is observed at concentrations of *nonylphenol* higher than 200 ng/ml, which is most likely due to the saturation of antibodies' binding sites.

The minimal registered concentration of *nonylphenol* was 1.2 ng/ml. The value of  $\delta d = 23$  nm at saturation is much larger than the length of a *nonylphenol* molecule of about 1.5 nm. The observed changes in the adsorption layer thickness are even more

<sup>a</sup> Parameters indicated with an asterisk (\*) were fixed during fitting.

dramatic than those described earlier for *T-2 mycotoxin*, which allowed us to assume the mechanism of binding of aggregates of *nonylphenol* molecules.

**Table 4.2-9** Changes in the adsorption layer thickness  $\delta d$  caused by *nonylphenol* binding dependant on *nonylphenol* concentration in solution.

<i>nonylphenol</i> concentration, ng/ml	$\delta d$ , nm
1.2	$0.289 \pm 0.058$
3.7	$0.74 \pm 0.396$
7.5	$1.9996 \pm 0.3897$
15	$1.985 \pm 0.3$
30	$4.982 \pm 2.192$
63	$9.782 \pm 2.947$
125	$17.521 \pm 2.816$
250	$22.543 \pm 0.718$
500	$23.672 \pm 0.4$
1000	$23.156 \pm 0.517$
10000	$23.2 \pm 0.232$

**Figure 4.2-20** Results of TIRE data fitting: the dependence of changes in the adsorption layer thickness on the concentration of *nonylphenol*

#### 4.2.3.2 TIRE kinetics measurements

The kinetics of the binding of *nonylphenol* to respective antibodies was studied by measuring TIRE spectra every  $\sim 1.5 - 3.0$  s during exposure to the *nonylphenol* solution (typically for 15 – 20 min). Then, time dependences of either  $\Psi$  or  $\Delta$  could be obtained at a selected wavelength. Typically, the time dependence of  $\Psi$  was used, since  $\Psi(\lambda)$  spectra give a wider linear range as compared to  $\Delta(\lambda)$  spectra.

Such measurements were repeated for different concentrations of *nonylphenol*: a typical kinetic spectra is presented in Fig. 4.2-21. The analysis of binding kinetics has been done similarly to that previously described for the *T-2 mycotoxin* routine (see §4.2.2). The obtained dependency of  $S(C)$  for *nonylphenol* is shown in Fig. 4.2-22. The obtained values for the coefficients of adsorption ( $k_a$ ) and desorption ( $k_d$ ), were:  $k_a = 1.555 \cdot 10^3 \text{ mol}^{-1} \cdot \text{l} \cdot \text{s}^{-1}$  and  $k_d = 9.15 \cdot 10^{-4} \text{ s}^{-1}$ , correspondingly. The association

constant ( $K_A$ ), being a ratio of adsorption and desorption coefficients, can therefore be found as  $K_A = 1.6 \cdot 10^6 \text{ mol}^{-1} \cdot \text{l}$ . The value of  $K_A$  obtained for *nonylphenol* binding is typical for highly specific reactions of antibody-antigen binding.

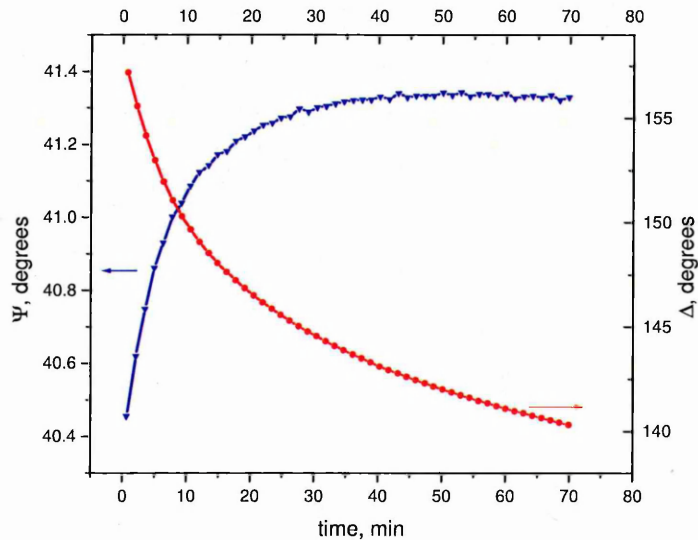


**Figure 4.2-21** Typical TIRE kinetics of binding *nonylphenol* from its 250 ng/ml solution to antibodies.

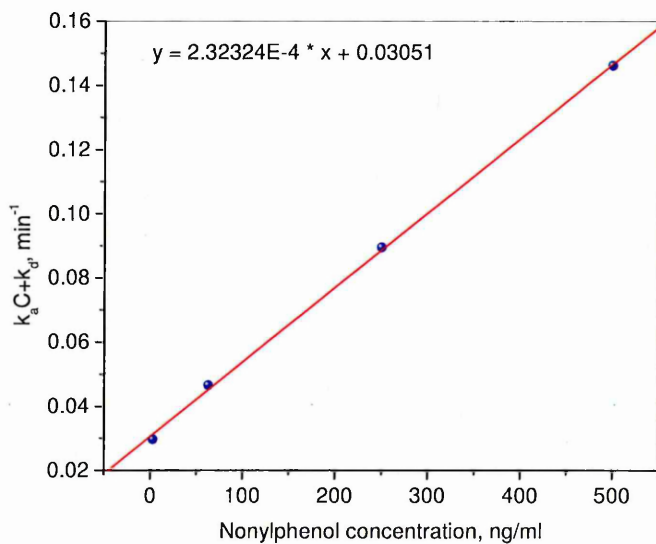


**Figure 4.2-22** Experimental points and the fitting graph (with equation) of a  $S=k_a C+k_d$  vs. concentration of *nonylphenol*.

### 4.2.3.3 The model of the nonylphenol micelle

The TIRE method demonstrated anomalously large responses for the binding of *nonylphenol* molecules. Since non-specific binding of *nonylphenol* and *T-2 mycotoxin* molecules was eliminated by washing in 25% methanol or acetonitril, the only remaining logical explanation was the binding of large molecular aggregates of *nonylphenol* molecules.

The adsorption of solvent, i.e. methanol or acetonitril, may also have contributed to the anomalous increase in both thickness and mass of adsorbed layers. However, a direct experimental check did not show any substantial mass changes after washing the samples in the above organic solvents.

The amphiphilic molecules of *nonylphenol* can form large aggregates, such as micelles, in aqueous solutions during the dilution of their initial solutions in organic solvents (methanol or acetonitril). Figure 4.2-23 shows a schematic diagram of such a micelle of *nonylphenol* molecules in an aqueous medium with hydrophilic phenol groups on the exterior and hydrophobic alkyl chains on the interior; a certain number of solvent molecules can be trapped inside the micelle.

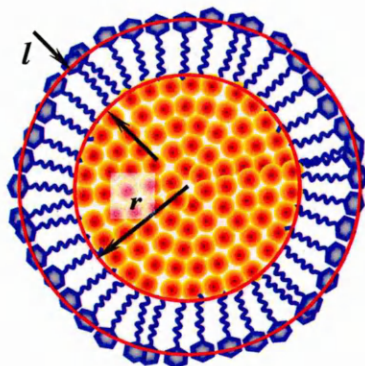


**Figure 4.2-23** Schematic representation of *nonylphenol* micelles formed in aqueous solutions.

The mass of the micelle ( $M_m$ ) can be estimated from the value of added mass  $\Delta m = 18.3 \mu\text{g} / \text{cm}^2$  obtained from the QCM experiment (see. Ref.<sup>[81]</sup>) and the surface concentration of adsorbed micelles ( $C_m$ ):

$$M_m = \frac{\Delta m}{C} = \Delta m \cdot A_m, \quad (4.5)$$

where  $A_m = 1/C_m$  is the area occupied by a single micelle specifically bound to the IgG molecule, e.g. an antibody, occupying the area of approximately  $100 \text{ nm}^2$ , so that  $A_m = 100 \text{ nm}^2$ . Thus  $M_m = 18.3 \cdot 10^{-5} (\text{kg} / \text{m}^2) \times 100 \cdot 10^{-18} (\text{m}^2) = 1.83 \cdot 10^{-20} (\text{kg})$ .

The mass of the micelle, having the radius  $r$ , consists of the mass of *nonylphenol* molecules on the micelle surface ( $A = 4\pi r^2$ ) and the mass of solvent trapped in the volume ( $V = \frac{4}{3}\pi r^3$ ) inside the micelle:

$$M_m = \frac{4\pi\rho}{3} r^3 + \frac{4\pi M}{A_0 N_A} r^2, \quad (4.6)$$

where  $\rho = 789 (\text{kg} / \text{m}^3)$  is the density of ethanol,  $M = 0.22039 (\text{kg} / \text{mol})$  is the molecular weight of *nonylphenol*,  $A_0 = 0.2 \text{ nm}^2 = 2 \cdot 10^{-19} \text{ m}^2$  is the area occupied by an alkyl chain of *nonylphenol* molecule in a closely packed monolayer on the micelle surface, and  $N_A$  is the Avogadro's number ( $1/\text{mol}$ ). The cubic equation (4) can be rewritten in the standard form:

$$ar^3 + br^2 + cr + d = 0, \quad (4.7)$$

$$\text{where } a = \frac{4\pi\rho}{3} = \frac{4 \times 3.14 \times 789}{3} \approx 3.305 \cdot 10^3 (\text{kg} / \text{m}^3),$$

$$b = \frac{4\pi M}{A_0 N_A} = \frac{4 \times 3.14 \times 0.22039}{2 \cdot 10^{-19} \times 6.022 \cdot 10^{23}} \approx 2.3 \cdot 10^{-5} (\text{kg} / \text{cm}^2),$$

$c = 0$ , and

$$d = -M_m = -3.66 \cdot 10^{-20} (\text{kg}).$$

Eq. (4.7) has the only physically feasible solution of  $r = 1.56 \cdot 10^{-8} \text{ m} = 15.6 \text{ nm}$ . Considering the length of the *nonylphenol* molecule,  $l = 1.5 \text{ nm}$ , the exterior diameter of the micelle (see Fig. 4.2-23) is equal to  $\varnothing = 2r + 2l = (2 \times 15.6) + (2 \times 1.5) = 34.2 (\text{nm})$ .

The obtained values of  $r$  and  $\varnothing$  for all three solvents used (ethanol, methanol, and acetonitril) are summarized in Table 4.2-10. As one can see, the micelle size does not alter very much with the type of solvent. The amount of solvent trapped inside the micelle is not really known, so the effective value of the density can vary.

**Table 4.2-10** The size of *nonylphenol* and *T-2 mycotoxin* micelles filled with different compounds.

Filling medium	$\rho$ , kg/m <sup>2</sup>	<i>nonylphenol</i>		<i>T-2 mycotoxin</i>	
		<i>r</i> , nm	$\emptyset$ , nm	<i>r</i> , nm	$\emptyset$ , nm
Ethanol	789	15.6	34.2	8.8	19.6
Methanol	791.8	15.6	34.2	8.8	19.6
Acetonitril	780	15.7	34.4	–	–
Air	1.168	28.1	59.2	13.9	29.8

The above model can be expanded to other molecules, for example for *T-2 mycotoxin*. A study of *T-2 mycotoxin* binding showed an increase in the film thickness of 4.5 nm in TIRE experiments and an added mass of 3.8  $\mu\text{g}/\text{cm}^2$  in QCM measurements<sup>[8]</sup>.

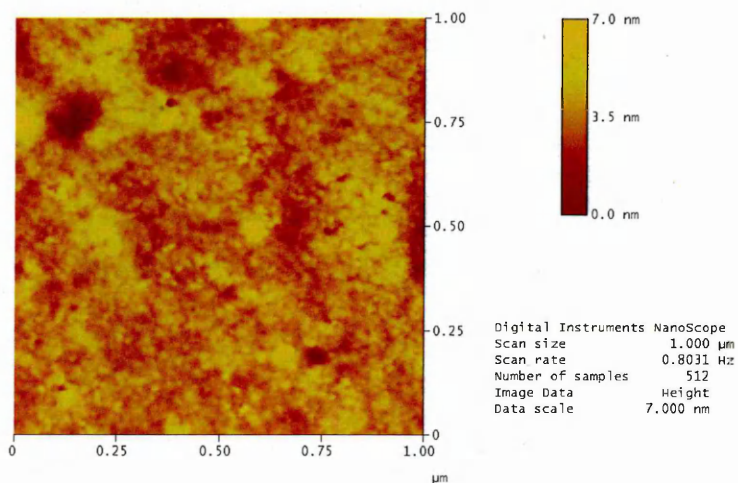
*T-2 mycotoxin* is a hydrophobic molecule soluble in organic solvents (ethanol and methanol were used), and therefore prone to form aggregates (micelles) in aqueous solution. Although a *T-2 mycotoxin* molecule has a more complex 3D configuration as compared to a straight molecule of *nonylphenol*, (see Table 2.6-2) the above model can still be formally applied. The resulting dimensions of *T-2 mycotoxin* aggregates are presented in Table 4.2-10.

However, the micelles may not be spherical and can be bound not to one antibody receptor but to two or more. In fact, the obtained area occupied by a micelle is therefore much larger than the antibody binding site, which means that binding to two or more antibodies is a very likely scenario. Because of all of the uncertainties mentioned above, the proposed micelle model gives only a very rough estimate of its size.

#### 4.2.2.4 AFM analysis of samples

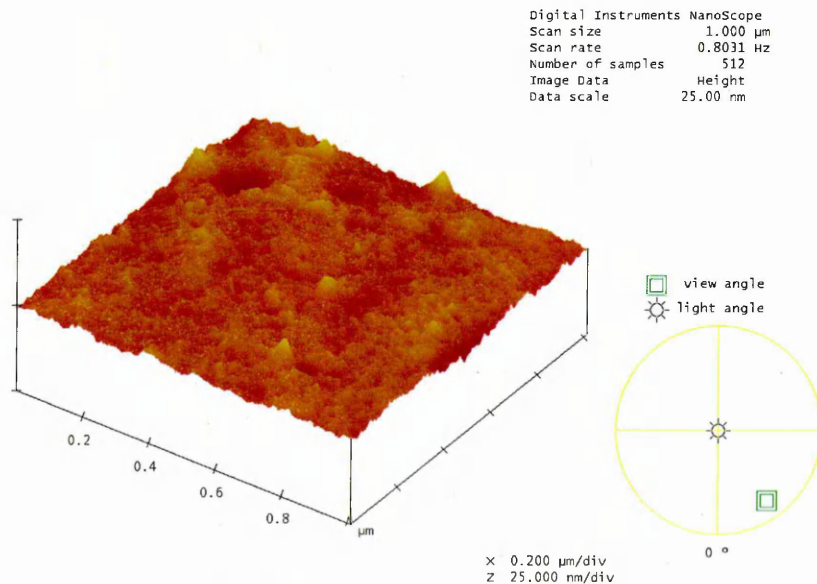
The formation of large micelles of *nonylphenol* on the chromium-gold surface was also directly observed with AFM. Both contact and tapping modes of the AFM scan showed an obvious transformation from a relatively homogenous layer (mean roughness

$R_a = 0.521 \pm 0.115$  nm) of immobilized antibodies to a much more rough (mean roughness  $R_a = 3.791 \pm 0.351$  nm) layer with distinguishing granular features after the binding of *nonylphenol* molecules from their 20 ng/ml solution. AFM images reflecting the height and roughness of the antiserum to *nonylphenol* and after binding of *nonylphenol* are presented in Figures 4.2-24a and 4.2-24b, correspondingly.



Antibody to Nonylphenol; Au/Cr glass slide  
ab-to-nf.007

a<sub>1</sub>



Antibody to Nonylphenol; Au/Cr glass slide  
ab-to-nf.007

a<sub>2</sub>

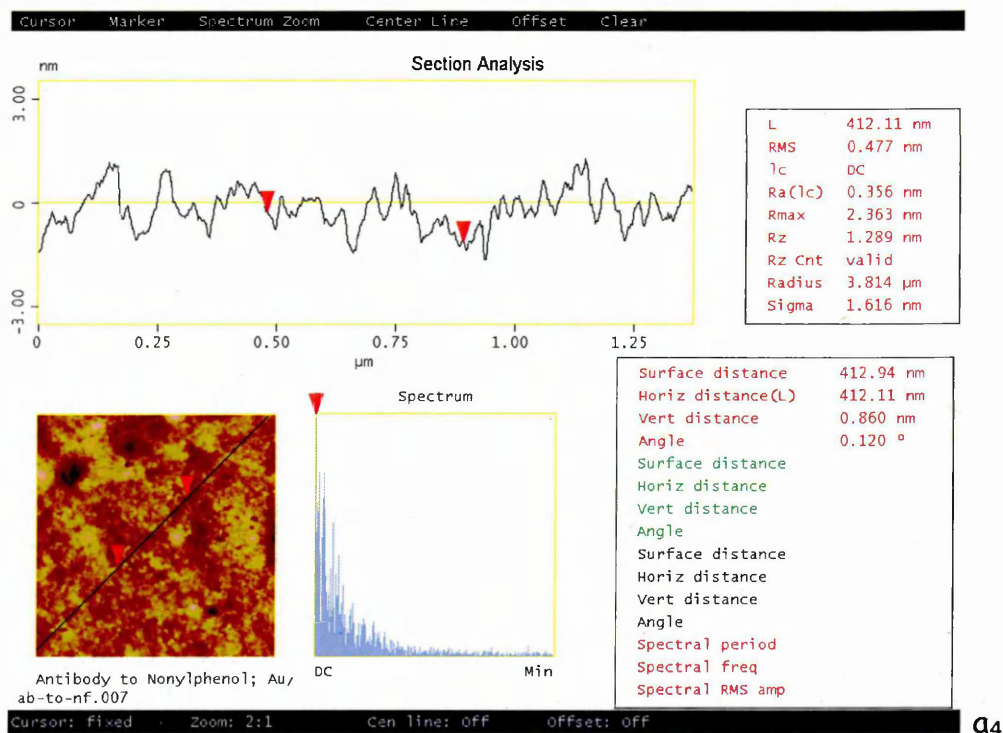
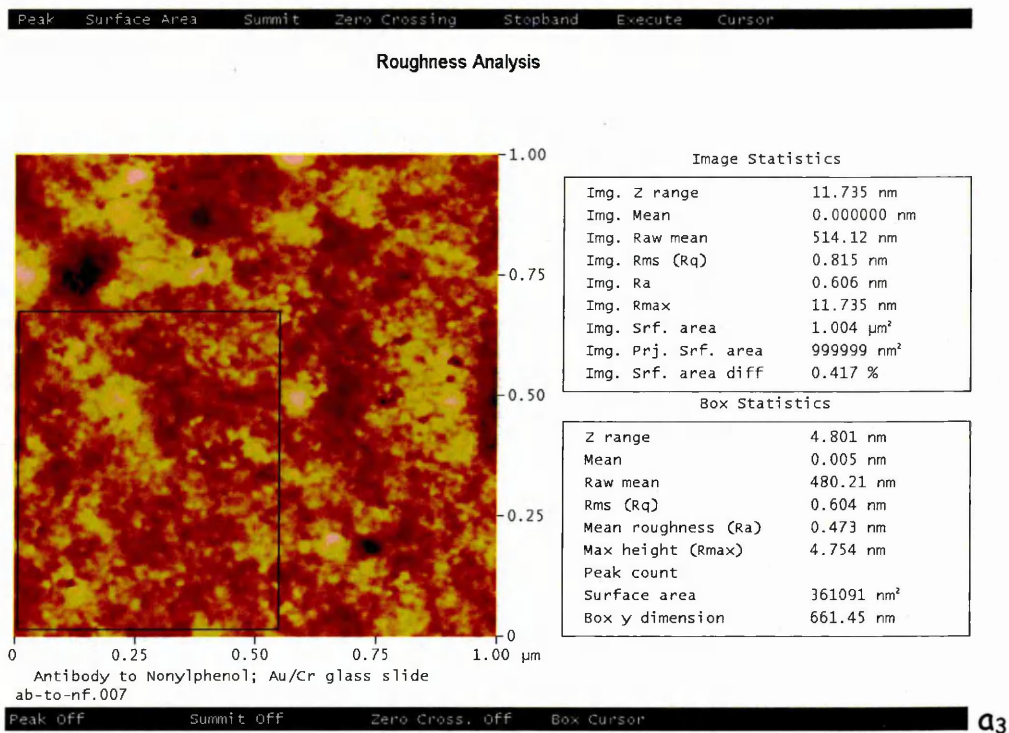
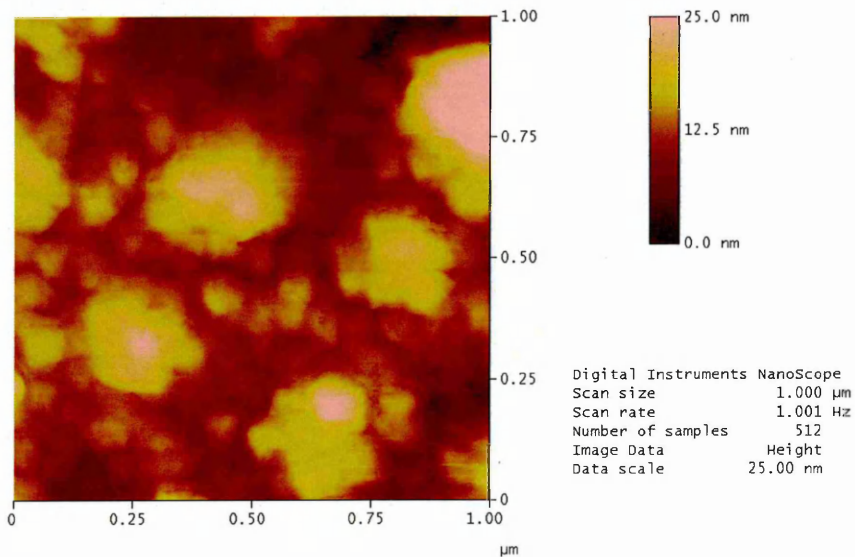
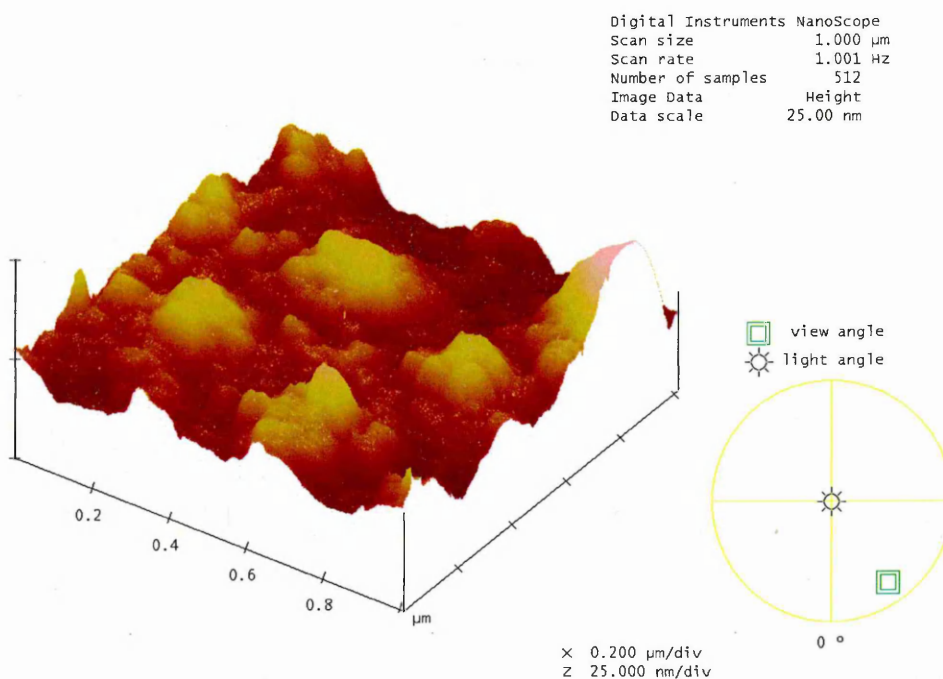


**Figure 4.2-24a** AFM tapping mode images of the layer of immobilized antibodies to *nonylphenol*: **a<sub>1</sub>** – height, **a<sub>2</sub>** – pseudo-3D, **a<sub>3</sub>** – roughness, **a<sub>4</sub>** – section analysis.



Antibody to NP + NP 20ng/ml; Au/Cr glass slide  
ab-to-np-and-np20ng.013

b<sub>1</sub>



Antibody to NP + NP 20ng/ml; Au/Cr glass slide  
ab-to-np-and-np20ng.013

b<sub>2</sub>

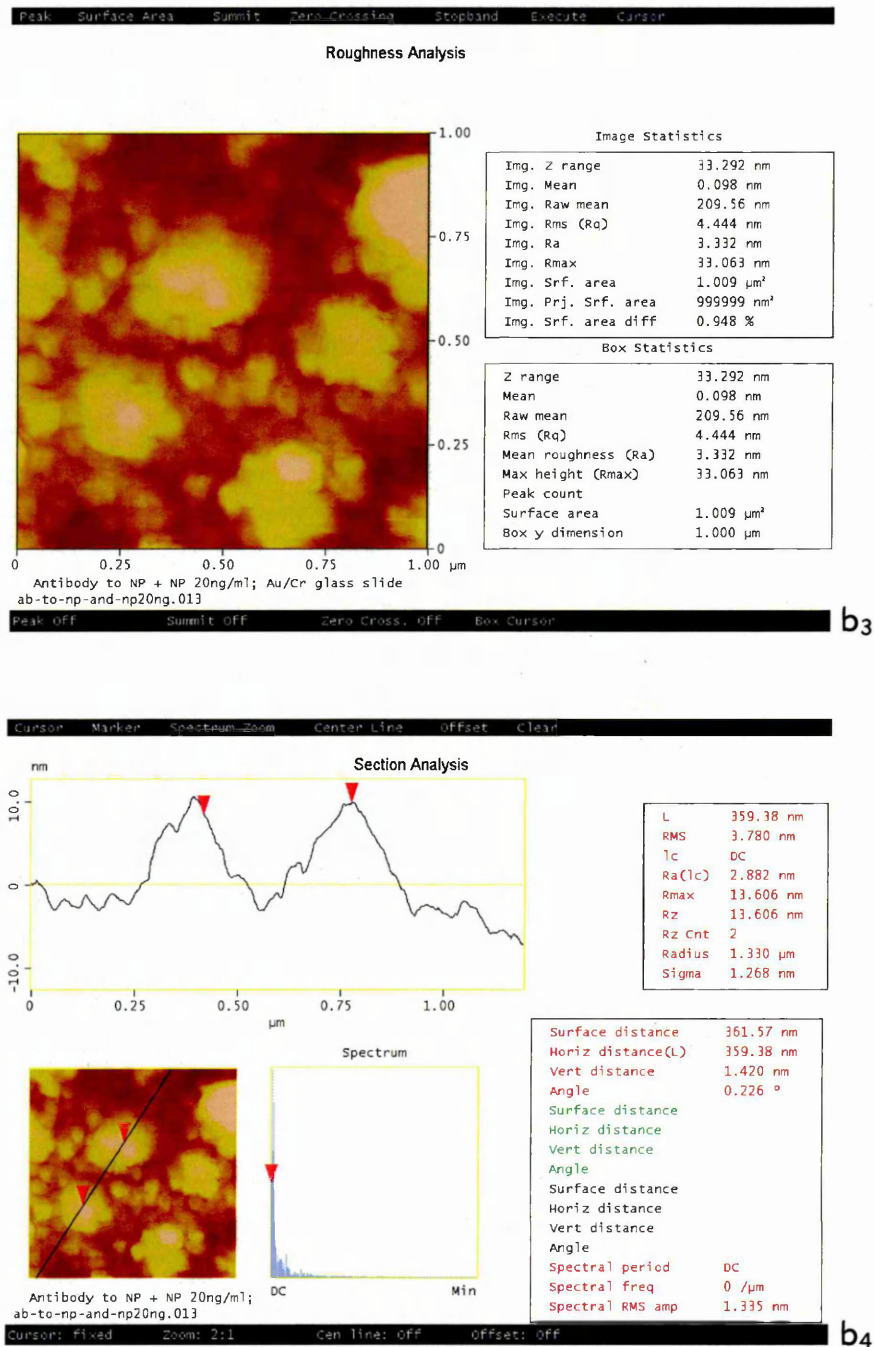


**Figure 4.2-24b** AFM tapping mode images of bounded *nonylphenol* molecules:  $b_1$  – height,  $b_2$  – pseudo-3D,  $b_3$  – roughness,  $b_4$  – section analysis.

As can be seen from the particle analysis of the AFM images (Fig. 4.2-25), the micelles are rather flat, which could be the result of their collapse after the drying of the sample.

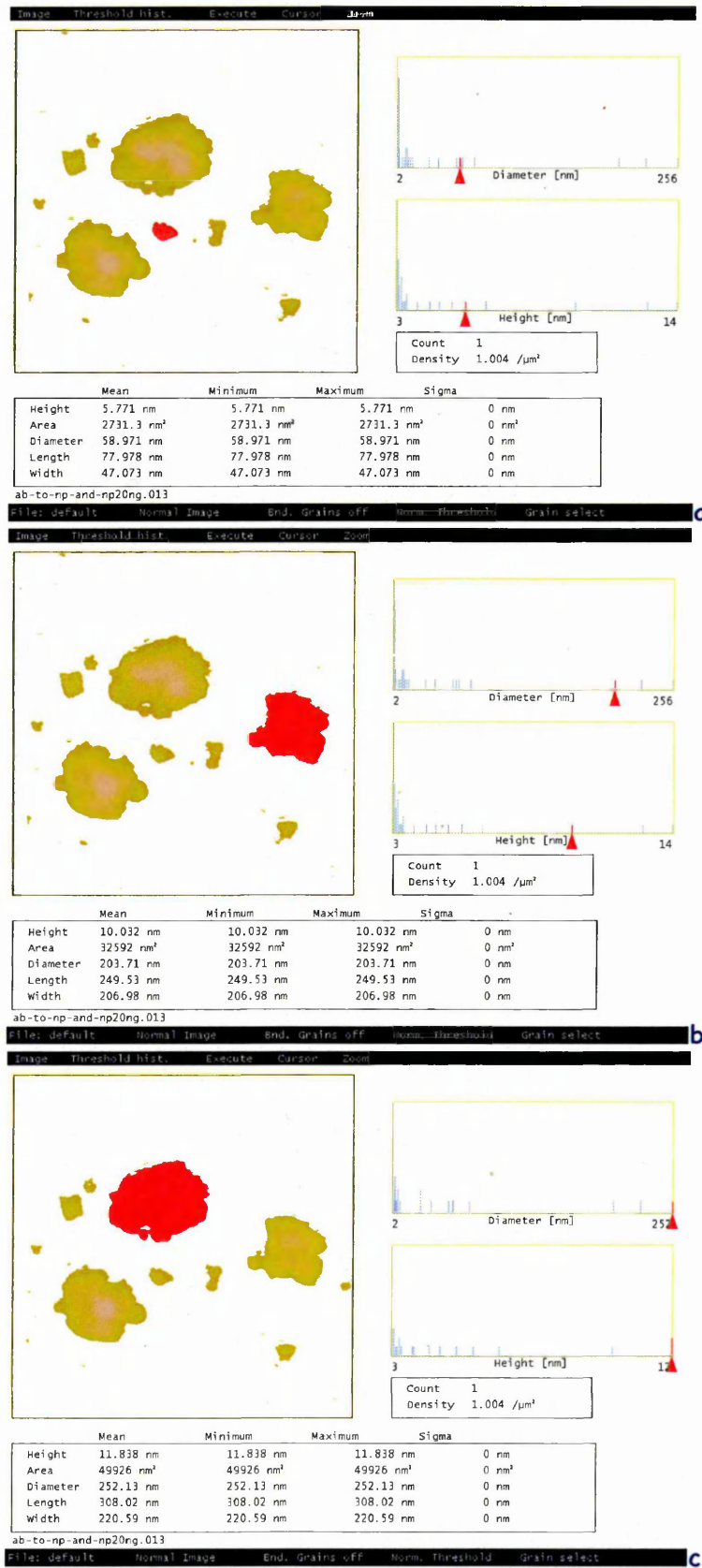


Figure 4.2-25 AFM particle analysis images of the layer of bounded *nonylphenol* molecules: **a** – micelle itself, **b** and **c** – aggregate of micelles.

The observed small grains are clustered on the surface to form larger aggregates. Height, width, length, and diameter of the observed grains and clusters of grains are summarised in Table 4.2-11. This observation is in good agreement with the model considering limited lateral accuracy of AFM due to the finite radius (4 – 7 nm) of the AFM tips.

**Table 4.2-11** Linear sizes of grains and clusters on the surface.

<i>parameter</i>	<i>size 1 (grains)</i>	<i>size 2</i>	<i>size 3</i>
Height, nm	5.184 ± 2.157	12.926 ± 2.435	22.82 ± 2.60
Diameter, nm	37.614 ± 4.188	219.43 ± 44.65	348.465 ± 32.081
Length, nm	47.621 ± 6.288	272.46 ± 44.51	426.48 ± 39.74
Width, nm	33.058 ± 2.662	196.55 ± 39.18	297.42 ± 75.50

## 4.3 Registration of Water Pollutants Using the Enzyme Sensor Array

### 4.3.1 Registration of the enzyme reactions

The sensitivity of the  $\text{Si}_3\text{N}_4$  planar waveguide transducer to enzyme reactions was investigated in order to prove the effectiveness of the portable planar waveguide sensor array device as an enzyme sensor. For that reason, a test was required. The test experiment was divided in to two parts:

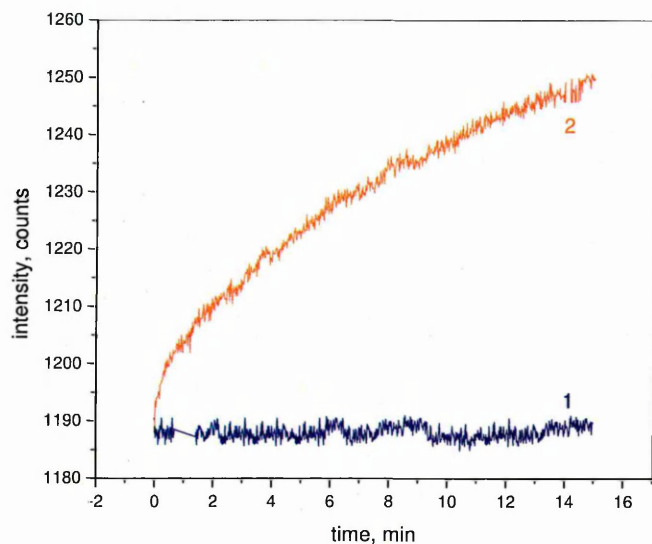
1. The effect of a substratum on the planar waveguide transducer coated with the organic dye/polyelectrolyte membrane was investigated.
2. Disposable nylon membranes with adsorbed enzymes were placed in the cell on top of the existing membrane, and the effect on the respective substratum was recorded again.

Following this procedure, it was established that the planar waveguide coated with the  $\text{PSS}-(\text{PAH}/\text{CTCT})_4$  membrane could successfully register the respective enzyme reaction. As shown in Figure 4.3-1a, in the case of the presence of the nylon membrane with the adsorbed *AChE* layer on top of the  $\text{PSS}-(\text{PAH}/\text{CTCT})_4$  membrane<sup>a</sup>, the output signal intensity of the planar waveguide enzyme sensor increased with the time of soaking in 10 mM acetylcholine chloride solution, in comparison to the one without the nylon membrane.

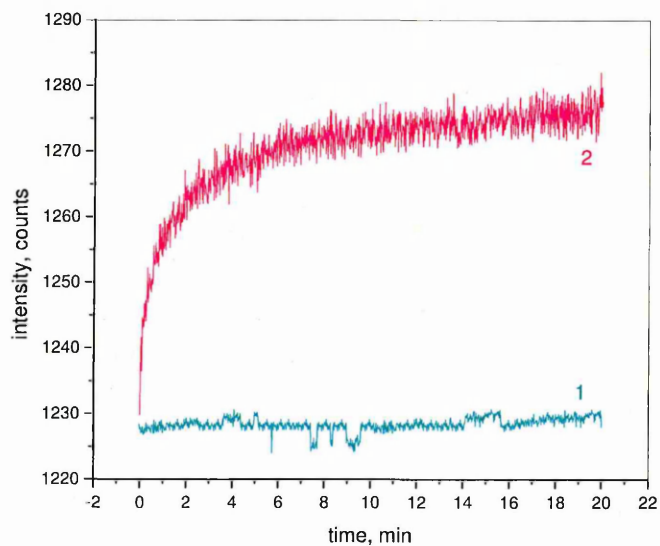
A similar effect was observed by soaking the planar waveguide with the  $[\text{PSS}-(\text{CTCT}/\text{PAH})_4 + \text{BChE}]$  membrane in a 10 mM butyrylcholine chloride solution. Figure 4.3-1b shows that the output signal intensity increased with time, indicating the production of choline and butyryl acid during the *BChE* enzyme reaction (a detailed description of enzyme reactions was given in §3.6).

---

<sup>a</sup> Henceforth referred to as  $[\text{PSS}-(\text{PAH}/\text{CTCT})_4 + \text{enzyme}]$  (i.e. *urease*, *AChE* or *BChE*) membrane. For example,  $[\text{PSS}-(\text{PAH}/\text{CTCT})_4 + \text{urease}]$  membrane or  $[\text{PSS}-(\text{PAH}/\text{CTCT})_4 + \text{BChE}]$  membrane.



a



b

**Figure 4.3-1** Kinetics of the *ChE* reaction. On both graphs: *1* – effect of acetylcholine (a) and butyrylcholine (b) on the PSS-(PAH/CTCT)<sub>4</sub> membrane; *2* – effect of acetylcholine (a) and butyrylcholine (b) on the [PSS-(PAH/CTCT)<sub>4</sub> + *ChE*] membrane.

Another type of enzyme reaction studied was the decomposition of *urea* catalysed by the enzyme *urease*. This effect was observed by soaking the planar waveguide with the [PSS-(CTCT/PAH)<sub>4</sub> + *urease*] membrane in a 100 mM *urea* solution (see Fig. 4.3-2).

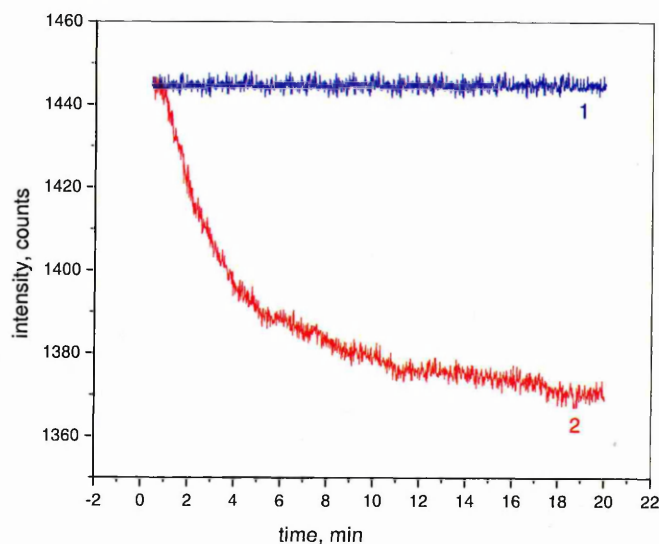


**Figure 4.3-2** Kinetics of the *urease* reaction: **1** – effect of urea on the PSS-(PAH/CTCT)<sub>4</sub> membrane, **2** – effect of urea on the [PSS-(PAH/CTCT)<sub>4</sub> + *urease*] membrane.

The response of the planar waveguide device for all enzyme reactions was significant. Generally, the noise signal was much smaller compared to the signal level. This was considered adequate to provide a sufficient dynamic range for response recording when the planar waveguide with [PSS-(CTCT/PAH)<sub>4</sub> + *enzyme*] membrane was exposed to some toxic agents.

### 4.3.2 Registration of heavy metal ions and pesticides using the enzyme sensor array

A number of experiments were carried out in order to analyse the effect of lead (Pb<sup>2+</sup>), cadmium (Cd<sup>2+</sup>), and nickel (Ni<sup>2+</sup>) ions, and pesticides (namely, imidacloprid and DVDP) on the activity of the immobilised enzymes in the three-channel enzyme sensor array. Generally, the inhibition of the enzymes *urease*, *AChE* and *BChE* by heavy metal ions and pesticides were detected in channels 2, 1 and 3, respectively.

The change in the output signal intensity was correlated to the reaction of a particular enzyme in the channel. For example, the decrease in the intensity of the

output signal in channel 2 indicated the decomposition of urea in this channel. However, the output signal intensities from channels 1 and 3 increasing with time indicated respectively the production of acetyl and butyryl acid during the *AChE* and *BChE* reaction (see Fig. 4.3-3a). Obtained results demonstrated that the response of each channel in the sensor array was similar to the response of a “single channel” planar waveguide (i.e. the same enzyme was in channels 1 and 3 while channel 2 was empty and served as a reference).

All enzymes were exposed to different concentrations of the heavy metal ions and pesticides in the range from 0.1 ppb to 1000 ppb. Exposing the planar waveguide coated with [PSS-(PAH-CTCT)<sub>4</sub> + enzyme] membrane to the substratum solution (or mixture of substrata) after the inhibition by heavy metal salts or pesticides, reduced the response of the enzyme reaction. Typical kinetics of the reactions of enzyme decomposition before and after inhibition in pollutants are presented in Fig. 4.3-3b. The routines for sample preparation, film deposition and measurements was described in detail in §3.6.

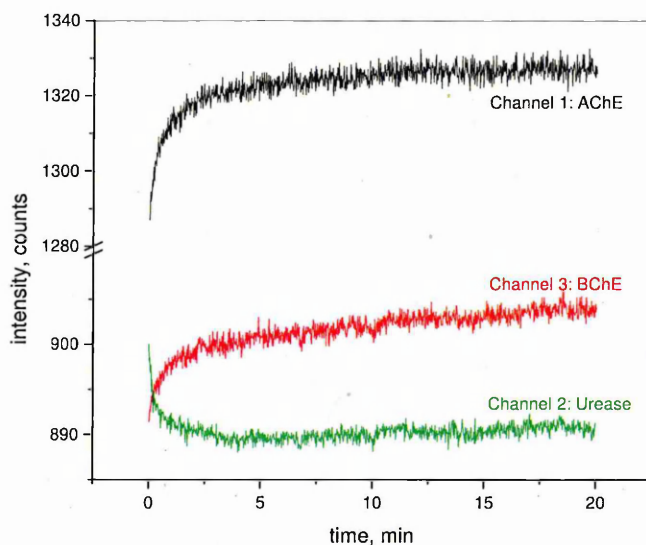
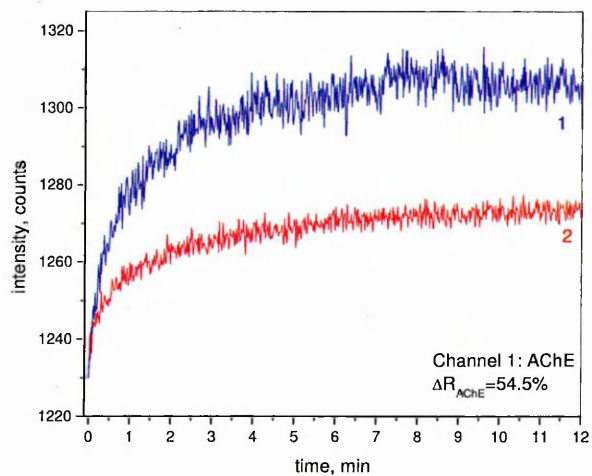
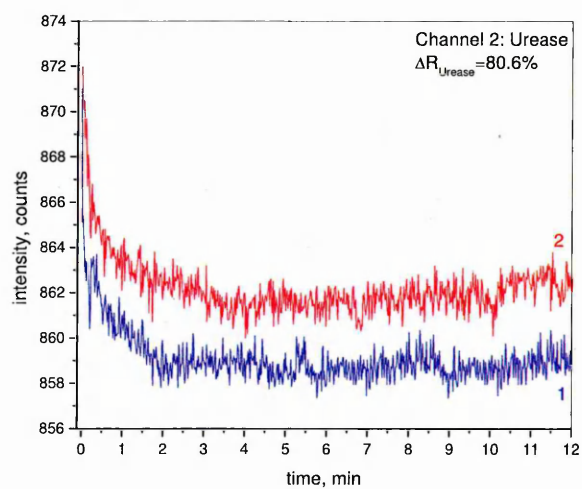


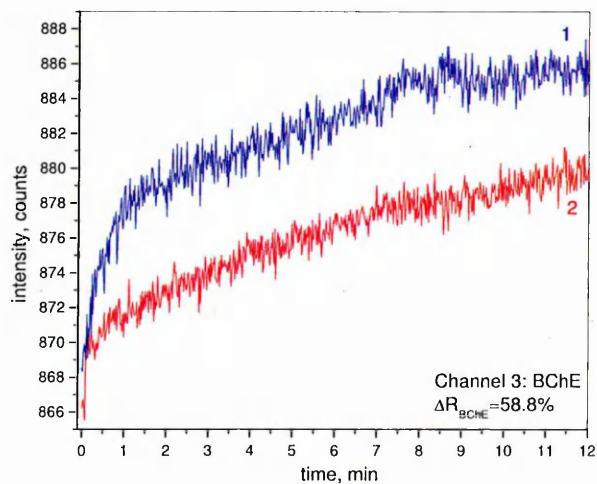
**Figure 4.3-3a** Kinetics of the enzyme reaction. Effect of mixture of substratum (100 Mm urea : 10 mM acetylcholine : 10 Mm butyrylcholine) on the [PSS-(PAH/CTCT)<sub>4</sub> + enzyme] membranes.



a



b



c

**Figure 4.3-3b** Typical kinetics of the reactions of enzyme decomposition in channels 1, 2 and 3: 1 – initial responses and 2 – responses after inhibition in 10 ppb imidacloprid.

Figure 4.3-4 represents the relative responses of *urease* (channel 2) to different concentrations of heavy metal ions and pesticides. The results show that the metal ions strongly and irreversibly inhibited the activity of *urease* to different extents. The residual activity of *urease* was found to decrease from ~86% down to ~9%, as the concentration of metal ions increased from 0.1 ppb to 10000 ppb.

As can be seen from the graph, lead ions are a stronger *urease* inhibitor than the other two metal ions. DVDP and imidacloprid showed a moderate inhibition effect on the enzyme *urease*; however, the *urease* activity was suppressed by DVDP more than imidacloprid. The toxicity of heavy metal ions and pesticides towards *urease* was found to decrease in the following order (see Table 4.3-1):

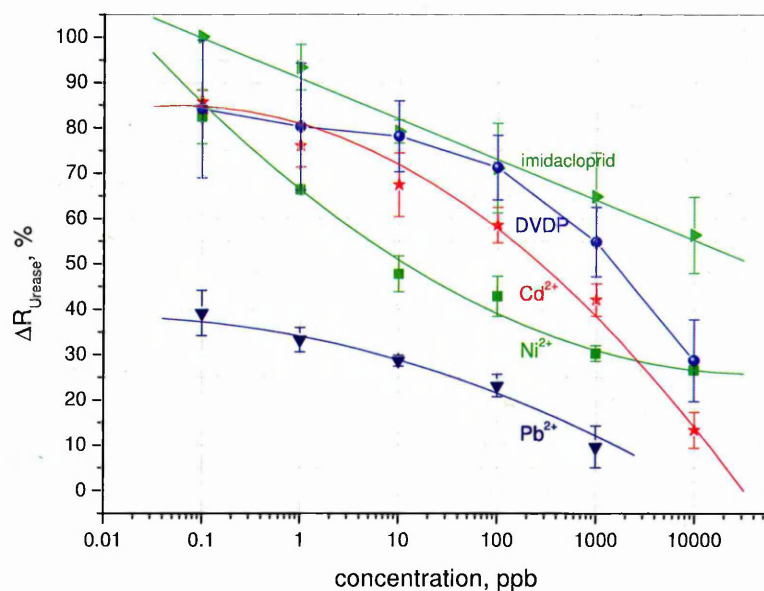


**Figure 4.3-4** Residual activity of *urease* as a function of the concentrations of the following pollutants: lead ( $Pb^{2+}$ ), nickel ( $Ni^{2+}$ ), cadmium ( $Cd^{2+}$ ), DVDP and imidacloprid.

The dependencies of residual activities of *AChE* and *BChE* on the concentration of heavy metal ions and pesticides are shown in Figures 4.3-5 and 4.3-6, respectively (obtained data also presented in Table 4.3-1). With good agreement with previous research (see chapter 2), the heavy metal ions were found to be less toxic to

both *cholinesterase* enzymes than to *urease*. The relative responses of the sensor signals were found to decrease from ~100% to ~50% for the *AChE* reaction and from ~85% to ~55% for the *BChE* reaction, after being exposed to different concentrations of heavy metal ions. The toxicity of heavy metal ions and pesticides towards *cholinesterase* enzymes was found to decrease in the following orders:

$DVDP > \text{imidacloprid} > \text{Ni}^{2+} > \text{Pb}^{2+} > \text{Cd}^{2+}$  for *AChE*

and

$\text{imidacloprid} > DVDP > \text{Pb}^{2+} > \text{Cd}^{2+} > \text{Ni}^{2+}$  for *BChE*.

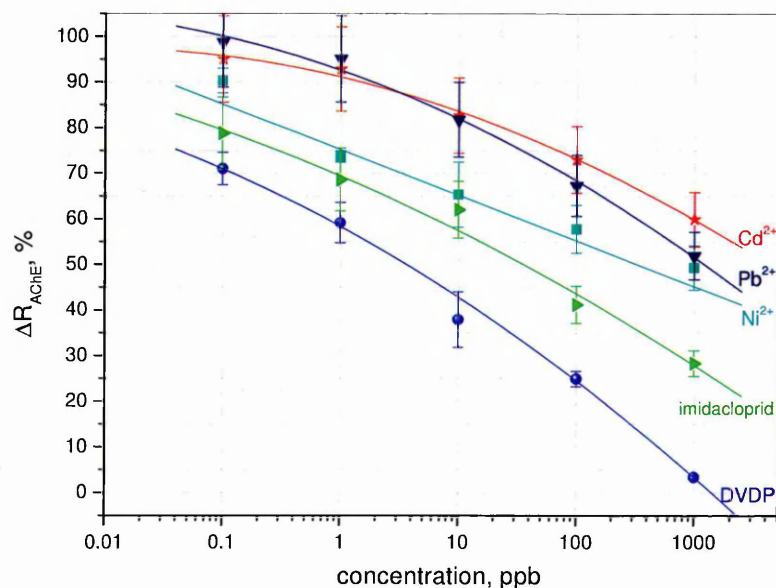


**Figure 4.3-5** Residual activity of *AChE* as a function of the concentrations of the following pollutants: lead ( $\text{Pb}^{2+}$ ), nickel ( $\text{Ni}^{2+}$ ), cadmium ( $\text{Cd}^{2+}$ ), DVDP and imidacloprid.

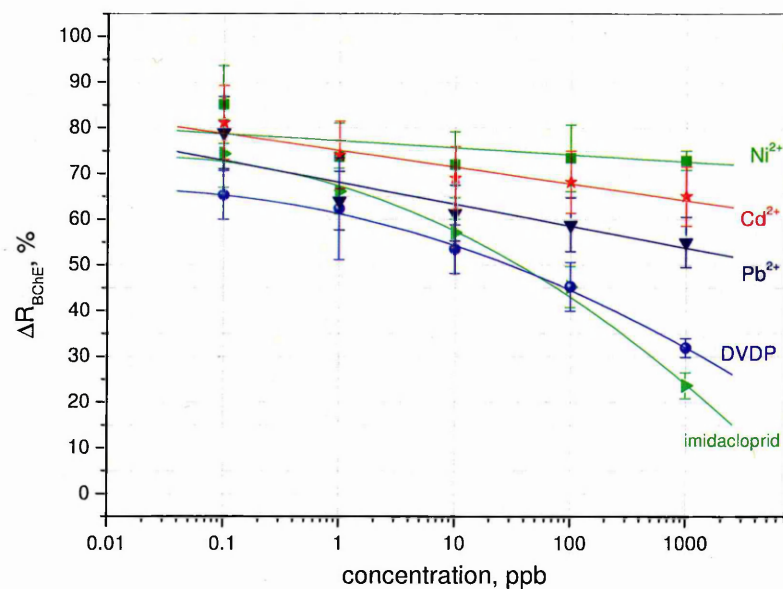


**Figure 4.3-6** Residual activity of *BChE* as a function of the concentrations of the following pollutants: lead ( $Pb^{2+}$ ), nickel ( $Ni^{2+}$ ), cadmium ( $Cd^{2+}$ ), DVDP and imidacloprid.

**Table 4.3-1** Dependencies of residual activity ( $\Delta R$ ) of *urease*, *AChE* and *BChE* on the concentration of different inhibitors.

<i>Pollutant</i>	<i>Concentration of pollutant, ppb</i>	$\Delta R_{AChE}, \%$	$\Delta R_{BChE}, \%$	$\Delta R_{Urease}, \%$
<i>Imidacloprid</i>	0.1	$78.65 \pm 7.9$	$74.23 \pm 7.42$	$100.0 \pm 5.0$
	1	$68.47 \pm 6.9$	$66.02 \pm 5.03$	$93.23 \pm 5.04$
	10	$61.895 \pm 6.2$	$56.94 \pm 2.97$	$79.09 \pm 2.58$
	100	$41.11 \pm 4.1$	$45.21 \pm 4.52$	$71.05 \pm 9.897$
	1000	$28.25 \pm 2.8$	$23.565 \pm 2.85$	$64.76 \pm 22.32$
	10000	–	–	$56.27 \pm 11.14$
<i>DVDP</i>	0.1	$70.92 \pm 3.55$	$65.21 \pm 5.31$	$84.10 \pm 15.20$
	1	$59.05 \pm 4.414$	$62.25 \pm 11.16$	$80.185 \pm 14.015$
	10	$37.852 \pm 6.121$	$53.41 \pm 5.31$	$78.10 \pm 7.81$
	100	$24.875 \pm 1.705$	$45.21 \pm 4.52$	$71.20 \pm 7.12$
	1000	$3.36 \pm 0.4$	$31.86 \pm 2.06$	$51.805 \pm 7.685$
	10000	–	–	$28.66 \pm 9.00$

<i>Pollutant</i>	<i>Concentration of pollutant, ppb</i>	$\Delta R_{AChE}, \%$	$\Delta R_{BChE}, \%$	$\Delta R_{Urease}, \%$
<i>Ni<sup>2+</sup></i>	0.1	90.2 ± 2.687	85.00 ± 8.48	82.37 ± 5.94
	1	73.52 ± 1.25	73.52 ± 7.44	66.26 ± 0.13
	10	65.23 ± 7.125	71.85 ± 7.23	47.72 ± 3.95
	100	57.68 ± 5.8	73.30 ± 7.32	42.80 ± 4.40
	1000	49.23 ± 4.9	72.78 ± 2.095	30.22 ± 1.72
	10000	–	–	26.455 ± 0.1
<i>Cd<sup>2+</sup></i>	0.1	95.00 ± 9.5	81.10 ± 8.11	85.73 ± 2.47
	1	92.80 ± 9.28	74.00 ± 7.42	75.99 ± 4.69
	10	82.58 ± 8.26	69.00 ± 6.91	67.40 ± 6.74
	100	72.897 ± 7.3	68.1 ± 6.82	58.52 ± 3.91
	1000	59.87 ± 5.99	65.00 ± 6.53	42.05 ± 3.56
	10000	–	–	13.31 ± 1.91
<i>Pb<sup>2+</sup></i>	0.1	98.70 ± 9.9	78.89 ± 7.91	39.10 ± 5.00
	1	95.00 ± 9.5	64.00 ± 6.42	32.69 ± 2.47
	10	81.69 ± 8.2	61.28 ± 6.14	27.98 ± 5.88
	100	67.21 ± 6.7	58.80 ± 5.92	23.14 ± 2.46
	1000	51.87 ± 5.2	55.01 ± 5.51	9.59 ± 4.65

The three-dimensional plot of residual activity of the enzymes (see Fig. 4.3-7) gives a visible inhibition pattern of pollutants: the areas of sensor responses to different heavy metal ions and pesticides are well separated, so all compounds can be easily distinguished according to their toxicity at different concentrations.

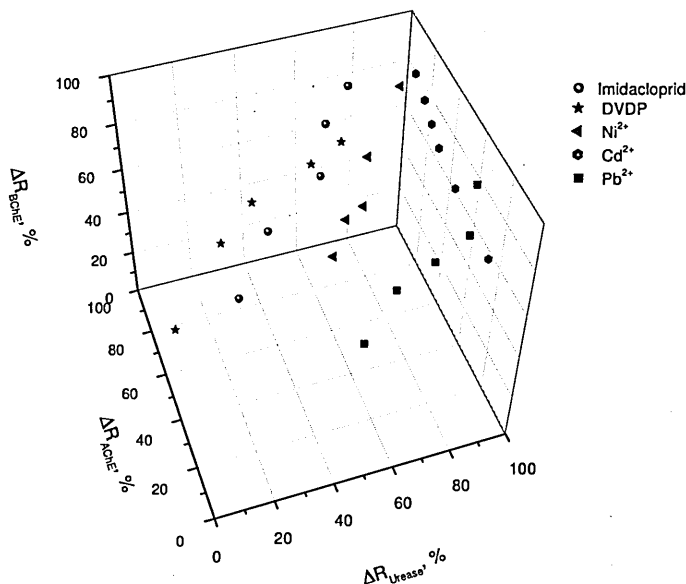
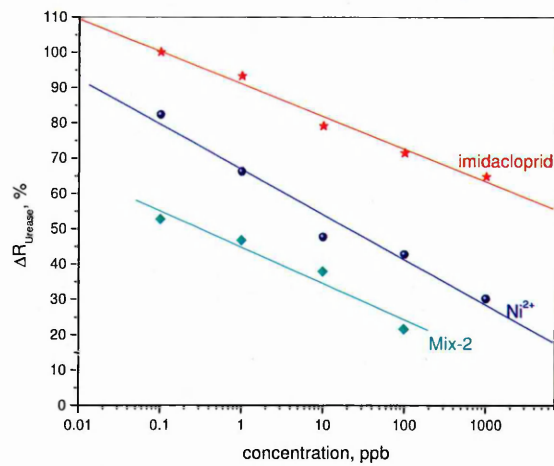


**Figure 4.3-7** Residual activities of *urease* ( $\Delta R_{Urease}$ ), *AChE* ( $\Delta R_{AChE}$ ) and *BChE* ( $\Delta R_{BChE}$ ) corresponded to different concentrations of heavy metal ions and pesticides.

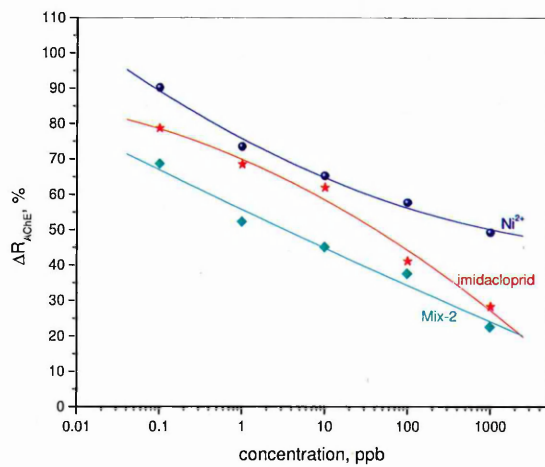
### 4.3.2 Registration of mixtures of pollutants using the enzyme sensor array

The response of the enzyme sensor array device to the mixture of pollutants and tap water samples from different sources was investigated in order to prove the potential use of it for multi-analyte detection. Two mixtures of the pollutants were prepared. The first mixture (Mix-1) was prepared by mixing DVDP and  $Cd^{2+}$ . The second one (Mix-2), was prepared by mixing pesticide imidacloprid and  $Ni^{2+}$ . Both mixtures were prepared in different concentrations ranging from 0.1 ppb to 1000 ppb.

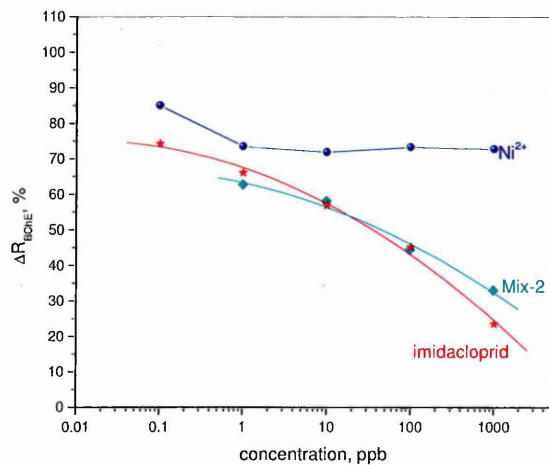
Experimental results show that the inhibition effect of Mix-2 on *urease* and *AChE* was lower than the effect of imidacloprid or nickel alone (Figures 4.3-7a and 4.3-7b). On the other hand, the sensor responses to the inhibition of *BChE* by Mix-2 were found to be similar to the effect of imidacloprid alone (Fig. 4.3-7c). Obtained experimental data are also summarised in Table 4.3-2.



a



b



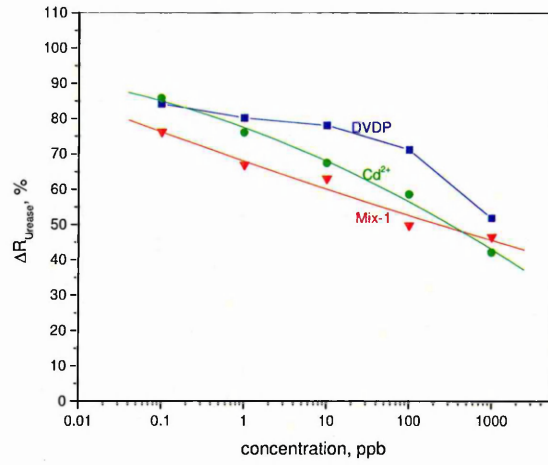
c

**Figure 4.3-7** Residual activity of enzymes (a – urease, b – AChE, and c – BChE) after exposure to Mix-2.

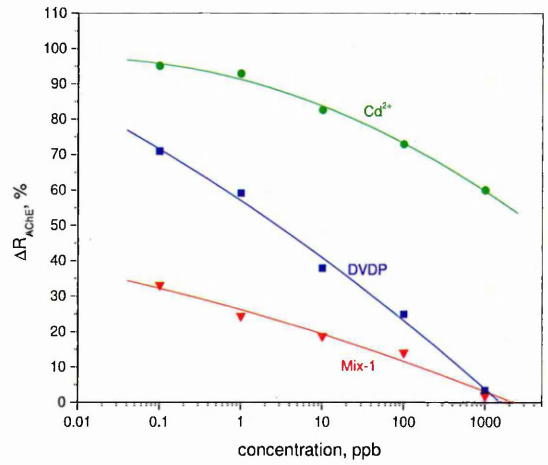
The effects of Mix-1 on the sensor response are shown in Fig. 4.3-8a,b,c and Table 4.3-2. As can be seen from Fig. 4.2-8, the mixture of DVDP and cadmium ions strongly suppressed the *AChE* activity. The inhibition of *BChE* by Mix-1 was slightly higher than that of DVDP. The sensor responses on the inhibition of *urease* by Mix-1 were found to be similar to the effect of cadmium alone (Fig. 4.3-8a).

As can be seen from the graphs, the presence of cadmium ions did most likely not affect the activity of the *cholinesterase* enzymes. This result suggests that the residual activity of these enzymes was strongly affected by their most toxic pollutant present in the mixture solution. Therefore, in the binary mixture containing DVDP and cadmium ions, sensor responses to the *urease* reaction were highly influenced by the cadmium ions, whereas the activities of the *cholinesterase* enzymes were strongly inhibited by DVDP pesticide. The combined inhibition effects of mixtures on enzymes were higher than the effects of a single pesticide or heavy metal ions.

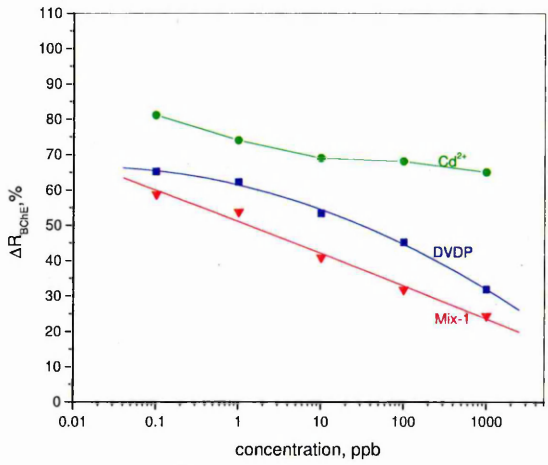
A three-dimensional plot of the residual activity for the three enzymes (*AChE*, *BChE*, *urease*) inhibited by heavy metal ions, pesticides and their mixtures taken at various concentrations is shown in Fig. 4.3-9. Sensor array responses to inhibition by Mix-1 (mixture of DVDP and cadmium ions) were near to the pesticide area, while the positions sensor array responses to inhibition by Mix-2 (mixture of imidacloprid and nickel ions) were close to the heavy metal ions area.



a



b



c

Figure 4.3-8 Residual activity of enzymes (a – urease, b – AChE, and c – BChE) after exposure to Mix-1.

**Table 4.3-2** Dependencies of residual activity ( $\Delta R$ ) of *urease*, *AChE* and *BChE* on the concentration of a mixture of pollutants.

<i>Enzyme</i>	<i>Pollutant</i>	<i>Concentration of pollutant, ppb</i>	$\Delta R, \%$
<i>Urease</i>	Mix-1: (DVDP + Cd <sup>2+</sup> )	0.1	76.26
		1	66.87
		10	62.94
		100	49.73
		1000	46.15
<i>AChE</i>	Mix-1	0.1	33.16
		1	24.42
		10	18.61
		100	14.12
		1000	1.89
<i>BChE</i>	Mix-1	0.1	58.75
		1	53.75
		10	40.82
		100	31.77
		1000	24.29
<i>Urease</i>	Mix-2: (imidacloprid + Ni <sup>2+</sup> )	0.1	52.67
		1	46.67
		10	37.81
		100	21.50
		1000	–
<i>AChE</i>	Mix-2	0.1	68.58
		1	52.20
		10	45.02
		100	37.82
		1000	22.44
<i>BChE</i>	Mix-2	0.1	–
		1	62.75
		10	58.11
		100	44.50
		1000	32.99

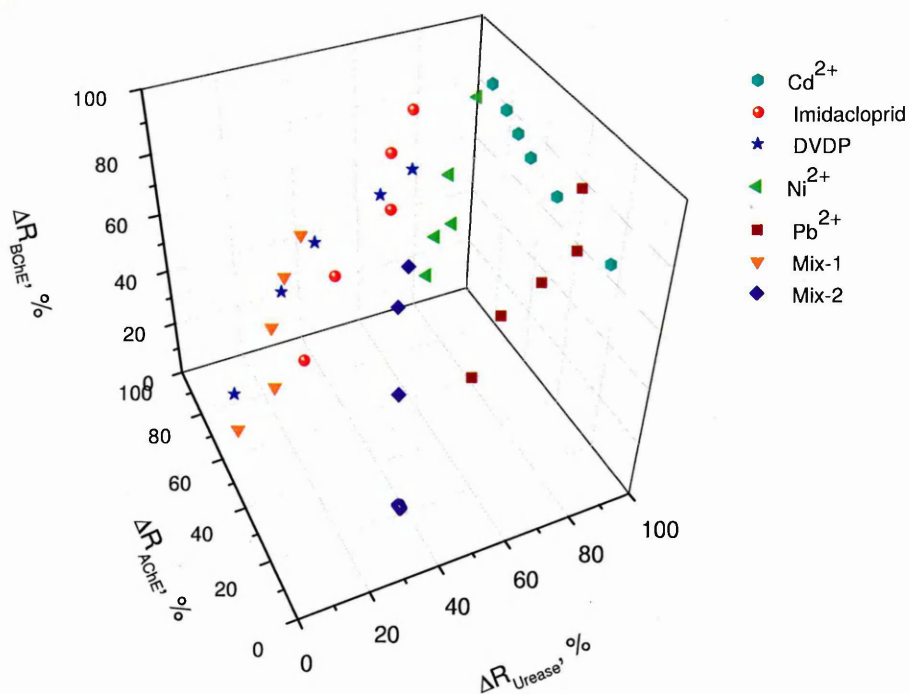


**Figure 4.3-9** Residual activities of *urease* ( $\Delta R_{Urease}$ ), *AChE* ( $\Delta R_{AChE}$ ) and *BChE* ( $\Delta R_{BChE}$ ) corresponded to different concentrations of heavy metal ions and pesticides.

### 4.3.3 Analysis of pollutants using ANN algorithm

Previous research<sup>[9, 10, 11, 12, 13, 14]</sup> has established that ANN based algorithms have a high accuracy in classifying experimental data obtained from enzyme sensor arrays. As was mentioned in §3.6 for the analysis of pollutants based on ANN algorithms, the experimental data were divided into two data sets, one of them was used for training, and another one was used for testing the network models. Tables 4.3-4 represent the data set used for training the network.

Classified pollutants were then quantified using individual network models. Despite the limited amount of data for training network models the successful classification and quantification of all data sets was obtained. That gave the hope that the neural network models could be used to analyse unknown compounds or their

mixtures, assuming that they belonged to the group of five analytes used to train the models.

**Table 4.3-4** Data set for training the neural network to classify the pollutants.

<i>c, ppb</i>	<i>Input value</i>			<i>Output value</i>			
	$\Delta R_{Urease}$	$\Delta R_{AChE}$	$\Delta R_{BChE}$	<i>Binary code</i>			<i>target analyte</i>
0.1	84.100	70.920	65.210	0	0	0	DVDP
1	80.185	59.050	62.250	0	0	0	
10	78.100	37.852	53.410	0	0	0	
100	71.200	24.875	45.210	0	0	0	
1000	51.805	3.360	31.860	0	0	0	
0.1	39.100	98.700	78.890	0	0	1	Pb <sup>2+</sup>
1	32.690	95.000	64.000	0	0	1	
10	27.980	81.690	61.280	0	0	1	
100	23.140	67.210	58.800	0	0	1	
1000	9.590	51.870	55.010	0	0	1	
0.1	85.730	95.000	81.100	1	0	0	Cd <sup>2+</sup>
1	75.990	92.800	74.000	1	0	0	
10	67.400	82.580	69.000	1	0	0	
100	58.520	72.897	68.100	1	0	0	
1000	42.050	59.870	65.000	1	0	0	
0.1	100.000	78.650	74.230	0	1	1	Imidacloprid
1	93.230	68.470	66.020	0	1	1	
10	79.090	61.895	56.940	0	1	1	
100	71.050	41.110	45.210	0	1	1	
1000	64.760	28.250	23.565	0	1	1	
0.1	82.370	90.200	85.000	1	0	1	Ni <sup>2+</sup>
1	66.260	73.520	73.520	1	0	1	
10	47.720	65.230	71.850	1	0	1	
100	42.800	57.680	73.300	1	0	1	
1000	30.220	49.230	72.780	1	0	1	

The vitality of the neural network model was tested with unknown samples. Four tap water samples from different sources were investigated (description of the samples was given in §3.6). A pattern recognition algorithm was exploited using ANN software to identify and quantify pollutants in these samples. The results revealed that all samples contained a relatively small amount of heavy metal ions (see Table 4.3-5).

**Table 4.3-5** Dependencies of residual activity ( $\Delta R$ , %) of *urease*, *AChE* and *BChE* on the concentration of pollutants in tap water samples.

<i>sample №</i>	<i>source</i>	$\Delta R_{Urease}$	$\Delta R_{AChE}$	$\Delta R_{BChE}$	<i>analyte</i>	<i>C<sub>analyte</sub></i> <i>ppb</i>
1	SHU, clean room, Millipore water	86.97	82.74	90.34	Ni <sup>2+</sup>	0.101
2	SHU, Lab 4L19, tap water	26.52	84.67	80.83	Pb <sup>2+</sup>	998.69
3	Sheffield, UK	28.57	85.00	85.38	Pb <sup>2+</sup>	0.120
4	Odessa, Ukraine	67.55	59.23	44.37	Ni <sup>2+</sup> + Imidacloprid	76.62

Obtained results were reasonable since the network models were trained using a limited amount of data and they established that the neural network models were able to generalize the information given and could be used to analyse unknown compounds.

## 4.4 Summary

The first section (4.1) in this chapter is devoted to the adsorption of protein BSA into PS and provides the results of both dynamic and static spectroscopic ellipsometry measurements for the study of the *in situ* adsorption of BSA into PS. Special attention is paid to the study of the morphology of PS layers. The porosity and amount of adsorbed BSA were determined by fitting the ellipsometric data to the Bruggeman effective medium approximation model. The presence of intermediate adsorbed layers of polyelectrolytes was found to increase protein adsorption.

Section 4.2 describes results of the registration of LMW environmental toxins, such as nonylphenol, atrazine, simazine, and T-2 mycotoxin, with the methods of surface plasmon resonance (SPR) and total internal reflection ellipsometry (TIRE). The immune assay approach was exploited for *in situ* registration of the above toxins with specific antibodies immobilized onto a gold surface via a polyelectrolyte layer using the electrostatic self-assembly (ESA) technique. TIRE showed a higher sensitivity than the SPR technique. The obtained responses of the TIRE method were higher than anticipated for the immune binding of single molecules of nonylphenol or T-2 mycotoxin. The mechanism of binding of large aggregates of these toxins to respective antibodies was suggested as a reason for this. The formation of large molecular aggregates of toxin molecules on the surface was later proven by the AFM study.

Section 4.3 gives the results of the registration of typical water pollutants such as heavy metal ions  $\text{Cd}^{2+}$ ,  $\text{Pb}^{2+}$ , and  $\text{Ni}^{2+}$ , and pesticides imidacloprid and DVDP with the planar waveguide enzyme sensor array over a wide range of concentrations (from 1000 ppb down to 0.1 ppb). Experimental data were analyzed with the ANN algorithm which allowed both the recognition of the pollutants and evaluation of their concentrations. The results of the registration of mixtures of pollutants and tap water samples from different sources using the enzyme sensor array are also presented in this section.

## References

### §4.1

- [1] Bisi O., Ossicini S. and Pavesi L. *Porous silicon: a quantum sponge structure for silicon based optoelectronics*, Surface Science Reports **38** (2000) 1-126.
- [2] *Guide to Using WVASE®*, J. A. Woollam Co. Inc., 2003.
- [3] Boukherroub R., Wayner D., Lockwood D. et al. *Passivated luminescent porous silicon*, Journal of Electrochemical Society **148** (2001) H91-H97.

### §4.2

- [4] Arwin H., Poksinski M. and Iohansen K. *Total internal reflection ellipsometry: principles and applications*, Applied Optics **43** (2004) 3028-3036.
- [5] Nabok A. *The method of total internal reflection ellipsometry for thin film characterisation and sensing*, ECOF-10 (2005) Riga, Latvia, Oral presentation.
- [6] Azzam R. M. A. and Bashara N. M. *Ellipsometry and polarized light*, North-Holland, Amsterdam, 1992.
- [7] Xia Liu, Jingyan Wei, Daqian Song, Ziwei Zhang, Hanqi Zhang and Guimin Luo *Determination of affinities and antigenic epitopes of bovine cardiac troponin I (cTnI) with monoclonal antibodies by surface plasmon resonance biosensor*, Analytical Biochemistry **314** (2003) 301-309.
- [8] Nabok A. V., Tsargorodskaya A., Holloway A., Starodub N. F. and Gojster O. *Registration of T-2 mycotoxin with total internal reflection ellipsometry and QCM impedance methods*, Biosensors and Bioelectronics **22** (2007) 885-890.

### §4.3

- [9] Haron S. *Planar waveguide enzyme sensors coated with nanocomposite membranes for water pollution monitoring*, Thesis for the degree of Doctor of Philosophy, Sheffield Hallam University, 2005.
- [10] Arkhytova V. N., Dzyadevych S. V., Soldatkin A. P., El'skaya A. V., Jaffrezic-Renault N., Jaffrezic H. and Martelet C. *Multibiosensor based on enzyme inhibition analysis for determination of different toxic substances*, Talanta **55** (2001) 919-927.
- [11] Starodub N. F., Kanjuk N. I., Kukla A. L. and Shirshov Yu. M. *Multi-enzymatic electrochemical sensor: field measurements and their optimisation*, Analytica Chimica Acta **385** (1999) 461-466.
- [12] Kukla A. L., Kanjuk N. I., Starodub N. F. and Shirshov Yu. M. *Multienzyme electrochemical sensor array for determination of heavy metal ions*, Sensors and Actuators B **57** (1999) 213-218.
- [13] Bachmann T. T., Leca B., Vilatte F., Marty J.-L., Fournier D. and Schmid R. D. *Improved multianalyte detection of organophosphates and carbamates with disposable multielectrode biosensors using recombinant mutants of Drosophila acetylcholinesterase and artificial neural networks*, Biosensors and Bioelectronics **15** (2000) 193-201.
- [14] Bachmann T. T. and Schmid R. D. *A disposable multielectrode biosensor for rapid simultaneous detection of the insecticides paraoxon and carbofuran at high resolution*, Analytica Chimica Acta **401** (1999) 95-103.

# *CHAPTER 5.*

## **CONCLUSIONS**

**and**

## **RECOMMENDATIONS**

This chapter presents the conclusions of the research described in the thesis. Proposals for future work are suggested.

## 5.1 Thesis Conclusions

### 5.1.1 Ellipsometric study of the adsorption of BSA into PS

The samples of porous silicon were studied with SEM and AFM techniques, and the morphology revealed the presence of pores having a wide range of dimensions from micrometers down to tens of nanometers. The method of spectroscopic ellipsometry was found to be suitable for studying porous silicon. The fitting of ellipsometric data to the three-layer EMA model yielded realistic parameters for the layers. The thickness and porosity obtained for the PS layers corresponded well to the results of SEM and gravimetry.

Adsorption of BSA into PS was studied *in situ* at the solid/liquid interface with spectroscopic ellipsometry. The results were analyzed with the help of a three-layer EMA model, which yielded the relative amounts of adsorbed BSA. It was found here that the adsorption of polyelectrolytes (either PAH or PSS) in porous silicon increased the amount of subsequently adsorbed BSA.

Comparison of static and dynamic spectroscopy ellipsometry measurements showed the advantages of the former as regards the amount and reliability of the information obtained.

### 5.1.2 Registration of low molecular weight environmental toxins with the method of total internal reflection ellipsometry

The low molecular weight (LMW) environmental toxins, such as herbicides simazine and atrazine, nonylphenol, and T-2 mycotoxin were registered with the optical methods of surface plasmon resonance (SPR) and total internal reflection ellipsometry (TIRE). The immune assay approach was exploited for *in situ* registration of the above toxins with specific antibodies immobilised onto the chromium-gold surface via a (poly)allylamine hydrochloride layer using the electrostatic self-assembly (ESA)

technique. The comparison of two methods of SPR and TIRE showed a higher sensitivity of the latter.

The method of TIRE was proven as an excellent analytical tool for biosensing, particularly for the registration of LMW molecules. For example, it allowed the registration of T-2 mycotoxin over a wide range of concentrations from 100  $\mu\text{g/ml}$  down to 0.15  $\text{ng/ml}$ . The TIRE kinetic measurements allowed the evaluation of adsorption and desorption coefficients, and the association constants for binding T-2 mycotoxin molecules to both poly- and monoclonal antibodies. Association constants of  $1.7 \cdot 10^6$  and  $1.9 \cdot 10^7 \text{ mol}^{-1} \cdot \text{l}$  for poly- and monoclonal T-2 antibodies, respectively, proved to be highly specific antibody/toxin binding reactions. Monoclonal antibodies appeared to be 10-fold more selective to T-2 mycotoxin than polyclonal ones, although polyclonal antibodies provided a wider range of linear response (0.1 – 150  $\text{ng/ml}$ ) to T-2 mycotoxin. The obtained changes in adsorbed layer thickness of 4 – 5 nm, caused by T-2/antibodies binding, were larger than the actual size of T-2 mycotoxin molecules.

The same method of TIRE was applied to study the specific binding of nonylphenol molecules to respective antibodies. An anomalously high increase in the film thickness was detected. Comparison of these findings with the results of the previous study of T-2 mycotoxin allowed us to suggest a common mechanism of binding of large aggregates of LMW hydrophobic toxins, such as nonylphenol and T-2 mycotoxin, to respective antibodies. This effect boosted the sensitivity of the biosensor by 3-4 orders of magnitude and allowed the exploitation of the direct immune assay approach. The use of the sensitive technique of TIRE makes possible the registration of very low concentrations of the above toxins in the sub-ppb range, which was previously only achievable using the competitive immune reaction approach.

The mechanism of specific binding of large aggregates of nonylphenol was suggested. The formation of large molecular aggregates of nonylphenol and T-2 mycotoxin molecules on the surface was directly confirmed with AFM measurements. Modelling of the micelle of amphiphilic nonylphenol molecules in aqueous solutions yielded a size of micelles of about 34 nm, which was in good agreement with experimental data obtained from the AFM study. The mechanism of specific binding of large molecular aggregates to respective antibodies can be extended to other hydrophobic low molecular weight toxins, such as T-2 mycotoxin.

### 5.1.3 Registration of water pollutants using the enzyme sensor array

The proposed sensor was based on  $\text{SiO}_2/\text{Si}_3\text{N}_4$  planar waveguide with a sensing window coated with electro-statically self-assembled film containing pH sensitive organic chromophore molecules. A disposable nylon membrane with adsorbed enzymes (urease, acetyl-, and butyryl- cholinesterase) was placed on the top of the composite film.

Enzyme reactions, as well as their inhibition by the traces of some typical water pollutants, such as heavy metal ions  $\text{Cd}^{2+}$ ,  $\text{Pb}^{2+}$ , and  $\text{Ni}^{2+}$  as well as the pesticides imidacloprid and DVDP, and their mixtures were registered by monitoring the changes in the intensity of light coming out from the planar waveguide.

A portable prototype sensor array set-up was built comprising a fan-beam laser diode, a semi-cylindrical lens, a planar waveguide with a three-channel cell attached, and a CCD array photodetector. Dedicated software was developed for CCD image processing.

The pattern of sensor responses was analysed further by using the artificial neural network algorithm. Despite the relatively small amount of experimental data, the trained neural networks were able to classify and quantify the pollutants.

The prototype sensor array device provided both the recognition of water pollutants and evaluation of their concentration over a wide range from 1000 ppb down to 0.1 ppb.

## 5.2 Recommendations for Future Work

1. One of the main targets in bio-sensing is increasing the effective adsorption area and thus the sensitivity. Porous silicon (PS) has surface area of more than 100 times larger than planar silicon samples. Physical phenomena in PS, which can be exploited for transducing bio-reactions on its surface into measurable physical parameters include optical interferometry, photoluminescence and electroluminescence (EL).

The EL seems to be more attractive because of the high sensitivity of luminescent measurements. EL requires much less experimental efforts and could be recommended for the development of portable PS biosensors. Although the method of EL is not selective, it is very suitable for registration of the general bio-toxicity of the environment. Further study of EL in PS can be directed towards registration of specific antigen–antibody binding.

2. The method of total internal reflection ellipsometry (TIRE) was successfully applied for the registration of the low molecular weight toxins in water down to a ppb level. Future work can be focused on the development of portable and cost effective sensing devices based on principles of TIRE, as well as on a wider implementation of the TIRE method for different sensing tasks, such as:

- Application of TIRE to a wider range of toxins including mycotoxins, alkylphenols, pesticides and herbicides for quality control of agricultural products and food;
- DNA analysis directed towards the recognition of the genomic DNA of different species, via electrostatic adsorption of a single strand DNA (ss-DNA) on the surface and subsequent binding of another ss-DNA from the solution. The adsorption of the complementary ss-DNA should result in a significant increase in the thickness due to the hybridization and subsequent formation of the DNA double helix structure, while adsorption of non-complementary ss-DNA should yield much smaller response;

- Determination of the organic vapours: the TIRE method should provide enough sensitivity to record small changes in the optical parameters of *phthalocyanine films* caused by the exposure to low concentrations (in ppm level) of the organic vapors such as alcohols, hydrocarbons, aromatic, etc.

- In addition, the method of TIRE can be used for evaluation of the optical parameters of the electrostatically assembled films containing CdS and ZnS colloid nanoparticles. Such nano-composite films are considered as promising candidates for the development of novel materials for tuneable light emitting device.

The phenomenon of specific binding of large aggregates of hydrophobic toxins and thus boosting the sensitivity can be widely exploited in bio-sensing. A new model, which takes into account the non-spherical shape of micelles and their simultaneous binding to several antibodies, should be developed instead of the simple model of a spherical micelle of nonylphenol molecules proposed in this thesis.

3. Although considerable time and efforts have been spent during this study for the development of a portable planar waveguide sensor array device, it is only a small part of a huge work. In order to overcome certain limitations and to ensure the ability of the device for monitoring water pollutants in a real environment, further work needs to be done, namely:

- The optical enzyme sensor array should be exposed to more complex pollutant mixtures and a larger variety of pollutants in order to further evaluate the ability of the portable sensor array device to identify and quantify different type of pollutants;

- The pattern recognition algorithm should be integrated with the portable sensor array device in order to have simultaneous *in situ* monitoring and analysis of the pollutants in aqueous solutions;

- Different enzymes should be tested as sensitive elements in the nano-composite membrane and the number of the channels in the cell should be increased.

# *APPENDICES*

## **Appendix A:**

A brief description of the software developed for the portable planar waveguide enzyme sensor array device is presented.

## **Appendix B:**

Here the methods of external reflection ellipsometry and total internal reflection ellipsometry are compared.

## **Appendix C:**

A very short introduction to the artificial neuron network is given.

## **Appendix D:**

The data definitions and abbreviation descriptions that appear in the AFM images are specified.

## **Appendix E:**

Abstracts of the published works.

## Appendix A

### Software for portable planar waveguide enzyme sensor array device

#### 1. Software overview

This software contains the following files, which are required to start it and control the C7557 MCD controller (see Table A1).

**Table A1** Files required to start software and control the C7557 MCD controller

<i>File Name</i>	<i>Description</i>
anna1.exe	Execution file for this software
McdCont.dll <sup>a</sup>	DLL file for controlling an MCD controller
McdMain.dll <sup>a</sup>	Interface DLL file for this software and an MCD controller

When this software starts up, the black DOS window as shown in Figure A1 appears on the screen.

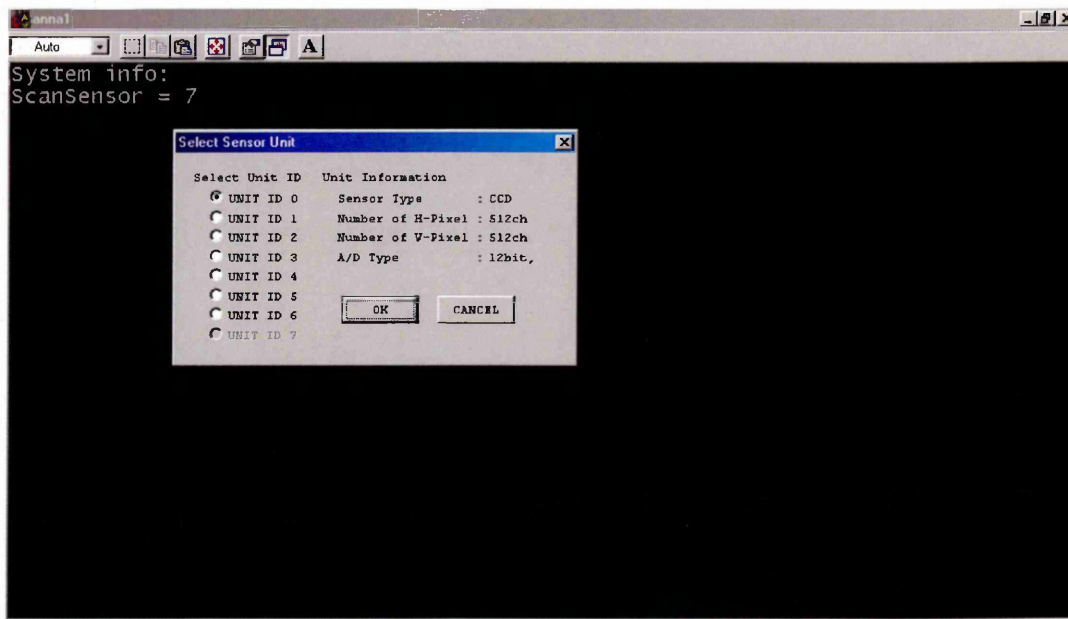


**Figure A1** Software window.

<sup>a</sup> Supplied by Hamamatsu Photonics K. K.

This window consists of three parts:

1. System information.
2. Measurement condition setup area.
3. Data display area.

Below a short description of each part is provided.

## 2. *System information*

### 2.1 Initialization.

*Function Name:* ScanSensor( );

*Description:* Check all the SCSI IDs, and confirm that the MCD controller is connected. If devices are connected, the return value represents the number of devices connected. The return value is "0" if no devices are connected.

*Return Values:*

1~7	:	Normal completion;
0	:	MCD controller not connected.

### 2.2 MCD Selection.

*Function Name:* SelectSensorUnit(Status);

*Description:* When multiple MCD controllers exist, it becomes necessary to select which is to be controlled. Running this function displays a selection dialog box from which the desired controller is selected. When a controller is selected, the status information is returned in the argument. The selected controller ID is returned with normal completion, and 0xffff(-1) in the case of an error.

*Return Values:*

1~7	:	Normal completion;
0xffff(-1)	:	No MCD controller connected.

### 2.3 Temperature Monitor.

*Description:* Obtains the monitor status for the sensor head.

*Return values:* 10-bit precision between 0 and 123.

## 3. *Measurement condition setup area*

### 3.1 Amp Gain Control.

*Description:* Controls the gain (Low/Middle/High) for the sensor output amp in the MCD controller.

*Recommended values:*  $0\pm 3$  for a bright signal and  $4\pm 6$  for a weak signal.

### 3.2 Exposure Time Control

*Description:* Controls the exposure timer for the sensor.

*Range :*  $x \sim 65535$  ms,  $x$  differs between types of sensors.

*Recommended value:* 100~ 500 ms.

### 3.3 Number (n) / Time of Measurement (t, min)

*Description:* Single shot measurement – acquires one shot of data ( $n = 0$ ).  
Continuous measurement – acquires data continuously. Only last set of data will be saved ( $n > 0$ ).

### 3.4 Delay time (sec)

*Description:* Delay time between sensor scan starts (continuous measurement).

### 3.5 Save Data

*Description:* Saves the average for three channels vs. intensity, pixels vs. intensity and  $\Delta I = I_{\text{end}} - I_0$  for each channel data as a measurement data files. The maximal length of the file name is 100 characters.

### 3.6 Exit (Y/N)

*Description:* quits this software.

## 4. Text of the program (C/C++)

```
// anna1.cpp : Defines the entry point for the console application.  
// Hamamatsu C7020 CCD array; Head type: S7010-0906.  
// * 14 Feb 2005 - 27 Mar 2007*  
// CCD.exe
```

```
#include "stdafx.h"  
#include <math.h>  
#include <iostream.h>
```

```

#include <stdlib.h>
#include <time.h>
#include <string.h>
#include <windows.h>
#include "McdMainapi.h"

#define WORD unsigned short int
#define LPWORD WORD*

struct tm *date_time;
time_t timer;
time_t start_time, cur_time;

int main(int argc, char* argv[])
{
    cout << " *** SYSTEM INFO: *** " << endl;
    cout << " " << endl;

    // Reading System Time
    time(&timer);
    date_time=localtime(&timer);
    cout << asctime(date_time) << endl;

    // Initialization.
    // Return Value: 1..7 - Normal completion; 0 - MCD controller NOT connected
    WORD n_scsi, status, scsi_id;
    SENSOR_STATUS sensor_status;

    // Checking Connected Devices.
    // Return Value: if devices are connected - 1, if no device is connected - 0x1001
    n_scsi = ScanSensor();
    printf( " ScanSensor = %x\n", n_scsi );
    for( int i = 0; i < n_scsi; i++ ) {
        status = CheckSensor( i, &sensor_status );
        if ( status != 1 )
        {
            printf( "CheckSensor[%d] = %x\n", i, status );
            return 0;
        }
    }

    // MCD section.
    // Return Value: 1..7 - Normal completion; 0xffff(-1) - No MCD controller connected
    scsi_id = SelectSensorUnit( &sensor_status );
    printf( " SelectSensorUnit = %d\n", scsi_id );

    /* S C A L E ! *
    // Amp Gain Control.
    // Return Value: 1 - Normal completion; and other than 1 with an error
    // Amp Gain: (Low/Middle/High)
    // Status acquisition 0:x1/2; 1:x1; 2:x2; 3:x5; 4:x10; 5:x20; 6:x50; 7:x100
    int AmpGain;
    cout << " " << endl;
    cout << " " << endl;
    cout << " *** MEASUREMENT CONTROL: *** " << endl;
    cout << " " << endl;
    cout << " " << endl;

```

```

cout << "      Set AmpGain {Low/Middle/High} [default 1]" << endl;
cout << "      0: x1/2;" << endl;
cout << "      1: x1; " << endl;
cout << "      2: x2; " << endl;
cout << "      3: x5; " << endl;
cout << "      4: x10; " << endl;
cout << "      5: x20; " << endl;
cout << "      6: x50; " << endl;
cout << "      7: x100;" << endl;
cin >> AmpGain;
cout << " " << endl;
status = SetAmpGain( scsi_id, AmpGain );
if ( status != 1 )
{
printf( "SetAmpGain = %d\n", status );
return 0;
}

// A/D Converter Control.
// Return Value: 1 - Normal completion; and other than 1 with an error
// Status acquisition: 0 - 12bit (1MHz); 1 - 16bit (250KHz)
status = SetADType( scsi_id, 1 );
if ( status != 1 )
{
printf( "SetADType = %d\n", status );
return 0;
}

// Trigger Mode Control.
// Return Value: 1 - Normal completion; and other than 1 with an error
// Status acquisition: 0 - internal trigger; 1 - external trigger; 2 - external start
status = SetTriggerMode( scsi_id, 0 );
if ( status != 1 )
{
printf( "SetTriggerMode = %d\n", status );
return 0;
}

// Delay Time of External Start Control.
// Return Value: 1 - Normal completion; and other than 1 with an error
// Status acquisition: 0..65535 ms range
status = SetDelayTime( scsi_id, 1 );
if ( status != 1 )
{
printf( "SetDelayTime = %d\n", status );
return 0;
}

// Trigger Polarity Control.
// Return Value: 1 - Normal completion; and other than 1 with an error
// Status acquisition: 0 - positive; 1 - negative
status = SetTriggerPolarity( scsi_id, 0 );
if ( status != 1 )
{
printf( "SetTriggerPolarity = %d\n", status );
return 0;
}

```

```
// PULSE OUT Control.
// Return Value: 1 - Normal completion; and other than 1 with an error
// Status acquisition: 0 - OFF; 1 - ON
status = SetShutterControl( scsi_id, 0 );
if ( status != 1 )
{
printf( "SetShutterControl = %d\n", status );
return 0;
}

// Delay Time of PULSE OUT Control.
// Return Value: 1 - Normal completion; and other than 1 with an error
// Status acquisition: 0..65535 ms range
status = SetShutterDelayTime( scsi_id, 10 );
if ( status != 1 )
{
printf( "SetShutterDelayTime = %d\n", status );
return 0;
}

// Pulse Width of PULSE OUT Control.
// Return Value: 1 - Normal completion; and other than 1 with an error
// Status acquisition: 0..65535 ms range
status = SetShutterDurationTime( scsi_id, 1 );
if ( status != 1 )
{
printf( "SetShutterDurationTime = %d\n", status );
return 0;
}

// Polarity of PULSE OUT Control.
// Return Value: 1 - Normal completion; and other than 1 with an error
// Status acquisition: 0 - positive; 1 - negative
status = SetShutterPolarity( scsi_id, 0 );
if ( status != 1 )
{
printf( "SetShutterPolarity = %d\n", status );
return 0;
}

// Sensor Type Control.
// Return Value: 1 - Normal completion; and other than 1 with an error
// Status acquisition: 0 - InGaAs; 1 - CCD; 2 - InGaAs (Sensor head C8060/61/62)
status = SetSensorType( scsi_id, 1 );
if ( status != 1 )
{
printf( "SetSensorType = %d\n", status );
return 0;
}

// Number of Pixels Control.
// Return Value: 1 - Normal completion; and other than 1 with an error
// Status acquisition: for C7020-S7010-0906
// Number of Active Pixels (512x60); Number of Total Pixels (532x64)
status = SetSensorVch( scsi_id, 64 );
if ( status != 1 )
{
printf( "SetSensorVch = %d\n", status );
```

```

return 0;
}

status = SetSensorHch( scsi_id, 512);
if ( status != 1)
{
printf( "SetSensorHch = %d\n", status );
return 0;
}

// Number of Summing Pixels Control.
// Return Value: 1 - Normal completion; and other than 1 with an error
// Status acquisition: for C7020-S7010-0906
// Number of Active Pixels (512x60); Number of Total Pixels (532x64)

status = SetSummingVch( scsi_id, 64 );
if ( status != 1)
{
printf( "SetSummingVch = %d\n", status );
return 0;
}

status = SetSummingHch( scsi_id, 1 );
if ( status != 1)
{
printf( "SetSummingHch = %d\n", status );
return 0;
}

// Mode Control.
// Return Value: 1 - Normal completion; and other than 1 with an error
// Status acquisition: Area scanning - 0 , line binning - 1 (when using a CCD sensor head)
status = SetModeSelect( scsi_id, 1 );
if ( status != 1)
{
printf( "SetModeSelect (line binning) = %d\n", status );
return 0;
}

// Exposure Time Control.
// Return Value: 1 - Normal completion; and other than 1 with an error
// Status acquisition: 0..65535 ms range
int exposure_time;
cout << " " << endl;
cout << "      Set Exposure Time (100..500 ms range) [default 150]: " << endl;
cin >> exposure_time ;
status = SetExposureTime( scsi_id, exposure_time );
if ( status != 1)
{
printf( "SetExposureTime = %d\n", status );
return 0;
}

// Temperature Control.
// Return Value: 1 - Normal completion; and other than 1 with an error
// Status acquisition: OFF - 0; ON - 1
status = SetPeltierControl( scsi_id, 0 );
if ( status != 1)

```

```

    {
    printf("SetPeltierControl = %d\n", status);
    return 0;
    }
// printf("Peltier Control - OFF \n");

// Peltier Power Control.
// Return Value: 1 - Normal completion; and other than 1 with an error
// Status acquisition: 0 - 5V; 1 - 6V
    status = SetPeltierPower( scsi_id, 0);
    if ( status != 1)
    {
    printf("SetPeltierPower = %d\n", status);
    return 0;
    }

// Temperature Monitor.
// Return Value: 0..1023 - Normal completion;
    status = GetTemperature( scsi_id);
    double temp = 0.0;
    double Temp = 0.0;
    double v = ( double)::GetTemperature( scsi_id) * ( 2.5 / 1023.0);
// Temperature Calculation: Sensor is InGaAs
    WORD SensorType = GetSensorType( scsi_id);
    if ( SensorType = 0) {
        Temp = ( 0.737 - v) / 0.01772;
    }
// Temperature Calculation: Sensor is CCD
    else if ( SensorType = 1) {
        double r = 100.0 / (( 2.5 / v) - 1.0);
        Temp = ( 1.0 / ((log( r / 10.0) / 3450.0) + ( 1.0 / 298.0))) - 273.0;
    }

    if ( status >= 1023)
    {
    printf("GetTemperature = %d\n", status);
    return 0;
    }

    printf(" Temperature (CCD head) = %lf\n", Temp);
    printf(" \n");
    cout << " " << endl;

// *** MEASUREMENT and READING DATA ***

// Channels size
    int channel1_first_pixel;
    int channel2_first_pixel;
    int channel3_first_pixel;
    int channel1_last_pixel;
    int channel2_last_pixel;
    int channel3_last_pixel;
    cout << "      Channel-1 first pixel:      ";
    cin >> channel1_first_pixel;
    cout << "      Channel-1 last pixel:      ";
    cin >> channel1_last_pixel;
    cout << " " << endl;

```

```

cout << "      Channel-2 first pixel:    ";
cin >> channel2_first_pixel;
cout << "      Channel-2 last pixel:    ";
cin >> channel2_last_pixel;
cout << " " << endl;
cout << "      Channel-3 first pixel:    ";
cin >> channel3_first_pixel;
cout << "      Channel-3 last pixel:    ";
cin >> channel3_last_pixel;
cout << " " << endl;

for (;;) {
int number_of_measurement, T;
cout << "      Number (n) / Time (min) of measurement? " << endl;
cout << "      If n = 0 than singleshot measurement!" << endl;
cin >> T;
cout << "      " << endl;

int a;
const int arraySize = 1024;
WORD Data[ arraySize ];
const WORD NumberOfCycles = 2;
char file_name[100];
float channel1;
float channel2;
float channel3;
float first_ave_data_1, raznost1;
float first_ave_data_2, raznost2;
float first_ave_data_3, raznost3;

int tm;
int cycle_time;
double dif_time;
cout << "      Set delay time (sec) " << endl;
cin >> tm;
cout << " " << endl;

cycle_time = tm + exposure_time/1000; // Cycle time in seconds
number_of_measurement = (int) floor(T * 60 / cycle_time) + 1;

cout << "Number of measurements: " << number_of_measurement << "\n";

cout << "      Input average data file name (*.dat):" << endl;
cin >> file_name;
strcat( file_name, ".dat" );
cout << " " << endl;
FILE *channels;
channels = fopen( file_name, "w" );

cout << "      Press ENTER to start..." << endl;
getchar();
cout << " " << endl;

//Time Measurements Unit
time( &start_time );
for(int duration = 0; duration < number_of_measurement; duration++) {
    status = GetProfile( scsi_id, NumberOfCycles, Data );
    time( &cur_time );
}

```

```

dif_time = difftime(cur_time, start_time);

// "Spectrum": pixels v intensity
for( a = 0; a < 512; a++)
    printf( "%d\t%d\n", a, Data[a] );

if ((duration % 5) == 0)
    printf("Current step: %d/%d,\n\tTime elapsed (min): %.2g\n\tEstimated time left (min):
%.2g\n",
          duration,          number_of_measurement,          dif_time/60.0,
dif_time/60.0*(number_of_measurement-duration)/duration);

// Make a delay (tm) seconds
Sleep(tm*1000); // sleep for (tm) seconds

// Channel-1 Average:
channel1 = 0.0;
for( int b = channel1_first_pixel; b < channel1_last_pixel; b++) {
    channel1 += Data[b];
}
channel1 /= (channel1_last_pixel - channel1_first_pixel);

// Channel-1 Raznost:
raznost1 = 0.0;
if( duration == 0) first_ave_data_1 = channel1;

// Channel-1 Delta:
double Delta1 = 0.0;
for ( int bb = channel1_first_pixel; bb < channel1_last_pixel; bb++){
    Delta1 += ( Data[bb] - channel1 ) * ( Data[bb] - channel1 );
}
Delta1 = sqrt ( Delta1 / (( channel1_last_pixel - channel1_first_pixel) - 1));

// Channel-2 Average
channel2 = 0.0;
for( int c = channel2_first_pixel; c < channel2_last_pixel; c++) {
    channel2 += Data[c];
}
channel2 /= ( channel2_last_pixel - channel2_first_pixel);

// Channel-2 Raznost:
raznost2 = 0.0;
if( duration == 0) first_ave_data_2 = channel2;

// Channel-2 Delta:
double Delta2 = 0.0;
for ( int cc = channel2_first_pixel; cc < channel2_last_pixel; cc++){
    Delta2 += ( Data[c] - channel2 ) * ( Data[c] - channel2 );
}
Delta2 = sqrt ( Delta2 / (( channel2_last_pixel - channel2_first_pixel) - 1));

// Channel-3 Average
channel3 = 0.0;
for( int d = channel3_first_pixel; d < channel3_last_pixel; d++) {
    channel3 += Data[d];
}
channel3 /= (channel3_last_pixel - channel3_first_pixel);

```

```

// Channel-3 Raznost:
    raznost3 = 0.0;
    if( duration == 0) first_ave_data_3 = channel3;

// Channel-3 Delta:
    double Delta3 = 0.0;
    for ( int dd = channel3_first_pixel; dd < channel3_last_pixel; dd++){
        Delta3 += ( Data[d] - channel3 ) * ( Data[d] - channel3 );
    }
    Delta3 = sqrt ( Delta3 / ((channel3_last_pixel - channel3_first_pixel) - 1));

//Save Average Data to File
    double real_data_time;
    real_data_time = duration * tm / 60.0;
    fprintf( channels, "%.3f\t%.1f\t%.1f\t%.1f\n", real_data_time, channel1, channel2,
channel3 );

// Save Average and Delta to File:
//    fprintf( channels, "%.3f\t%.1f\t%.1f\t%.1f\t%.1f\t%.1f\t%.1f\n", real_data_time,
channel1, channel2, channel3, Delta1, Delta2, Delta3 );

//End of Time Measurements Unit
    }

    fclose( channels );

    cout << "        Input 'spectrum' data file name (*.dat): " << endl;
    cin >> file_name;
    strcat( file_name, ".dat" );
    FILE *data;
    data = fopen( file_name, "w" );
    for( a = 0; a < 512; a++)
        fprintf( data, "%d\t%d\n", a, Data[a] );
    fclose( data );

    if ( status != 1)
    {
        printf( "GetProfile = %d\n", status );
        return 0;
    }

//Raznost I_0 - I_last:
    cout << " " << endl;
    raznost1 = channel1 - first_ave_data_1;
    printf("Delta I_1 = %.3f\n", raznost1);

    raznost2 = channel2 - first_ave_data_2;
    printf("Delta I_2 = %.3f\n", raznost2);

    raznost3 = channel3 - first_ave_data_3;
    printf("Delta I_3 = %.3f\n", raznost3);

    cout << " " << endl;
    cout << "        Input Delta_I data file name (*.dat):" << endl;
    cin >> file_name;
    strcat( file_name, ".dat" );
    cout << " " << endl;
    FILE *raznost;

```

```
raznost = fopen( file_name, "w" );
fprintf( raznost, "%.3f\t%.3f\t%.3f\t", raznost1, raznost2, raznost3 );
fclose( raznost);

cout << " " << endl;
cout << "*****" << endl;
char bukva;
cout << " " << endl;
cout << "      EXIT ? (y/n)\n" << endl;
cin >> bukva ;
if ( bukva == 'y' ) return 1;
}

return 1;
}
```

## Appendix B

### Total Internal Reflection Ellipsometry: modelling and comparison

Here the methods of external reflection ellipsometry and TIRE are compared by the modelling of their responses to the changes in the thickness and refractive index of thin dielectric film deposited on the surface of gold.

The modelling of the response of TIRE and conventional ellipsometry to changes in the dielectric film thickness and refractive index was performed using the WVASE-32<sup>®</sup> software (J. A. Woollam Co.).

The calculations of  $\Psi$  and  $\Delta$  spectra were performed for both external reflection ellipsometry and TIRE in both media (air and water) by solving the main ellipsometry equation:  $\rho = tn\Psi e^{i\Delta}$  for different thicknesses (varied from 0 to 30 nm with the step of 5 nm) and fixed refractive index of the dielectric layer ( $A = 1.45$ ,  $B = 0.01$ ,  $C = 0$ ) or vice-versa for the fixed thickness ( $d = 10$  nm) and varied refractive index ( $A$  varied from 1.2 to 1.8 with the step of 0.1,  $B = 0.01$ ,  $C = 0$ ).

The results of such calculations for the in air' medium are shown in Figs. B1-B4. As one can see, the external reflection ellipsometry does not show any peculiarities in  $\Psi$  and  $\Delta$  spectra in Figs. B1 and B2. The dependences of  $\Psi$  and  $\Delta$  values at the selected wavelength of 633 nm shown in Fig. B1c are close to linear with the gradients of 0.15 and 0.63 deg/nm, respectively. This means that  $\Delta$  is about 4 times more sensitive than  $\Psi$  to changes in the thickness of dielectric film. The sensitivity towards changes in refractive index is nearly 10 times higher for  $\Delta$  (1.2 deg/step) than for  $\Psi$  (0.13 deg/step) as shown in Fig. B2c.

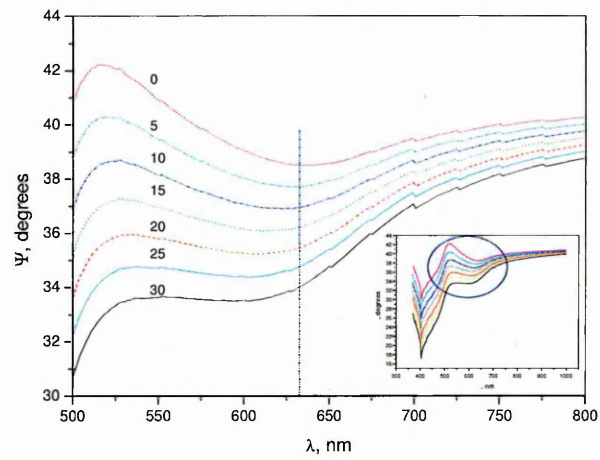
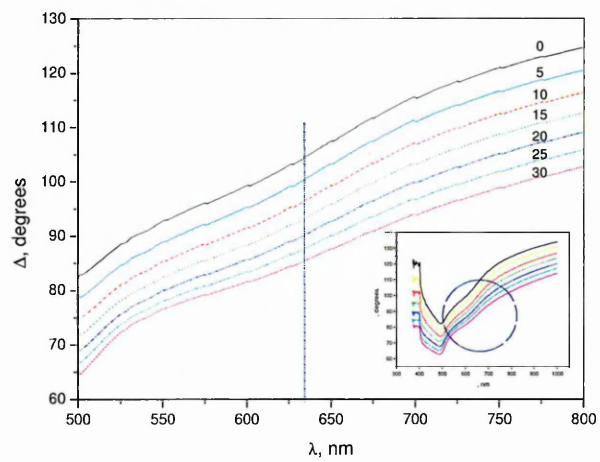
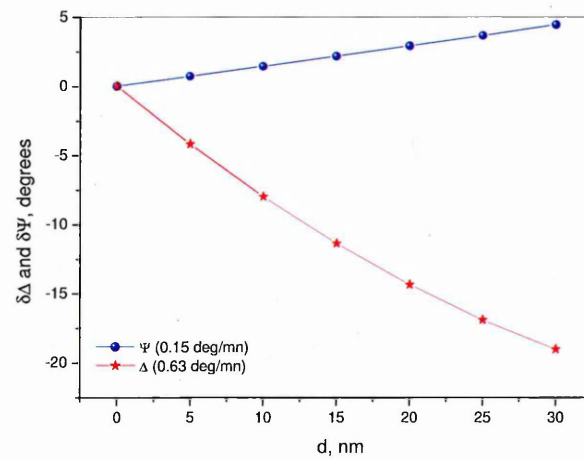
Completely different behaviour of  $\Psi$  and  $\Delta$  spectra is observed in the case of TIRE (see Figs. B3 and B4). Both the  $\Psi$  and  $\Delta$  spectra show peculiarities:  $\Psi(\lambda)$  spectra (Figs. B3a and B4a) resembles typical SPR curve, with the reflected intensity reaching the minimum at the plasmon resonance conditions, while the  $\Delta(\lambda)$  spectra (Figs. B3b

and B4b) demonstrate a sharp drop in the phase from  $270^\circ$  down to  $-90^\circ$  near the resonance.

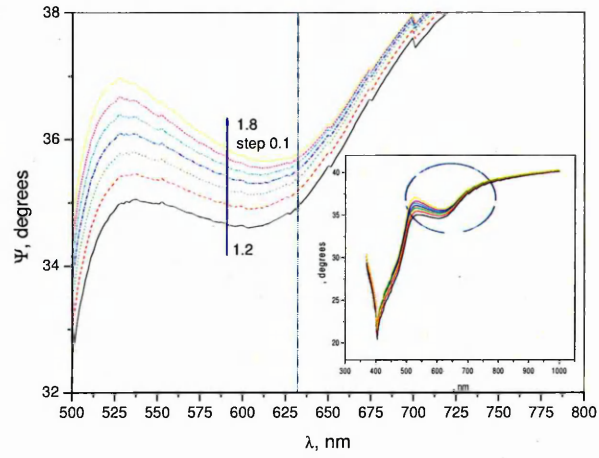
The dependencies of  $\Psi$  and  $\Delta$  values at selected wavelengths in Figs. B3c and B4c are much more pronounced, as compared to external reflection ellipsometry spectra in Figs. B1c and B2c, yielding much higher respective gradients of 0.67 deg/nm and 1.13 deg/step for  $\Psi$  and 6.4 deg/nm and 11.7 deg/step for  $\Delta$ .

In addition to this, the changes in the optical parameters of dielectric film can be monitored by plotting the value of a spectral shift for both  $\Psi$  and  $\Delta$  at selected levels (see Figs. B3d and B4d). This gives the possibility of another type of kinetics study by monitoring the spectral shift in the course of a chemical (bio-) reaction. Surprisingly the shift in  $\Delta$  is only slightly (1.5 to 2 times) higher than that in  $\Psi$ .

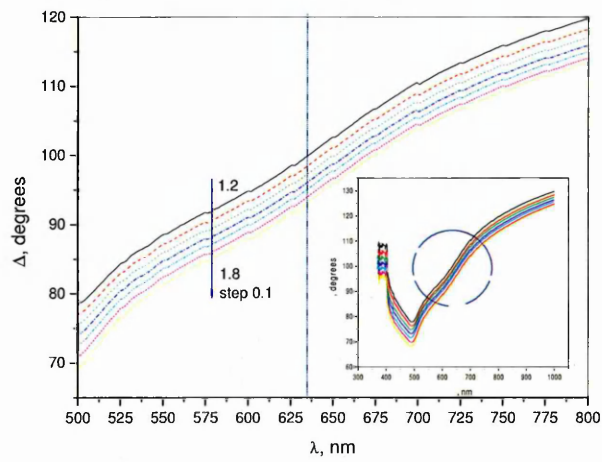
Similar calculations have been done for the aqueous medium. The values of gradients and spectral shifts obtained by the modelling of  $\Psi(\lambda)$  and  $\Delta(\lambda)$  spectra for external and internal reflection ellipsometry in both air and water media are presented in Table B1.


**a**

**b**

**c**

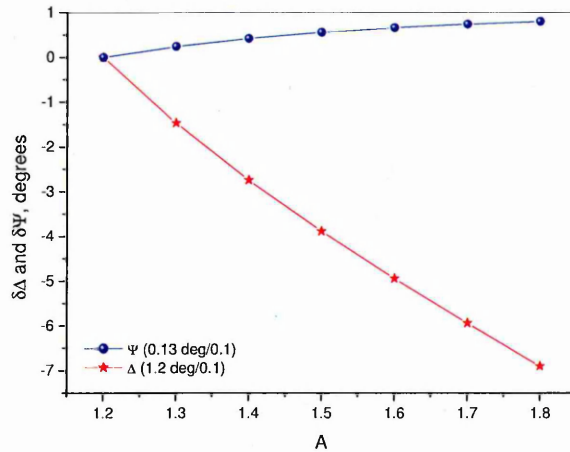
**Figure B1** Results of the modelling of external reflection ellipsometry in air ( $A = 1.45$ ,  $d$  is variable): **a** –  $\Psi(\lambda)$  spectra; **b** –  $\Delta(\lambda)$  spectra, **c** – changes in  $\Psi$  and  $\Delta$  at a fixed wavelength.



a

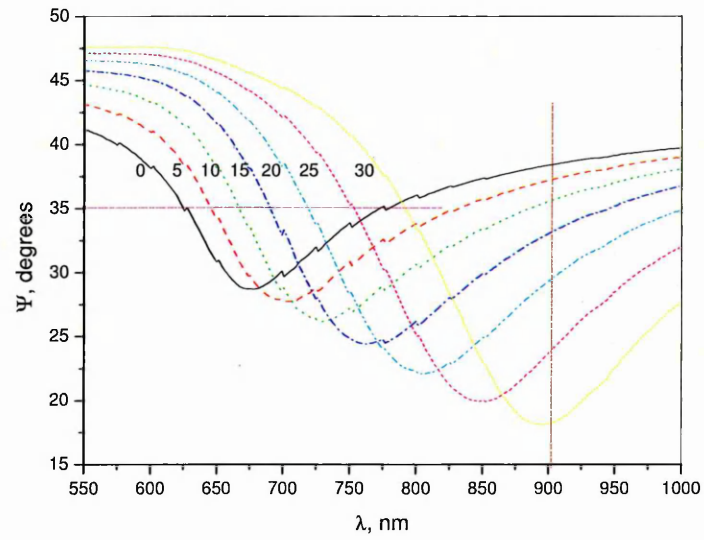


b

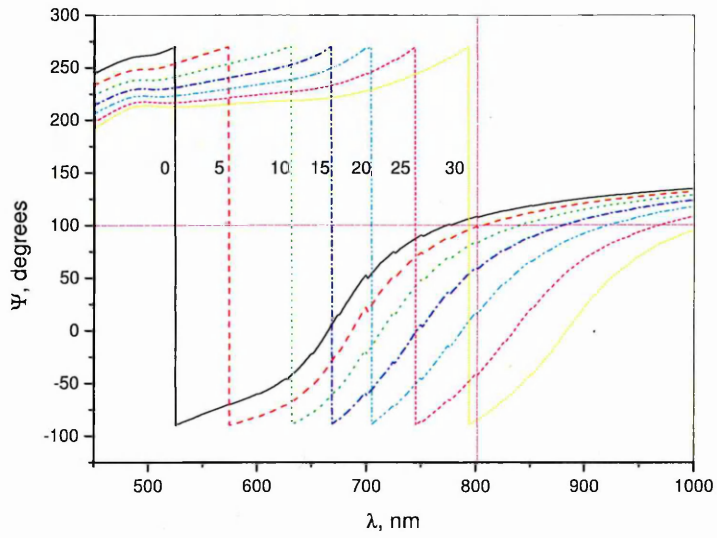


c

**Figure B2** Results of the modelling of external reflection ellipsometry in air ( $d = 10$  nm,  $A$  is variable): **a** –  $\Psi(\lambda)$  spectra; **b** –  $\Delta(\lambda)$  spectra, **c** – changes in  $\Psi$  and  $\Delta$  at a fixed wavelength.

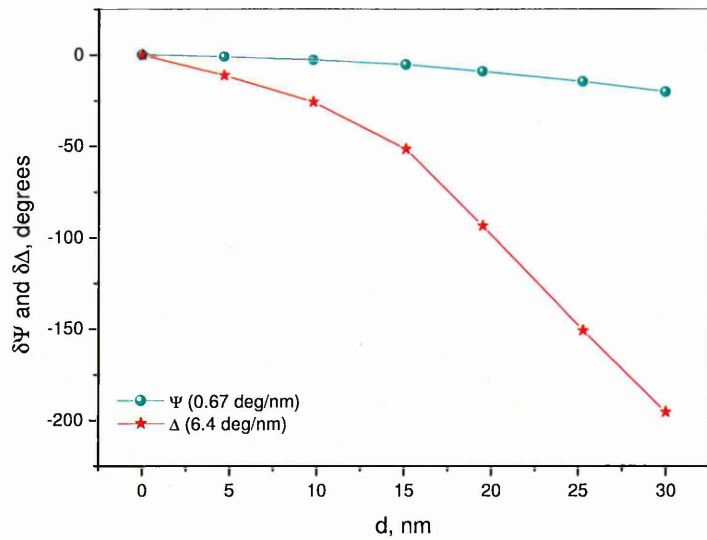


**a**

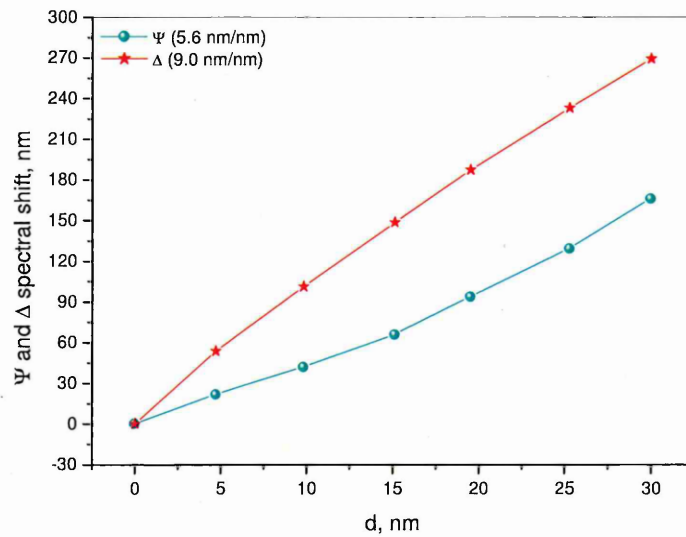


**b**

**Figure B3-1** Results of the modelling of TIRE in air ( $A = 1.45$ ,  $d$  is variable): **a** –  $\Psi(\lambda)$  spectra; **b** –  $\Delta(\lambda)$  spectra.

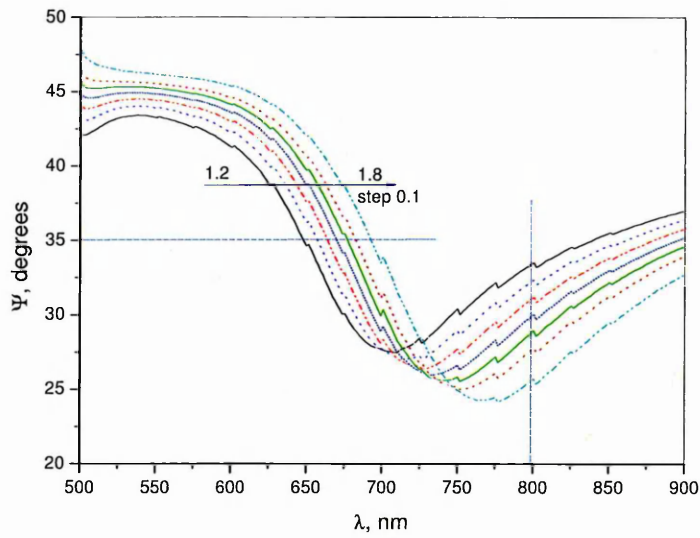


c

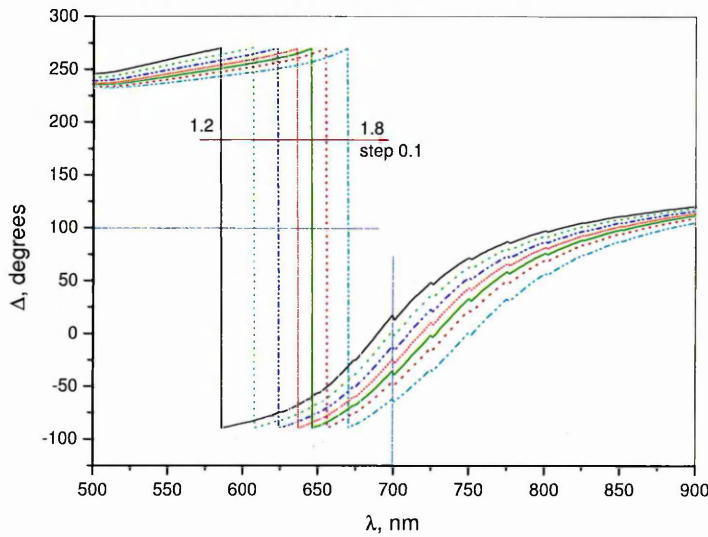


d

**Figure B3-2** Results of the modelling of TIRE in air ( $A = 1.45$ ,  $d$  is variable): **c** – changes in  $\Psi$  and  $\Delta$  at a fixed wavelength, **d** – spectral shift of  $\Psi$  and  $\Delta$ .

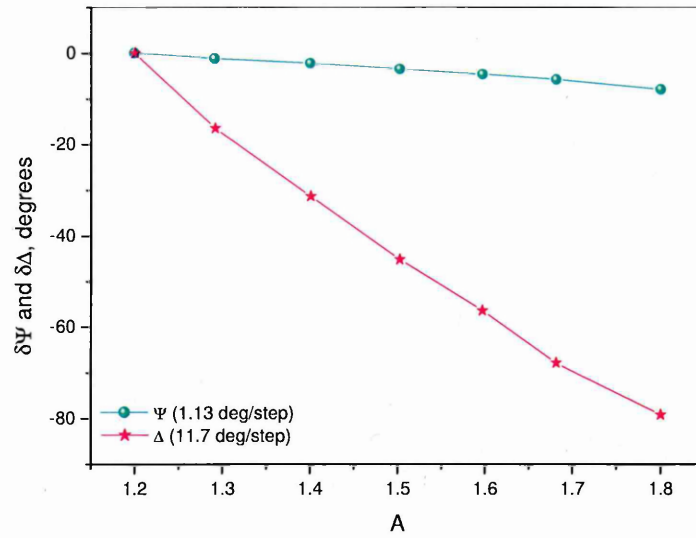


**a**

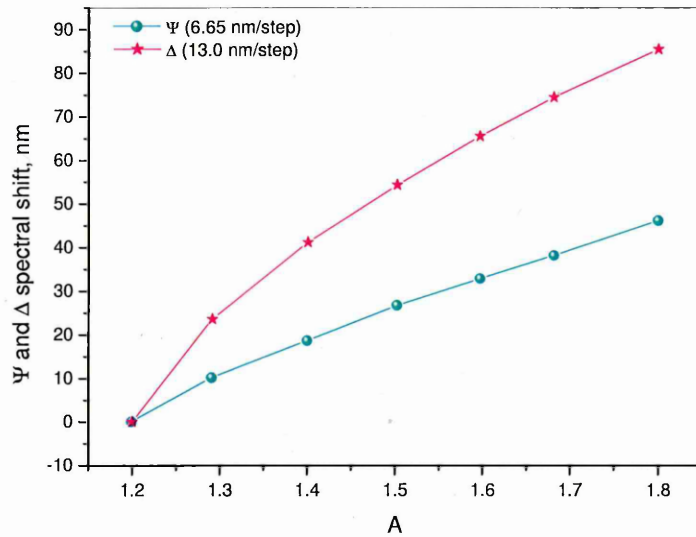


**b**

**Figure B4-1** Results of the modelling of TIRE in air ( $d = 10$  nm,  $A$  is variable): **a** –  $\Psi(\lambda)$  spectra; **b** –  $\Delta(\lambda)$  spectra.



c



d

**Figure B4-2** Results of the modelling of TIRE in air ( $d = 10$  nm,  $A$  is variable): **c** – changes in  $\Psi$  and  $\Delta$  at a fixed wavelength; **d** – spectral shift of  $\Psi$  and  $\Delta$ .

**Table B1** The values of gradients and spectral shifts for external and internal reflection ellipsometry

<i>Parameter</i>	<i>external reflection ellipsometry (in air)</i>	<i>TIRE (in air)</i>	<i>TIRE (in water)</i>
$\delta\Psi$ (deg/nm)	0.15	0.67	0.21
$\delta\Delta$ (deg/nm)	0.63	6.4	2.1
$\delta\Psi$ (deg/0.1step)	0.13	1.13	1.28
$\delta\Delta$ (deg/0.1step)	1.2	11.7	13.2
$\Psi$ spectral shift (nm/nm)		5.6	2.8
$\Delta$ spectral shift (nm/nm)		9.0	3.4
$\Psi$ spectral shift (nm/0.1step)		6.65	18
$\Delta$ spectral shift (nm/0.1step)		13.0	20.6

## Conclusions

The modelling of the response of external and internal reflection ellipsometry to changes in the thickness and refractive index of thin dielectric coating on the surface of gold showed that TIRE was generally 10 times more sensitive than conventional external reflection ellipsometry.

Within the TIRE method, the spectra of the phase related parameter  $\Delta$  was about 10 times more sensitive than the spectra of the amplitude related parameter  $\Psi$ , which was similar to traditional SPR curves. In other words, the phase SPR measurements were more sensitive than conventional SPR, and therefore can be used for various applications in thin film characterisation and sensing.

## Appendix C

### Introduction to the Artificial Neuron Network

The ANN consists of simple processing elements or "*neurons*" grouped together. A typical artificial neuron and the modeling of a multilayered neural network are illustrated in Fig.C1. In this configuration, the information enters the network at the *input* layer and is fed forward through the *hidden* layer until it reaches the *output* layer.

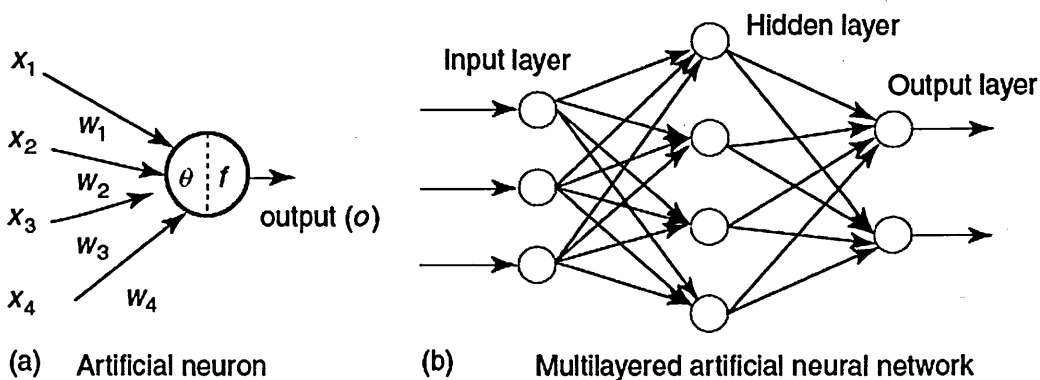


**Figure C1** Architecture of an artificial neuron and a multilayered neural network (after Ref.<sup>[1]</sup>).

The activity of the *input* units represents the raw information that is fed into the network. Each neuron in the input layer is connected to every neuron in the hidden layer.

The activity of each *hidden* unit is determined by the activities of the input units and the weights of the connections between the input and the hidden units. The number of hidden neurons affects how well the network is able to separate the data. A large number of hidden neurons will ensure correct learning, and the network will be able to correctly predict the data it has been trained on, but its performance on new data and its ability to generalize, will be compromised. With too few hidden neurons, the network may be unable to learn the relationships amongst the data and the error will fail to fall below an acceptable level. Each hidden layer neuron in turn is connected to every neuron in the next output layer. The behaviour of the *output* units depends on the activity of the hidden units and the weights between the hidden and output units.

Each neuron has a certain number of inputs, each of which have a *weight* assigned to them. The weight is an indication of how “important” the incoming signal is for that input. The *net* value of the neuron is then calculated – the net is the weighted sum of all the inputs multiplied by their specific weight.

Each neuron has its own unique threshold value, and if the net is greater than the threshold, the neuron fires (output is 1), otherwise it stays quiet (output is 0). The output is then fed into all of the neurons it is connected to.

The neurons in both the hidden layer and the output layer have a non-linear transfer function to their summed inputs. The combination of non-linear transfer functions and the large number of connections allows the ANN to model complex relationships between its inputs and outputs. The neuron output signal  $O$  is given by the following relationship:

$$O = f(\text{net}) = f\left(\sum_{j=1}^n w_j x_j\right), \quad (\text{C1})$$

where  $w_j$  is the weight factor,  $x_j$  input signal, and  $f(\text{net})$  is an activation function. The variable *net* is defined as a scalar product of the weight and input vectors:

$$\text{net} = w_1 x_1 + \dots + w_n x_n. \quad (\text{C2})$$

There are many different activation functions; one of the most commonly used is the hyperbolic tangent:

$$f(S) = \frac{\exp(S) - \exp(-S)}{\exp(S) + \exp(-S)}, \quad (\text{C3})$$

where  $S$  is the sum of  $n$  weighted input signals:

$$S = \sum_{j=1}^n w_j x_j. \quad (\text{C4})$$

ANN typically requires a large set of data. Generally, the networks are trained, so that a particular input leads to a specific target output. During training, the weights of the network are adjusted to minimize the average squared error between the network outputs ( $a$ ) and the target outputs ( $t$ ), normally known as mean squared error (MSE):

$$\text{MSE} = \frac{1}{n} \sum_{i=1}^n (e_i)^2 = \frac{1}{n} \sum_{i=1}^n (t_i - a_i)^2. \quad (\text{C5})$$

where  $n$  is the total number of the network inputs.

The weights of the network are optimised by several different training algorithms, such as Levenberg-Marquardt, backpropagation, etc.<sup>[2]</sup>.

## References

---

- [1] Abraham A. *Artificial Neural Networks* in *Handbook of Measuring System Design*, Ed. Sydenham P. H. and Thorn R., John Wiley & Sons Ltd., 2005.
- [2] [http://en.wikipedia.org/wiki/Artificial\\_neural\\_network](http://en.wikipedia.org/wiki/Artificial_neural_network) (accessed 28 May 2007).

## Appendix D

### AFM Data Definition

The data definitions and abbreviation descriptions that appear in the AFM images are given below. All information is taken from "*NanoScope Command Reference Manual. v.5.12*" by  and .

#### 1. Image information.

**Scan rate** – The Scan Rate sets the number of fast scan lines performed per second.

**Number of samples** – Number of data points collected during each upward (retraction) and downward (extension) travel cycle of the piezo.

#### 2. Roughness data definition

The *Roughness* command generates statistics for surfaces. “Image” statistics are reported for the entire image. “Box” statistics are reported only for the region defined within a cursor box.

##### 2.1. Image Statistics

**Img. Z range** – Maximum vertical distance between the highest and lowest data points in the image (same as *Img. R<sub>max</sub>*).

**Img. Rms (*R<sub>q</sub>*)** – Root mean square average of height deviations taken from the mean

data plane, expressed as: 
$$R_q = \sqrt{\frac{\sum Z_i^2}{n}}$$

**Img. *R<sub>a</sub>*** – Arithmetic average of the absolute values of the surface height deviation

measured from the mean plane: 
$$R_a = \frac{1}{n} \sum_{j=1}^n |Z_j|.$$

**Img. *R<sub>max</sub>*** – Maximum vertical distance between the highest and lowest data points in the image.

## 2.2 Box Statistics

**Rms ( $R_q$ )** – This is the standard deviation of the Z values within the box cursor and is

calculated as:  $R_q = \sqrt{\frac{\sum Z_i^2}{n}}$ , where  $Z_i$  is the current Z value, and  $n$  is the number of points within the box cursor.

**Mean Roughness ( $R_a$ )** – Arithmetic average of the absolute values of the surface height

deviation measured from the mean plane within the box cursor:  $R_a = \frac{1}{n} \sum_{j=1}^n |Z_j|$ .

**Max peak ht ( $R_p$ )** – Maximum peak height within the analyzed area with respect to the mean data plane.

**Max depth ( $R_v$ )** – Lowest data point in examined region.

**Z range** – Peak-to-valley difference in height values within the analyzed region.

**Mean** – The average of all the Z values within the enclosed area. The mean can be a negative value because the Z values are measured relative to the Z value when the microscope is engaged.

## 3. Particle analysis data

The *Particle Analysis* command defines particles based on the height of pixel data. This analysis is designed for analyzing well isolated particles. Particles may be analyzed singly or in quantities. *Particles* in this context, are conjoined pixels above or below a given threshold height. The analysis includes a histogram of particle size, which can be used to identify specific particles by size. Measurements on this analysis include: the mean area and standard deviation (sigma) of the particle sizes, the total number of particles, a correlation histogram, a bearing ratio curve and a depth histogram.

## 4. Section analysis

The *Section* command displays a top view image, upon which reference line may be drawn. The cross-sectional profiles and fast Fourier transform (FFT) of the data along the reference line are shown. Roughness measurements are made of the surface

along the reference line defined. The *Section* command does not reveal what is below the surface – only the profile of the surface itself.

### *Section Data Definitions*

***L*** – Length of the roughness curve.

***RMS*** (Standard Deviation) — Standard deviation of the *Z* values between the reference

markers, calculated as follows:  $RMS = \sigma = \sqrt{\frac{\sum (Z_i - Z_{ave})^2}{n}}$ , where  $Z_i$  is the current *Z*

value,  $Z_{ave}$  is the average of the *Z* values between the reference markers, and *N* is the number of points between the reference markers.

***l<sub>c</sub>*** – Cut-off length (in nanometers) of the high-pass filter used in creating the roughness curve. The FFT period is equal to  $l_c$ .

***R<sub>a</sub>*** (Mean Roughness) – Mean value of the roughness curve relative to the center line,

calculated as:  $R_a = \frac{1}{L} \int_0^L |f(x)| dx$ , where *L* is the length of the roughness curve and  $f(x)$

is the roughness curve relative to the center line.

***R<sub>max</sub>*** (Maximum Height) – Difference in height between the highest and lowest points on the cross-sectional profile relative to the center line (not the roughness curve) over the length of the profile, *L*.

***R<sub>z</sub>*** (Ten-Point Mean Roughness) – Average difference in height between the five highest peaks and five lowest valleys relative to the center line over the length of the profile, *L*. In cases where five pairs of peaks and valleys do not exist, this is based on fewer points.

## Appendix E

### Abstracts of the published papers

1. Nabok A., Tsargorodskaya A., Holloway A., Starodub N. F., Demchenko A. *Specific binding of large aggregates of amphiphilic molecules to respective antibodies*, *Langmuir* **23** (2007) 8485-8490.

**Abstract:** The binding of nonylphenol to respective antibodies immobilized on solid substrates was studied with the methods of total internal reflection ellipsometry (TIRE) and QCM (quartz crystal microbalance) impedance spectroscopy. The binding reaction was proved to be highly specific having an association constant of  $K_A = 1.6 \times 10^6 \text{ mol}^{-1} \text{ L}$  and resulted in an increase in both the adsorbed layer thickness of 23 nm and the added mass of  $18.3 \mu\text{g}/\text{cm}^2$  at saturation. The obtained responses of both TIRE and QCM methods are substantially higher than anticipated for the immune binding of single molecules of nonylphenol. The mechanism of binding of large aggregates of nonylphenol was suggested instead. Modelling of the micelle of amphiphilic nonylphenol molecules in aqueous solutions yielded a micelle size of about 38 nm. The mechanism of binding of large molecular aggregates to respective antibodies can be extended to other hydrophobic low-molecular-weight toxins such as T-2 mycotoxin. The formation of large molecular aggregates of nonylphenol and T-2 mycotoxin molecules on the surface was proved by the AFM study.

2. Nabok A. V., Tsargorodskaya A. *The method of total internal reflection ellipsometry for thin films' characterisation and sensing*, *Thin Solid Films* (2007) accepted.

**Abstract:** Recently developed method of Total Internal Reflection Ellipsometry (TIRE) represents a very successful combination of the spectroscopic ellipsometry instrumentation with the Kretschmann type Surface Plasmon Resonance (SPR) geometry of the experiment. The modelling shows much higher sensitivity of the TIRE method to small changes in optical parameters (thickness and refractive index) of thin films, as compared to both traditional external reflection ellipsometry and SPR. Considering another advantage of performing the measurements in media of different optical density (and even opaque media), TIRE becomes very convenient for different sensing applications in both gaseous and liquid media, as well as for thin film characterisation. This work presents examples of applications of the TIRE method for the study of DNA hybridization and the registration of low molecular weight toxins.

3. Nabok A. V., Tsargorodskaya A., Holloway A., Starodub N. F., Gojster O. *Registration of T-2 mycotoxin with total internal reflection ellipsometry and QCM impedance methods*, *Biosensors and Bioelectronics* **22** (2007) 885-890.

**Abstract:** A sensitive optical method of total internal reflection ellipsometry (TIRE) in conjunction with immune assay approach was exploited for the registration of T-2 mycotoxin in a wide range of concentrations from  $100 \mu\text{g}/\text{ml}$  down to  $0.15 \text{ ng}/\text{ml}$ . Association constants of  $1.4 \cdot 10^6$  and  $1.9 \cdot 10^7 \text{ mol}^{-1} \text{ s}$  for poly- and monoclonal T-2 antibodies, respectively, were evaluated from TIRE kinetic measurements. According to TIRE data fitting, binding of T-2 molecules to antibodies (at saturation) has resulted in the increase in adsorbed layer thickness of 4-5 nm. The QCM impedance measurements data showed anomalously large mass increase and film softening, most likely, due to the binding of large T-2 aggregates to antibodies.

4. Nabok A. V., Tsargorodskaya A., Hassan A. K., Starodub N. F. *Total internal reflection ellipsometry and SPR detection of low molecular weight environmental toxins*, Applied Surface Science **246** (2005) 381-386.

**Abstract:** The environmental toxins, such as herbicides simazine and atrazine, and T2 mycotoxin were registered with the optical methods of surface plasmon resonance (SPR) and recently developed total internal reflection ellipsometry (TIRE). The immune assay approach was exploited for in situ registration of the above low molecular weight toxins with specific antibodies immobilised onto the gold surface via (poly)allylamine hydrochloride layer using electrostatic self-assembly (ESA) technique. The comparison of two methods of SPR and TIRE shows a higher sensitivity of the latter.

5. Tsargorodskaya A., Nabok A. V., Ray A. K. *Ellipsometric study of adsorption of BSA into porous silicon*, Nanotechnology **15** (2004) 703-709.

**Abstract:** The method of spectroscopic ellipsometry has been applied to study in situ the adsorption of bovine serum albumin (BSA). The porosity and amount of adsorbed bsa were determined by fitting the ellipsometric data to the Bruggeman effective medium approximation model. The presence of intermediate adsorbed layers of polyelectrolytes was found to increase protein adsorption.